

SYNTHESIS, FABRICATION, AND CHARACTERIZATION OF POLYMERS- CARBON BASED FLEXIBLE NANOGENERATOR FOR ENERGY HARVESTING APPLICATIONS

**A Thesis Submitted
in Partial Fulfilment of the Requirements
for the Degree of**

DOCTOR OF PHILOSOPHY

By

**SHILPA RANA
(2K19/PHD/AP/08)**

Under the Supervision of

Dr. BHARTI SINGH

Assistant Professor
Departement of Applied Physics
Delhi Technological University



**DEPARTMENT OF APPLIED PHYSICS
DELHI TECHNOLOGICAL UNIVERSITY
(Formerly Delhi College of Engineering)
Shahbad Daultapur, Main Bawana Road, Delhi-110042. India**

August 2025

© Delhi Technological University (DTU), 2025
All rights reserved.

DEDICATION

This dissertation is dedicated to my family and supervisor.

ACKNOWLEDGEMENT

First and foremost, I thank the Almighty for granting me fortitude and resilience required to navigate these years of commitment and hard work. This acknowledgment is a small but heartfelt token of appreciation for all those who supported and guided me along this journey.

I sincerely thank my supervisor, **Dr. Bharti Singh**, for her excellent mentorship, invaluable support, and continuous support which help me navigate the complex aspects of this research. I am deeply appreciative of her insightful advice, constructive feedback, and constant encouragement, which have all contributed to the successful completion of my thesis. Her mentorship not only enriched my academic development but also taught me invaluable lessons that extend beyond the realm of research. I am truly fortunate to have had the privilege to work under her guidance, and I will carry forward the lessons she has imparted with immense respect and gratitude. For all of this and more, I am sincerely thankful and will always remain deeply indebted to her.

My sincere thanks also go to **Prof. Prateek Sharma** Hon'ble Vice-Chancellor, DTU for providing marvellous research environment and ample research facilities to conduct this research. I extend my sincere gratitude to **Prof. Rinku Sharma**, Dean (Academic-PG), DTU, and **Prof. Vinod Singh**, Head of the Department of Applied Physics, DTU, along with all the faculty and staff members, for their support and cooperation throughout my research journey.

My heartfelt thanks to **Prof. Nitin K. Puri**, **Dr. Amrish Panwar**, and **Dr. Renuka Bakolia** for creating a supportive research environment and providing essential resources. I am deeply grateful for their insightful discussions, invaluable guidance, and the trust they placed in me throughout my research, as well as for granting me access to their lab facilities.

I am immensely grateful to my seniors **Dr. Vishal Singh** and **Dr. Km. Komal** who stood by me unwaveringly, serving as pillars of support through every high and low. The memories we shared will forever hold a special place in my heart, and bidding farewell to this chapter leaves me with a profound sense of nostalgia. I am truly grateful for the friendship and camaraderie we've cultivated. The laughter, the shared experiences, and the bonds forged during our time together will remain etched in my memory as cherished

moments of joy and companionship. Their support and companionship have undoubtedly left a lasting impression on me, for which I am immensely thankful. I am grateful to my labmates, **Mrs. Rekha, Mr. Praveen, Ms. Ankita Dahiya, and Mr. Dibayjyoti** for their enthusiasm, fresh perspectives, and willingness to assist whenever needed. Your energy and curiosity have been a wonderful source of motivation.

A special thanks to my close friend **Ms. Naima Tyagi**, whose unwavering support, encouragement, and companionship have been a constant source of strength throughout this journey. Your friendship has been my anchor during challenging times, filling my days with laughter, warmth, and positivity. Thank you for standing by me through every high and low, for cheering on my successes, and for lifting my spirits whenever I felt overwhelmed. Furthermore, I wish to express my gratitude to my friends at DTU, including **Dr. Sakshi Verma, Ms. Megha Narwan, Mr. Sunil, Mr. Hemant Arrora, Mr. Jasveer, Ms. Ankita Banwal, Mr. Surya, Ms. Umang, Dr. Ritika Khatri, and Dr. Nikita Jain** for their unwavering technical guidance, valuable suggestions, and support throughout this journey. I am deeply thankful for the enriching discussions and invaluable guidance they provided throughout our research endeavors. I am incredibly fortunate to have friends like you, and I will always cherish the memories we've created together during this journey.

I am profoundly grateful to my father, **Mr. Shiv Charan Rana**, and my mother **Mrs. Anita Rana**, who mean the world to me and have always given me the freedom to follow my own path. I deeply admire them for their selfless love, care, sacrifices, and unwavering support in shaping my life. I would also like to express my heartfelt gratitude to my brother, **Mr. Sagar Rana**, and my sisters, **Ms. Nicky Rana** and **Ms. Nidhi Rana**, for their belief in me, as well as their kindness and understanding. They have always encouraged me to think beyond the ordinary and strive for excellence, pushing me to step outside my comfort zone and explore new horizons. Their infectious laughter and lighthearted presence have been a source of comfort, brightening my challenging Ph.D. journey and offering moments of joy and innocence. I dedicate this achievement to their boundless encouragement and love.

Shilpa Rana



DELHI TECHNOLOGICAL UNIVERSITY

(Govt. of National Capital Territory of Delhi)

Shahbad Daultpur, Bawana Road, Delhi-110042

CANDIDATE'S DECLARATION

I, **Ms. Shilpa Rana (2K19/PHD/AP/08)**, hereby certify that the work which is being presented in the thesis entitled “**Synthesis, Fabrication, and Characterization of Polymers-Carbon based Flexible Nanogenerator for Energy Harvesting Applications**” in partial fulfillment of the requirements for the award of the Degree of Doctor of Philosophy, submitted in the Department of Applied Physics, Delhi Technological University is an authentic record of my own work carried out during the period from **July 2019 to August 2025** under the supervision of **Dr. Bharti Singh, Department of Applied Physics, Delhi Technological University.**

The matter presented in the thesis has not been submitted by me for the award of any other degree of this or any other Institute.

Candidate's Signature

This is to certify that the student has incorporated all the corrections suggested by the examiners in the thesis and the statement made by the candidate is correct to the best of our knowledge.

Signature of Supervisor

Signature of External Examiner



DELHI TECHNOLOGICAL UNIVERSITY

(Govt. of National Capital Territory of Delhi)

Shahbad Daulatpur, Bawana Road, Delhi-110042

CERTIFICATE BY THE SUPERVISOR

Certified that **Ms. Shilpa Rana** (2K19/PHD/AP/08) has carried out her research work presented in this thesis entitled **“Synthesis, Fabrication, and Characterization of Polymers-Carbon based Flexible Nanogenerator for Energy Harvesting Applications”** for the award of Doctor of Philosophy from Department of Applied Physics, Delhi Technological University, Delhi, under my supervision. The thesis embodies results of original work, and studies are carried out by the student herself and the contents of the thesis do not form the basis for the award of any other degree to the candidate or to anybody else from this or any other University/Institution.

Dr. Bharti Singh

(Supervisor)

Assistant Professor

Department of Applied Physics

Delhi Technological University

Delhi-110042, India

Date:

ABSTRACT

The rapid surge in global energy demand, coupled with environmental concerns linked to usage of conventional fossil fuels, underscores the need for sustainable energy solutions. Energy harvesting technologies have emerged as promising alternatives for addressing these challenges, enabling the conversion of ambient mechanical energy into usable electrical power. This thesis explores the potential of piezoelectric and triboelectric nanogenerators (PENG and TENG) as an efficient platform for harvesting mechanical energy to power small electronic devices, particularly in self-sustaining, battery-free applications. These nanogenerators leverage the unique properties of polymers and polymers-carbon based nanocomposite materials, transforming wasted energy from daily activities into a renewable power source. Furthermore, by incorporating a piezoelectric material as one of the components in a triboelectric nanogenerator, both effects can work together. This hybrid approach not only amplifies the electrical output but also broadens the range of mechanical energies it can capture, making the device highly versatile for applications that require reliable, self-sustained power sources in environments with diverse energy sources, such as wearable electronics, IoT devices, and environmental remediation applications.

With this aim, the present thesis provide a comprehensive study on the design, synthesis, and application of high-performance nanogenerators for sustainable energy harvesting and environmental remediation applications. The first part of the research focuses on a piezoelectric nanogenerator (PENG) based on polyvinylidene fluoride (PVDF) and heteroatom-doped reduced graphene oxide (rGO) with boron (B), nitrogen (N), and boron-nitrogen (BN) codopants. The integration of these doped rGO variants into the PVDF matrix significantly enhances the piezoelectric response of the nanocomposite films. Among them, the PVDF/BN-rGO based nanogenerator demonstrates the highest output, achieving highest voltage and current of 20.4 V and 15.9 μA , which are substantially higher than those of pristine PVDF. Frequency-dependent analysis reveals optimal performance at 6 Hz. Moreover, increased β -phase content in PVDF is ascribed due to the formation of a conductive network that enhances charge transfer. This PENG effectively converts biomechanical energy from human motions such as finger tapping, wrist bending, and elbow folding into electrical power. To further enhance the output, a hybrid nanogenerator (HNG) was developed by layering the PVDF/BN-rGO nanocomposite with a PDMS thin film, combining piezoelectric and triboelectric

effects. The hybrid configuration achieved an impressive output voltage of 57.6 V, which was sufficient to charge capacitors, light LEDs, and power a calculator. This study introduces a promising approach to enhance the nanogenerator performance for self-powered wearable electronics by utilizing graphene derivatives as nanofillers.

Further, the effects of rGO, nitrogen-doped rGO (N-rGO) concentration and electrospinning technique on the output of PVDF-based triboelectric nanogenerators (TENGs) was studied. The optimal nanofiller concentration was identified at 1.5 wt% of rGO and N-rGO, where the PVDF nanocomposite demonstrated the highest output of 156 V, approximately double that of pristine PVDF. However, performance declines at higher concentrations due to the formation of conductive networks within the matrix. Nanofiber mats produced by electrospinning yielded even greater enhancements, with the PVDF/N-rGO nanofiber-based TENG reaching a peak output voltage of 368 V and a power density of $\sim 282.8 \mu\text{W}/\text{cm}^2$. The study also reveals that both tapping frequency and impact force significantly influence output, with increased frequency and force boosting charge transfer and capacitance. Finite element analysis was performed to provide quantitative insight into surface potential distribution. Subsequently, the capability of the fabricated TENG was demonstrated by successfully powering small electronic devices and functioning as a self-sustained motion sensor, capable of automatically turning on light in response to human movement at night. This highlights its promising applications in advance human-machine interfaces and wireless sensing technologies.

Finally, to broaden the applications of TENGs, PVDF nanofibers incorporated with boron-nitrogen codoped rGO (BN-rGO) were utilized for energy harvesting and environmental remediation. The optimal performance was achieved with a BN-rGO concentration of 1.5 wt%, resulting in maximum outputs of 380 V, 36 μA , and 336 $\mu\text{W}/\text{cm}^2$. The study also investigated the effect of various counter triboelectric layer materials, including PTFE, PDMS, PET, paper, and nitrile gloves, replacing nylon. It has been found that TENG based on PVDF/BN-rGO and nylon demonstrated superior output, which may be attributed to the greater electronegativity difference between PVDF/BN-rGO and nylon. Thereafter, a self-powered system using a TENG as power source was developed for degrading methylene blue in wastewater. While the TENG alone required 12 hours for complete dye degradation, the addition of a BN-rGO as an catalyst significantly reduced the time to 100 minutes. This research provides an effective strategy for developing high-performance TENGs for sustainable applications in energy harvesting, self-powered sensing, and environmental remediation.

LIST OF PUBLICATIONS

Publications in Peer Reviewed Journals

1. **Shilpa Rana**, Vishal Singh, Bharti Singh “Recent trends in 2D materials and their polymer composites for effectively harnessing mechanical energy” *iScience*, 25(2) (2022), 103748 (Review paper)
2. **Shilpa Rana**, Vishal Singh, Bharti Singh “Tailoring the Output Performance of PVDF-Based Piezo–Tribo Hybridized Nanogenerators via B, N-Codoped Reduced Graphene Oxide”, *ACS Applied Electronic Materials*, 4 (2022), 5893-5904
3. **Shilpa Rana**, Bharti Singh, “Polymer nanocomposite film based piezoelectric nanogenerator for biomechanical energy harvesting and motion monitoring”, *Journal of Materials Science: Materials in Electronics*, 34 (2023), 1764
4. **Shilpa Rana**, Bharti Singh, “rGO-Embedded Polymer Nanocomposite Layer for Improved Performance of Triboelectric Nanogenerator.” *Journal of Electronic Materials*, 53(11) (2024), 6640-6649
5. **Shilpa Rana**, Himani Sharma, Renuka Bokolia, Kamlesh Bhatt, Rajendra Singh, Ramcharan Meena, Bharti Singh “PVDF/N-rGO nanofibers based sustainable triboelectric nanogenerator for self-powered wireless motion sensor” *Carbon*, 234 (2025), 119926

Publications not included in this thesis

1. Abhinav Bhatt, Vishal Singh, Priyanka Bamola, Deepali Aswal, Saurabh Rawat, **Shilpa Rana**, Charu Dwivedi, Bharti Singh, Himani Sharma “Enhanced piezoelectric response using TiO₂/MoS₂ heterostructure nanofillers in PVDF based nanogenerators” in *Journal of Alloys and Compounds* 960 (2023), 170664
2. Vishal Singh, **Shilpa Rana**, Renuka Bokolia, Amrish K. Panwar, Ramcharan Meena, Bharti Singh “Electrospun PVDF-MoSe₂ nanofibers based hybrid triboelectric nanogenerator for self-powered water splitting system” *Journal of Alloys and Compounds* 978 (2024), 173416

3. Munni, Himani, **Shilpa Rana**, Jasvir Dalal, Bharti Singh “Enhanced energy conversion efficiency in PVDF/WS2 hybrid piezoelectric nanogenerators”. *Discover Materials*, 5 (2025), 165.

Publication in Conference

1. Deshraj Meena, Vinay Kumar Verma, Divya, Perna, **Shilpa Rana** (2021)” Investigation the effect of Zn doping on structural and optical properties of SnO2” *Materials Today: proceedings*

Book Chapters

1. **Shilpa Rana**, Vishal Singh, Himani Sharma and Bharti Singh (2022) Chapter titled: “Fluoropolymer Nanocomposites for Piezoelectric Energy Harvesting Application” in the book:- *Advanced Fluoropolymer Nanocomposites: Fabrication, Processing, Characterizations, and Applications*
2. Priyanka Bamola, **Shilpa Rana**, Bharti Singh, Charu Dwivedi, Himani Sharma (2021) Book chapter entitled “Nanostructured Oxide Based Ceramic Materials for Light and Mechanical Energy Harvesting Applications” in book: *Advanced Ceramics for Energy and Environmental Applications*

Conference Contributions-Poster

1. **Shilpa Rana**, Bharti Singh, “*Piezoelectric nanogenerator performance modulation via varied PVDF morphology*” at International Conference on Atomic, Molecular, Material, Nano and Optical Physics with Applications (ICAMNOP–2023) held in Delhi Technological University from 20th -22nd December, 2023
2. **Shilpa Rana**, Bharti Singh, “*Chemically modify rGO nanosheets based triboelectric nanogenerator for powering portable electronics*” at annual International conference on Recent Progress in Graphene and 2D materials Research (RPGR-2023), held in Bengaluru from 20th -23rd November 2023
3. **Shilpa Rana**, Bharti Singh, “*rGO embedded polymer nanocomposite layer for improved performance of Triboelectric nanogenerator*” at 28th International

Conference On Nuclear Tracks & Radiation Measurements (28th ICNTRM-2023) held in Gurugram University, Haryana from 6th -10th November 2023

4. **Shilpa Rana**, Bharti Singh, *“Nitrogen Doped Reduced Graphene Oxide functionalized polymer composite Based Flexible Triboelectric Nanogenerator For Harnessing The Mechanical Energy”* at 11th International Conference on Materials for Advanced Technologies (IUMRS-ICAM & ICMAT 2023), held in Singapore from 26th -30th June 2023, organized by the Materials Research Society of Singapore
5. **Shilpa Rana**, Bharti Singh, *“Boron and Nitrogen Co-Doped Reduced Graphene Oxide Based Flexible Piezoelectric-Triboelectric Hybrid Nanogenerator”* at the International Conference in Asia-2022 (IUMRS-ICA 2022), organized by Materials Research Society of India at Indian Institute of Technology, Jodhpur, India on December 19th -23rd , 2022
6. **Shilpa Rana**, Bharti Singh, *“Improved piezoelectric performance of the PVDF/rGO based flexible piezoelectric nanogenerator by introduction of heteroatom”* at International Conference on Nanotechnology: Opportunities & Challenges (ICNOC 2022), organized by department of Applied Sciences & Humanities, Jamia Millia Islamia, New Delhi, India on November 28th -30th , 2022

TABLE OF CONTENTS

	<i>Page No.</i>
<i>Acknowledgement</i>	<i>i</i>
<i>Candidate's Declaration.....</i>	<i>iii</i>
<i>Certificate by the Supervisor</i>	<i>iv</i>
<i>Abstract.....</i>	<i>v</i>
<i>List of Publications</i>	<i>vii</i>
<i>Table of Contents</i>	<i>x</i>
<i>List of Tables</i>	<i>xiv</i>
<i>List of Figures</i>	<i>xv</i>
<i>List of Abbreviations</i>	<i>xxii</i>
 Chapter 1: Introduction	 1-30
1.1 Background and Motivation	2
1.2 Nanogenerators for Mechanical Energy Harvesting.....	4
1.2.1 Piezoelectric Nanogenerator	5
1.2.2 Triboelectric Nanogenerators.....	8
1.3 Hybridization of Piezoelectric and Triboelectric Nanogenerators.....	11
1.4 Polymers for Piezoelectric and Triboelectric Nanogenerators.....	12
1.4.1 Polyvinylidene Fluoride (PVDF): A Ferroelectric Polymer	14
1.4.2 Methods for Improving Performance of PVDF based Nanogenerator.....	15
1.5 Nanofiller Materials.....	16
1.5.1 Reduced Graphene Oxide (rGO) as an Effective Nanofiller	17
1.6 Research Challenge.....	18
1.7 Thesis Problem.....	19
1.7.1 Research Objectives.....	19
1.7.2 Overview of Thesis	20
References.....	26

Chapter 2: Synthesis and Characterization Techniques31-56

2.1	Synthesis of Reduced Graphene Oxide (rGO) and its Heteroatom Doped Variants.....	32
2.1.1	Modified Hummer's Method.....	32
2.1.2	Hydrothermal Synthesis Route	33
2.2	Film Preparation Techniques	35
2.2.1	Drop Casting Method.....	35
2.2.2	Electrospinning Technique.....	36
2.3	Characterization Techniques	38
2.3.1	X-ray Diffraction (XRD)	38
2.3.2	Fourier Transform Infrared Spectroscopy.....	40
2.3.3	Raman Spectroscopy.....	42
2.3.4	Field Emission Scanning Electron Microscopy (FESEM)	44
2.3.5	Energy Dispersive X-ray Spectroscopy (EDS or EDX) for Elemental Analysis.....	45
2.3.6	X-ray Photoelectron Spectroscopy (XPS)	46
2.3.7	Polarisation vs Electric field Measurements (P-E Loops)	47
2.3.8	Dielectric/Impedance Analyser.....	48
2.3.9	Atomic Force Microscopy (AFM)	49
2.3.9.1	Kelvin Probe Force Microscopy (KPFM).....	51
2.3.10	Ultraviolet-Visible Spectroscopy (UV-Vis).....	52
2.4	Electrical Measurements of Nanogenerators	53
	References.....	55

Chapter 3: Effect of pristine and heteroatom doped rGO on the output performance of the PVDF nanocomposite based piezoelectric nanogenerator for biomechanical energy harvesting applications 57-83

3.1	Introduction.....	58
3.2	Experimental Section.....	60
3.2.1	Materials	60
3.2.2	Synthesis Procedure for rGO, B-rGO, N-rGO, and BN-rGO.....	60
3.2.3	Preparation of PVDF Nanocomposite and PDMS Films.....	61
3.2.4	Device Fabrication.....	62
3.3	Results and Discussion	62

3.3.1	Material Characterization.....	62
3.3.2	Films Characterization	66
3.3.3	Electrical Characterization of PENG	70
3.3.4	Electrical Characterization of Hybrid Nanogenerator	72
3.4	Applications of PENG and Hybrid Nanogenerator	75
3.4.1	Biomechanical Energy Harvesting using PENG	75
3.4.2	Capacitor Charging and Powering of Electronics Devices.....	76
3.5	Summary	78
	References.....	79

Chapter 4: Synergistic effect of N-doped rGO nanofillers concentration and electrospinning technique on the output performance of PVDF nanocomposite based triboelectric nanogenerator for self-powered electronics and wireless sensor applications84-122

4.1	rGO Embedded Polymer Nanocomposite Layer for Improved Performance of Triboelectric Nanogenerator.....	85
4.1.1	Introduction.....	85
4.1.2	Experimental Section	86
4.1.2.1	Synthesis of PVDF and PVDF/rGO Nanocomposite Films	86
4.1.2.2	Fabrication of TENG	87
4.1.3	Results and Discussion	87
4.1.3.1	Material Characterization.....	87
4.1.3.2	Electrical Characterization of TENG.....	90
4.1.4	Summary.....	93
4.2	PVDF/N-rGO Nanofibers based Sustainable Triboelectric Nanogenerator for Self-Powered Wireless Motion Sensor.....	94
4.2.1	Introduction.....	94
4.2.2	Experimental Details.....	95
4.2.2.1	Synthesis of PVDF and PVDF/N-rGO Nanocomposite Films and Nanofibers.....	95
4.2.2.2	Synthesis of Nylon film and Nanofibers.....	96
4.2.2.3	Fabrication of TENG	96
4.2.3	Results and Discussion	97
4.2.3.1	Material Characterization.....	97

4.2.3.2	Theroretical Investigations and COMSOL Simulation.....	106
4.2.3.3	Electrical Characterization of TENG.....	108
4.2.4	Applications of TENG	114
4.2.4.1	Capacitor Charging and Deriving Electronic Devices.....	114
4.2.4.2	Biomechanical Energy Harvesting	115
4.2.4.3	TENG as Self-powered Motion Sensor	116
4.2.5	Summary	118
	References.....	119

Chapter 5: Optimizing B, N Co-doped rGO concentration in electrospun PVDF Nanofibers for triboelectric nanogenerator-driven water remediation.....123-142

5.1	Introduction.....	124
5.2	Experimental Section.....	125
5.2.1	Synthesis of PVDF/BN-rGO and Nylon Nanofibers	125
5.2.2	Fabrication of TENG	126
5.3	Results and Discussion	126
5.3.1	Material Characterization.....	126
5.3.2	Electrical Characterization of TENG.....	130
5.4	Applications of TENG	135
5.4.1	TENG as a Power Source for Electrochemical Reduction of Methylene Blue Dye	135
5.5	Summary	137
	References.....	139

Chapter 6: Conclusions and Future Scope of Work.....143-148

6.1	Summary of Research Work	144
6.2	Future Prospectives	146

Publication Proofs.....149

Bio-data154

LIST OF TABLES

<i>Table No.</i>	<i>Title</i>	<i>Page No.</i>
4.1	Comparison of the output performance of fabricated TENG with other reported TENG	113

LIST OF FIGURES

<i>Figure No.</i>	<i>Figure Title</i>	<i>Page No.</i>
Figure 1.1	Various renewable and sustainable source of energy present in surrounding	3
Figure 1.2	A schematic showing the working mechanism of PENG	6
Figure 1.3	A schematic showing the working mechanism of TENG	9
Figure 1.4	The four fundamental working modes of TENG	10
Figure 1.5	Overview of key TENG modeling parameters affecting performance of TENG	11
Figure 1.6	A schematic illustration of change conformation of α , β , and γ phase in PVDF	14
Figure 1.7	Flowchart for the organisation of the thesis	25
Figure 2.1	A schematic showing hydrothermal autoclave set-up used in hydrothermal synthesis	34
Figure 2.2	A schematic illustration of drop casting method to prepare polymer nanocomposite films	36
Figure 2.3	Illustration of electrospinning setup for synthesis of nanofibers	37
Figure 2.4	A schematic showing the components of XRD diffractometer	39
Figure 2.5	A schematic showing the diffraction of X-rays obeying Brags law	40
Figure 2.6	Michelson interferometer schematic	41
Figure 2.7	Instrumental setup for FTIR spectroscopy	42
Figure 2.8	Schematic of a Raman spectrometer setup	43
Figure 2.9	Schematic illustrating the components of FESEM	45

Figure 2.10	A schematic illustration of the XPS system, highlighting the various components involved in its operation	47
Figure 2.11	Schematic showing the components of a AFM	50
Figure 2.12	Variation in force of interaction between tip and sample as a function of distance	51
Figure 2.13	Schematic representation of working mechanism of UV-Vis spectrometer.	53
Figure 3.1	A schematic showing the step by step procedure for (a) hydrothermal synthesis of rGO and heteroatom doped rGO, and (b) synthesis of PVDF/ doped rGO composite film prepared via drop casting method	61
Figure 3.2	(a) Raman spectra, (b) XPS survey spectra of the rGO, B-rGO, N-rGO and BN-rGO powder sample	63
Figure 3.3	Deconvoluted C1s core level XPS spectra of (a) rGO, (b) B-rGO, (c) N-rGO and (d) BN-rGO	64
Figure 3.4	Deconvoluted B1s core level spectra of (a) B-rGO, and (b) BN-rGO, N1s core level spectra of (c) N-rGO and (d) BN-rGO samples	65
Figure 3.5	FESEM micrographs of (a) rGO, (b) B-rGO, (c) N-rGO, (d) BN-rGO, and (e-i) EDX spectrum with the elemental mapping image of all element present in BN-rGO	66
Figure 3.6	(a) XRD and (b) FTIR spectra of PVDF, PVDF/rGO, PVDF/N-rGO and PVDF/BN-rGO thin film, (c) polarization versus electric field (P-E) hysteresis loop and (d) room temperature dielectric constant of PVDF and PVDF nanocomposite films after doping of rGO, N-rGO and BN-rGO	67
Figure 3.7	A schematic illustration of interaction of BN-rGO nanosheet with the PVDF chain	69
Figure 3.8	SEM images of (a) PVDF, (b) PVDF/rGO, (c) PVDF/B-rGO, (d) PVDF/N-rGO, (e) PVDF/BN-rGO films	70

Figure 3.9	(a)The open-circuit voltage, and (b) rectified short-circuit current produced by PVDF, PVDF/rGO, PVDF/B-rGO PVDF/N-rGO, and (d) PVDF/BN-rGO nanocomposite film at 6 Hz frequency	71
Figure 3.10	(a) PENGs output performance analyzed by varying the input frequency in the range from 1Hz to 10Hz, (b) PVDF/BN-rGO nanocomposite fim-based PENG output voltage as a function of variable frequency	71
Figure 3.11	A schematic representation of piezo-tribo hybrid nanogeneration with the electrical connections	73
Figure 3.12	Comparision between the (a-b) rectified open-circuit voltage, and (c-d) short-circuit current of piezo, tribo and hybrid nanogenerator of PVDF and PVDF/BN-rGO composite film	74
Figure 3.13	The output voltage and power density curve of PVDF/BN-rGO film based HNG as a function of resistance	75
Figure 3.14	A schematic representation of different parts of human body from which energy can be harvested. The output voltage generated by PBR film based PNG by (b) one finger, (c) two fingers, (d) thumb tapping, (e) clapping, (f) wrist bending, (g) elbow bending, (h) knee folding, and (i) foot tapping, (j) variation in the output performance of PNG by slow, moderate and fast finger tapping, (k) The voltage produced by PNG by bending elbow at different angles	76
Figure 3.15	(a) charging of 1 μ F capacitor by individual PENG, TENG and hybrid nanogenerator, (b) energy stored in 1 μ F capacitor by individual PENG, TENG and hybrid nanogenerator, (c) capacitiior voltage characteristic curves of 1, 2.2, 10, and 47 μ F capacitor charged through PVDF/BN-rGO composite film based HNG, (d) charging and discharging cycle of 1 μ F capacitor, (e) A photographic image of powering of 15 LEDs and a calculator by the PVDF/BN-rGO composite film based hybrid	77

Figure 4.1.1	(a) XRD pattern, (b) FTIR spectra, (c) content of electroactive polar β phase and (d) dielectric constant of PVDF nanocomposite films with different weight percentage of rGO	88
Figure 4.1.2	FESEM micrographs of (a-e) PVDF and PVDF nanocomposite films with varied concentration of rGO	90
Figure 4.1.3	Measured open-circuit voltage, and short-circuit current waveforms of the TENG obtained by (a-b) varying the concentration of rGO in PVDF, (c-d) by varying input frequency, and (e-f) impact force on the TENG with 1.5 wt% of rGO	91
Figure 4.1.4	(a) Output voltage and power density measurements as a function of varied resistance, and (b) Durability of PVDF/rGO based TENG with 1.5 wt% of rGO	92
Figure 4.2.1	A schematic representation of step by step synthesis of PVDF and PVDF nanocomposite films prepared via drop casting and electrospinning method	96
Figure 4.2.2	Photographic image of PVDF and PVDF nanocomposite films with different weight percentage of N-rGO prepared by drop-casting method	97
Figure 4.2.3	FESEM images of (a-f) drop casted PVDF and PVDF nanocomposite films with different weight percentage of N-rGO (0, 0.25, 0.5, 1, 1.5, and 2 wt%), and (g-i) electrospun PVDF, PVDF/N-rGO(1.5 wt%), and nylon nanofibers mat	98
Figure 4.2.4	EDAX spectrum with the elemental mapping image of all elements present in PVDF film	98
Figure 4.2.5	EDAX spectrum with the elemental mapping image of all elements present in PVDF/N-rGO film with 0.5 wt % of N-rGO	99

Figure 4.2.6	EDX spectrum with the elemental mapping image of all elements present in PVDF/N-rGO film with 1 wt % of N-rGO	99
Figure 4.2.7	EDX spectrum with the elemental mapping image of all elements present in PVDF/N-rGO film with 1.5 wt % of N-rGO	99
Figure 4.2.8	EDX spectrum with the elemental mapping image of all elements present in PVDF/N-rGO film with 2 wt % of N-rGO	99
Figure 4.2.9	(a) XRD, and (b) FTIR, analysis of drop casted PVDF, and PVDF nanocomposite films with different weight percentage of N-rGO (0, 0.25, 0.5, 1, 1.5, and 2 wt%) and electrospun PVDF and PVDF/N-rGO (1.5 wt%) nanofibers prepared by electrospinning technique	101
Figure 4.2.10	Dielectric constant measurements of drop casted and electrospun PVDF, and PVDF nanocomposite films/nanofibers	102
Figure 4.2.11	(a-f) KPFM surface potential mapping of pristine PVDF, PVDF/N-rGO (1.5 wt%) and nylon films and electrospun nanofibers mat scanned over a surface of $2 \times 2 \mu\text{m}^2$	103
Figure 4.2.12	(a-b) A schematic band diagram illustrating the characteristic electronic energy level to describe TENG mechanism	105
Figure 4.2.13	Electron cloud potential well model of (a) PVDF and (b) PVDF/N-rGO composite films	106
Figure 4.2.14	COMSOL simulation of (a) PVDF and (b) PVDF/N-rGO nanocomposite films	108
Figure 4.2.15	(a) The open-circuit voltage, (b) short-circuit current, and (c) charge measurements of drop casted PVDF and PVDF nanocomposite films with different weight percentage of N-rGO (0, 0.25, 0.5, 1, 1.5, and 2 wt%)	109
Figure 4.2.16	The output (a) voltage, and (b) current measurements of PVDF and PVDF nanocomposite films based TENG as a function of varied frequency	110

Figure 4.2.17	The open-circuit voltage, short-circuit current and charge measurements of (a-c) pristine PVDF nanofibers mat, and (d-f) PVDF/N-rGO (1.5 wt%) nanofibers mat based TENG at variable frequency, (g-i) output performance of the PVDF/N-rGO (1.5 wt%) based TENG under different impact force	111
Figure 4.2.18	The variation of (a) output voltage and (b) power density of TENGs as a function of load resistance	112
Figure 4.2.19	(a) Durability of PVDF/N-rGO nanofiber based TENG with stable output voltage over 5 months, and its (b) Mechanical stability with consistent current output over 5000 seconds	114
Figure 4.2.20	(a) Capacitor charging curves of various capacitors (1, 2.2, 10, 33 μ F) charged through TENG, (b)) A schematic circuit diagram for powering LEDs with inset showing the photographic images of LEDs powered by TENG	114
Figure 4.2.21	The charging/discharging curve of capacitor to power (a) thermometer, (b) digital watch, and (c) hygrometer from the energy harvested by TENG after storing it to capacitor	115
Figure 4.2.22	The output voltage waveforms produced by PVDF/N-rGO(1.5 wt%) nanofibers based TENG from various human motions (a-c) Tapping with one, two and three fingers, (d) thumb tapping, (e) pinching of TENG with different pace, (f) blowing, (g-i) fist, elbow and foot tapping	116
Figure 4.2.23	(a) A schematic showing the block diagram of a self-powered smart lighting system for automatically ON the lights in night time, with (b-c) photographic image of signal acquisition unit and signal processing unit	117
Figure 5.1	(a) XRD, and (b) FTIR spectra of electrospun PVDF nanofibers with different weight percentage of BN-rGO	127
Figure 5.2	FESEM micrographs of electrospun PVDF and PVDF composite nanofibers with different weight percentage of BN-rGO	128

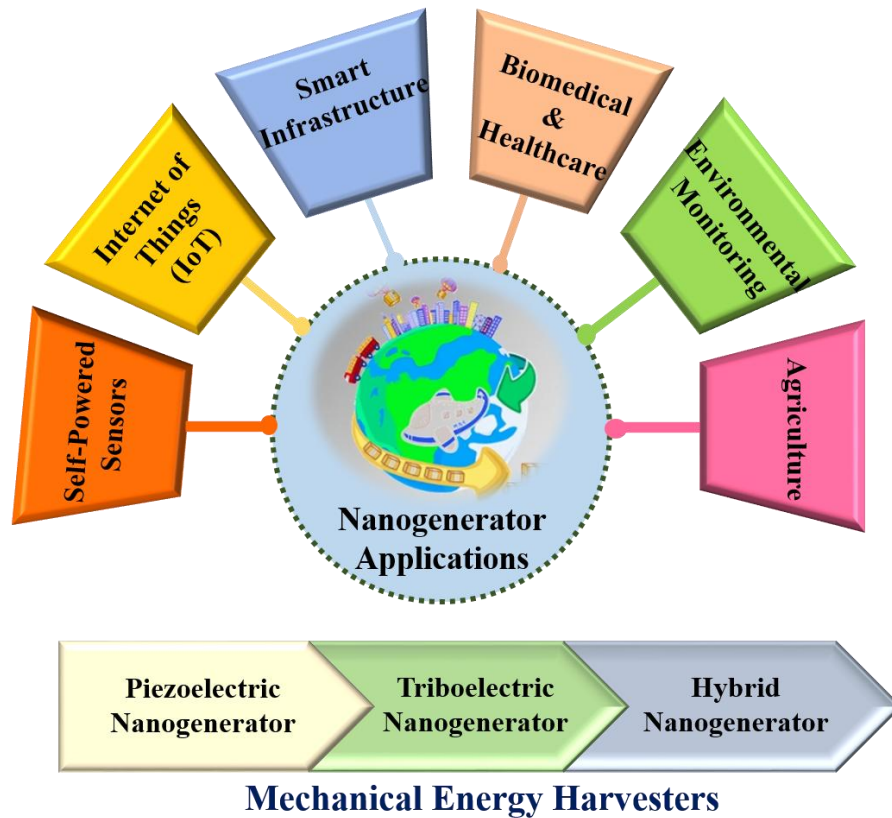
Figure 5.3	Dielectric constant measurements of electrospun PVDF and PVDF composite nanofibers with different weight percentage of BN-rGO	129
Figure 5.4	(a) The open-circuit voltage, and (b) short-circuit current measurements of electrospun PVDF and PVDF composite nanofibers with different weight percentage of BN-rGO	130
Figure 5.5	(a) The open-circuit voltage, and (b) short-circuit current measurements of electrospun PVDF and PVDF composite nanofibers as a function of varied frequency	131
Figure 5.6	The open-circuit voltage, short-circuit current, and charge measurements of electrospun PVDF/BN-rGO (1.5 wt%) composite nanofibers based TENG with (a-c) as a function of varied frequency, and (d-f) under different impact force	132
Figure 5.7	(a) The open-circuit voltage, and (b) short-circuit current measurements of electrospun PVDF/BN-rGO (1.5 wt%) composite nanofibers based TENG by varying the second triboelectric layer	133
Figure 5.8	The variation of output voltage and power density of PVDF/BN-rGO (1.5 wt %) based TENG as a function of load resistance	134
Figure 5.9	Durability of PVDF/BN-rGO (1.5 wt %) nanofiber based TENG with consistent current output over 1500 seconds	134
Figure 5.10	A schematic of self-powered dye degradation system for methylene blue dye	135
Figure 5.11	UV-vis spectra of dye degradation of methylene blue driven by TENG (a) when platinum is used as active electrodes and, (b) when BN-rGO is used as an active electrode	136
Figure 5.12	The degree of degradation of methylene blue dye driven by TENG (a) when platinum is used as active electrodes and, (b) when BN-rGO is used as an active electrode	137

LIST OF ABBREVIATIONS

Acronyms	Meaning
GO	Graphene oxide
rGO	Reduced graphene oxide
B-rGO	Boron doped rGO
N-rGO	Nitrogen doped rGO
BN-rGO	Boron nitrogen codoped rGO
PVDF	Polyvinylidene fluoride
PENG	Piezoelectric nanogenerator
TENG	Triboelectric nanogenerator
HNG	Hybrid nanogenerator
ΔV_{CPD}	Contact potential difference
E_F	Fermi level
V_{oc}	Open circuit voltage
I_{sc}	Short circuit current
PDMS	Polydimethylsiloxane
PTFE	Polytetrafluoroethylene
PET	Polyethylene terephthalate
DMF	N, N di-methyl formamide
Al	Aluminium
wt%	Weight percentage
XRD	X-ray diffraction
FTIR	Fourier transform infrared spectroscopy
FESEM	Field-emission scanning electron microscopy
EDS	Energy dispersive x-ray spectroscopy
P-E	Polarization- Electric field
XPS	X-ray photoelectron spectroscopy
AFM	Atomic force microscopy
KPFM	Kelvin probe force microscopy
IoT	Internet of things

CHAPTER 1

Introduction



This chapter provides an in-depth exploration of the technologies associated with energy harvesting, emphasizing their applications in diverse fields. Specifically, it provides a detailed discussion on mechanical energy harvesting technologies, focusing on piezoelectric and triboelectric nanogenerators. It aims to address the urgent need for sustainable energy sources to reduce fossil fuel dependence and advance technologies that capture abundant ambient energy. By examining the principles, challenges, and advancements in energy harvesting, this chapter outlines the pathway toward a more energy-efficient future. It also reviews strategies to improve nanogenerator efficiency, such as material selection, structural optimization, and hybrid designs. The chapter concludes with the research objectives, emphasizing the development of high-performance nanogenerators, and provides an outline of the thesis structure.

1.1 Background and Motivation

The escalating energy demand, fuelled by rapid technological advancements and a burgeoning population, has spurred scientific and industrial communities to seek sustainable and renewable energy generation methods. The abusive use of non-renewable energy sources, especially fossil fuels, become increasingly strained and environmentally damaging, therefore it is essential to explore alternative energy generation technique from the naturally available energy. Energy harvesting presents a promising solution to this challenge by capturing and utilizing ambient energy from the environment, such as solar, thermal, mechanical, and wind energy. Figure 1.1 illustrates several types of renewable energy harvesting source present in our surrounding. Moreover, the advancement in technology produced a plethora of portable, multifunctional, miniaturized and customized electronic system which require a lightweight, affordable power supply in order to be used in a variety of applications. The power supply that is being used at present for powering these smart electronic devices is electrochemical batteries. However, conventional batteries suffer from limited life term, short charging and discharging cycles, durability, and high disposal costs which poses a significant inconvenience and expense in wireless monitoring systems with large sensory networks. Additionally, with advancement in nanotechnology, the power consumption of smart electronics and sensors, reduces from milliwatts to microwatts. This shift has sparked substantial interest in energy harvesting from ambient sources to develop self-powered sensors, rechargeable smart electronics, and support global energy reduction efforts. Renewable and sustainable energy sources are thus being adapted to answer the pressing need for clean and reliable energy generation with long life spans. They are plentiful renewable energy sources which are pervasive, and simple to obtain in our daily lives. Solar energy is one of the most widely recognized and utilized renewable resources, available consistently throughout daylight hours and can be converted to electrical energy via solar cells. However, solar energy availability drops significantly at night or in indoor environments, limiting its use in certain settings. Despite its high energy output, solar energy harvesting technology is not ideally suited for powering small, portable, or wearable electronics, as it generally requires a fixed setup to operate efficiently[1, 2]. Thermoelectric generator are used to convert thermal energy from various sources, such as heat dissipated by engines

in factories and vehicles, heat produced by human activities, thermoregulation in inner organs into electrical energy based on seebeck effect[3, 4]. However, thermal energy harvesting is highly dependent on the temperature differential between the heat source and the surrounding environment. As a result, thermoelectric generators are less suitable for wearable applications in hot or tropical climates, where the limited temperature gradient between the skin and the external environment reduces their efficiency. In a similar way, wind energy can be harnessed by placing turbines in optimal locations such as farms, mountainous areas, or remote regions[5]. This approach can yield significant economic benefits while being environmentally sustainable. However, wind energy is not well-suited for powering portable electronic devices due to its dependence on specific environmental conditions. Another abundant energy source in the environment that remains unaffected by external conditions is mechanical energy. This includes vibrations from buildings and structures, human movement, transportation, wind and water flow, and ocean waves. Harvesting vibration energy from these mechanical sources is a promising approach, as it allows for energy capture in situations where solar or thermal energy may not be applicable.

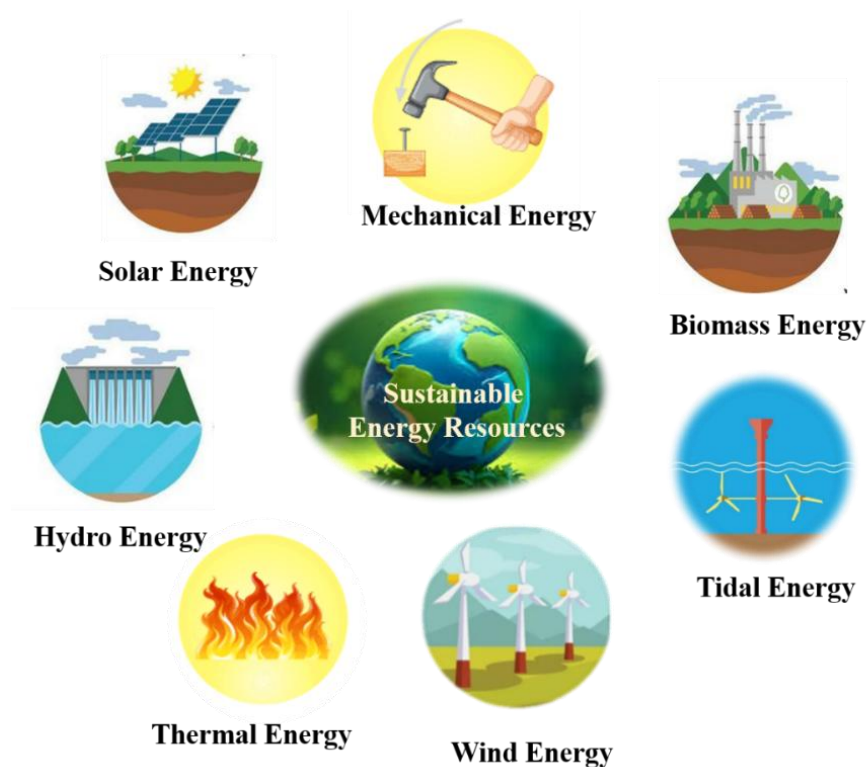


Figure 1.1 Various renewable and sustainable source of energy present in surrounding.

In this regard, the present thesis introduces advanced strategies for harnessing mechanical energy by leveraging both piezoelectric and triboelectric effects. A central focus is placed on a comprehensive understanding of the underlying mechanisms to optimize the design and functionality of energy-harvesting devices. This research aims to develop hybrid devices by integrating piezoelectric and triboelectric effects that are not only efficient but also simple to construct and operate. Key objectives include designing polymers carbon nanocomposite films based efficient piezoelectric and triboelectric nanogenerator for scavenging the ambient mechanical energy, while ensuring that these devices are durable, cost-effective, and most importantly, environmentally sustainable. The outcomes of this study contribute to the development of robust and scalable solutions for sustainable energy applications, highlighting the potential of these technologies in addressing future energy demands.

1.2 Nanogenerators for Mechanical Energy Harvesting

Nanogenerators are innovative devices that capture and convert mechanical energy from the environment into electrical power, harnessing small-scale energy sources to enable sustainable energy generation. These compact, efficient devices have become integral to the field of energy harvesting, especially as the demand grows for renewable and portable power solutions that can support the expanding ecosystem of modern smart technologies. In applications such as wearable electronics, Internet of Things (IoT) sensors, and biomedical devices, nanogenerators enable continuous, reliable power without the dependency on conventional batteries, which often have limited lifespans, larger form factors, and environmental drawbacks associated with disposal and chemical waste. The concept of nanogenerator was first introduced by Prof. Zhong Lin Wang group in 2006, where they have utilized conducting AFM tip to deflect the ZnO nanowires and corresponding voltage is measured, demonstrating a novel approach by generating electricity from the mechanical force using piezoelectric properties of the nanowires[6]. Thereafter, several efforts have been made in field of nanogenerators with different structures and functions to improve the efficiency and understand the mechanism of electricity generation. Later on, this group in 2012 introduced an innovative approach to convert mechanical energy into electrical energy using the triboelectric effect[7]. This technique harnesses the electrostatic charge generated when certain materials come into contact and then separate, creating a

potential difference that can be used to produce electricity. Since its inception, this method has catalyzed substantial research and technological advancements, particularly in optimizing the design, efficiency, and versatility of triboelectric nanogenerators (TENGs). These developments have expanded their potential applications across a wide range of fields, from powering small electronics and wearable devices to contributing to the self-sustaining energy needs of smart cities and IoT infrastructure.

In the upcoming sections, we will be briefly discussing about the principles and mechanisms of piezoelectric and triboelectric nanogenerators, along with their roles in mechanical energy harvesting for variety of applications. We will examine how these devices convert mechanical energy into electrical energy, as well as strategies for designing efficient energy harvesters. This will include a discussion of fundamental configurations and signal transduction techniques central to these applications.

1.2.1 Piezoelectric Nanogenerator

Piezoelectric nanogenerator converts mechanical energy into electrical energy based on the piezoelectric effect, which describes how applying mechanical stress to non-centrosymmetric materials deforms their crystal structure, generating polarization charges that create a potential difference across the material. The generation of electric potential by application of mechanical stress is known as the direct piezoelectric effect which is widely implemented in energy harvesting systems. While in the converse piezoelectric effect, mechanical strain is induced in the material when subjected to electrical signal/voltage and is applicable to vibration damping, acoustic emitter, and actuators. In general, the piezoelectric effect is a reversible process and the materials which exhibit the piezoelectric properties are known as the piezoelectric materials which demonstrate plenty of application in energy transducers, actuators, sensors, and energy harvesters[8-10]. The crystal structure of these piezoelectric materials is non-symmetric but has a balanced equilibrium between charges such that the effect of the positive and the negative charges exactly cancel out each other. When these materials come in the application of the applied mechanical stress or force, dipoles are no longer aligned in the way to cancel out the effect of each other which results in the generation of net polarization charge on the surface of the materials (Figure 1.2).

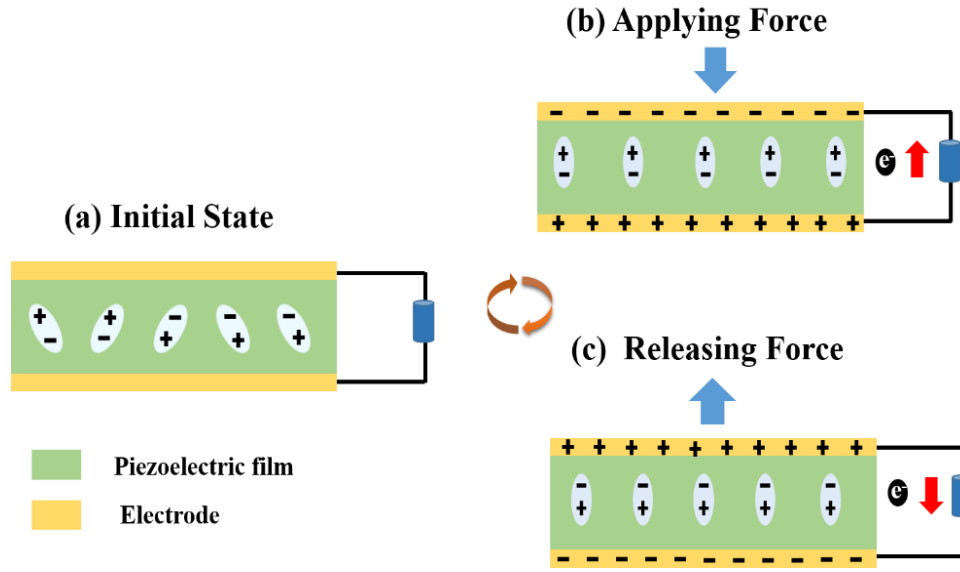


Figure 1.2 A schematic showing the working mechanism of PENG.

The number of dipoles present in the piezoelectric material plays a crucial role in their performance and behaviour, therefore to acquire more dipoles these materials are subjected to a strong electric field near the curie temperature and this process is known as the ‘poling’ and this process imparts a net permanent polarization in the materials which also change with the applied stress as a result further enhance the piezoelectricity. Most of the ferroelectric materials show piezoelectric behaviour but the converse is not true [11-13]. The Piezoelectric effect is the coupling phenomenon between the electrical and mechanical properties of the materials. The electrical behavior of the material is given as

$$D_i = \sum_{j=1}^3 \epsilon_{ij} E_j \text{ or } D = \epsilon E \quad (1.1)$$

Where ϵ_{ij} is electric permittivity, D_i is electric displacement, E_j is the electric field.

Mechanical behavior is given by the relation between stress and strain under small deformation

$$T_{ij} = \sum_{k,l=1}^3 c_{ijkl} S_{kl} \quad (1.2)$$

where c_{ijkl} is the elastic stiffness of the material. The above equation 1.2 can be interpreted reversely as

$$S_{ij} = \sum_{k,l=1}^3 s_{ijkl} T_{kl} \quad (1.3)$$

where s_{ijkl} is elastic compliance of the material. The reduced tensor notation of the coupled constitution equation of piezoelectric material are depicted[14] as

$$D_i = E_j \epsilon_{ij}^T + d_{ij} T_j \quad (1.4)$$

$$S_I = d_{Ij} E_j + s_{Ij}^E T_j \quad (1.5)$$

where the superscripts T and E mean the coefficients at constant stress and electric and, d_{ij} is the piezoelectric strain constants respectively.

In general, the piezoelectric material has two functioning modes to begin, the device is said to work in d_{33} mode when the direction of the applied stress is the same as the direction of polarization, and the generated piezoelectric charge is given by

$$Q_{PENG} = A \sigma d_{33} \quad (1.6)$$

where σ is the stress along the direction of applied force, A is the area of the piezoelectric material, d_{33} is the piezoelectric charge coefficient. The corresponding piezoelectric potential for the open circuit condition is obtained by

$$V_{PENG} = t \sigma g_{33} \quad (1.7)$$

where t is the thickness of the piezoelectric material, g_{33} is the piezoelectric voltage coefficient respectively.

Second, when the direction of the applied stress is perpendicular to the direction of the polarization, the device is said to work in d_{31} mode. For this, the piezoelectric charge and voltage can be expressed as

$$Q_{PENG} = A \sigma d_{31} \quad (1.8)$$

$$V_{PENG} = t \sigma g_{31} \quad (1.9)$$

Furthermore, to enable real-world applications and commercial viability of piezoelectric nanogenerators (PENGs), it is essential to enhance their output performance. In this regard, several strategies are employed, focusing on material enhancements, structural optimization, and device engineering. The key approaches that can significantly improve the piezoelectric performance are selection of suitable piezoelectric material,

3D printing, poling, electrospinning, hot pressing, structural modifications, and so on[15]. Each of these strategies, when carefully applied, can significantly improve the power density of piezoelectric nanogenerators, enhancing their efficiency and making them more viable for practical applications in energy harvesting.

1.2.2 Triboelectric Nanogenerators

Triboelectric nanogenerator works on the principle of triboelectric effect, where contact and separation between two materials with differing electron affinities generate an electric potential. A few instances of the triboelectric effects are rubbing glass through fur, plastic comb through the hair, and rubbing the balloon on hair is generally caused by static electricity. Whether the material acquires positive charge or negative charge and the strength of the charges they acquired, depend upon the relative polarities, surface roughness, strain, and other properties of materials. Therefore, the materials which have an affinity to gain electrons will become the negative charge and another become the positive charge. Depending on the affinity of material to gain or lose electrons, materials are placed in a systematic order in a series known as the triboelectric series[16, 17]. Although, the triboelectric effect is considered as a negative effect that has brought various disastrous risks in the industry, human life, nature, electronics but it shows great potential in small scale energy harvesting.

The Prof. Wang group in 2012, invented the first Triboelectric Nanogenerator (TENG) which uses these static charges to harness ubiquitous ambient small scale mechanical energy [18]. TENG works on combined properties of the triboelectric effect and electrostatic induction where contact electrification provides the polarized charge and the role of electrostatic induction is to convert mechanical energy to electrical energy. Therefore, when two materials with different electron affinity are brought in contact with each other by an external force, triboelectric charges with opposite polarities are induced on the surface of the materials. After removing the external force, the charged surface gets separated which will induce the potential difference on the electrode. Thus, by connecting the external load between these two electrodes, charges will flow through the outer circuit to screen out the electric field. A later renewed contact between these surfaces results in the disappearance of these triboelectric charges hence, giving rise to the charge to flow in opposite directions. So, by contacting and separating the materials by an external force,

the charges will flow back and forth via the external circuit[19, 20]. A schematic showing the working mechanism of TENG is illustrated in Figure 1.3.

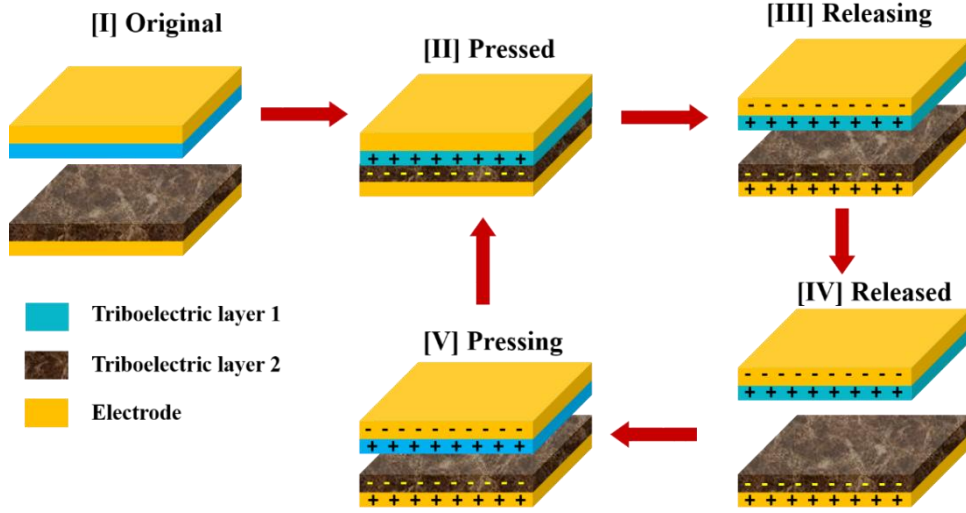


Figure 1.3 A schematic showing the working mechanism of TENG.

The output voltage generated by TENG is given by

$$V = -\frac{Q}{C(x)} + V_{oc}(x) \quad (1.10)$$

is also known as V-Q-x relation and represents the inherent capacitive behaviour of TENG where V_{oc} is the open-circuit voltage, $C(x)$ is the capacitance between two electrodes, Q is transferred charge between two electrodes. The output current generated across the load is given by

$$I = \frac{dQ}{dt} = C \frac{dV}{dt} + V \frac{dC}{dt} \quad (1.11)$$

where, C is the capacitance of the system, V is the voltage across electrodes. The first term in the equation corresponds to the current produced due to change in voltage across the non-contact surface of the electrode with time and the second term corresponds to current introduced by variation in capacitance due to cyclic contact and separation. Under the short circuit condition (SC), the charges which transfer across the electrode Q_{sc} completely cancel out the voltage generated by this triboelectric charge, and above equation becomes

$$0 = -\frac{Q_{sc}}{C(x)} + V_{oc}(x) \quad (1.12)$$

And the fundamental relation among Q_{SC} , C , and V_{OC} is given by

$$Q_{SC}(x) = CV_{OC}(x) \quad (1.13)$$

In comparison to other energy harvesters, TENG are advantageous because of its high output voltage at low frequencies, lightweight, ease of fabrication, scalability, and highly adaptable design, enabling them to be fabricated in multiple configurations to harness mechanical energy from a wide range of sources, including body movements, tidal waves, vibrations from machinery and transportation, rotational motions, and even wind energy. Therefore, depending on the electrode configuration and the various ways in which triboelectric layers can be stacked, four major modes of TENG are put forward (Figure 1.4) including vertical contact separation, lateral sliding, freestanding triboelectric layer and single electrode modes.

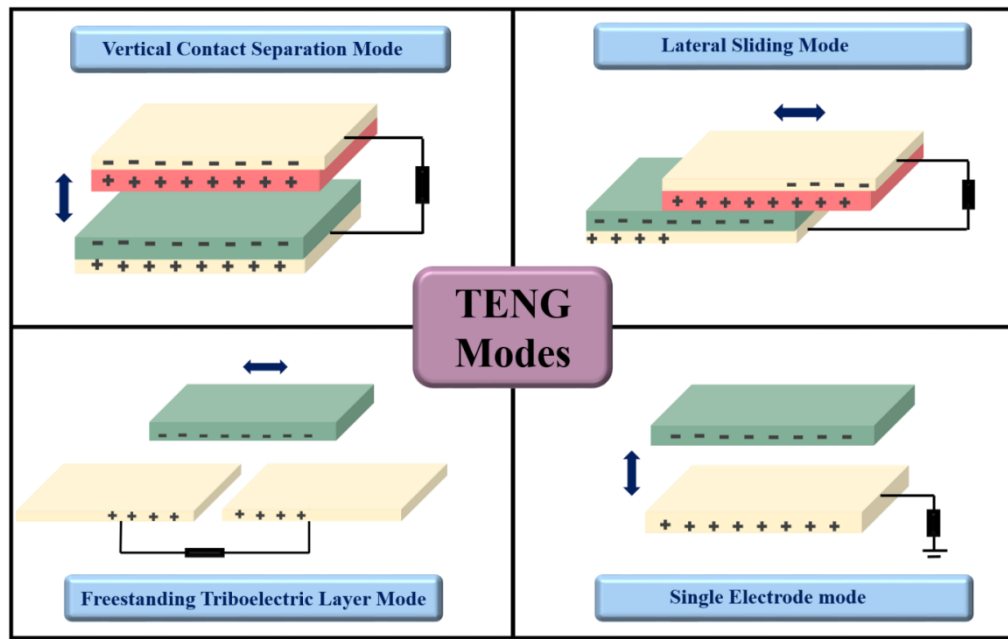


Figure 1.4 The four fundamental working modes of TENG.

The vertical contact-separation mode is known for generating significantly higher output compared to other TENG operating modes due to the efficient transfer of charge during the contact and separation process. This mode allows for a more pronounced mechanical deformation, resulting in a larger electrical potential difference. Given its superior performance in terms of energy generation, we have selected the vertical contact-separation mode as the preferred configuration for our research. By utilizing

this mode, we aim to enhance the efficiency and output of the TENGs we fabricate, ensuring their suitability for powering small devices or self-powered sensors in various applications. In addition to this, there are several modeling parameters that need to be kept in mind to design an efficient TENG with improved power density[21]. These modeling parameters are illustrated in Figure 1.5.

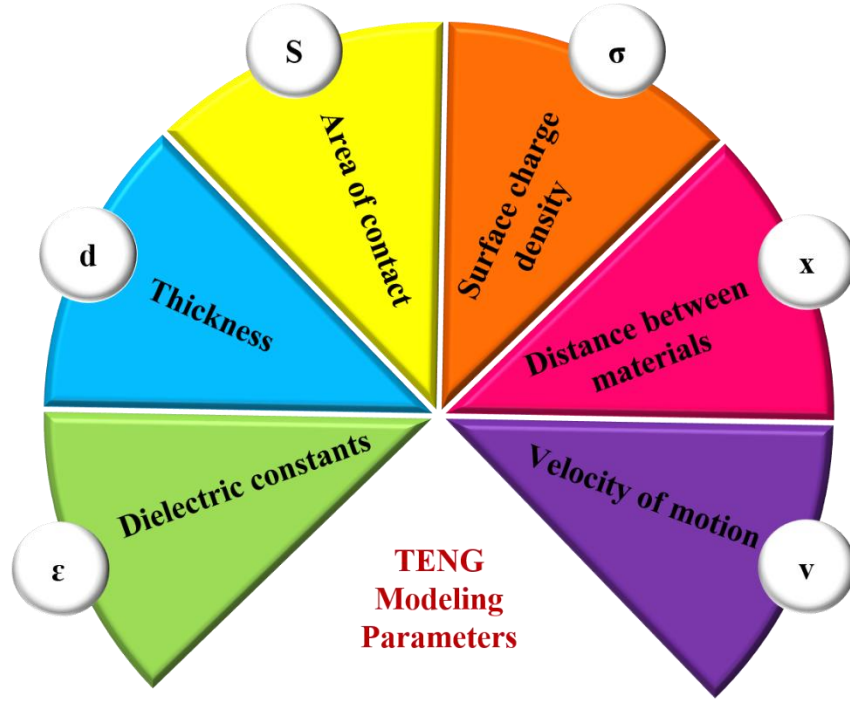


Figure 1.5: Overview of key TENG modeling parameters affecting performance of TENG[21].

1.3 Hybridization of Piezoelectric and Triboelectric Nanogenerators

Although, individual energy harvesting mechanism have demonstrated considerable efficiency for its practical applications, however their output power still remains inadequate for continues operation of these devices. To overcome this limitation, integrating multiple energy harvesting mechanisms within a single device using a common input source has become a compelling focus in energy harvesting research. Therefore, in the current thesis we have hybridized piezoelectric and triboelectric nanogenerator to enhance the energy harvesting capability of nanogenerator by combining the strength of each mechanism and corresponding details are discussed in Chapter 3 of thesis. While TENGs generate high voltage at low current levels through triboelectric effects, PENGs produce moderate voltage with higher current through piezoelectric effects. By integrating these two systems into a single device, it is possible

to achieve an energy harvester that captures both high-voltage and high-current outputs, improving the overall efficiency and adaptability of the device for a variety of applications. This hybrid approach not only boosts the charging performance but also increases the versatility of energy harvesters in areas where reliable and continuous energy generation is required, such as in wearable electronics, remote sensing systems, and IoT devices. To date, numerous works have been reported to demonstrate the successful implementation of hybrid systems combining triboelectric and piezoelectric elements, showing substantial improvements in energy output. By strategically designing the structural configuration of hybrid nanogenerators, the device can simultaneously or sequentially engage both mechanisms, capturing mechanical energy more efficiently. The hybridization technique also opens up possibilities for integrating other complementary energy harvesting systems, such as photovoltaic or electromagnetic generators, further amplifying the device's power generation potential.

1.4 Polymers for Piezoelectric and Triboelectric Nanogenerators

Plenty of materials have been explored to fabricate the nanogenerators for harvesting the ambient mechanical energy via piezoelectric and triboelectric effect. Among the various materials, polymers are promising for fabricating nanogenerator owing to its inherent flexibility, lightweight nature, and ease of processing make polymers ideal for wearable electronics, self-powered sensors, and other flexible devices[22, 23]. Initially, piezoelectric properties were thought to be exclusive to ceramic materials. However, this perspective began to shift in 1963, when researchers discovered that certain polymers, specifically poly(methyl methacrylate) (PMMA) and poly(vinyl chloride) (PVC), also exhibited piezoelectric behavior. This finding opened new avenues for exploring piezoelectricity in materials beyond ceramics, revealing the potential for polymers in energy harvesting and sensing applications. A groundbreaking finding about the piezoelectric properties of poly(vinylidene fluoride) (PVDF) was made in 1969 by researchers Kawai and Kureha. They observe that when PVDF is polarized, it demonstrates an impressive piezoelectric coefficient of 6–7 pC/N[24]. This coefficient is remarkably high, approximately ten times greater than those observed in any other known polymers at the time. The discovery marked a significant advancement in polymer science, positioning PVDF as an exceptional material for applications requiring efficient

mechanical-to-electrical energy conversion. Poly(vinylidene fluoride) (PVDF) and its copolymers are known for their remarkable flexibility and exhibit a unique combination of properties, including strong piezoelectric, pyroelectric, ferroelectric, and dielectric characteristics[25]. These qualities make PVDF and its copolymers highly versatile, enabling them to effectively convert mechanical, thermal, and electrical energy. This exceptional combination of properties allows PVDF-based materials to be widely used in sensors, actuators, and energy-harvesting applications, where both flexibility and efficient energy conversion are essential. In addition to PVDF, several other polymers, such as poly(tetrafluoroethylene) (PTFE)[26], nylon [27], polyacrylonitrile (PAN)[28], poly(vinyl acetate) (PVA)[29], and even poly(methyl methacrylate) (PMMA)[30] etc. Compared to piezoceramics, these piezoelectric polymers, while having lower intrinsic piezoelectric properties, present several key advantages for emerging technology applications. Piezoceramics, such as lead zirconate titanate (PZT), indeed offer high piezoelectric constants, but their rigidity and brittleness limit their use in flexible, small-scale, or wearable designs. When repeatedly subjected to mechanical stress, piezoceramics are prone to developing cracks, which can significantly degrade their performance over time. This makes them less suitable for applications where continuous or repetitive stress is expected. Therefore, in this research, we focus on designing flexible nanogenerators using polymer materials, selecting PVDF among various polymers due to its high piezoelectric coefficient, flexibility, environmental stability, biocompatibility, and potential for molecular customization. In addition to its piezoelectric capabilities, PVDF also acts as an effective negative triboelectric material in triboelectric nanogenerators (TENGs) due to the presence of electronegative fluorine atoms in its structure. This unique attribute further enhances PVDF's versatility, enabling it to play dual roles in hybrid nanogenerators that combine piezoelectric and triboelectric mechanisms, thereby maximizing the energy harvested from mechanical sources.

In the subsequent section, a detailed examination of the structural and functional properties of PVDF and its associated nanostructures will be presented, forming the foundation for the research discussed in this thesis.

1.4.1 PolyvinylideneFluoride (PVDF): A Ferroelectric Polymer

PVDF is a semi-crystalline polymer produced by the repetition of polymeric chain of ($-\text{CH}_2\text{-CF}_2-$) monomers, which can be crystallized into five distinct phases, i.e. α , β , γ , δ , and ϵ . Among these electrically active polar phase α , β , and γ are mostly investigated where γ is the translation state between α , and β phase[31-33]. The α -phase has trans-gauche-trans-gauche (TGTG') conformation, where dipoles are aligned anti-parallel to each other and hence non-polar in nature. While, β -phase exhibits all-trans conformation (TTTT) means all dipoles of individual molecules are aligned parallel to each other producing a net non-zero dipole moment as a result manifests large spontaneous polarization and high piezoelectric sensitivity among all the phases. As γ -phase is the intermediate stage between α , and β phase, therefore, it also exhibit a dipole moment but less than that of β -phase[34]. The chain conformation of different phases of PVDF is illustrated in Figure 1.6.

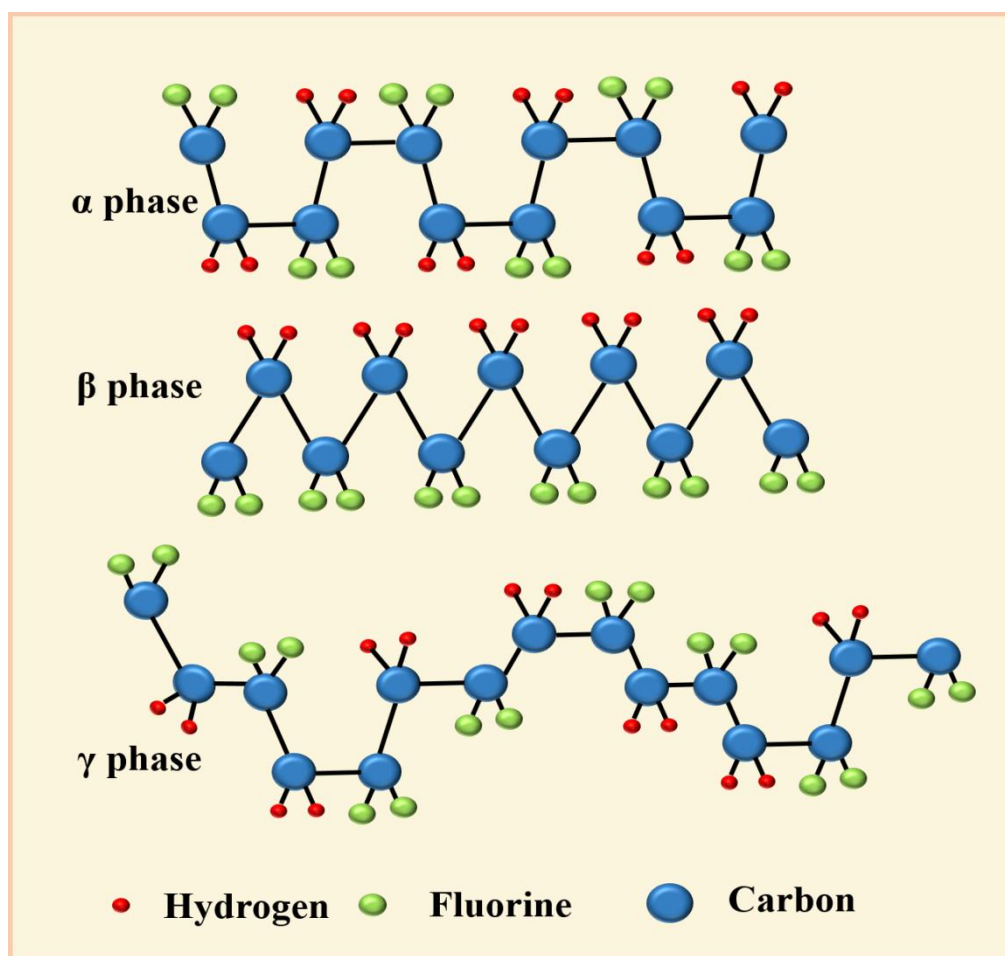


Figure 1.6 A schematic illustration of change conformation of α , β , and γ phase in PVDF.

The piezoelectric properties of PVDF largely depend on its crystalline phases[35]. Specifically, its piezoelectricity arises from the presence of polar crystalline phases, with the β -phase having the highest electric dipole moment among all crystalline forms[36].

Consequently, enhancing the β -phase content in PVDF is a key strategy to boost the piezoelectric performance of PVDF-based devices, such as sensors, actuators, and energy harvesters. Additionally, PVDF stands out as an excellent material choice for fabricating triboelectric nanogenerators (TENGs) owing to its good dielectric properties, which enhance its effectiveness in charge generation and storage during triboelectric interactions[37]. The presence of fluorine atoms in PVDF provides high electron affinity, significantly boosting its ability to attract and retain electrons when in contact with other materials. This characteristic is critical for TENG performance, as it facilitates efficient charge transfer upon repeated contact and separation cycles, thereby increasing the device's output performance. Thus, PVDF's exceptional piezoelectric, dielectric properties, strong mechanical resilience, and notable electron affinity position it as an ideal material for fabricating piezoelectric and triboelectric nanogenerator. These qualities make PVDF highly effective for generating and sustaining electrical output, especially in applications that demand durability and efficient energy transfer. Therefore, in this study, we have chosen PVDF as the primary material for fabricating nanogenerators aimed at a range of applications, leveraging its advantageous properties to optimize device performance.

1.4.2 Methods for Improving Performance of PVDF based Nanogenerator

For efficient use of PVDF based nanogenerator in energy harvesting applications, several strategies are implemented. One key approach is optimizing the crystalline phases of PVDF, particularly by increasing the β -phase content, which possesses a high dipole moment. This can be achieved through mechanical stretching, high-temperature annealing, and electric field poling, all of which align the materials dipoles and maximize its piezoelectric properties[15, 38]. Additionally, incorporation of nanofillers such as graphene, reduced graphene oxide (rGO)[39], carbon nanotubes (CNTs)[40], barium titanate (BaTiO_3)[41], zinc oxide (ZnO)[42], and lead zirconate

titanate (PZT)[43] also significantly enhances the dielectric constant, electron affinity, and electroactive β -phase in PVDF, resulting in increased charge density, improved charge transfer, and boosted piezoelectric and triboelectric output. Although, ceramic materials such as PZT and BaTiO_3 are effective nanofillers options, their use is limited by toxicity concerns and the complexity of their preparation processes.

Moreover, modifying the surface roughness of PVDF is another effective method; creating micro- or nano-patterns increases contact area, leading to higher triboelectric charge generation when PVDF interacts with other materials[44]. The electrospinning of PVDF into nanofibers increases surface area and improves β -phase alignment, enhancing both piezoelectric and triboelectric performance due to the nanofibers high surface-area-to-volume ratio[45]. Finally, applying an external electric field during or after fabrication aligns the dipoles, stabilizing the β -phase and maximizing the piezoelectric response. Together, these strategies improve the efficiency, durability, and adaptability of PVDF-based nanogenerators, making them highly suitable for applications like self-powered sensors, wearable electronics, and sustainable energy harvesting. In this thesis, we demonstrate two key approaches i.e. addition of nanofillers and electrospinning technique to improve the output performance of the PVDF based nanogenerator. Specifically, we introduced reduced rGO and its heteroatom-doped variants into PVDF matrix and examined how addition of these nanofillers improves its piezoelectric and triboelectric properties.

1.5 Nanofillers Materials

The performance of PVDF-based nanogenerators can be significantly enhanced by incorporating different kinds of piezoelectric materials, conductive and non-conducting nanofillers with specific amount of dopant. These nanofillers introduce modifications at the molecular and structural levels, enabling better charge generation and energy conversion. Several materials including ceramics, perovskite, metal oxides, 2D materials, organic and inorganic materials are utilized as nanofillers materials[46, 47]. Among the commonly used piezoelectric fillers, materials such as lead zirconate titanate (PZT), potassium sodium niobate (KNN), barium titanate (BaTiO_3), bismuth ferrite (BiFeO_3), potassium niobate (KNbO_3), lead titanate (PbTiO_3), and zinc oxide (ZnO) are notable due

to their high piezoelectric coefficient. These fillers interact with the PVDF matrix to improve the alignment of dipoles and increase the overall piezoelectric output. However, the use of these materials poses certain challenges. For example, PZT contains lead, which raises environmental and health concerns, while BaTiO₃ and KNN, though lead-free, have a brittle nature that limits their application in flexible and wearable devices. Additionally, 2D materials such as molybdenum disulfide (MoS₂), tungsten disulfide (WS₂), hexagonal boron nitride (hBN), graphene, MXenes etc. have also reported to be effective nanofillers[48-50]. These materials are characterized by their unique layered structures, high surface areas, and excellent mechanical and electrical properties. When incorporated into the PVDF matrix, they reinforce its mechanical strength, enhance its dielectric properties, and improve charge mobility. In the present thesis we have chosen carbon-based nanomaterials such as rGO as the nanofillers materials for improving the performance of PVDF-based nanogenerators. These materials offer a combination of exceptional properties, such as superior electrical and thermal conductivity, mechanical flexibility, chemical stability and biocompatibility[51, 52]. When integrated into the PVDF matrix, carbon-based materials enhance the dielectric constant through interfacial polarization and improve charge transfer efficiency, resulting in higher energy conversion performance. Additionally, their lightweight nature, nanoporous architecture, high aspect ratio and ease of functionalization and interactions ensure uniform dispersion and compatibility with PVDF, unlike some rigid piezoelectric or ceramic fillers. Furthermore, incorporating carbon-based materials into the PVDF matrix serves as a nucleating agent, promoting increased β -phase content and enhancing the crystallinity of PVDF film. Additionally, the charge-trapping and conductive properties of these nanofillers improve polarization efficiency, thereby generating more dipoles and charges within the PVDF matrix, resulting in improved performance of nanogenerator[39, 53]. These characteristics make carbon-based nanomaterials a highly effective choice for advancing PVDF-based nanogenerators, particularly in applications requiring flexible, efficient, and sustainable energy harvesting devices.

1.5.1 Reduced Graphene Oxide (rGO) as an Effective Nanofiller

Reduced graphene oxide is a derivative of graphene, consisting of a single layer of carbon atoms arranged in a 2D honeycomb lattice[54]. rGO is obtained by chemically reducing

graphene oxide (GO), which is graphene that has been oxidized to introduce oxygen-containing functional groups like hydroxyl, epoxide, and carboxyl groups on its surface. This reduction process removes some of these oxygen groups, restoring much of the electrical conductivity of graphene while maintaining the structure and some of the chemical functionalities of GO. It is highly promising material for energy harvesting applications due to its exceptional electrical conductivity, high surface area, and flexibility, combined with its ability to be easily functionalized to enhance its properties. Additionally, rGO's tunable chemical properties allow for functionalization with various dopants, such as nitrogen, boron, or sulphur, to further enhance its performance[55, 56]. For instance, nitrogen doping can increase the charge carrier density and electron affinity, while boron doping can improve the material's catalytic activity, which is beneficial in energy conversion processes. These modifications can further improve the energy harvesting capabilities of rGO-based composites, allowing for optimized devices that can be tailored to specific applications. Also, rGO exhibits inherent piezoelectric properties due to the introduction of oxygen-containing groups (such as hydroxyl or epoxy) during the reduction process can disrupt this symmetry, enabling piezoelectric behaviour[57-59]. Further, the insertion of heteroatoms such as nitrogen, boron, or sulphur into the rGO structure can enhance this asymmetry, inducing stronger piezoelectric effects. These heteroatoms introduce additional electronic states that further break the symmetry and create dipole moments in the material. As a result, rGO becomes piezoelectric, and this effect is more pronounced when heteroatoms are introduced. In TENG, the incorporation of rGO into the triboelectric layer enhances its electron affinity, leading to better charge accumulation and transfer when the material comes into contact with other surfaces. Together, these properties make rGO and its heteroatom-doped variants highly effective nanofillers for PVDF-based nanogenerators, supporting the development of efficient, flexible, and durable devices suitable for applications in sustainable energy harvesting, wearable electronics, and self-powered sensors.

1.6 Research Challenge

The field of piezoelectric and triboelectric nanogenerators (PENGs and TENGs) has seen significant advancements in recent years, yet several key challenges remain that hinder

their broader application, particularly in energy harvesting and self-powered systems. One of the primary challenges is the relatively low output performance of these devices. While both PENGs and TENGs can convert mechanical energy into electrical energy, the power generated is often insufficient to power high-demand devices, especially in low-energy environments where mechanical vibrations or movements are irregular and unpredictable. Additionally, the power output tends to be inconsistent, affected by factors such as frequency, amplitude, and environmental conditions, making reliable and sustained operation difficult. Consequently, fully eliminating the reliance on batteries remains a significant challenge. Furthermore, energy harvesting devices may experience fluctuating outputs over time due to factors such as environmental changes, wear, and mechanical degradation. Another key challenge in this field is the integration of energy harvesting and self-powered technologies into a unified platform. This integration often leads to an increase in the size, weight, and overall volume of the system, which complicates its practical use, particularly for applications requiring compact and lightweight solutions. A critical consideration for self-powered IoT platforms is achieving the seamless integration of energy harvesting, sensing, power management, processing, and transmission components within the limited physical space available in the device.

1.7 Thesis Problem

The key objective of this thesis is to enhance the output performance of PVDF-based nanogenerator, with a particular emphasis on understanding the role of nanofillers in improving the overall device efficiency for a wide range of applications. In addition to optimizing the performance of PVDF-based nanogenerators through the incorporation of nanofillers, the present work explores the advantages of fabricating hybrid devices. This hybrid approach holds promise for expanding the applicability of nanogenerators in self-powered systems, such as wearable electronics, IoT devices, and biomedical sensors, where compactness, high efficiency, and sustained power output are crucial.

1.7.1 Research Objectives

The main research objective of this thesis is the development of PVDF nanocomposite films based nanogenerator for multifunctional applications, specifically by leveraging

piezoelectric and triboelectric effects for harnessing ambient mechanical energy. The main objectives of this research are outlined as follows:

- ❖ To study the effect of the pristine and heteroatom doped reduced graphene oxide in the output performance of the PVDF-rGO based flexible piezoelectric nanogenerator.
- ❖ To study the effect of hybridization of piezoelectric and triboelectric nanogenerator in improving the output performance of the heteroatom doped reduced graphene oxide based nanogenerator.
- ❖ To analyse the effect of wt% of reduced graphene oxide on the output performance of PVDF-rGO/Nylon based triboelectric nanogenerator.
- ❖ To study the effect of drop-casting and electrospinning in improving the output performance of PVDF/N-rGO based triboelectric nanogenerator for self-powered electronic devices and wireless sensor applications.
- ❖ To study the effect of variation of weight percentage of B, N Co-doped reduced graphene oxide in electrospun PVDF nanofibers based triboelectric nanogenerator for self-powered water remediation.

1.7.2 Overview of Thesis

Chapter 1: Introduction

This chapter provide a brief introduction about the need of sustainable energy solutions, emphasizing the importance of energy harvesting technologies in addressing global energy demands. Furthermore, as we are marching into the smart era, where wearable and portable electronics have become widespread in variety of fields, such as healthcare, artificial intelligence, Internet of things (IoT), wireless sensor networks etc. The powering of these electronic devices still remains a major issue. In this regard, it is necessary to look towards the cleaner, and renewable power sources for these wearable and portable electronics to address this issue. In light of this, several energy harvesting technologies have been developed over the years, based on mechanisms such as piezoelectric, triboelectric, electromagnetic, and pyroelectric phenomena. Among the various energy harvesting technologies, mechanical energy harvesters are of utmost importance as they

can capture ambient mechanical energy, for instance, vibrations, movements, and minor pressure changes and convert it into electricity with the help of piezoelectric and triboelectric nanogenerator. This ability makes them ideal for powering distributed IoT devices and smart systems that require low-power, continuous energy supplies without relying on conventional power grids or frequent battery replacements. The present chapter will then explore how piezoelectric and triboelectric nanogenerators, as innovative technologies, are particularly well-suited to fulfil these energy requirements due to their efficiency, scalability, and potential for integration into various applications and can contribute to a more sustainable and energy-efficient future, addressing the energy challenges posed by the rapidly growing number of smart devices and systems.

Chapter 2: Synthesis and characterization techniques

Chapter 2 provides an overview of the various experimental techniques used to synthesize and examine the samples, along with their relevant theoretical foundations. Reduced graphene oxide (rGO) and heteroatom (boron, nitrogen and boron nitrogen) doped rGO have garnered significant attention from researchers due to their excellent electronic, optical, and mechanical properties, as well as their non-toxic nature. Additionally, PVDF and its copolymers are highly valued in the fabrication of nanogenerators for its lightweight, high flexibility, cost-effectiveness, and ease of processing. The chapter begins, by briefly discussing the common processes used for synthesizing rGO and heteroatom doped rGO using hydrothermal methods, and the techniques employed in fabricating PVDF/rGO and PVDF/heteroatom doped rGO nanocomposite thin films, including drop casting and electrospinning. It then delves into the characterization techniques used to analyse the prepared samples, including powder X-ray diffraction, XPS, FESEM, EDAX, FTIR, Raman, KPFM, PE loop tracer, dielectric analysis, and more, providing a detailed examination of each method.

Chapter 3: Effect of pristine and heteroatom doped rGO on the output performance of the PVDF nanocomposite based piezoelectric nanogenerator for biomechanical energy harvesting applications

This chapter presents a high-performance nanogenerator based on PVDF/heteroatom (Boron, nitrogen and boron nitrogen) doped rGO for generating electrical power. The

result demonstrates that the addition of rGO and heteroatom doped rGO (B-rGO, N-rGO, and BN-rGO) in the PVDF matrix has significantly enhances the piezoresponse of PVDF nanocomposite films. A maximum output voltage and current of 20.4 V and 15.9 μ A, respectively is generated by PVDF/BN-rGO based piezoelectric nanogenerator which is ~ 2 and ~ 6 times higher than the voltage and current produced by the pristine PVDF based piezoelectric nanogenerator. The impact of varying input frequency was also examined for all PENGs, revealing that each device exhibited the highest response at a frequency of 6 Hz. The enhanced performance of PENGs are ascribed to nucleation of electroactive polar β -phase content in PVDF nanocomposite films and formation of the conducting network within the polymer matrix which facilitate the better charge transfer and hence enhance the resultant output of PVDF nanocomposite films. The as fabricated PENG is then utilized to harness biomechanical energy from different human motions including finger tapping, wrist bending, foot tapping, leg and elbow folding. To further enhance the nanogenerators output performance, a hybrid nanogenerator (HNG) combining piezoelectric and triboelectric effects was developed by layering the high-output PVDF/BN-rGO nanocomposite film with a PDMS thin film. A maximum output voltage of 57.6 V is generated by PVDF/BN-rGO based HNG. The generated output power is then utilized to charge variety of capacitors, LEDs and calculator. This study presents an effective approach for creating high-performance energy harvesters for self-powered wearables by using graphene derivatives as nanofillers in a PVDF matrix. It also shows that combining different mechanisms in a single device can boost energy harvesting efficiency in the resulting HNG, enabling more effective mechanical energy capture.

Chapter 4: Synergistic effect of N-doped rGO nanofillers concentration and electrospinning technique on the output performance of PVDF nanocomposite based triboelectric nanogenerator for self-powered electronics and wireless sensor applications

As we have concluded in the previous chapter that addition of heteroatom doped rGO enhances the piezoelectric as well triboelectric properties of drop casted PVDF film but the concentration of nanofillers in the PVDF also have significant impact on device performance. Therefore, in this chapter we have presented two important aspects of

nanogenerator to boost the performance of triboelectric nanogenerators. The initial approach is to identify the ideal concentration of the nanofillers (i.e. rGO, and N-rGO) in PVDF matrix and second approach involves the usage of the electrospinning technique for fabrication of nanofibers mat, which improves the surface area and mechanical properties of the TENG. For this, we have fabricated the different triboelectric energy harvesters using PVDF nanocomposite films and nylon film by varying the weight percentage (0.025 %, 0.5%, 1 %, 1.5 % and 2 wt %) of rGO and N-rGO in PVDF matrix prepared via drop casting technique. The incorporation of nanofillers (i.e. rGO and N-rGO) in PVDF matrix enhanced its triboelectric output. In comparison to bare PVDF film, the triboelectric nanogenerator with 1.5 wt% of rGO and N-rGO as a nanofillers in PVDF matrix can generate maximum output voltage of 98.4 V and 156 V at 8 Hz frequency, while pure PVDF film based nanogenerator produce 67.2 V output voltage. The results demonstrate that 1.5 wt% of rGO and N-rGO is ideal doping concentration for triboelectric nanogenerator. Above 1.5 wt% of rGO and N-rGO the triboelectric performance of the nanogenerator abruptly declined due to formation of conducting network of rGO and N-rGO within the PVDF matrix. Moreover, the heteroatom doped rGO (i.e. N-rGO) can generate more power in comparison to pure rGO based TENG which might be due to higher capacitance of N-rGO in comparison to rGO. Furthermore, nanofibers mat of PVDF, PVDF/N-rGO with 1.5 wt% of N-rGO and nylon are fabricated by the electrospinning technique. A maximum voltage, current and power density of 368 V, 35 μ A and \sim 282.8 μ W/cm² is generated by the PVDF/N-rGO nanofibers mat based TENG, which is six times higher than the power density of the drop casted PVDF/N-rGO film based TENG under impedance matching condition. The effects of tapping frequency and impact force on TENG's triboelectric performance were also analysed, showing that higher frequency and force enhances output performance due to faster charge transfer and increased effective area and capacitance. Additionally, incorporating N-rGO raises the polar crystalline β -phase content and dielectric constant in PVDF/N-rGO nanofiber mats and films, boosting triboelectric performance. The dispersed N-rGO nanosheets in PVDF also increase surface potential, improving charge transfer density and significantly enhancing the output of the PVDF/N-rGO and Nylon-based TENG. Finite element analysis using COMSOL have also been carried out for quantitative understanding of

the surface potential distribution between two triboelectric layers of the TENG. Furthermore, the power generated by TENG is utilized to power small power electronic devices, such as, LEDs, thermometer, digital watch, and hygrometer and also used to harness mechanical energy from the human movements. Finally, the constructed TENG is employed as a self-powered motion sensor, automatically turning on lights when there is human motion at night. This study suggests a cost-effective method for developing a high-performance TENG for designing self-powered human-machine interface for managing wireless sensing system.

Chapter 5: Optimizing B, N Co-doped rGO concentration in electrospun PVDF nanofibers for triboelectric nanogenerator-driven water remediation

In this chapter, to further improve the efficiency of TENG, we have constructed the nanofibers of PVDF and PVDF nanocomposites with different weight percentage of B, N Co-doped rGO and coupled it with nylon fibres and demonstrates its application in degradation of organic pollutants from wastewater. At first, the effect of BN-rGO wt% on the triboelectric performance of PVDF/BN-rGO nanofiber films were compared with pristine PVDF, and it was discovered that 1.5 wt% of BN-rGO is the ideal amount for triboelectric energy harvesting. The as fabricated TENG can generate a maximum voltage, current and power of 380 V, 36 μ A and 336 μ W/cm² respectively. Also, the as fabricated TENG is subjected to variable tapping force and frequency to examine the output performance of the TENG. The TENG's output performance improves as frequency increases which might be attributed to faster charge transfer at higher frequencies and moreover when we increase the force, the effective area and capacitance of the triboelectric films also grow, resulting into enhanced output performance of TENG. The effect of different triboelectric layer is also studied by varying the second triboelectric layer (i.e. nylon) with the PTFE, PDMS, PET, Paper and nitrile gloves. However, the maximum output performance corresponds to PVDF/BN-rGO and nylon nanofiber based TENG. The electronegativity difference between PVDF/BN-rGO and Nylon may be responsible for the increased performance. Finally, a self-powered dye degradation system is constructed by employing TENG as a power supply source to degrade methylene blue dye from the wastewater. The methylene blue takes 12 hours to completely degrade when TENG is used as power

source and no catalysis is used while in presence of both catalysis and TENG, it takes only 100 minutes to completely degrade the dye. The presents study sheds light on the development of efficient and sustainable TENG/catalyst system for wastewater remediation by utilizing the mechanical energy.

Chapter 6: Conclusions and future scope of work

This chapter provides a comprehensive summary of the key findings of thesis with a detailed focus on mechanical energy harvesting technologies, particularly piezoelectric and triboelectric nanogenerators. Additionally, it highlights promising avenues for future research that pave the way toward self-sustaining energy solutions, enhancing the practicality of nanogenerators in real-world applications. The arrangement of the various thesis chapters are shown in flowchart, which is illustrated in Figure 1.7.

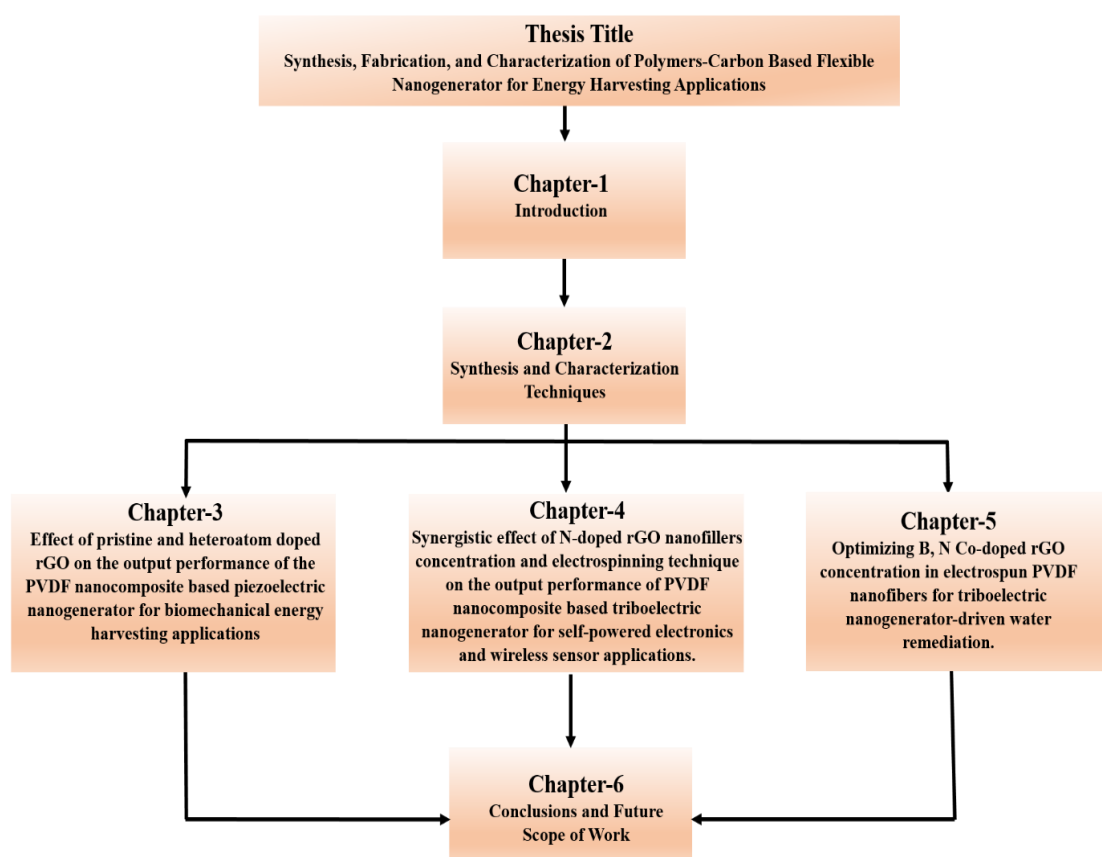


Figure 1.7: Flowchart for the organisation of the thesis.

References

- [1] M.D.P. Emilio, Microelectronic circuit design for energy harvesting systems, Springer, 2017.
- [2] H. Fang, C. Yu, T. Ma, J. Qiu, Boron-doped graphene as a high-efficiency counter electrode for dye-sensitized solar cells, Chemical Communications, 50 (2014) 3328-3330.
- [3] N.S. Hudak, G.G.J.J.o.A.P. Amatuucci, Small-scale energy harvesting through thermoelectric, vibration, and radiofrequency power conversion, 103 (2008) 5.
- [4] D. Wang, Y. Lin, D. Hu, P. Jiang, X. Huang, Multifunctional 3D-MXene/PDMS nanocomposites for electrical, thermal and triboelectric applications, Composites Part A: Applied Science and Manufacturing, 130 (2020) 105754.
- [5] R. Saidur, N.A. Rahim, M.R. Islam, K.H. Solangi, Environmental impact of wind energy, Renewable and sustainable energy reviews, 15 (2011) 2423-2430.
- [6] Z.L. Wang, J. Song, Piezoelectric nanogenerators based on zinc oxide nanowire arrays, Science, 312 (2006) 242-246.
- [7] F.-R. Fan, Z.-Q. Tian, Z. Lin Wang, Flexible triboelectric generator, Nano Energy, 1 (2012) 328-334.
- [8] Q. Liao, Z. Zhang, X. Zhang, M. Mohr, Y. Zhang, H.-J. Fecht, Flexible piezoelectric nanogenerators based on a fiber/ZnO nanowires/paper hybrid structure for energy harvesting, 7 (2014) 917-928.
- [9] S.J. Rupitsch, Piezoelectric Sensors and Actuators, Springer, 2018.
- [10] S.C. Masmanidis, R.B. Karabalin, I. De Vlaminck, G. Borghs, M.R. Freeman, M.L. Roukes, Multifunctional nanomechanical systems via tunably coupled piezoelectric actuation, Science, 317 (2007) 780-783.
- [11] S. Mishra, L. Unnikrishnan, S.K. Nayak, S. Mohanty, Advances in piezoelectric polymer composites for energy harvesting applications: A systematic review, Macromolecular Materials and Engineering, 304 (2019) 1800463.
- [12] K.S. Ramadan, D. Sameoto, S. Evoy, A review of piezoelectric polymers as functional materials for electromechanical transducers, Smart Materials and Structures, 23 (2014) 033001.
- [13] S. Datta, K. Mondal, Conceptualizing Implementation of Piezoelectric Materials in Transportation to Harvest Energy, (2019).

- [14] Z. Wang, X. Pan, Y. He, Y. Hu, H. Gu, Y.J.A.i.M.S. Wang, Engineering, Piezoelectric nanowires in energy harvesting applications, 2015 (2015).
- [15] D. Hu, M. Yao, Y. Fan, C. Ma, M. Fan, M. Liu, Strategies to achieve high performance piezoelectric nanogenerators, Nano energy, 55 (2019) 288-304.
- [16] Z.L. Wang, L. Lin, J. Chen, S. Niu, Y. Zi, Triboelectric nanogenerators, Springer, 2016.
- [17] S. Pan, Z. Zhang, Fundamental theories and basic principles of triboelectric effect: A review, Friction, 7 (2019) 2-17.
- [18] F.-R. Fan, Z.-Q. Tian, Z.L. Wang, Flexible triboelectric generator, Nano energy, 1 (2012) 328-334.
- [19] S. Niu, Z.L.J.N.E. Wang, Theoretical systems of triboelectric nanogenerators, 14 (2015) 161-192.
- [20] C. Wu, A.C. Wang, W. Ding, H. Guo, Z.L. Wang, Triboelectric nanogenerator: a foundation of the energy for the new era, Advanced Energy Materials, 9 (2019) 1802906.
- [21] S.A. Basith, G. Khandelwal, D.M. Mulvihill, A. Chandrasekhar, Upcycling of Waste Materials for the Development of Triboelectric Nanogenerators and Self-Powered Applications, Advanced Functional Materials, (2024) 2408708.
- [22] A.C. Wang, C. Wu, D. Pisignano, Z.L. Wang, L. Persano, Polymer nanogenerators: Opportunities and challenges for large-scale applications, Journal of Applied Polymer Science, 135 (2018) 45674.
- [23] H. Kaczmarek, B. Królikowski, E. Klimiec, M. Chylińska, D. Bajer, Advances in the study of piezoelectric polymers, Russian Chemical Reviews, 88 (2019) 749.
- [24] H. Kawai, The piezoelectricity of poly (vinylidene fluoride), Japanese journal of applied physics, 8 (1969) 975.
- [25] R. Fu, S. Chen, Y. Lin, S. Zhang, J. Jiang, Q. Li, Y. Gu, Improved piezoelectric properties of electrospun poly (vinylidene fluoride) fibers blended with cellulose nanocrystals, Materials Letters, 187 (2017) 86-88.
- [26] M. Wegener, W. Wirges, R. Gerhard-Multhaupt, Piezoelectric polyethylene terephthalate (PETP) foams—specifically designed and prepared ferroelectret films, Advanced Engineering Materials, 7 (2005) 1128-1131.
- [27] S. Anwar, M. Hassanpour Amiri, S. Jiang, M.M. Abolhasani, P.R. Rocha, K. Asadi, Piezoelectric nylon-11 fibers for electronic textiles, energy harvesting and sensing, Advanced Functional Materials, 31 (2021) 2004326.

- [28] J. Tao, Y. Wang, X. Zheng, C. Zhao, X. Jin, W. Wang, T. Lin, A review: Polyacrylonitrile as high-performance piezoelectric materials, *Nano Energy*, (2023) 108987.
- [29] J. Liu, S. Li, S. Zhou, Z. Chen, J. Xu, N. Cui, M. Yuan, B. Li, L. Gu, A high-performance, biocompatible, and fully biodegradable piezo-triboelectric hybrid nanogenerator based on PVA/Glycine/PVA heterostructured piezoelectric film, *Nano Energy*, 122 (2024) 109310.
- [30] X. Zhang, J. Villafuerte, V. Consonni, J.-F. Capsal, P.-J. Cottinet, L. Petit, M.-Q. Le, Characterizing and optimizing piezoelectric response of ZnO nanowire/PMMA composite-based sensor, *Nanomaterials*, 11 (2021) 1712.
- [31] Q. Zhang, V. Bharti, G. Kavarnos, Poly (vinylidene fluoride)(PVDF) and its copolymers, *Encyclopedia of smart materials*, (2002).
- [32] L. Ruan, X. Yao, Y. Chang, L. Zhou, G. Qin, X. Zhang, Properties and applications of the β phase poly (vinylidene fluoride), *Polymers*, 10 (2018) 228.
- [33] J. Martín, D. Zhao, T. Lenz, I. Katsouras, D.M. de Leeuw, N. Stingelin, Solid-state-processing of δ -PVDF, *Materials Horizons*, 4 (2017) 408-414.
- [34] P. Martins, A. Lopes, S. Lanceros-Mendez, Electroactive phases of poly (vinylidene fluoride): Determination, processing and applications, *Progress in Polymer Science*, 39 (2014) 683-706.
- [35] H. Liu, J. Zhong, C. Lee, S.-W. Lee, L. Lin, A comprehensive review on piezoelectric energy harvesting technology: Materials, mechanisms, and applications, *Applied physics reviews*, 5 (2018).
- [36] G. Zhu, Z. Zeng, L. Zhang, X. Yan, Piezoelectricity in β -phase PVDF crystals: A molecular simulation study, *Computational Materials Science*, 44 (2008) 224-229.
- [37] J.P. Lee, J.W. Lee, J.M. Baik, The progress of PVDF as a functional material for triboelectric nanogenerators and self-powered sensors, *Micromachines*, 9 (2018) 532.
- [38] S. Rana, V. Singh, H. Sharma, B. Singh, 10 - Fluoropolymer nanocomposites for piezoelectric energy harvesting applications, in: K. Deshmukh, C.M. Hussain (Eds.) *Advanced Fluoropolymer Nanocomposites*, Woodhead Publishing, 2023, pp. 317-358.
- [39] S. Rana, B. Singh, rGO-Embedded Polymer Nanocomposite Layer for Improved Performance of Triboelectric Nanogenerator, *Journal of Electronic Materials*, 53 (2024) 6640-6649.

- [40] C.-M. Wu, M.-H. Chou, W.-Y. Zeng, Piezoelectric Response of Aligned Electrospun Polyvinylidene Fluoride/Carbon Nanotube Nanofibrous Membranes, *Nanomaterials*, 8 (2018) 420.
- [41] B. Dudem, D.H. Kim, L.K. Bharat, J.S.J.A.E. Yu, Highly-flexible piezoelectric nanogenerators with silver nanowires and barium titanate embedded composite films for mechanical energy harvesting, 230 (2018) 865-874.
- [42] H.H. Singh, N. Khare, Flexible ZnO-PVDF/PTFE based piezo-tribo hybrid nanogenerator, *Nano Energy*, 51 (2018) 216-222.
- [43] S. Bano, B. Gupta, S.K. Sharma, R. Singh, Coupling of Triboelectric and Piezoelectric Effects in Nafion-Containing Polyvinylidene Fluoride: Lead Zirconium Titanate Nanofiber-Based Nanogenerators for Self-Powered Systems, *ACS Applied Nano Materials*, 7 (2024) 15425-15437.
- [44] C. Li, Y. Bai, J. Shao, H. Meng, Z. Li, Strategies to Improve the Output Performance of Triboelectric Nanogenerators, *Small Methods*, 8 (2024) 2301682.
- [45] K. Shi, B. Sun, X. Huang, P. Jiang, Synergistic effect of graphene nanosheet and BaTiO₃ nanoparticles on performance enhancement of electrospun PVDF nanofiber mat for flexible piezoelectric nanogenerators, *Nano Energy*, 52 (2018) 153-162.
- [46] A. Veved, G.W. Ejuh, N. Djongyang, Review of emerging materials for PVDF-based energy harvesting, *Energy Reports*, 8 (2022) 12853-12870.
- [47] K. Uchino, The development of piezoelectric materials and the new perspective, in: *Advanced Piezoelectric Materials*, Elsevier, 2017, pp. 1-92.
- [48] S.A. Han, J. Lee, J. Lin, S.-W. Kim, J.H. Kim, Piezo/triboelectric nanogenerators based on 2-dimensional layered structure materials, *Nano Energy*, 57 (2019) 680-691.
- [49] Y. Dong, S.S.K. Mallineni, K. Maleski, H. Behlow, V.N. Mochalin, A.M. Rao, Y. Gogotsi, R.J.N.E. Podila, Metallic MXenes: A new family of materials for flexible triboelectric nanogenerators, 44 (2018) 103-110.
- [50] P. Yadav, T.D. Raju, S.J.A.A.E.M. Badhulika, Self-poled hBN-PVDF nanofiber mat-based low-cost, ultrahigh-performance piezoelectric nanogenerator for biomechanical energy harvesting, 2 (2020) 1970-1980.
- [51] M.A. Gabris, J. Ping, Carbon nanomaterial-based nanogenerators for harvesting energy from environment, *Nano Energy*, 90 (2021) 106494.
- [52] S. Muniandy, S.J. Teh, K.L. Thong, A. Thiha, I.J. Dinshaw, C.W. Lai, F. Ibrahim, B.F. Leo, Carbon nanomaterial-based electrochemical biosensors for

foodborne bacterial detection, *Critical reviews in analytical chemistry*, 49 (2019) 510-533.

[53] H.H. Singh, S. Singh, N.J.C.S. Khare, Technology, Design of flexible PVDF/NaNbO₃/RGO nanogenerator and understanding the role of nanofillers in the output voltage signal, 149 (2017) 127-133.

[54] M. Aleksandrak, E. Mijowska, Graphene and its derivatives for energy storage, *Graphene Materials: Fundamentals and Emerging Applications*, (2015) 191-224.

[55] R. Kumar, S. Sahoo, E. Joanni, R.K. Singh, K. Maegawa, W.K. Tan, G. Kawamura, K.K. Kar, A. Matsuda, Heteroatom doped graphene engineering for energy storage and conversion, *Materials Today Communications*, 39 (2020) 47-65.

[56] S.J. Lee, J. Theerthagiri, P. Nithyadharseni, P. Arunachalam, D. Balaji, A.M. Kumar, J. Madhavan, V. Mittal, M.Y. Choi, Heteroatom-doped graphene-based materials for sustainable energy applications: A review, *Renewable and Sustainable Energy Reviews* 143 (2021) 110849.

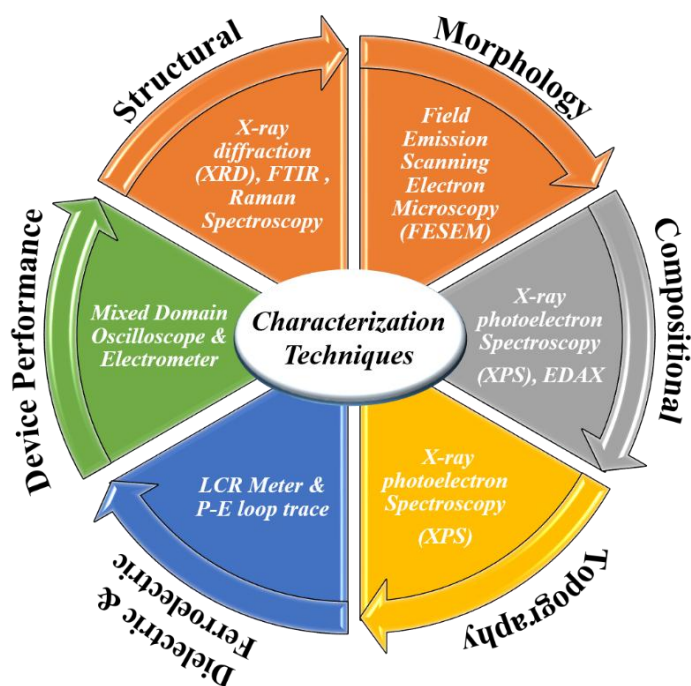
[57] M.T. Ong, E.J. Reed, Engineered piezoelectricity in graphene, *ACS Nano*, 6 (2012) 1387-1394.

[58] J. Xue, L. Wu, N. Hu, J. Qiu, C. Chang, S. Atobe, H. Fukunaga, T. Watanabe, Y. Liu, H. Ning, Evaluation of piezoelectric property of reduced graphene oxide (rGO)–poly (vinylidene fluoride) nanocomposites, *Nanoscale*, 4 (2012) 7250-7255.

[59] J.-H. Ji, B.S. Kim, J. Kang, J.-H. Koh, Improved output performance of hybrid composite films with nitrogen-doped reduced graphene oxide, *Ceramics International*, (2021).

CHAPTER 2

Synthesis and characterization techniques



This chapter provides a comprehensive summary of the synthesis and fabrication methods used for nanostructured materials and polymer nanocomposite films, along with the characterization techniques employed. Nanostructures are synthesized via the hydrothermal method, while nanocomposite films and nanofiber mats are fabricated through drop-casting and electrospinning. Structural and morphological analyses, including X-ray diffraction (XRD) and field emission scanning electron microscopy (FESEM), reveal crystallinity and surface features. X-ray photoelectron spectroscopy (XPS) and energy dispersive X-ray spectroscopy (EDS) assess chemical composition and elemental distribution. Fourier transform infrared spectroscopy (FTIR) identifies different phases, and dielectric studies examine electrical properties. Polarization-electric field (P-E) loop and Kelvin probe force microscopy (KPFM) measurements evaluate piezoelectric and ferroelectric behavior, alongside surface potential distribution. Furthermore, the chapter discusses the fabrication of nanogenerators based on these nanocomposite films, followed by extensive electrical characterization to evaluate their performance in energy harvesting applications. All of these techniques and methodologies are concisely summarized in this chapter.

2.1 Synthesis of Reduced Graphene Oxide (rGO) and its Heteroatom Doped Variants

Numerous techniques are available for synthesis of graphene and its derivative by tailoring the structure and properties for a wide range of applications. These methods are classified into two categories : 1) Top-down and 2) Bottom-up approaches. The top-down approach aim to extract nanostructures from bulk materials by overcoming the interlayer forces. The key techniques used in this approach are mechanical exfoliation, plasma etching, ball milling, electrochemical exfoliation. In contrast, bottom down focuses on building nanostructures by facilitating interactions among atoms and molecules, resulting in the formation of material clusters. Therefore, selecting the appropriate synthesis route is important before investigating the properties and potential applications of the graphene oxide and its derivative. As high-quality nanomaterials must be produced in large quantities for their successful commercialization and industrial application. Therefore, to synthesize reduced graphene oxide, first graphene oxide is produced using modified Hummer's method and then hydrothermal technique is used for synthesis of rGO and its heteroatom doped variants. The various synthesis methods employed in present work are briefly summarized in the sections below.

2.1.1 Modified Hummer's Method

The modified Hummer's method is a well establish chemical procedure for synthesis of graphene oxide (GO) from graphite[1]. This method is the improvement on the original Hummer's method and utilize strong oxidizing agents, including potassium permanganate (KMnO_4) and sulfuric acid (H_2SO_4). This process/ method is favored for its improved efficiency, safety and high yield.

The key features of Modified Hummer's method are:

1. **Efficient Oxidation Agents:** The usage of high concentration of potassium permanganate along with the phosphoric acid (H_3PO_4) contributes in more efficient and controlled oxidation of graphite, resulting in GO with a higher oxygen content and better structural integrity.

2. **Optimized Reaction Conditions/ Controlled Reaction Kinetics:** In comparison to the original Hummers' method, the modified method operates at a lower temperature, which helps in reducing the possibility of runaway reactions and violent exothermic reactions that can occur with the original method by controlling the reaction rate, making the process more manageable.
3. **Higher Yield and Quality:** This method produces higher yield of GO with enhanced exfoliation of graphite layers, leading to an improved surface area of GO. Additionally, the formation of oxygen-containing functional groups (such as hydroxyl, carboxyl, and epoxy groups) on the graphene sheets improves its dispersion in solutions.
4. **Better Structural Integrity:** The GO prepared by modified hummer's method typically has a better structural integrity with fewer defects and improved carbon to oxygen(C/O) ratios, which is crucial for applications in electronics, energy storage, and sensors.
5. **Reduction of Hazardous Byproducts:** Unlike the conventional method, the modified Hummers method removes the usage of sodium nitrate (NaNO_3), which in the traditional process generates harmful gases like nitrogen dioxide (NO_2) and dinitrogen tetroxide (N_2O_4), posing significant environmental and safety risks. This modification not only improves safety but also makes the process more environmentally sustainable.

2.1.2 Hydrothermal Synthesis Route

In the current work, hydrothermal method is employed for synthesizing reduced graphene oxide and its heteroatom doped variants. This method is first reported by Karl Emil von Schafhäütl, a German geologist in 1845 and thereafter, collaborative efforts by researchers and scientists have propelled worldwide in the advancement of this method. The hydrothermal method involves synthesis of nanostructured materials through chemical reaction taking place within a Teflon lined stainless steel autoclave, containing reagents in aqueous media under specific temperature and pressure conditions. This process allows materials to dissolve and then crystallize, which is not achievable at normal temperature and pressure. To obtain the nanomaterials with specific morphology

and properties, a fixed amount of solution containing reagent is introduced into the Teflon lined autoclave, maintaining the required pressure throughout the process. It is important to avoid any overflow of the Teflon liner during the reaction. By optimizing key parameters such as temperature, pressure, and reaction time in a high-temperature oven, a significant yield of well-crystallized nanostructured materials can be achieved[2]. Figure 2.1 illustrates the setup of the hydrothermal autoclave utilized in the synthesis process. The hydrothermal reaction includes the following components:

1. **Precursors:** These are the starting materials that undergo chemical reactions in suitable solvents, leading to the production of the desired nanomaterial.
2. **Mineralizing Substance and Other Additives:** Various acids and bases are introduced throughout the reaction to attain specific pH levels. These compounds, known as mineralizers, are essential to the process. Furthermore, other additives, such as, chelating agents, reducing agents, and stabilizers are used to regulate the morphology and properties of synthesized nanomaterials.

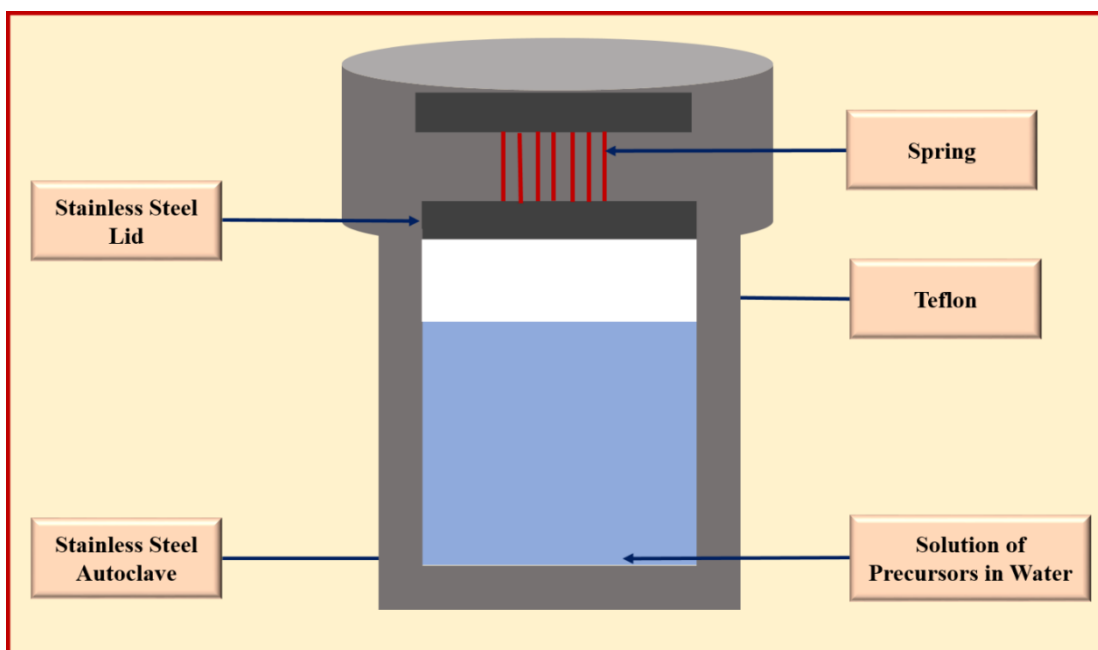


Figure 2.1 A schematic showing hydrothermal autoclave set-up used in hydrothermal synthesis.

The hydrothermal approach presents numerous advantages for synthesizing nanomaterials, particularly in controlling particle size, morphology, and crystallinity. The key advantages include:

1. **Controlled Morphology and Crystallinity:** It offers precise control over nanomaterials size, morphology, and crystallinity by adjusting temperature, pressure, and reaction time, enhancing its versatility.
2. **Cost-effectiveness and Scalability:** This method is highly feasible for the inexpensive and large-scale production of nanomaterials, making it suitable for both laboratory and industrial applications.
3. **Compatibility with other Synthesis Techniques:** This method can be effortlessly combined with various other techniques, including electrochemical microwave synthesis and sonochemical, broadening the scope for synthesizing new nanomaterials.
4. **User-friendly Experimental Setup:** The experimental setup is simple and easy to operate. Once established, it can be reused multiple times for nanomaterial synthesis, enhancing its practicality and efficiency.

2.2 Film Preparation Techniques

In present thesis, two different approaches drop casting and electrospinning techniques are employed for preparation of films/fibers of polymer and polymer nanocomposites where each method offers unique advantages.

2.2.1 Drop Casting Method

The drop casting method is a straightforward and effective method widely utilized for preparing thin films with controlled thickness and composition. In this study, we employed this approach to fabricate flexible films from polymer and polymer nanocomposite materials. This method is especially beneficial for the area, where exact control over the properties of films is required. The drop-casting process begins with dissolving the solutes in a selected solvent at a fixed concentration. To achieve homogeneity, the solution is first thoroughly mixed with a magnetic stirrer and then subjected to ultrasonic agitation in an ultrasonic bath to ensure a uniform mixture. The concentration of the solute and the choice of solvent are pivotal in attaining the desired film characteristics. A preset volume of the solution is then taken using a micropipette and dropped onto the glass substrate, as illustrated in Figure 2.2. After this, solvent is

allowed to evaporate by placing the substrate in an oven maintained at a fixed temperature, leading to the formation of a film with the desired thickness.

This technique is valued for its simplicity, low cost, and capability to control film thickness and composition through adjustments in solution concentration and deposition volume. However, it is essential to note that some variation in film thickness may occur, and the final characteristics of the film might be affected by factors, such as, substrate surface properties and solvent evaporation rate. Therefore, optimizing these parameters is necessary for producing smooth, uniform films with consistent thickness.

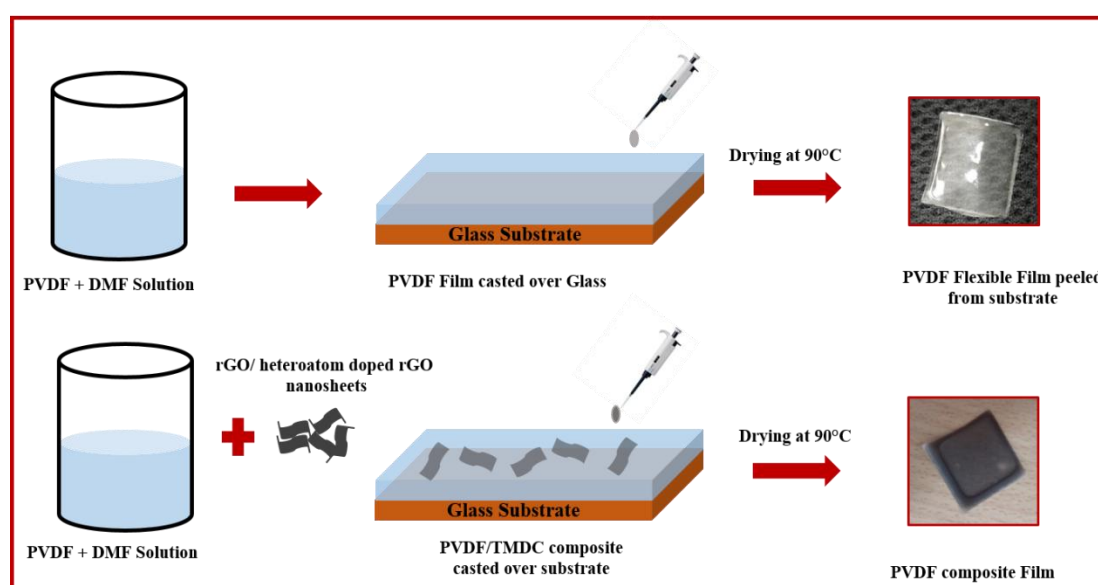


Figure 2.2 A schematic illustration of drop casting method to prepare polymer nanocomposite films.

2.2.2 Electrospinning Technique

Electrospinning is one of the most versatile technique used for synthesis of ultrafine nanofibers with the diameter ranging from 2 nm to several micrometers from wide range of materials including polymers, ceramics and composites. It enables precise control over nanofibers morphology, structure, and properties, resulting in key benefits such as, high surface-to-volume ratio, tunable porosity, and good mechanical properties. These advantages make electrospinning technique as a valuable technique across various fields including nanocatalysis, energy harvesters, tissue engineering, sensors, defense, security and environmental engineering[3, 4]. The electrospinning process involves application

of high DC voltage in the range of several tens of kVs to a polymer solution or melt which creates an electrostatic force that draw solution into thin continuous jet. As the jet moves towards the collector, it undergoes stretching and thinning due to electrostatic repulsion resulting in formation of continuous nanofibers. Figure 2.3 shows the typical setup for the electrospinning system which mainly consists of three part a spinneret containing the polymer solution, a high voltage power supply attached to the needle of the syringe, and a ground collecting plate. In this process, polymer solution is held by its surface tension at the end of the capillary, therefore when we apply high electric field across it, a charged jet of solution ejects form needle tip and move towards the collector, and due to rapid whipping of jet it results in evaporation of solvent during its trajectory, leaving behind the polymer fibers. In addition to this, several factors influence the electrospinning process, such as viscosity of solution, collector distance, applied voltage, flow rate, humidity therefore these parameters need to be optimized for achieving the nanofibers with the desired characteristics.

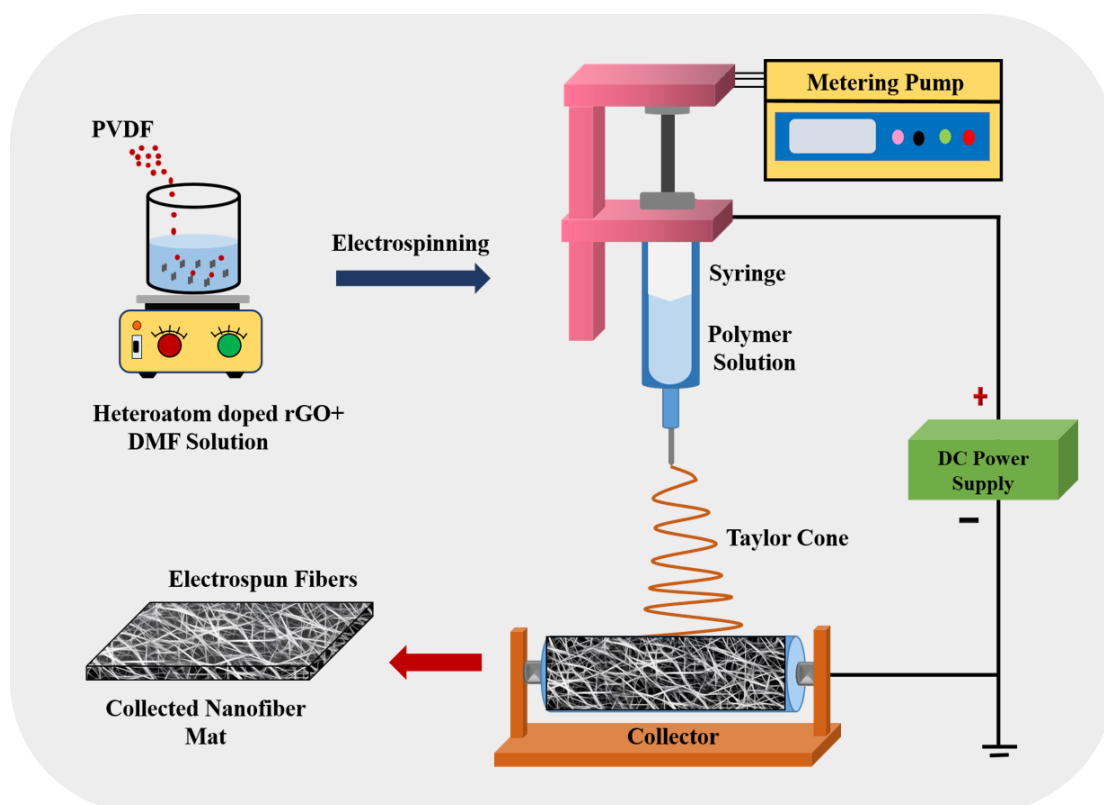


Figure 2.3 Illustration of electrospinning setup for synthesis of nanofibers.

2.3 Characterization Techniques

Several characterization techniques are utilized to confirm the successful synthesis of rGO and its heteroatom doped variants together with their polymer nanocomposite films. This section will provide a concise overview of the operating principles of each characterization techniques that have been used in the entire thesis work.

2.3.1 X-Ray Diffraction (XRD)

The x-ray diffraction technique is an analytical technique in the field of material characterization, providing valuable insights into the crystal structure of the materials. It helps in determining material's phase composition, crystallinity, and lattice parameters by analyzing interaction of X-rays with the atomic planes of a crystal[5]. The process of X-ray diffraction involves the irradiation of sample with high energy x-ray radiations with the wavelength ranging from 0.1 Å to 100 Å. However, for precise diffraction analysis, X-rays with wavelengths between 0.5 Å and 2.5 Å are commonly utilized, as these wavelengths correspond closely to the size of crystal lattices.

X-rays are generally produced in x-ray tube containing a cathode (usually made of tungsten filament) and copper anode. When tungsten filament is heated, it emits high energy electrons that are accelerated towards anode. Upon collision, these electrons displace electrons from the innermost shell of the copper anode. Thereafter, transition of electron from L and M shells to K shell take place to fill these vacancies, which results in emission of CuK_α and CuK_β x-rays with wavelengths of 1.54 Å and 1.39 Å, respectively and to obtain monochromatic radiation, CuK_β radiations are filter out using nickel filter, ensuring that analysis relies on desired CuK_α lines[6].

The typical experimental setup for X-ray diffractometer is shown in Figure 2.4 which consists of a x-ray tube that directs the x-ray onto the sample at a specified incident angle (θ). The intensity of the diffracted X-rays is then recorded by the detector placed at angle 2θ and the resulting data is analyzed to get the information about crystal structure.

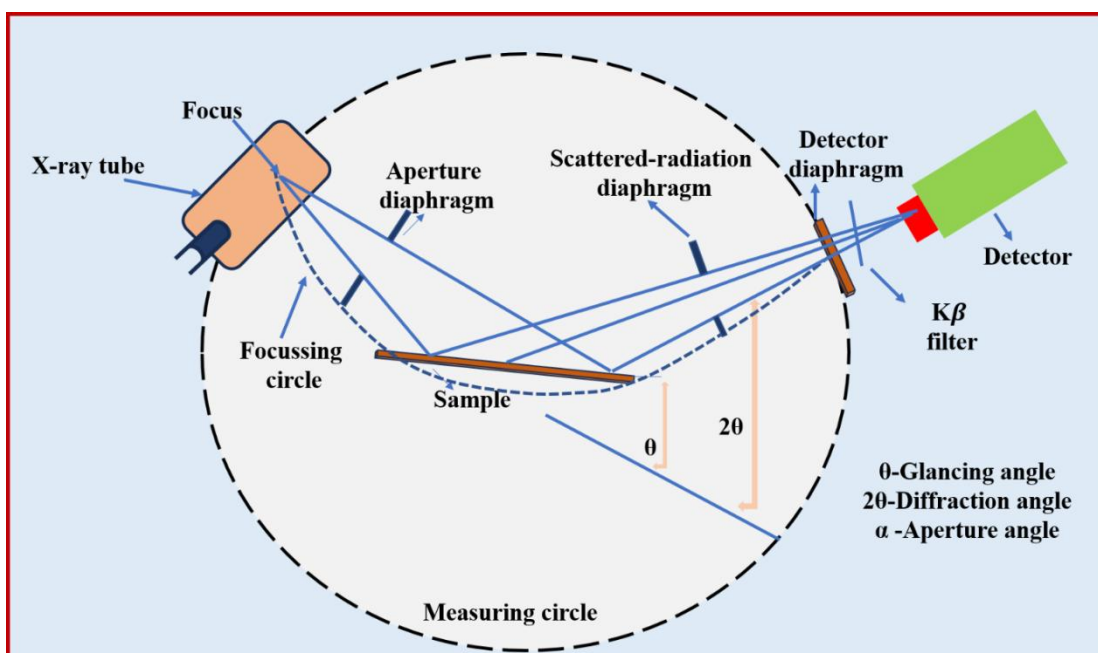


Figure 2.4 A Schematic showing the components of XRD diffractometer.

Bragg's law is used to interpret the interference pattern generated by the scattered X-rays, which proposed that crystal can be conceptualized as a series of parallel planes with defined spacing (d), where atoms are periodically arranged (Figure 2.5). Therefore, when X-rays reflect off ions in parallel planes, they produce sharp intensity peaks, and if reflected from successive planes, constructive interference will take place resulting in enhanced peak formation, as illustrated in Figure 2.5. For constructive interference, the path difference between the reflected X-rays must equal an even integer multiple of half the wavelength. This Bragg's condition can be mathematically expressed by the equation:

$$2d\sin\theta = n\lambda \quad (2.1)$$

Where d is interplanar spacing, θ is diffraction angle and , n represent order of diffraction, and λ is wavelength of x-rays. Thus, by analyzing the diffracted x-ray, one can deduce the crystal structure of the material as, diffraction pattern is unique for each material.

In this study, X-ray diffraction (XRD) patterns were obtained using a Rigaku, Ultima IV X-ray diffractometer using $\text{CuK}\alpha$ radiation with a wavelength of 1.5406 \AA . The measurements were performed at room temperature (RT) with scan speed of 2° per minute and a step size of 0.02° .

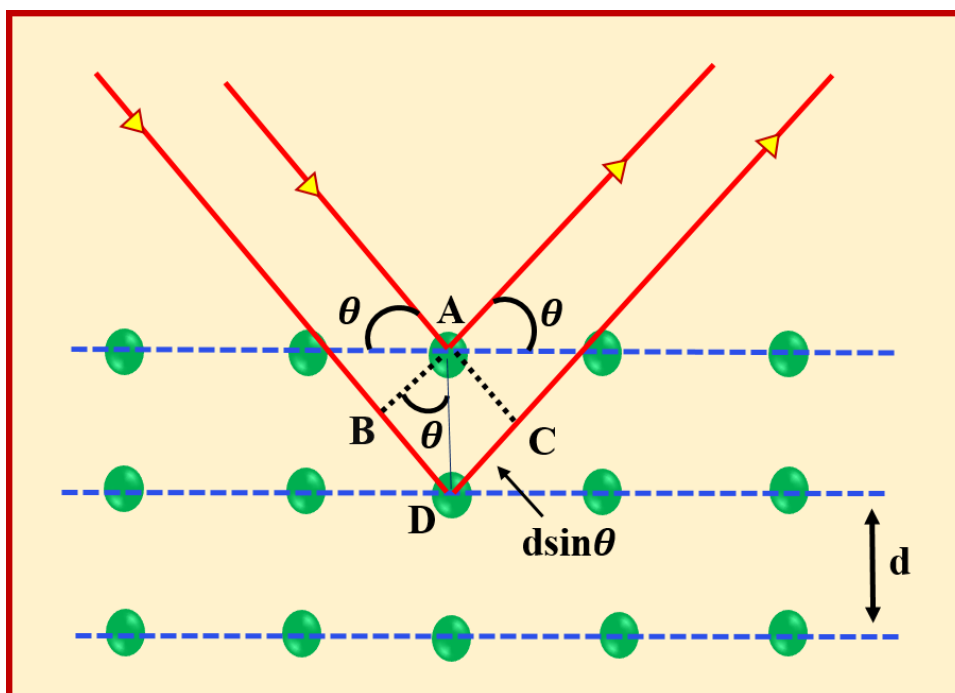


Figure 2.5 A Schematic showing the diffraction of X-rays obeying Brags law.

2.3.2 Fourier Transform Infrared Spectroscopy (FTIR)

Fourier transform infrared spectroscopy is an analytical technique that is utilized infrared radiation spanning a broad spectrum from 400 cm^{-1} to 4000 cm^{-1} to analyze the composition and molecular structure of the sample. It is a non-destructive technique and can be used to investigate materials of any nature including, organic and inorganic compounds, polymers, and composites[7]. The fundamentals of FTIR is based on the irradiation of sample through infrared radiation(IR), where different molecular bonds absorb specific wavelengths of the infrared light, causing vibrations in the molecular structure. Materials are made up of different chemical elements that are linked by strong covalent bonds, forming molecules. The type of bonds between these elements is determined by the electronic arrangement of the atoms involved. These bonds are in constant motion, including vibrations, stretching, and rotation, within the structure of the material, with their energy primarily found in the ground state. Therefore, when IR lights pass through sample, the interaction between infrared light and the molecules in a sample will take place, resulting in absorption of light by molecules at a particular frequency corresponding to their vibrational modes[8, 9]. This results in generation of a series of spectral lines, known as infrared spectrum, which is unique for every material

which provide crucial information about the chemical composition of the material or substance and thereby act as molecular fingerprint of the material.

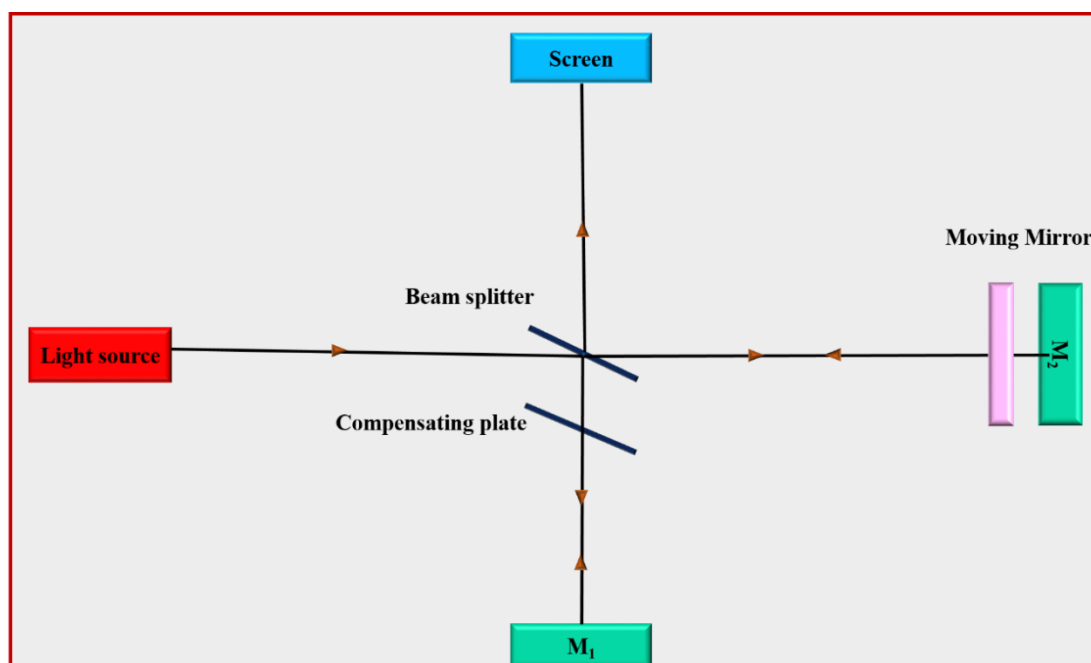


Figure 2.6 Michelson interferometer schematic.

In this method, an interferometer is utilized, which initially splits the light from the source lamp into two separate beams (Figure 2.6). These beams pass through an optical system and are recombined at the beam splitter, creating an optically interfered beam that contains all MIR wavelengths in a single signal, referred to as an interferogram. This interferogram is then directed through the sample, where specific wavelengths are absorbed according to the material's properties. The absorption of radiation causes the molecules in the sample to transition to an excited state, followed by a return to the ground state, during which radiation characteristic of the energy difference is emitted. The output interferogram is recorded by detector, which transforms the beam into an electrical signal. The recorded signals, needs to be decoded to plot the intensity corresponding to each IR, which is achieved by Fourier transform mathematics. Hence the name Fourier transform infrared spectroscopy originates. The resulting graph displays the wavenumber on the x-axis against the "transmittance" or "absorption" of the infrared radiation on the y-axis (Figure 2.7). The graph may reveal many peaks based on the molecule's properties. These peaks are carefully examined and compared to known standard IR peaks associated with various materials and bonds.

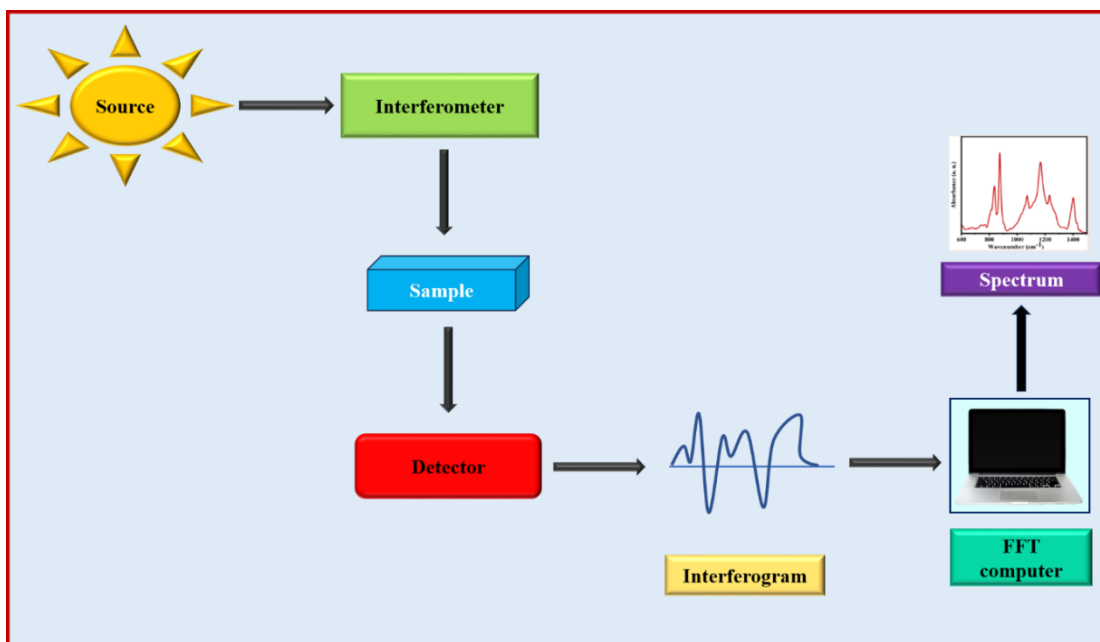


Figure 2.7 Instrumental setup for FTIR spectroscopy.

In this study, the Perkin Elmer Spectrum 2 FTIR spectrometer, equipped with an attenuated total reflectance (ATR) accessory, is utilized to analyze the various phases present in PVDF and PVDF nanocomposite films. Additionally, it is employed to quantify the β -phase content in these materials.

2.3.3 Raman Spectroscopy

Raman spectroscopy is an effective technique to examine a material's vibrational, rotational and other low-frequency modes. This spectroscopy technique is based on the Raman effect and bears its name from C.V. Raman, an Indian scientist who discovered the Raman phenomenon in 1928. This method is frequently employed to characterize a variety of materials, such as gases, liquids, and solids and provide comprehensive details regarding molecules bonding, composition, and structure, thereby providing a distinctive molecular fingerprint, which aids in the identification of different compounds[10]. Raman spectroscopy operates on the principle of inelastic scattering of light, also known as Raman scattering. In this method, when a ray of monochromatic light illuminates the sample, most of the light is elastically scattered and a very small fraction of light approximately 1 in 10^{-6} undergoes inelastic scattering. The elastically scattered light results in generation of Rayleigh lines also

known as Raman lines and have the same frequency as that of incident light. Whereas, inelastic scattered light results in manifesting of Stokes and anti-Stokes lines with a shift in energy. In Stokes scattering, the scattered light possesses a lower frequency compared to the incident light, whereas in anti-Stokes scattering, the scattered light has higher energy relative to the incident light. This shift in energy towards higher and lower energy sides is known as Raman shift gives information about the molecules vibrational modes present in sample[11, 12].

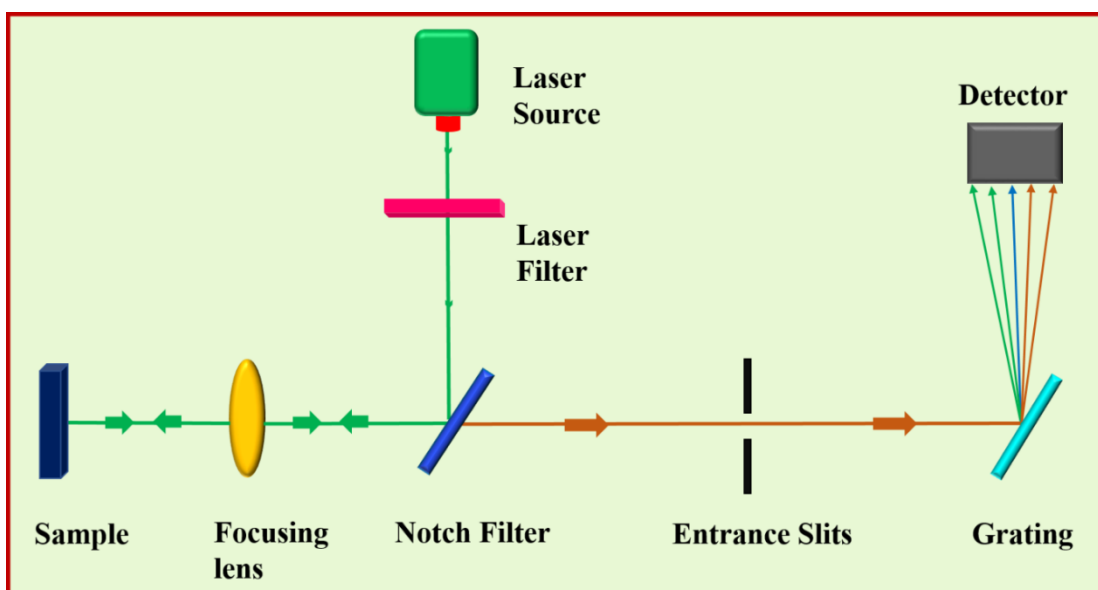


Figure 2.8 Schematic of a Raman spectrometer setup.

The experimental setup of the Raman spectrometer is shown in Figure 2.8 which consist of a laser source, sample illumination system and a spectrometer. Lasers as a source of light is favored in Raman spectrometer owing to their monochromaticity, high-intensity nature, resulting in favorable signal-to-noise (S/N) ratios. Moreover, this technique often outperforms IR spectroscopy in its ability to analyze inorganic systems in aqueous solutions. This advantage arises because Raman spectroscopy is based on molecular polarizability, rather than relying on changes in the electric dipole moment during molecular vibrations, as is the case with IR spectroscopy. This technique is extremely useful in fields of nanotechnology, especially for biotechnology, where only small amount of sample is sufficient for its analysis. In addition to this, Raman spectroscopy is an important tool for providing insights into the presence of structural defects in carbon based nanomaterials. Here, we use WITec alpha 300 RA Raman

spectrometer to detect and measure the defects and various vibrational bonds present in reduced graphene oxide and its heteroatom doped variants.

2.3.4 Field Emission Scanning Electron Microscopy (FESEM)

FESEM is an advanced microscopy technique that utilizes a field emission source to obtain the high-resolution images of the sample surface by scanning the surface of sample in zigzag pattern. It is similar to scanning electron microscopy (SEM) technique except that it uses field emission gun as its electron source, which enables a narrower electron beam and much improved resolution compared to conventional SEM technique [13]. FESEM also gathers secondary electrons using a scintillator detector, which then transforms them into photons. However, as FESEM operates at higher vacuum levels, the sample must be coated with a very thin layer of gold (Au) or palladium (Pd) to improve conductivity and imaging quality. Figure 2.9 shows the typical setup of the FESEM, consisting of field emission gun that emits a narrow beam of electrons which is collimated through electromagnetic lenses to form a thin monochromatic beam. This highly focused electron beam when interact with the sample, several complex process will take place which results in generation of various types of electrons such as secondary electrons, backscattered electrons, auger electrons etc., each with distinct characteristics and significance. Secondary and backscattered electrons are essential for imaging samples. Secondary electrons are emitted when primary electrons collide with the specimen, transferring enough energy to eject lower-energy electrons from the outer atomic shells. Their low energy and high sensitivity to surface features make them vital for topographic imaging, resulting in high-resolution images with fine surface detail. Backscattered electrons, on the other hand, are primary electrons that are elastically scattered off the atomic nuclei and return to the detector and are mainly responsible for image contrast based on the composition. FESEM is notably more effective than conventional SEM, providing images with spatial resolutions as fine as 0.5 nanometers and significantly reduced electrostatic distortions making it particularly useful for examining nanoscale structures, materials, and biological specimens[14]. Zeiss Gemini SEM 500 field emission scanning electron microscope is used to examine the surface morphology of nanomaterials and nanocomposite films.

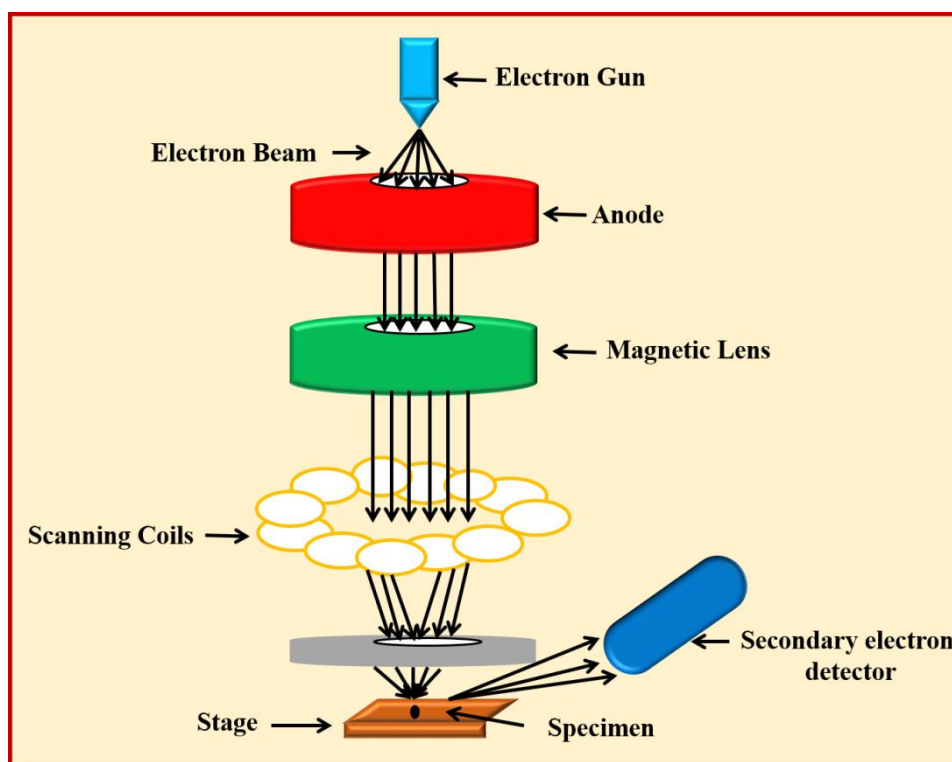


Figure 2.9 Schematic illustrating the components of FESEM

2.3.5 Energy-dispersive X-ray Spectroscopy (EDS or EDX) for Elemental Analysis

It is an analytical technique used to determine the different elements present in the sample. In this technique, when high energy electrons remove the electron from innermost shell of atom, then transition of electrons from higher state to lower state take place which results in emission of characteristic x-ray[15]. The energy of these characteristic x-rays depends on the energy level difference of electrons in atom, which in turn depends on atomic number. Therefore, by measuring the energy of these emitted x-ray by energy-dispersive detector in EDS system, elemental composition can be easily identified as each element in the sample emits X-rays at specific energy levels, which correspond to its unique atomic structure. This technology enables a quick and accurate determination of the elemental composition, making it particularly valuable for examining the chemical makeup of solid materials, thin films, and nanostructures. In this work, we have used EDS technique to evaluate the presence of boron, nitrogen elements in rGO matrix which is attached with Zeiss Gemini SEM 500 for EDS studies.

2.3.6 X-ray Photoelectron Spectroscopy (XPS)

It is an analytical technique utilized to characterize a material's surface, providing comprehensive details about the elemental composition, chemical states, and electronic surroundings of atoms on a material's surface[16]. The technique is based on the photoelectric effect, where the material is irradiated with monochromatic soft X-rays (commonly MgK_α (1253.6 eV) or AlK_α (1486.6 eV)). The kinetic energy of the emitted electrons is then measured, and the resulting data displayed in terms of number of electrons detected as a function of their energy (ranging from 0 to the source energy). Moreover, when X-rays with a known energy $h\nu$ irradiates the specimen, and electrons with a binding energy of E_B are released and the kinetic energy (E_k) of these electrons is measured by the spectrometer and given by the following equation

$$E_k = h\nu - E_B - \phi_S - \phi_{SP} \quad (2.2)$$

Here ϕ_S and ϕ_{SP} are the work function of specimen and spectrometer. This measured kinetic energy of electrons is then used to deduce the binding energies of electron. As the binding energy is characteristic of specific elements and their chemical states, XPS provides both qualitative and quantitative information about the elements present on the surface[17].

A schematic representation of the key components in an XPS setup is illustrated in Figure 2.10 which comprises of an X-ray source, sample holder, an electron energy analyzer, and detector, all operated under ultra-high vacuum (UHV) conditions. The setup also includes electronics to convert the detected current into a readable spectrum. In this study, Nexsa Surface Analysis XPS spectrometer of thermoscientific with hemispherical analyzer chamber is utilized to check the presence of different heteroatom in rGO matrix and analyze their chemical structure. The sample's position can be adjusted along multiple axes, and rotationally (θ) using a manipulator. Emitted photoelectrons are collected by a four-element lens and analyzed with a hemispherical analyser. Data acquisition is performed via a channeltron and subsequently processed using a computer.

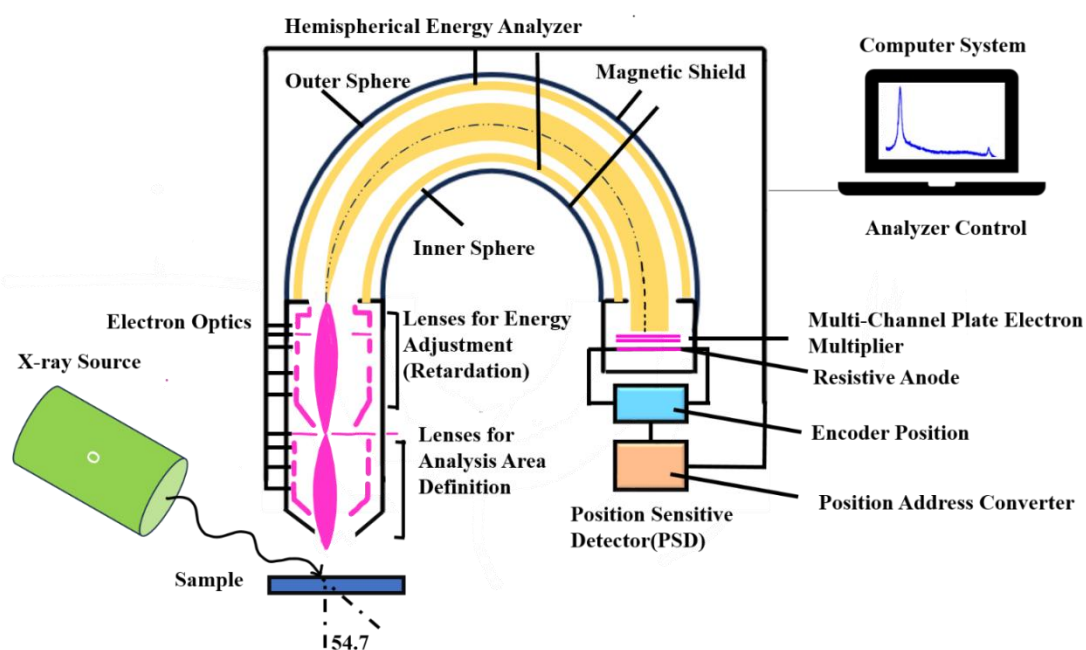


Figure 2.10 A schematic illustration of the XPS system, highlighting the various components involved in its operation.

2.3.7 Polarization vs Electric Field Measurements (P-E Loops)

The polarization-electric field (P-E) measurements are used to analyze the distinctive behavior of ferroelectric materials, which possess spontaneous electric polarization. In this method, an electric field is applied across the sample, and polarization induced across its surface is measured, which provides important insights into the material's ferroelectric characteristics, such as domain switching behavior and polarization saturation. Ferroelectric materials possess intrinsic electric polarization, which can be modified and reoriented through external electric field application. Initially, dipoles in ferroelectric materials are randomly oriented, resulting in net zero polarization. However, once the electric field is applied, the dipoles start to align in the same direction, resulting in net polarization. Up until saturation, this polarization grows; beyond that, additional increases in the electric field have no effect on the polarization. When the electric field is reduced to zero, the dipoles remain in their reoriented state, leading to residual polarization. The dipoles eventually shift to the opposite orientation as the field is reversed in the negative direction. When the field reverts to zero following this reversal, the negative remnant polarization occurs. This entire process

generates a characteristic hysteresis loop, reflecting the material's ferroelectric behavior. Important details concerning ferroelectric properties like remnant polarization, coercive field, and domain stability can be learned from the P-E loop size and shape. The charge generated across the sample is measured by the Sawyer-Tower circuit. A reference capacitor with much lower capacitance than the ferroelectric sample is placed in series. In this setup, a reference capacitor with much lower capacitance than the ferroelectric sample is placed in series for less voltage drop across it. This design distributes the majority of the applied voltage over the ferroelectric sample, whereas the voltage measured across the reference capacitor reflects the sample's polarization. In present work, ferroelectric properties of PVDF and PVDF nanocomposite films/fibers are examined using Marine India P-E loop tracer by sandwiching these films between two metal electrodes.

2.3.8 Dielectric/Impedance Analyzer

Dielectric measurements evaluate a material's dielectric characteristics, or how it reacts to an electric field. It evaluates a material's ability to absorb and release electrical energy, which is important in applications requiring insulators, capacitors, and other electronic devices. When assessing a material's appropriateness for electronic and energy applications, its permittivity (dielectric constant), dielectric loss, and electrical conductivity are all determined by these measures. The method can be used to evaluate variations in parameters such as the loss factor ($\tan\delta$) and real and imaginary permittivity (ϵ' and ϵ'') with respect to changes in temperature or frequency. In the dielectric measurements, a thin film of polymer and polymer nanocomposite is sandwiched between two brass plates acts as electrode and its capacitance is measured. The formula for the capacitance of the parallel plate capacitor with dielectric material inserted between them is given by the following equation

$$C = \frac{\epsilon' \epsilon_0 A}{d} \quad (2.3)$$

where, C is capacitance of sample measured, ϵ' is dielectric constant of material, ϵ_0 is permittivity of free space, A is area of electrode, and d is thickness of film. In addition,

the loss tangent ($\tan\delta$) and imaginary component of dielectric (ϵ'') of the samples are given as

$$\epsilon'' = \epsilon' \tan\delta \quad (2.4)$$

Here, $\tan\delta$ represents the "dielectric loss tangent," which denotes the energy lost from the applied field into the sample.

The setup for the dielectric measurements encompass the feature of varying frequency and temperature, therefore by altering these parameters, various parameters such as inductance (L), capacitance (C), and resistance (R) can be measured. In the present work, we have used Agilent E4980A precision LCR meter to perform the dielectric measurements in 20 Hz- 104 Hz frequency range.

2.3.9 Atomic Force Microscopy (AFM)

AFM is a scanning probe microscopy technique which is designed to study the surface topography of the samples. This technique is first developed by the prominent scientists Gerd Binnig, Calvin Quate, and Christoph Gerbe in 1986 and thereafter it becomes one of the powerful tool used in several field to provide high-resolution topographical images of sample surface, including conducting as well as non-conducting samples [18]. The fundamental principle of AFM is based on the interactive force between probe/tip of the cantilever and sample surface. In this method, when the AFM tip mounted on flexible cantilever scans across the sample surface, it deflects the cantilever due to force between tip and sample. These deflections are monitored by the laser beam reflected off the cantilever and fed onto photodetector to construct detailed image of surface topography. The schematic representation of AFM working mechanism is illustrated in figure. Furthermore, the separation between the probe's tip and the sample is depend on the type and magnitude of force experienced between them (Figure 2.11). If the relative distance between probe and sample is less than 0.1 nm, quantum mechanical exchange-correlation force predominates because of overlapping of probe wave function with sample wave function. Whereas, van der Waals force predominates when the value of relative distance between probe and sample is greater than or equal to

1 nm, and this force is attractive in nature (Figure 2.12). Therefore, by analyzing the different types of force and their magnitude, one gets information about the surface features/properties of the sample[19].

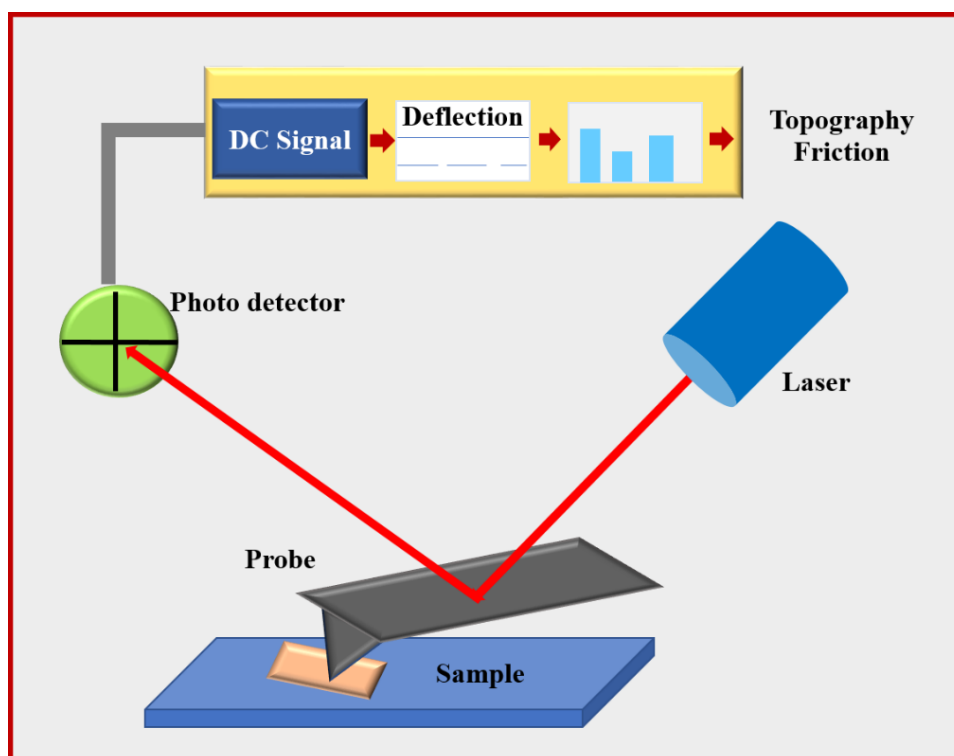


Figure 2.11 Schematic showing the components of a AFM.

The AFM can mainly operate in three different modes: contact mode, non-contact mode and tapping mode to analysis the surface topography of the samples. In contact mode, the probe is in constant contact with the sample as it scans over the sample surface to provide high-resolution image. However, this method exerts lateral force on the sample therefore not suitable for analysis of surface for soft or delicate materials. In non-contact mode, the probe is not in direct physical contact by sample surface, but interact with attractive van der Waal forces. This method is suitable for soft and sensitive samples. Whereas, in tapping mode the probe is in periodic contact mode with the sample surface as the cantilever is set to oscillate near its resonant frequency, which reduces damage on sample surface and increase the deflection amplitude. Thus, improve the feedback loop control for providing high-resolution images of surface topography without continuous direct contact.

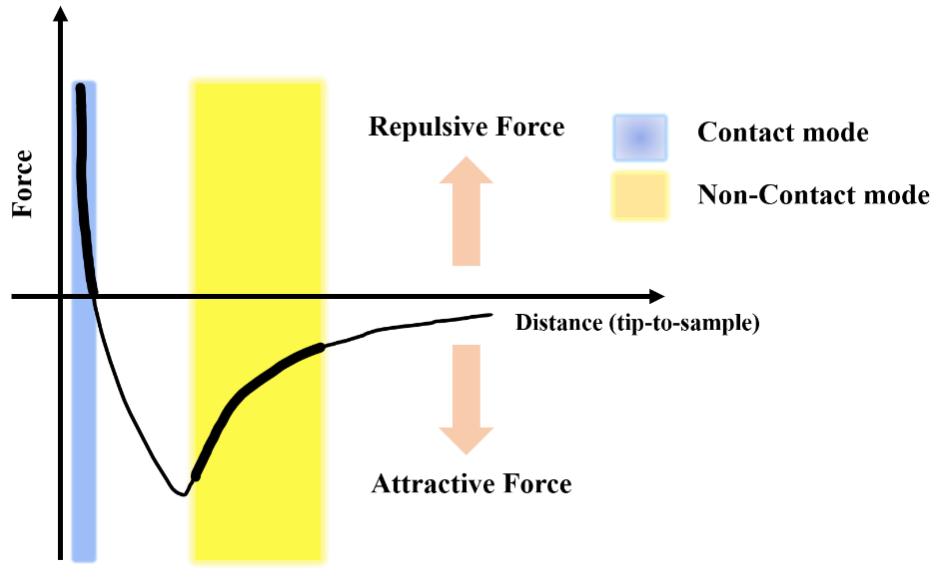


Figure 2.12 Variation in force of interaction between tip and sample as a function of distance.

2.3.9.1 Kelvin Probe Force Microscopy (KPFM)

KPFM is an advanced non-contact variant of AFM technique utilized to determine surface potential and work function variations between tip and sample at nanoscale precision. It is an effective technique for studying the behavior of materials in a range of domains, including semiconductors, photovoltaics, nanotechnology, and corrosion research, because it can offer high-resolution electrical property mapping in addition to surface topography[20]. KPFM operation mainly relies on measuring the change in electrostatic force between AFM tip and sample surface which arises due to difference in their work function. The work function of the sample can be estimated by the following equation[21]

$$\phi_{tip} = \phi_s + eV_{CPD} \quad (2.5)$$

Where, ϕ_{tip} and ϕ_s is the work function of tip and the sample V_{CPD} is the contact potential difference between them. Therefore, when we bring tip and sample close to each other, it results in generation of contact potential difference between them. This contact potential difference (CPD) can be compensated by applying the external voltage known as bias voltage between tip and sample, which will nullify the electrostatic force between them. When the bias voltage is equal to the contact potential difference

between tip and sample, no force will be experienced by tip. Thus, by measuring this CPD value of a sample, we can estimate the amount of charge generated on the sample and work function of the material.

In the current study, we utilized the Bruker Dimension Icon XR system to measure the work functions of polymer and polymer nanocomposite films and fibers. This advanced system is also employed to analyze the surface potential of these materials, providing detailed insights into their electrical properties at the nanoscale. Through the precise measurements offered by the Bruker Dimension Icon XR, we gained a comprehensive understanding of the variations in surface potential and work function, which are crucial for optimizing the performance of triboelectric nanogenerator for energy harvesting applications.

2.3.10 Ultraviolet-Visible Spectroscopy (UV-Vis)

UV-Vis spectroscopy is an analytical technique that employs electromagnetic radiation in the ultraviolet and visible spectrum to investigate electronic transitions among atoms, ions, and molecules. It works on the principle of interaction of light with matter. When ultraviolet or visible light passes through a sample, certain wavelengths are absorbed by the molecules present, triggering electronic transitions that cause electrons to move from one energy level to another. Each molecule uniquely absorbs specific wavelengths of light, resulting in a characteristic absorption profile. By analyzing these wavelengths, researchers can determine the energies associated with these transitions, gaining valuable insights into the molecular structure and properties of the sample[22]. This technique provides crucial insights into the absorption characteristics of different substances and finds applications across numerous fields, including biotechnology, biochemistry, and materials science. Consequently, it serves as an essential tool for characterizing the optical properties of a wide range of materials, such as polymers and nanoparticles. Figure 2.13 demonstrates the working mechanism of UV-Vis spectrometer.

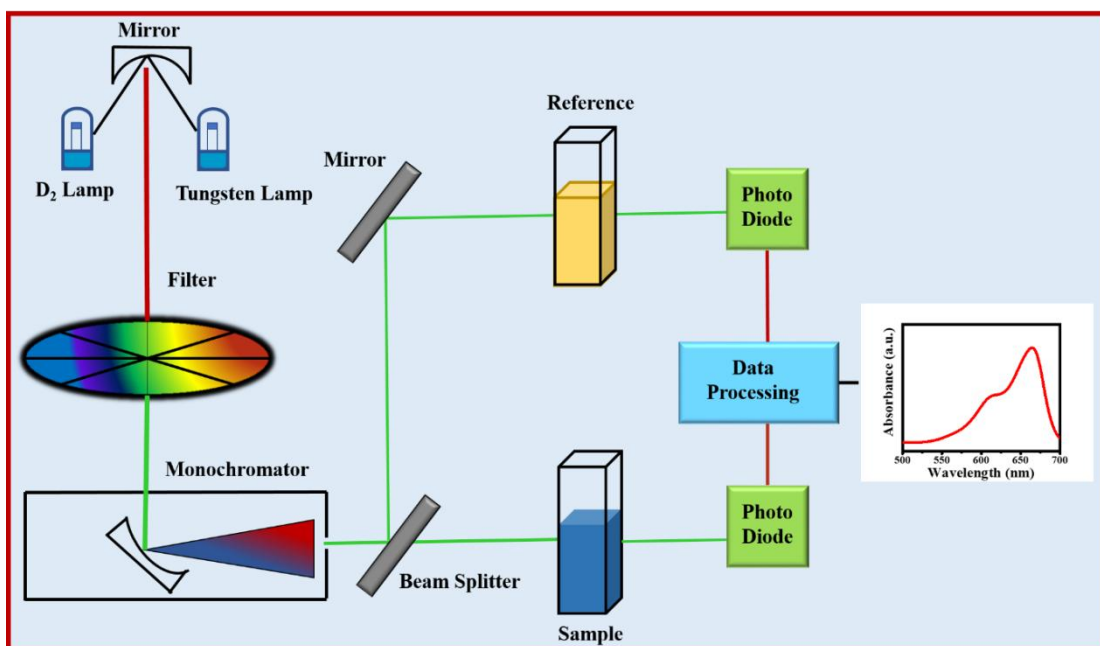


Figure 2.13 Schematic representation of working mechanism of UV-Vis spectrometer.

In the present work, we have used UV-Vis spectroscopy technique to record the absorbance through methylene blue dye solution. The Beer's Lambert law is used to measure the absorbance, which correlates concentration of solution and path length of light through solution to the absorbance of light. The absorbance (A) can be given by the following equation;

$$A = \log \frac{I}{I_0} = \epsilon c L \quad (2.6)$$

Here, I is the intensity of incident light, I_0 is intensity of light after passing through sample, ϵ is molar absorption coefficient, c is molar concentration, and L is optical path length. In present study, Perkin Elmer lambda UV-Vis spectrometer is employed for absorbance measurements.

2.4 Electrical Measurements of Nanogenerators

The electrical characterization of the piezoelectric nanogenerator, triboelectric nanogenerator and hybrid device is carried out by adhering the aluminum electrode onto the polymer and polymer nanocomposite film. Copper wires are drawn from these electrodes to establish the necessary electrical connections. The output performance of

the nanogenerators is evaluated by tapping them with the help of a dynamic shaker (Micron MEV-0025), which provides mechanical vibrations at variable forces and frequencies. Voltage measurements are taken using a mixed-domain oscilloscope (Tektronix MDO34) with a TPP series probe (TPP0500B), while current measurements are recorded with a digital multimeter (Keithley DMM7510). Additionally, a Keysight electrometer (B2985B) is employed to monitor the current and charge generated by the nanogenerators. A full-wave bridge rectifier IC (DB107) is used to measure the rectified output performance of the nanogenerators in terms of voltage and current.

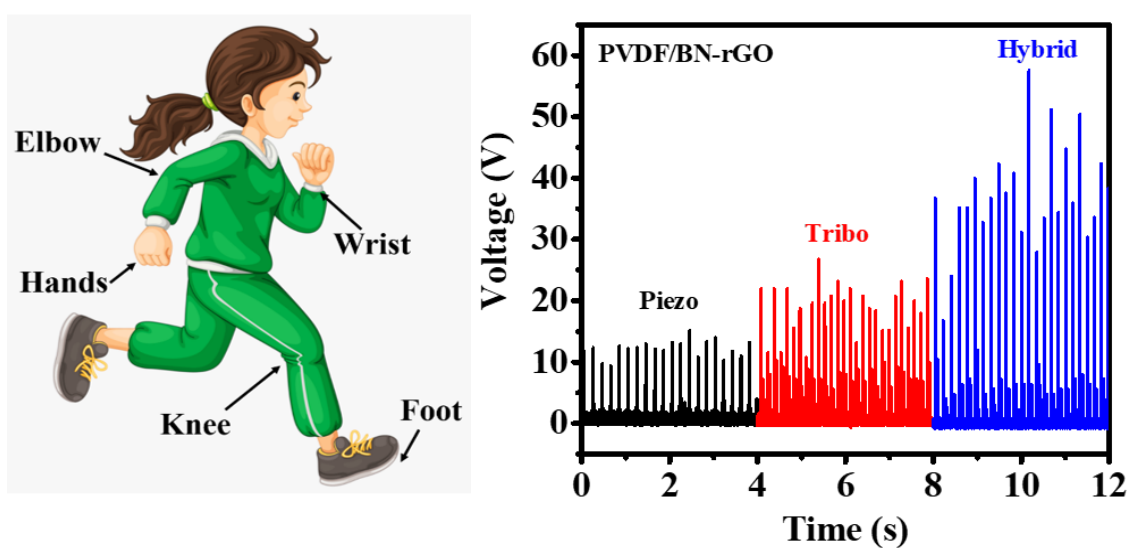
References

- [1] D.C. Marcano, D.V. Kosynkin, J.M. Berlin, A. Sinitskii, Z. Sun, A. Slesarev, L.B. Alemany, W. Lu, J.M. Tour, Improved synthesis of graphene oxide, *ACS Nano*, 4 (2010) 4806-4814.
- [2] J. Li, Q. Wu, J. Wu, Synthesis of nanoparticles via solvothermal and hydrothermal methods. 12, in, Springer international publishing Switzerland, 2016.
- [3] N. Bhardwaj, S.C. Kundu, Electrospinning: A fascinating fiber fabrication technique, *Biotechnology Advances*, 28 (2010) 325-347.
- [4] Y. Li, J. Zhu, H. Cheng, G. Li, H. Cho, M. Jiang, Q. Gao, X. Zhang, Developments of advanced electrospinning techniques: A critical review, *Advanced Materials Technologies*, 6 (2021) 2100410.
- [5] A.W. Hull, A new method of X-ray crystal analysis, *Physical Review*, 10 (1917) 661.
- [6] C. Kittel, P. McEuen, Introduction to solid state physics, John Wiley & Sons, 2018.
- [7] W.M. Doyle, Principles and applications of Fourier transform infrared (FTIR) process analysis, *Process Control Qual*, 2 (1992) 11-41.
- [8] G.C. Schatz, R.P. Van Duyne, J. Chalmers, P. Griffiths, Handbook of vibrational spectroscopy, New York: Wiley, 1 (2002) 759.
- [9] D. Titus, E.J.J. Samuel, S.M. Roopan, Nanoparticle characterization techniques, in: Green synthesis, characterization and applications of nanoparticles, Elsevier, 2019, pp. 303-319.
- [10] M.J. Pelletier, Quantitative analysis using Raman spectrometry, *Applied spectroscopy*, 57 (2003) 20A-42A.
- [11] I.R. Lewis, H. Edwards, Handbook of Raman spectroscopy: from the research laboratory to the process line, CRC press, 2001.
- [12] J.R. Ferraro, Introductory raman spectroscopy, Elsevier, 2003.

- [13] M.A. Sutton, N. Li, D. Joy, A.P. Reynolds, X. Li, Scanning electron microscopy for quantitative small and large deformation measurements part I: SEM imaging at magnifications from 200 to 10,000, *Experimental mechanics*, 47 (2007) 775-787.
- [14] A. Ul-Hamid, *A beginners' guide to scanning electron microscopy*, Springer, 2018.
- [15] Y. Leng, *Materials characterization: introduction to microscopic and spectroscopic methods*, John Wiley & Sons, 2013.
- [16] J. Chastain, R.C. King Jr, *Handbook of X-ray photoelectron spectroscopy*, Perkin-Elmer Corporation, 40 (1992) 221.
- [17] B.V. Crist, *Handbook of monochromatic XPS spectra: The elements of native oxides*, John Wiley & Sons, 2000.
- [18] D. Rugar, P. Hansma, Atomic force microscopy, *Physics today*, 43 (1990) 23-30.
- [19] F.J. Giessibl, Advances in atomic force microscopy, *Reviews of modern physics*, 75 (2003) 949.
- [20] W. Melitz, J. Shen, A.C. Kummel, S. Lee, Kelvin probe force microscopy and its application, *Surface science reports*, 66 (2011) 1-27.
- [21] T. Glatzel, M.C. Lux-Steiner, E. Strassburg, A. Boag, Y. Rosenwaks, Principles of Kelvin probe force microscopy, *Scanning Probe Microscopy: Electrical and Electromechanical Phenomena at the Nanoscale*, (2007) 113-131.
- [22] L.D.S. Yadav, L.D.S. Yadav, *Ultraviolet (UV) and visible spectroscopy*, *Organic spectroscopy*, (2005) 7-51.

CHAPTER 3

Effect of pristine and heteroatom doped rGO on the output performance of the PVDF nanocomposite based piezoelectric nanogenerator for biomechanical energy harvesting applications



This chapter presents the development of piezoelectric nanogenerators for biomechanical energy harvesting, enhanced by the incorporation of pristine and heteroatom-doped reduced graphene oxide (rGO) into polyvinylidene fluoride (PVDF) nanocomposites. The study examines the influence of rGO, boron-doped rGO, nitrogen-doped rGO, and boron-nitrogen co-doped rGO on the output performance of piezoelectric nanogenerator (PENG). Among the fabricated devices, PVDF/BN-rGO film based PENG demonstrated superior performance. This high-performing film is then coupled with polydimethylsiloxane (PDMS) film to fabricate a hybrid nanogenerator capable of harvesting mechanical energy through both piezoelectric and triboelectric effect. A maximum voltage and current of 57.6 V and 28.8 μ A is generated by this hybrid device. The improved performance of the nanogenerator is ascribed to the synergistic effect of piezoelectric and triboelectric effects together with the addition of co-doped rGO in PVDF matrix, which increases the remnant polarization and dielectric property of the PVDF nanocomposite film. The present work has shown the importance of rGO and its derivative for energy harvesting applications.

3.1 Introduction

An upsurge in the growing energy demands, with the development of the Internet of things (IoT), portable electronics, and wearable/wireless technologies has sparked great interest in the field of energy harvesting technologies. Among the various energy harvesting technologies, the scavenging of electrical energy from the wasted mechanical energy via piezoelectric and triboelectric effects has stirred up a huge interest not only in overcoming energy crisis issues to power the microelectronic system, but also in realizing their application in designing a flexible, wearable, self-powered system [1-4]. In this direction, a piezoelectric nanogenerator (PENG) devices have profound great importance in energy harvesting due to their thin, highly flexible, and mechanical stretchable nature (in some cases), which allows them to be mounted on any type of surface. However, there has been only a minor improvement in the output performance of nanogenerators from a few nW to a few μ W since the invention of the first PENG, which hinders their application in high-powered devices[5, 6]. Further, a triboelectric nanogenerator (TENG) based on triboelectrification and electrostatic induction has demonstrated to generate more output power with high energy conversion efficiency (85%), and its diverse material choice, simple structure, cost-effectiveness, and ease of fabrication make it more promising to scavenge energy under different small mechanical and biomechanical actions with variable amplitude and frequency [7-9]. However, standard practices used for enhancing the performance of TENG, such as, physical and chemical surface modification [10], charge-injection [11], printing of specific structure [4], and electric polarization [12] are complex and difficult to implement on large scale. Therefore, integrating both piezoelectric and triboelectric effects to harvest energy from a single source (mechanical energy), presents a promising strategy for developing self-powered and sustainable power systems with improved energy conversion efficiency[13]. This approach is advantageous because the fabrication of piezo-triboelectric hybrid nanogenerators does not require significant alterations to the device structure. The only key requirement is that one of the two selected triboelectric materials must also possess piezoelectric properties. In this regard, polyvinylidene fluoride (PVDF), a well explored piezoelectric polymer, known for its excellent flexibility, biocompatibility and mechanical strength, making it an ideal candidate for use as both a piezoelectric and triboelectric material[13-15]. PVDF exists in five

distinct phases i.e. α , β , γ , δ and ϵ , among which β (TTTT) and γ (T₃GT₃G') phase are of utmost importance due to the spontaneous polarization and high piezoelectric sensitivity. The piezoresponse of the PVDF can be enhance further by addition of suitable materials in it, for example ZnO[16, 17], PZT [18], BaTiO₃ [19], ZnSnO₃ [20], NaNbO₃ [21], KNbO₃ [22], and so on. Additionally, carbon-based materials like carbon nanotube (CNT), graphene and its derivative, carbon black have been shown to significantly improve the performance of piezoelectric nanogenerators (PENGs). These materials aid in nucleation, dipole alignment, stress reinforcement, and the formation of micro-capacitors.

Zhang et.al. reported a flexible PENG by adding graphene oxide (GO) and reduced graphene oxide (rGO) in PVDF polymer matrix [23]. The results show that, rGO incorporated in polymer matrix has higher content of β phase and can generate high voltage and current as compared to GO. A maximum voltage and current of 16 V and 700 nA is generated by PVDF-rGO based PENG. The fact that rGO has fewer functional groups than GO accounts for its higher output. Tiwari et.al. reported that addition of sulfonated graphene oxide in polymer nanofiber decreases the diameter of fiber and enhances the electroactive phase upto 88% confirmed by spectroscopic and thermal studies[24]. Karan et.al. demonstrate a self-poled Fe-RGO/PVDF based PENG with 5.1 V output voltage, which is 12 times greater than the voltage produced by the pristine PVDF film [25]. This enhancement in performance of PENG is attributed due to nucleation of γ phase rather than electroactive β phase in PVDF which can stabilize polar γ phase upto ~99%. Marina et.al. recently reported manifestation of piezoelectric properties in the vertically aligned CNTs after introducing nitrogen atom, where the main source of existence of anomalous piezoelectric properties in nitrogen doped CNTs is formation of bamboo-like bridges and pyrrole-like defects in the cavity of the nanotube which results in an uncompensated dipole moment due to curvature of graphene sheet surface [26]. Furthermore, recent doping of rGO with nitrogen has shown to enhance the output performance of piezoelectric energy harvesting device by improving rGO conductivity [27]. Because when we dope the nitrogen and other heteroatoms in the rGO matrix, they react to vacancies and defects in the material, improving its electrical and structural properties [28, 29]. Moreover, compared to single heteroatom doped rGO, co-doping of two or more types of heteroatoms has shown

better electrochemical properties and electrical conductivity. As the addition of two different types of dopants boron and nitrogen with alike size but with opposite doping effect (p-type and n-type) in carbon network of GO can induce strong charge polarization between boron and nitrogen atom and also helps in providing more active sites for electrocatalytic activity and enhanced charge transfer abilities in comparison to single heteroatom doped rGO due to synergistic effect of co-doping[28, 31].

In this chapter, we first design a flexible PVDF-based piezoelectric nanogenerator by incorporating rGO, boron-doped rGO (B-rGO), nitrogen-doped rGO (N-rGO), and boron-nitrogen co-doped rGO (BN-rGO) nanosheets, and demonstrated its potential for biomechanical energy harvesting through various human motions. To further enhance the nanogenerator output performance, we fabricate a hybrid piezoelectric and triboelectric nanogenerator by combining the PVDF/BN-rGO film, which exhibits superior piezoelectric properties, with a PDMS film as the two triboelectric layers. This hybrid design shows that the introduction of BN-rGO into the PVDF matrix not only improves its piezoelectric response but also enhances the triboelectric effect, resulting in a more efficient configuration for harnessing mechanical energy.

3.2 Experimental Details

3.2.1 Materials

PVDF powder used in this work was procured from Alfa Aesar. Urea, boric acid, potassium permanganate, sulphuric acid, graphite powder, orthophosphoric acid, hydrochloric acid, hydrogen peroxide, N, N di-methyl formamide were procured from Fisher Scientific. Polydimethylsiloxane (PDMS) was procured from dow corning. All the chemicals utilized are of analytical grade.

3.2.2 Synthesis Procedure for rGO, B-rGO, N-rGO, and BN-rGO

A modified hummers method was used to synthesize graphene oxide(GO) from graphite flakes[32]. In order to synthesize BN-rGO, 0.5g of boric acid and 0.5g of urea is added simultaneously in 70 ml aqueous solution of GO (1.5 mg/ml) and ultrasonicated for 1 hour for uniform dispersion. The prepared solution was then transferred to a 100 ml Teflon-lined autoclave for the hydrothermal reaction at 180° for 12 hr. The black

precipitate obtained after natural cooling down of autoclave was then washed multiple times with DI water ethanol and kept in oven 60°C for drying. A similar hydrothermal procedure was used to make rGO, but without the use of any heteroatom sources. Similarly, boron doped rGO (B-rGO) and nitrogen doped rGO (N-rGO) was synthesized through a similar hydrothermal process by using boric acid and urea as precursors. The schematic for hydrothermal synthesis of powder sample is shown in Figure 3.1(a).

3.2.3 Preparation of PVDF Nanocomposite and PDMS Films

The flexible films of the polymer nanocomposite materials were prepared via drop casting method. Initially, PVDF and N, N dimethylformamide (DMF) were mixed together in a 1:10 ratio and stirred to obtain a clear viscous solution. After that, 10 mg of rGO, B-rGO, N-rGO, and BN-rGO nanosheets were added separately to the above solution and stirred for 45 minutes for uniform dispersion of nanosheets. The obtained solution was then drop cast on the glass substrate and kept in the hot-air oven at 90° for 2 hours (Figure 3.1(b)). Then, by dipping the films in DI water, the films were detached from the glass substrate and freestanding films of PVDF nanocomposites were obtained.

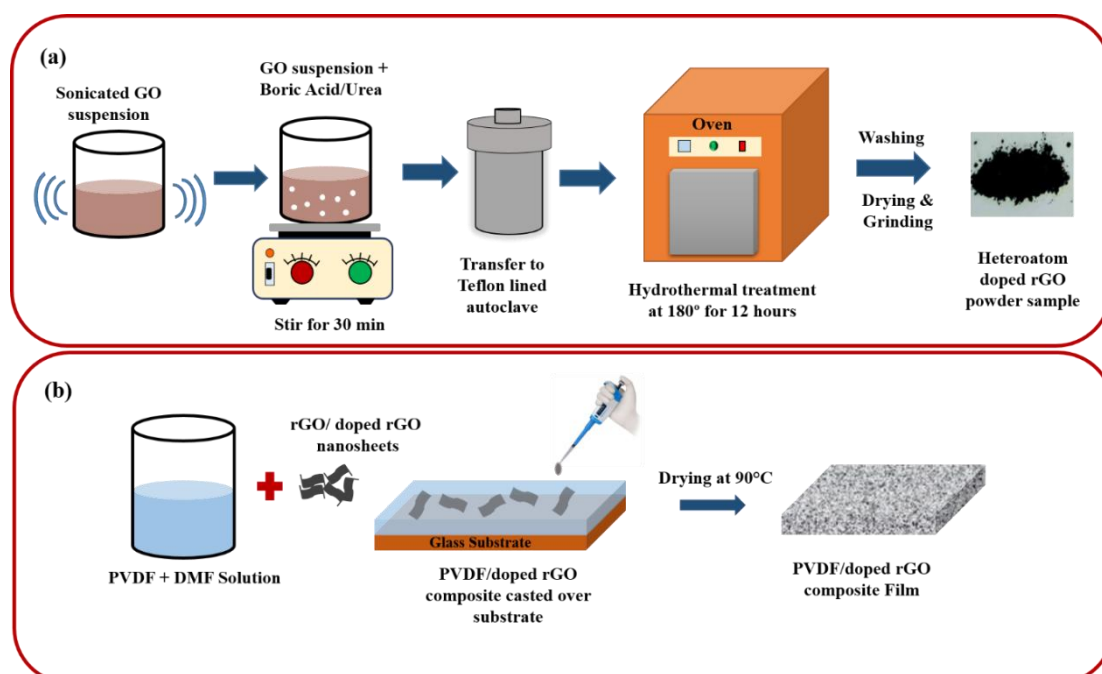


Figure 3.1 A schematic showing the step by step procedure for (a) hydrothermal synthesis of rGO and heteroatom doped rGO, and (b) synthesis of PVDF/ doped rGO composite film prepared via drop casting method.

A thin film of PDMS was prepared by mixing the base resin and curing agent (Sylgard 184, Dow Corning Co.) in a weight ratio of 10:1. Afterward, the resultant solution was vacuumed to remove the air bubbles. Then, the solution is spin-coated on the glass substrate followed by drying in the oven to remove any moisture contents.

3.2.4 Device Fabrication

To fabricate a PENG device, PVDF and its nanocomposite films were cut in the requisite shape (with effective working area of 1.75 cm x 1.75 cm) and 100 nm thin aluminium layer is deposited on both sides of film as top and bottom electrode by thermal evaporation technique, then copper wires are attached on the two electrodes to take measurements across the fabricated device.

To fabricate hybrid nanogenerator (HNG), the PVDF composite film with Al electrode on both sides serve as bottom piezoelectric component of HNG, and a PDMS film with a thin film of Al on back side, served as top component of HNG. Finally, both the films were attached to an acrylic substrate, making HNG to operate in vertical contact-separation mode.

3.3 Results and Discussion

3.3.1 Material Characterization

Figure 3.2 (a) shows the Raman spectra of as-synthesized nanosheets of rGO, B-rGO, N-rGO, and BN-rGO respectively. Apparently, all the samples exhibit two characteristic peaks assigned to D and G band at approximately 1344 cm^{-1} and 1586 cm^{-1} , respectively, while a wide 2D band corresponding to the carbon structure in rGO is present around 2800 cm^{-1} . The D band originates as a result of the structural defects and partially disordered structure within sp^2 domain, whereas, G band arises because of E_{2g} vibration mode of sp^2 hybridization in a hexagonal lattice. It has been observed from the spectra that the intensity ratio of the D and G band (I_D/I_G) which can be used to evaluate the degree of disorder in graphene materials, increases after the incorporation of foreign heteroatom (i.e. boron and nitrogen) in rGO. In comparison to rGO

($I_D/I_G=0.99$), the ratio of I_D/I_G for B-rGO, N-rGO and BN-rGO increased to 1.01, 1.02 and 1.04, respectively, indicating successful doping of boron and nitrogen respectively. The following factors can be responsible for increase in the value of the I_D/I_G ratio (a) increase in the number of vacancies or defects after doping of heteroatom which cause lattice distortion by increasing disorder; (b) complex bonding configurations (C–B, C–N, and C–N–B) cause severe electronic asymmetry and polarization [33]. Moreover, the largest value of I_D/I_G ratio in BN-rGO shows the highest structural defects and most complete reduction.

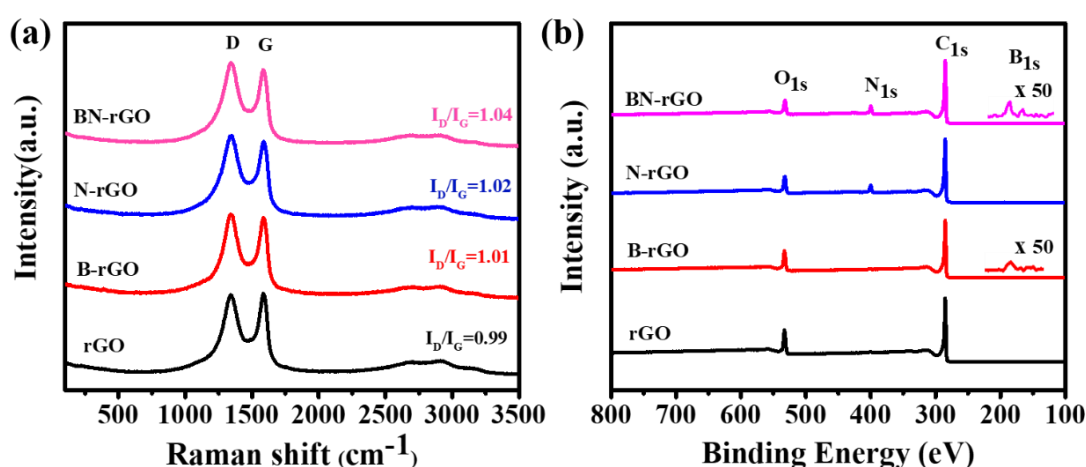


Figure 3.2 (a) Raman spectra, (b) XPS survey spectra of the rGO, B-rGO, N-rGO and BN-rGO powder sample.

To further confirm the successful doping of boron and nitrogen in rGO, X-ray photoelectron spectroscopy analyses (XPS) was conducted. Figure 3.2 (b) shows XPS survey spectra of pristine rGO, B-rGO, N-rGO, and BN-rGO where two additional peaks at 191eV (B1s) and 400.1eV (N1s) shows that boron and nitrogen atoms are successfully doped in corresponding samples. Also, it has been observed that the oxygen contents in B-rGO, N-rGO, and BN-rGO is relatively low than in rGO, which is ascribed to the effective removal of oxygenated groups (i.e., carboxyl, hydroxyl) in the hydrothermal process. Also, the high concentration of nitrogen in BN-rGO as compared to N-rGO, indicates the mutual promotion of heteroatom (boron & nitrogen) in co-doping process.

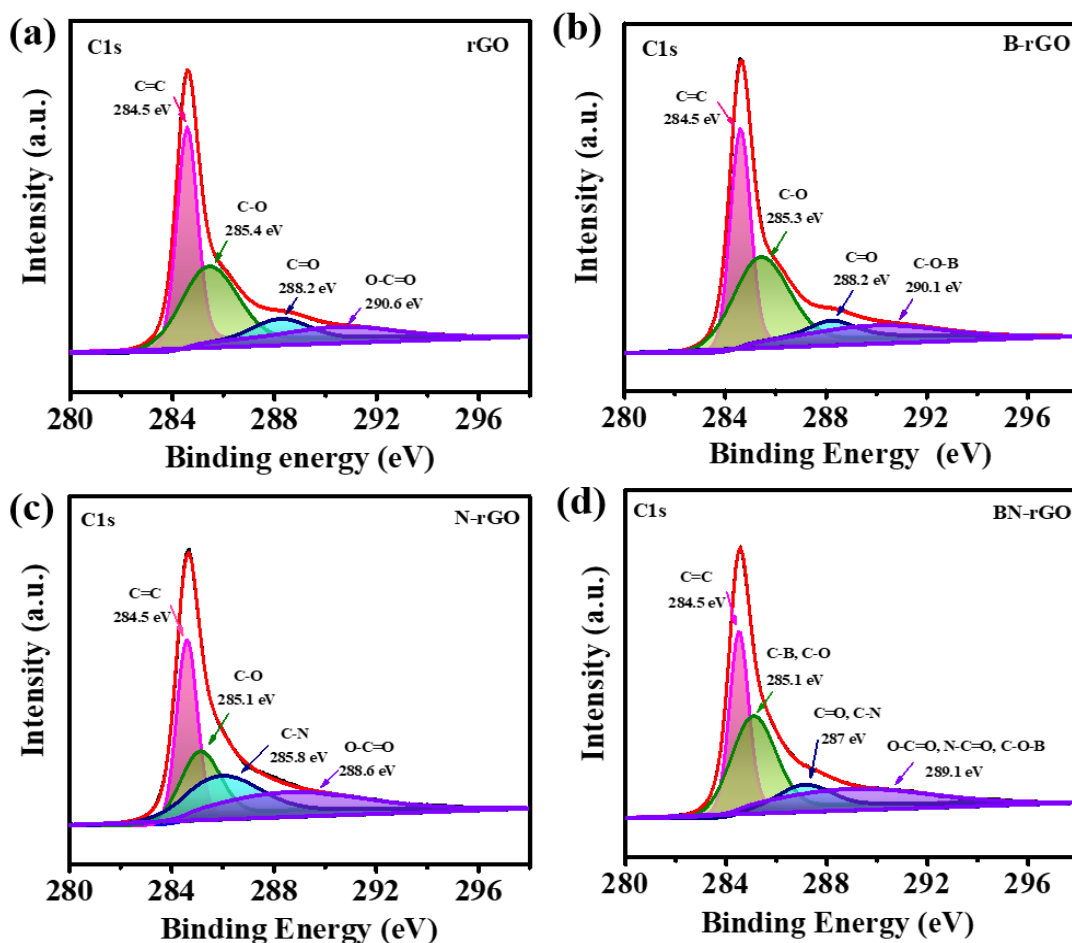


Figure 3.3 Deconvoluted C1s core level XPS spectra of (a) rGO, (b) B-rGO, (c) N-rGO and (d) BN-rGO.

The high-resolution C1s spectra of rGO (Figure 3.3 (a)) was deconvoluted in four distinguishable peaks at 284.5 eV, 285.4 eV, 288.2 eV, 290.6 eV corresponding to sp^2 hybridized C=C, C-O, C=O, and O-C=O respectively[30]. The C1s spectra of B-rGO and N-rGO also exhibit the same functional group as that of rGO except that in B-rGO peak at 290.6 eV is shifted to 290.1 eV and this new peak corresponds to the C-O-B bond, whereas in N-rGO this peak disappears and a new peak corresponds to the C-N bond is observed at 285.8 eV (Figure 3.3 (b-c)). Furthermore, C1s spectra of BN-rGO exhibits the new peaks corresponding to C-O-B and N-C=O (289.1 eV), as well as C-B (285.06 eV), C-N (287 eV) in addition to the characteristic peak of C=O, O-C=O and sp^2 hybridized C=C, indicating the successful doping of boron and nitrogen atoms [34] (Figure 3.3 (d)).

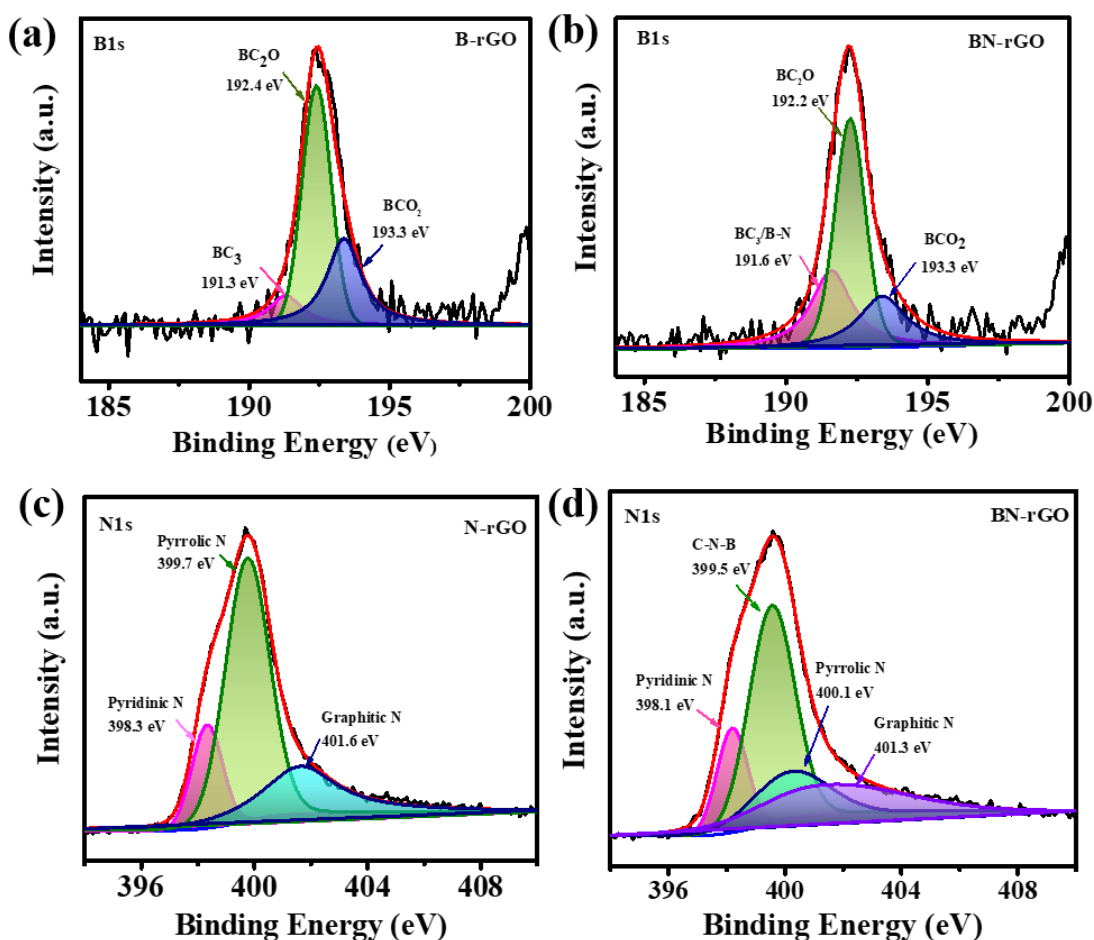


Figure 3.4 Deconvoluted B1s core level spectra of (a) B-rGO, and (b) BN-rGO, N1s core level spectra of (c) N-rGO and (d) BN-rGO samples

The high resolution B1s spectra of B-rGO and BN-rGO is shown in Figure 3.4 (a-b), which is deconvoluted in three peaks at binding energies 191.3, 192.4 and 193.3 eV. The B1s spectra demonstrates that boron can exist in three different form, first is by substitution of carbon atom by boron atom in the rGO network to form bond BC_3 , second is co-doping with the oxygen to form BC_2O bond which creates nanovoids in layer and third is BCO_2 bond resulting from the formation of functional groups[37] [38, 39].

There are three major nitrogen bonded configurations in the N1s XPS spectra of the N-rGO i.e. pyridinic N (398.3), pyrrolic N (399.7 eV), and graphitic N (401.6 eV) as shown in Figure 3.4 (c). It has been observed that the N1s spectra of the BN-rGO change significantly as compared to the N-rGO. The spectra show the four peaks corresponding to pyridinic N (398.1), pyrrolic N (400.1 eV), graphitic N (401.3 eV), and C-N-B (399.5 eV).

and C-N-B (399.5 eV) respectively (Figure 3.4 (d)). The presence of C-N-B bonds suggests that some of the carbon atoms among the C-N bond are displaced by boron atoms and combined with neighbouring nitrogen atoms and sub-adjacent carbon atoms to form C-N-B [40, 41].

Furthermore, all of the samples were also analysed for morphology and elemental composition. Figure 3.5 (a-d) shows the FE-SEM micrograph of rGO, B-rGO, N-rGO, and BN-rGO which shows that all the samples exhibit laminated structure comprised of planar sheets with wrinkled surface and corrugations because of doping of boron and nitrogen atom together with the residual functional groups. Moreover, the elemental composition of heteroatom doped rGO was further confirmed by EDX analysis. Figure 3.5 (e) depicts the EDX spectra of BN-rGO nanosheets with the corresponding element maps of C, O, B and N (Figure 3.5 (f-i)) which further confirms that boron and nitrogen have been successfully doped in rGO.

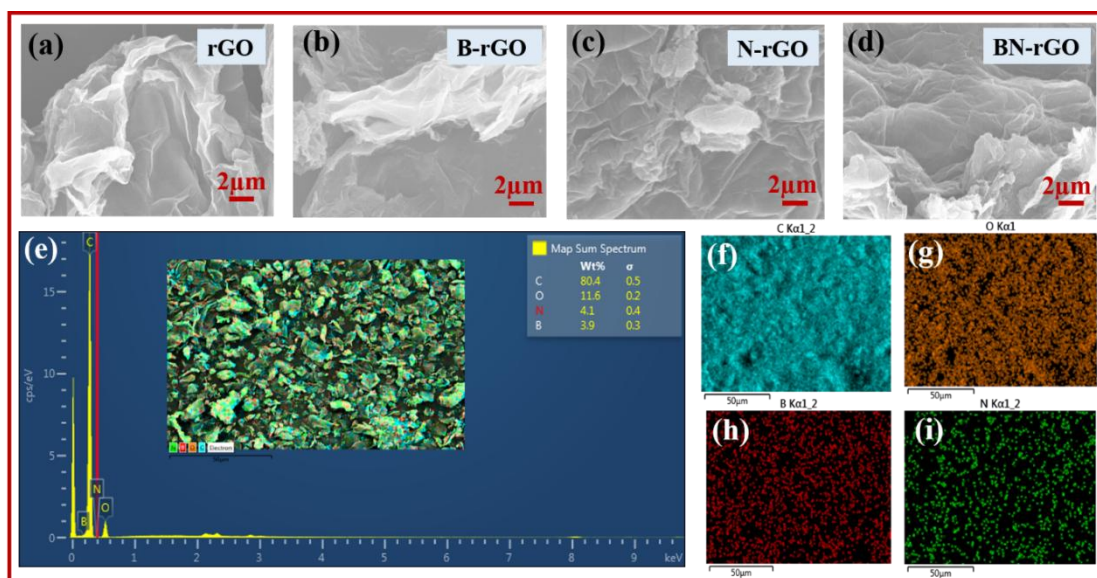


Figure 3.5 FE-SEM micrographs of (a) rGO, (b) B-rGO, (c) N-rGO, (d) BN-rGO, and (e-i) EDX spectrum with the elemental mapping image of all element present in BN-rGO.

3.3.2 Films Characterization

As we know that high content of electroactive polar phase (i.e. β and γ phase) in PVDF is desirable for improved piezoelectric properties. Therefore, XRD and FTIR analysis was used to confirm presence of various phase of PVDF and to investigate the effect of

doping of rGO, N-rGO and BN-rGO on the PVDF crystalline structure. Figure 3.6 (a) depicts the XRD pattern of pristine PVDF and heteroatom doped rGO based nanocomposite films, which consists of two characteristic peaks one ascribed to non-polar α phase at 18.4° and another at $\sim 20.2^\circ$ corresponds to electroactive polar phase of PVDF [42] are observed in all samples. It has been observed that compared to pristine PVDF film, the peak intensity corresponding to polar electroactive phase increases in PVDF nanocomposite films. This indicates that even a small amount of pure rGO and doped rGO is sufficient to nucleate polar electroactive phase, that can enhance the overall piezoelectric response of the PVDF polymer.

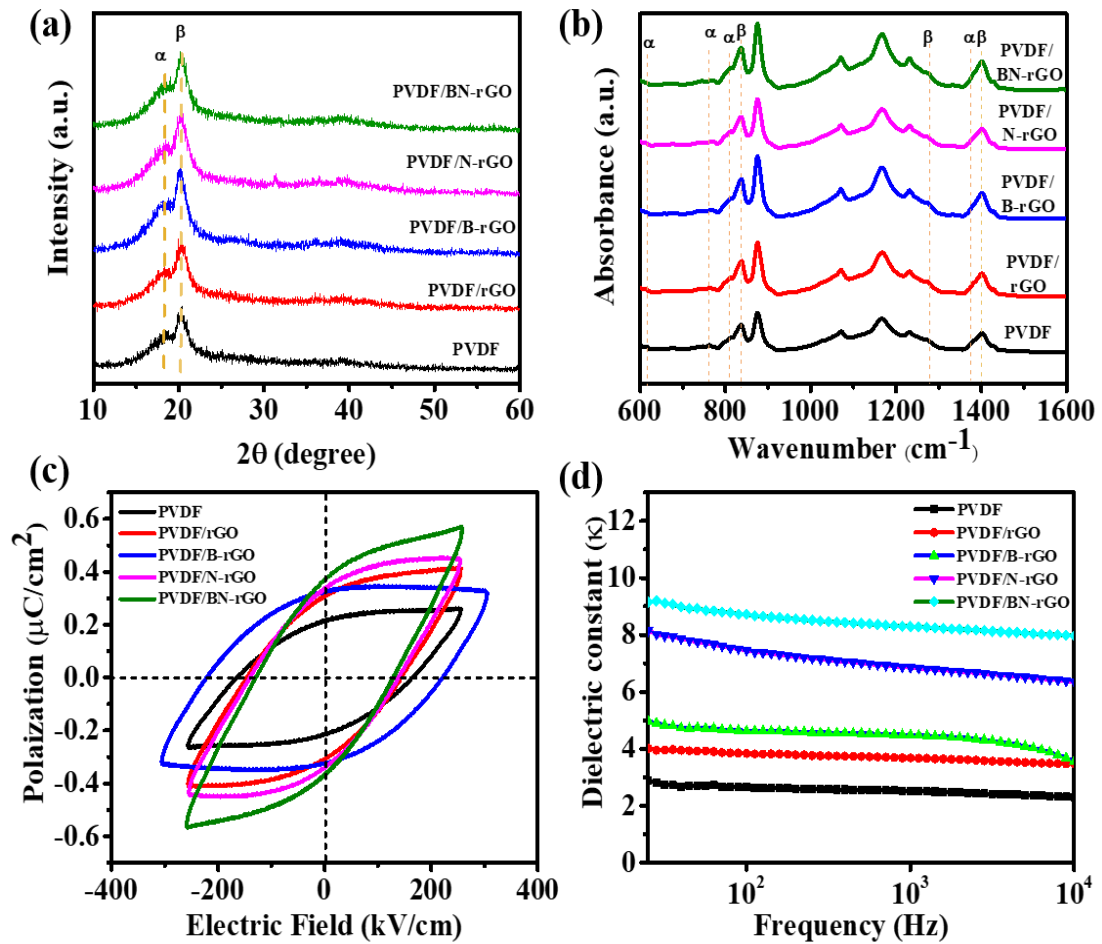


Figure 3.6 (a) XRD and (b) FTIR spectra of PVDF, PVDF/rGO, PVDF/N-rGO and PVDF/BN-rGO thin film, (c) polarization versus electric field (P-E) hysteresis loop and (d) room temperature dielectric constant of PVDF and PVDF nanocomposite films after doping of rGO, N-rGO and BN-rGO.

The content of electroactive polar phase in PVDF and composite films are determined using FTIR. Figure 3.6 (b) shows the FTIR spectra of PVDF, PVDF/rGO, PVDF/B-rGO, PVDF/N-rGO and PVDF/BN-rGO films, showing that all samples exhibit characteristic peak at 840 cm^{-1} corresponding to the combined β and γ phase of PVDF. The peak ascribed to non polar α -phase is marked by the peak at $612, 762, 795$ and 1382 cm^{-1} , while peaks at 1279 , and 1400 cm^{-1} attributed to the polar β and γ phase of the PVDF[43, 44]. The relative fraction of electroactive polar phase of PVDF can be calculated by Beer-Lambert law given by the equation

$$F(EA) = \frac{A_{840}}{\left(\frac{k_{840}}{k_{762}}\right)A_{762} + A_{840}} \times 100\% \quad (3.1)$$

where A_α and A_β are absorbance at 762 cm^{-1} and 840 cm^{-1} , $k_\alpha = 6.1 \times 10^4\text{ cm}^2/\text{mol}$ and $k_\beta = 7.7 \times 10^4\text{ cm}^2/\text{mol}$ represents absorption coefficients at corresponding wavenumber [45].

For the PVDF, value of the fraction of electroactive polar phase content is 61.34% while after doping of rGO, B-rGO, N-rGO and BN-rGO in PVDF its value increases upto 75%, 80%, 85.27% and 87.1%, respectively. It was observed that the value of electroactive polar phase in the PVDF/BN-rGO composite film is highest among all the doped samples. The substantially increased value of electroactive polar phase results from the increased electrostatic interaction of $-\text{CH}_2$ and $-\text{CF}_2$ dipoles of PVDF with surface charge (developed due to presence of B, N particles, oxygen containing functional groups and delocalized π electron in rGO) of BN-rGO as shown in schematic drawn in Figure 3.7. Therefore, when we insert it into PVDF, the positive charge present at the basal plane of BN-rGO interact with the flourine group of PVDF i.e. boron and carbonyl group in BN-rGO interect with flourine group of PVDF. Also, the H atom in $-\text{CH}_2/-\text{CF}_2$ dipole tends to approach BN-rGO surface, and interact with nitrogen and oxygen containing functional groups present in BN-rGO which assist rotation of polymer chain for formation of all trans conformation. Thus, these results indicate that additon of BN-rGO in PVDF induces polar phase formation by providing a substrate for the crystal nucleation in PVDF and thus, acts as a nucleating agent.

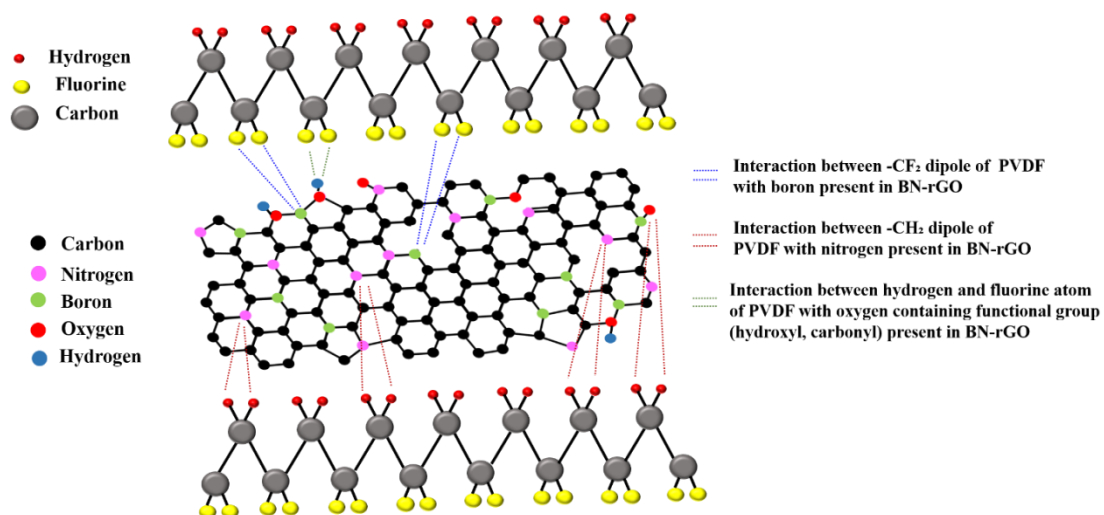


Figure 3.7 A schematic illustration of interaction of BN-rGO nanosheet with the PVDF chain.

Furthermore, to analyze the effect of doping on ferroelectric properties of PVDF, polarization versus electric field (P-E) measurements are carried out on PVDF and PVDF nanocomposite films as illustrated in Figure 3.6 (c). The P-E measurements results clearly affirmed the enhanced ferroelectric behavior of PVDF after incorporation of rGO and heteroatom doped rGO in polymer matrix. The values of the remnant polarization (P_r) obtained from P-E loops for PVDF, PVDF/rGO, PVDF/B-rGO, PVDF/N-rGO and PVDF/BN-rGO are 0.21, 0.30, 0.32, 0.33 and 0.37 $\mu\text{C}/\text{cm}^2$ respectively. The enhanced value of the remnant polarization depicts that addition of rGO and heteroatom doped rGO helps in alignment of dipoles in PVDF which result in an increased electroactive polar phase in nanocomposite films. To further support the enhancement in the performance of the nanogenerator, the frequency dependent dielectric measurements were carried out on pristine PVDF and PVDF nanocomposite films using the LCR meter at room temperature. Figure 3.6 (d) shows the variation in the dielectric constant of pristine PVDF and PVDF nanocomposite films after doping of rGO and heteroatom doped rGO in the polymer matrix. It has been observed from the graph that after doping of rGO, B-rGO, N-rGO and BN-rGO in the PVDF matrix the value of dielectric coefficient is enhanced significantly. The value of dielectric constants for PVDF, PVDF/rGO, PVDF/B-rGO, PVDF/N-rGO and PVDF/BN-rGO are 2.6, 4.1, 5, 8.2 and 9.2 respectively. The highest dielectric constant value of PVDF/BN-rGO sample can be attributed to improved surface charge density of film after boron and nitrogen co-doping in the rGO structure, which increases the dielectric constant[27].

The surface morphology of PVDF, PVDF nanocomposite films are shown in Figure 3.8 (a-e) which shows that heteroatom doped rGO is uniformly distributed in PVDF matrix while slight agglomeration of rGO nanosheets is observed in PVDF/rGO composite film.

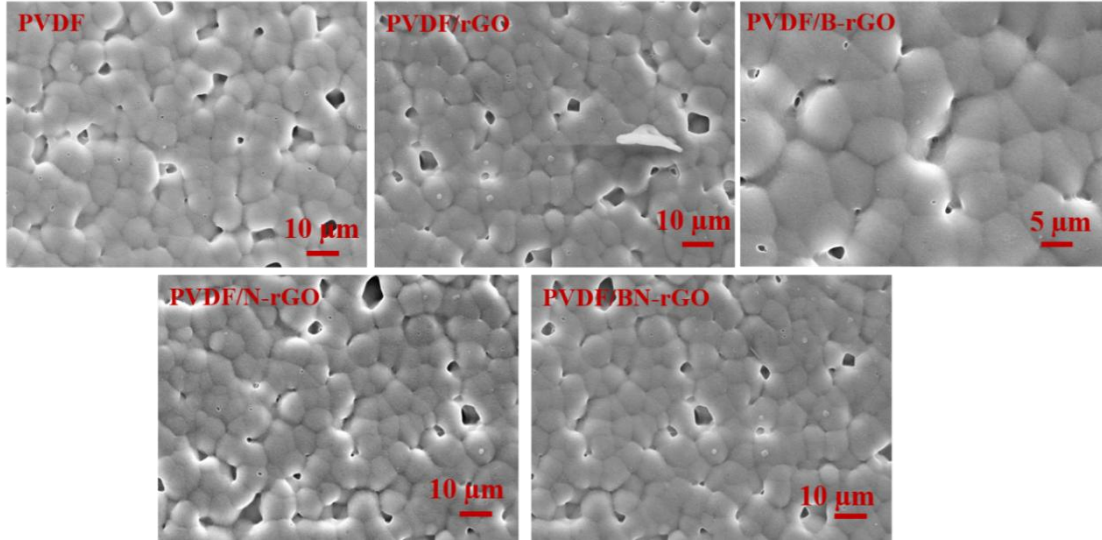


Figure 3.8 SEM images of (a) PVDF, (b)PVDF/rGO, (c) PVDF/B-rGO, (d) PVDF/N-rGO, (e) PVDF/BN-rGO films.

3.3.3 Electrical Characterization of PENG

To evaluate the piezoresponse and energy harvesting performance of the PVDF, rGO and heteroatom doped rGO nanocomposite films, the films were sandwiched between two aluminum electrodes to fabricate PENG device and their output performance were examined by continuous tapping of the nanogenerator with the help of commercially available electrodynamic shaker at 6 Hz frequency. The voltage produced by pristine PVDF, PVDF/rGO, PVDF/B-rGO, PVDF/N-rGO, and PVDF/BN-rGO film based nanogenerators are shown in Figure 3.9 (a). The results demonstrate that among the various fabricated PENG, the highest voltage of 20.4 V(peak to peak) is generated by PVDF/BN-rGO based composite film which is ~2 times greater than the voltage generated by PVDF film. Furthermore, we have also performed short-circuit current measurements at the same frequency and amplitude as applied in voltage measurements case, and the corresponding values of the rectified current obtained for PVDF, PVDF/rGO, PVDF/B-rGO, PVDF/N-rGO, and PVDF/BN-rGO nanocomposite films based nanogenerators are 2.6 μ A, 5.1 μ A, 5.9 μ A, 8.7 μ A and 15.9 μ A respectively (Figure 3.9 (b)).

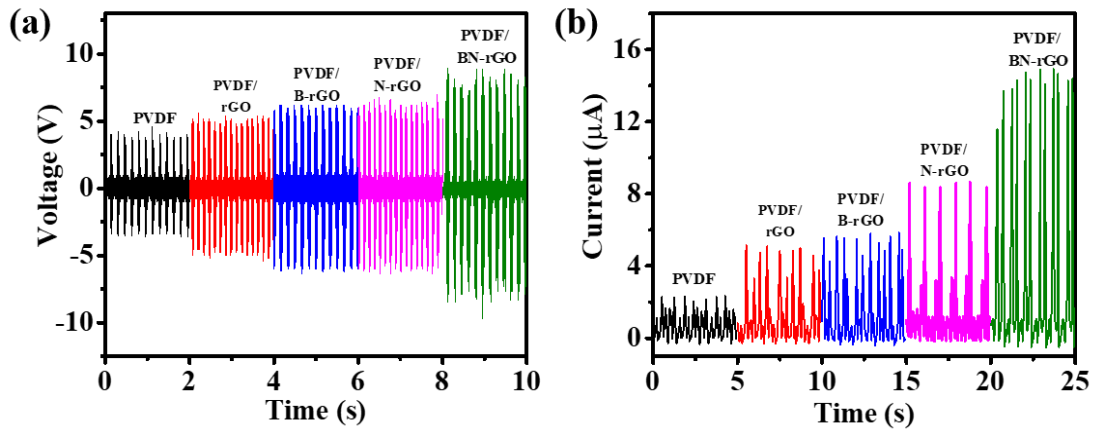


Figure 3.9 (a) The open-circuit voltage, and (b) rectified short-circuit current produced by PVDF, PVDF/rGO, PVDF/B-rGO, PVDF/N-rGO, and (d) PVDF/BN-rGO nanocomposite film at 6 Hz frequency.

Figure 3.10 (a) depicts the open-circuit voltage of PENGs as a function of tapping frequency, indicating that all films follow a similar pattern in which the output voltage first increases and reaches a maximum at 6 Hz frequency, then begins to decrease as frequency increases. The maximum peak to peak voltage achieved by PVDF, PVDF/rGO, PVDF/B-rGO, PVDF/N-rGO, PVDF/BN-rGO nanocomposite films are 9.2 V, 12.4 V, 13.8 V, 14.2 V, and 20.4 V respectively. The open-circuit voltage generated by PVDF/BN-rGO nanocomposite film based PENG by varying the input frequency in the range from 1 Hz to 10 Hz is illustrated in Figure 3.10 (b).

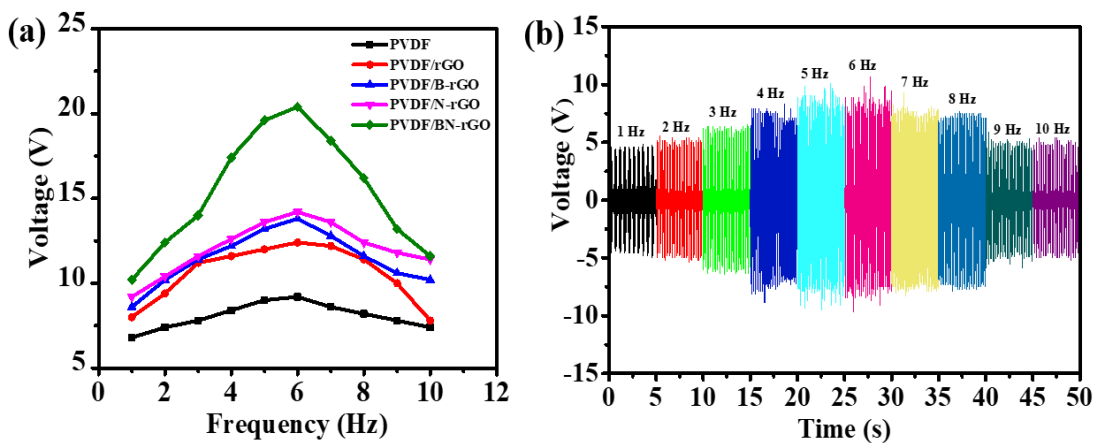


Figure 3.10 (a) PENGs output performance analyzed by varying the input frequency in the range from 1 Hz to 10 Hz, (b) PVDF/BN-rGO nanocomposite film-based PENG output voltage as a function of variable frequency.

These results demonstrate that in both the voltage and current measurement, the maximum value corresponds to the PVDF/BN-rGO films based nanogenerator. The enhanced piezoelectric performance of PVDF/BN-rGO film in comparison with PVDF film may be attributed to the following facts: First, is the enhanced nucleation of polar phase after introduction of BN-rGO in PVDF matrix which increases remanent polarization of the nanocomposite film as confirmed by XRD, FTIR and P-E studies. Second, is that addition of rGO in PVDF increases the local stress of the film, which boosts the mechanical property of nanocomposite film[46]. Third, is that when we add B, N co-doped rGO in PVDF matrix, it forms conduction network in the polymer matrix which can effectively reduce internal resistance of PENG resulting in facilitating better charge transfer and hence enhanced output voltage. Fourth is that, although graphene is non-piezoelectric, but Ong et.al. demonstrated by first principal study that piezoelectricity in graphene can be induced by selective surface adsorption of atoms which break the inversion symmetry in graphene and hence exhibit piezoelectricity[47].

3.3.4 Electrical Characterization of Hybrid Nanogenerator

It may be noted that even though the PENG based on PVDF/BN-rGO has the highest output power, but it is not sufficient to drive the practical devices. Therefore, to further improve the mechanical energy conversion efficiency of device, we fabricate a hybrid nanogenerator (HNG) which will utilize both triboelectric and piezoelectric effects in single press and release cycle and enhances device performance [48, 49]. For this, we have coupled the PDMS film with PVDF/BN-rGO nanocomposite film having highest piezoelectric output as two triboelectric layer that works in vertical contact separation mode.

A schematic of device structure of HNG is shown in Figure 3.11, where connection from aluminium deposited on back side of PDMS and PVDF nanocomposite film gives triboelectric output, whereas connection from top and bottom of PVDF nanocomposite film gives the piezoelectric output. Furthermore, to mitigate the issue of voltage

degradation arises from the mismatch between the internal resistance of triboelectric and piezoelectric units, two full wave bridge rectifier are fed to output terminals of triboelectric and piezoelectric units which helps in eliminating the voltage cancellation effect arises due to phase mismatch. First, output performance of piezoelectric and triboelectric nanogenerator are measured individually and then to acquire the combined output of HNG the positive and negative terminal of the bridge rectifiers are short together.

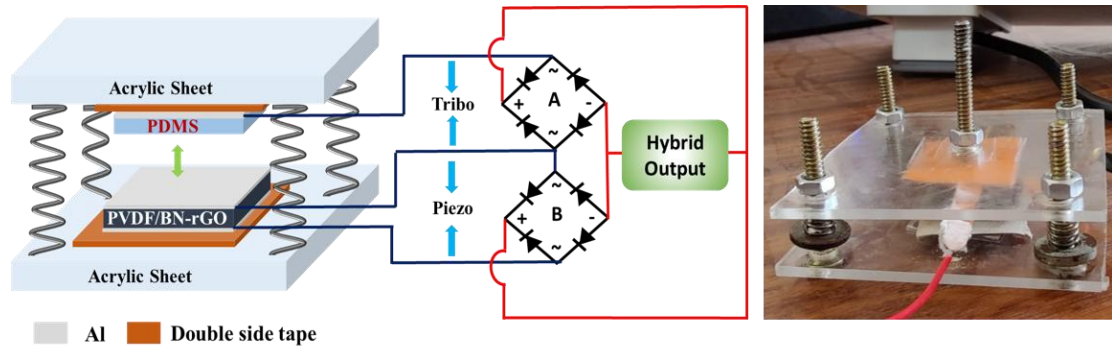


Figure 3.11 A schematic representation of piezo-tribo hybrid nanogeneration with the electrical connections.

Figure 3.12 (a-d) demonstrates the comparison of rectified output voltage and current response of PVDF and PVDF/BN-rGO nanocomposite film generated from the individual PENG, TENG and HNG. It is observed from graph that not only the hybrid performance of the device get enhanced after addition of nanofiller in PVDF matrix, but there is also significant enhancement in both the piezoelectric and triboelectric performance of PVDF/BN-rGO film based nanogenerator when compared to PVDF based nanogenerator. After incorporation of BN-rGO, the output voltage in piezoelectric case increases from 6.4V to 15.2V, while in the case of triboelectric its value increases from 16.8 V to 26.8 V. Moreover, when the both outputs are combined, a rise in voltage observed from 25.2 V to 57.6 V for PVDF/BN-rGO composite film based hybrid nanogenerator. The electrical current generated by PENG, TENG and HNG are 11.7 μ A, 18.2 μ A and 28.8 μ A for PVDF/BN-rGO nanocomposite film whereas for PVDF film its values are 6.4 μ A, 13.6 μ A and 22.3 μ A respectively.

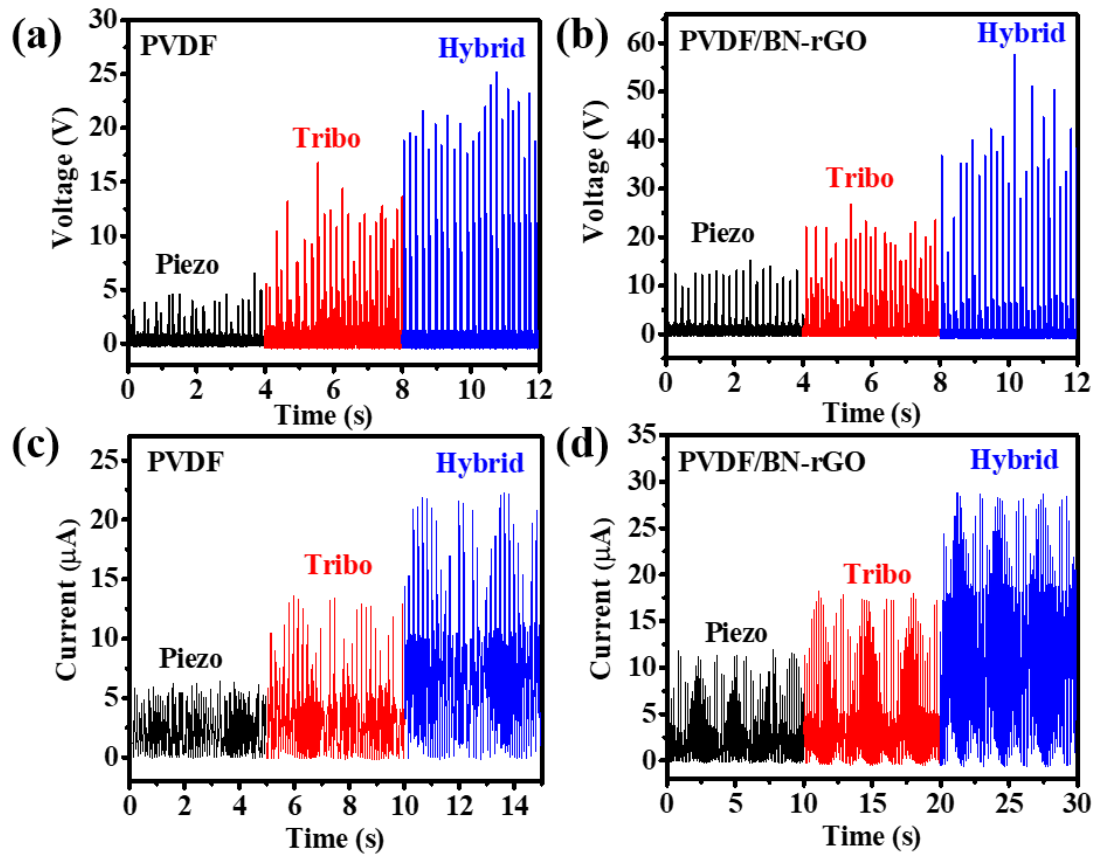


Figure 3.12 Comparison between the (a-b) rectified open-circuit voltage, and (c-d) short-circuit current of piezo, tribo and hybrid nanogenerator of PVDF and PVDF/BN-rGO composite film.

The high output performance of HNG in comparison with the PENG and TENG component can be understood by the fact that when PDMS film and PVDF/BN-rGO nanocomposite films are brought in contact with each other by external force, opposite charges are produced on the surface due to triboelectrification. On further increase in the external force, a net non-zero dipole moment is induced in the PVDF/BN-rGO nanocomposite film which creates an piezoelectric potential between upper and lower surface of the nanocomposite films. As a result, additional charges are induced on the surface of the electrode due to synergetic effect of both piezoelectric potential and triboelectric charge which contribute in improving the output performance of the hybrid nanogenerator[50, 51]. The load matching studies of HNG is shown in Figure 3.13, showing a maximum power density of $70.65 \mu\text{W}/\text{cm}^2$ generated by the HNG at $1 \text{ M}\Omega$ resistance.

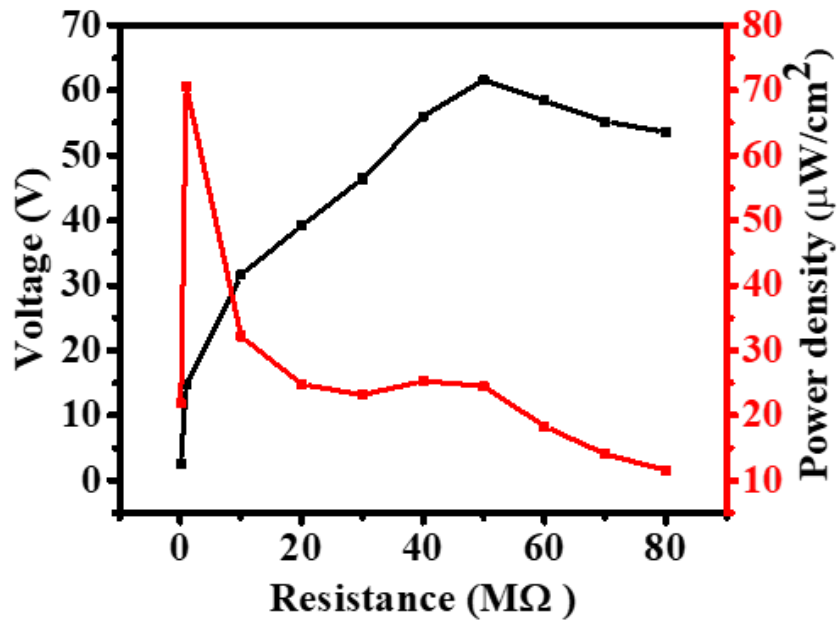


Figure 3.13 The output voltage and power density curve of PVDF/BN-rGO film based HNG as a function of resistance.

3.3.5 Applications of PENG and Hybrid Nanogenerator

3.3.5.1 Biomechanical Energy Harvesting using PENG

Furthermore, the as fabricated nanogenerator is utilized to harness biomechanical energy from human body by attaching it to different parts of the body and a schematic representation of human body parts from which energy has been harvested is shown in Figure 3.14 (a). Figure 3.14 (b-d) illustrates the output voltage generated by PENG by tapping it with one finger, two finger and thumb. The output voltage generated by nanogenerator by clapping and attaching it to wrist, elbow, knee, and tapping it with foot are illustrated in Figure 3.14 (e-i). The variation of the tapping with finger in slow, moderate and high speed is also illustrated in Figure 3.14 (j). We also measured PENG output voltage by bending elbow at various angles (30°, 45° and 90°) as illustrated in Figure 3.14 (k). The above results demonstrate the flexible PVDF nanocomposite film based PENG is an effective device that can harness biomechanical energy from the human motion. Thus, by harvesting the energy associated with these various biomechanical motions, it is possible to design a pervasive, sustainable and environmental friendly energy solution for the bioelectronics which will revolutionize the future of wearable electronics in upcoming era of IoT and artificial intelligence[47-49].

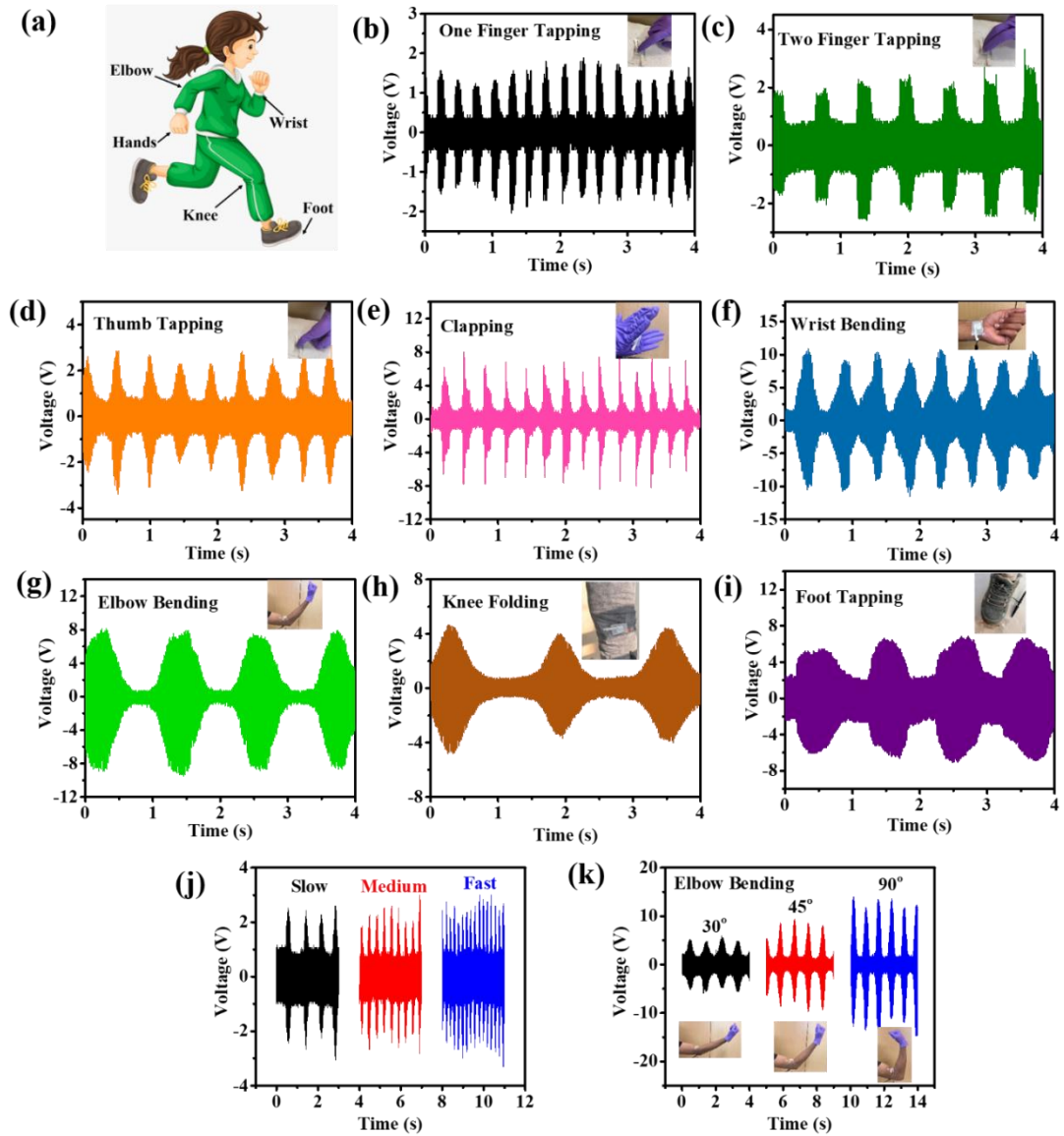


Figure 3.14 (a) A schematic representation of different parts of human body from which energy can be harvested. The output voltage generated by PBR film based PNG by (b) one finger, (c) two fingers, (d) thumb tapping, (e) clapping, (f) wrist bending, (g) elbow bending, (h) knee folding, and (i) foot tapping, (j) variation in the output performance of PNG by slow, moderate and fast finger tapping, (k) The voltage produced by PNG by bending elbow at different angles.

3.3.5.1 Capacitor Charging and Powering of Electronic Devices

Figure 3.15 (a) shows the comparison of charging of 1 μ F capacitor by PENG, TENG and HNG and their corresponding energy stored in the capacitor is calculated by the formula $W = \frac{1}{2}CV^2$ where W is energy, C is capacitance and V is the voltage. For the PENG, TENG, and hybrid nanogenerator, the energy stored in the capacitor are $\sim 4.5\mu$ J, $\sim 20.4\mu$ J and 28.8μ J, respectively (Figure 3.15 (b)). The charging of various capacitor

with the help of PVDF/BN-rGO composite film based hybrid nanogenerator is shown in Figure 3.15 (c). The $1\mu\text{F}$ capacitor can charge upto 7.6 V in 40 s, while $2.2\mu\text{F}$, $10\mu\text{F}$ and $47\mu\text{F}$ capacitor can charge upto 7 V, 3.4 V and 1.1 V respectively.

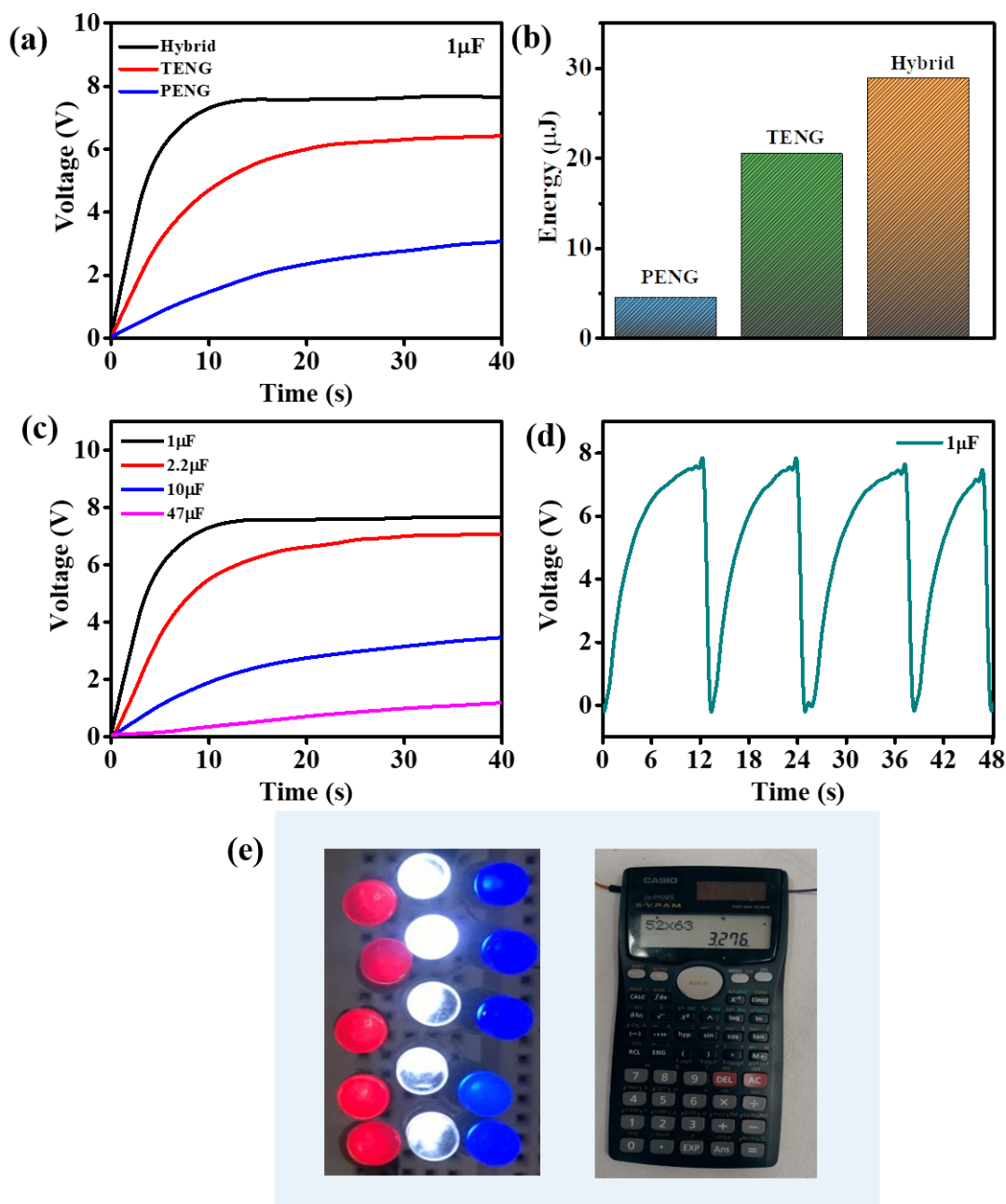


Figure 3.15 (a) charging of $1\mu\text{F}$ capacitor by individual PENG, TENG and hybrid nanogenerator, (b) energy stored in $1\mu\text{F}$ capacitor by individual PENG, TENG and hybrid nanogenerator, (c) capacitor voltage characteristic curves of 1, 2.2, 10, and $47\mu\text{F}$ capacitor charged through PVDF/BN-rGO composite film based HNG, (d) charging and discharging cycle of $1\mu\text{F}$ capacitor, (e) A photographic image of powering of 15 LEDs and a calculator by the PVDF/BN-rGO composite film based hybrid nanogenerator.

Figure 3.14 (d) demonstrates the charging and discharging characteristics of the hybrid nanogenerator. Furthermore, to demonstrate the practical feasibility of PDMS and PVDF/BN-rGO film based hybrid nanogenerator, the output power generated by the hybrid generator is used to glow up 15 LEDs connected in series and powering of calculator as shown in Figure 3.14 (e). Thus, the present work propose an effective strategy for developing a high-performance energy harvester for self-powered wearable devices by employing graphene and its derivative as an effective nanofiller material in a PVDF matrix.

3.4 Summary

In summary, we have succesfully examined the effect of doped rGO nanosheets in PVDF matrix for harvesting the mechanical energy from pure piezoelectric nanogenerator, and piezo-triboelectric hybrid nanogenerator based structure. Among the various fabricated devices, PENG based on PVDF/BN-RGO nanocomposite film has highest peak to peak voltage of 20.4 V and current of 15.9 μ A, which is greater than pristine PVDF based PENG. This composite film was then coupled with the PDMS film to fabricate the hybrid nanogenerator and can produce a maximum voltage of 57.6 V. The improved performance of HNG is ascribed to the improved piezoelectric and triboelectric property of PVDF after addition of BN/rGO in it. The increase in the piezoelectricity can be attributed to the fact that when we add the codoped rGO in polymer matrix, the content of electroactive polar β -phase increases because of the interaction between $-\text{CF}_2$ and $-\text{CH}_2$ groups of PVDF with the various groups present in BN-rGO, resulting in an increase in piezoelectric properties of the nanocomposite film. Also, additional surface charges are induced due to the synergic effect of piezoelectric potential and trbioelectrictrification, which improves the output performance of the HNG. Furthermore, the energy generated by the HNG is stored in the 1 μ F capacitor and used to lightup 15 series-connected LEDs and powering calculator. These results showcase a novel strategy for enhancing nanogenerator performance and highlight the potential application of the PVDF/BN-rGO hybrid nanogenerator in wearable and bioelectronic devices.

References

- [1] X. Pu, L. Li, M. Liu, C. Jiang, C. Du, Z. Zhao, W. Hu, Z.L. Wang, Wearable self-charging power textile based on flexible yarn supercapacitors and fabric nanogenerators, *Advanced Materials*, 28 (2016) 98-105.
- [2] L. Liu, X. Guo, W. Liu, C. Lee, Recent Progress in the Energy Harvesting Technology—From Self-Powered Sensors to Self-Sustained IoT, and New Applications, *Nanomaterials* 11 (2021) 2975.
- [3] S. Rana, V. Singh, B. Singh, Recent trends in 2D materials and their polymer composites for effectively harnessing mechanical energy, *iScience*, (2022) 103748.
- [4] C. Qian, L. Li, M. Gao, H. Yang, Z. Cai, B. Chen, Z. Xiang, Z. Zhang, Y. Song, All-printed 3D hierarchically structured cellulose aerogel based triboelectric nanogenerator for multi-functional sensors, *Nano Energy*, 63 (2019) 103885.
- [5] Z.L. Wang, J.J.S. Song, Piezoelectric nanogenerators based on zinc oxide nanowire arrays, 312 (2006) 242-246.
- [6] L. Algieri, M.T. Todaro, F. Guido, V. Mastronardi, D. Desmaële, A. Qualtieri, C. Giannini, T. Sibillano, M. De Vittorio, Flexible piezoelectric energy-harvesting exploiting biocompatible AlN thin films grown onto spin-coated polyimide layers, *ACS Appl. Energy Mater.*, 1 (2018) 5203-5210.
- [7] C. Wu, A.C. Wang, W. Ding, H. Guo, Z.L. Wang, Triboelectric nanogenerator: a foundation of the energy for the new era, *Advanced Energy Materials*, 9 (2019) 1802906.
- [8] A.M. Abdullah, A. Flores, A.R. Chowdhury, J. Li, Y. Mao, M.J. Uddin, Synthesis and fabrication of self-sustainable triboelectric energy case for powering smart electronic devices, *Nano Energy*, 73 (2020) 104774.
- [9] W. Tang, T. Jiang, F.R. Fan, A.F. Yu, C. Zhang, X. Cao, Z.L. Wang, Liquid-metal electrode for high-performance triboelectric nanogenerator at an instantaneous energy conversion efficiency of 70.6%, *Advanced Functional Materials*, 25 (2015) 3718-3725.
- [10] D. Kim, S. Lee, Y. Ko, C.H. Kwon, J. Cho, Layer-by-layer assembly-induced triboelectric nanogenerators with high and stable electric outputs in humid environments, *Nano Energy*, 44 (2018) 228-239.

- [11] Z. Wang, L. Cheng, Y. Zheng, Y. Qin, Z.L. Wang, Enhancing the performance of triboelectric nanogenerator through prior-charge injection and its application on self-powered anticorrosion, *Nano Energy*, 10 (2014) 37-43.
- [12] P. Bai, G. Zhu, Y.S. Zhou, S. Wang, J. Ma, G. Zhang, Z.L. Wang, Dipole-moment-induced effect on contact electrification for triboelectric nanogenerators, *Nano Research* 7(2014) 990-997.
- [13] S.K. Karan, S. Maiti, J.H. Lee, Y.K. Mishra, B.B. Khatua, J.K. Kim, Recent advances in self-powered tribo-/piezoelectric energy harvesters: all-in-one package for future smart technologies, *Advanced Functional Materials* 30 (2020) 2004446.
- [14] S.D. Mahapatra, P.C. Mohapatra, A.I. Aria, G. Christie, Y.K. Mishra, S. Hofmann, V.K. Thakur, Piezoelectric materials for energy harvesting and sensing applications: Roadmap for future smart materials, *Advanced Science*, 8 (2021) 2100864.
- [15] P. Sahatiya, S. Kannan, S.J.A.M.T. Badhulika, Few layer MoS₂ and in situ poled PVDF nanofibers on low cost paper substrate as high performance piezo-triboelectric hybrid nanogenerator: Energy harvesting from handwriting and human touch, 13 (2018) 91-99.
- [16] P. Fakhri, B. Amini, R. Bagherzadeh, M. Kashfi, M. Latifi, N. Yavari, S.A. Kani, L. Kong, Flexible hybrid structure piezoelectric nanogenerator based on ZnO nanorod/PVDF nanofibers with improved output, *RSC Adv.*, 9 (2019) 10117-10123.
- [17] H.H. Singh, N. Khare, Flexible ZnO-PVDF/PTFE based piezo-tribo hybrid nanogenerator, *Nano Energy*, 51 (2018) 216-222.
- [18] S.H. Wankhade, S. Tiwari, A. Gaur, P. Maiti, PVDF-PZT nanohybrid based nanogenerator for energy harvesting applications, *Energy Reports*, 6 (2020) 358-364.
- [19] K. Shi, B. Chai, H. Zou, P. Shen, B. Sun, P. Jiang, Z. Shi, X. Huang, Interface induced performance enhancement in flexible BaTiO₃/PVDF-TrFE based piezoelectric nanogenerators, *Nano Energy*, 80 (2021) 105515.
- [20] J.M. Wu, C. Xu, Y. Zhang, Z.L. Wang, Lead-free nanogenerator made from single ZnSnO₃ microbelt, *ACS Nano*, 6 (2012) 4335-4340.
- [21] J.H. Jung, M. Lee, J.-I. Hong, Y. Ding, C.-Y. Chen, L.-J. Chou, Z.L. Wang, Lead-free NaNbO₃ nanowires for a high output piezoelectric nanogenerator, *ACS Nano*, 5 (2011) 10041-10046.

- [22] M. Aleksandrova, T. Tsanev, I. Pandiev, G. Dobrikov, Study of piezoelectric behaviour of sputtered KNbO₃ nanocoatings for flexible energy harvesting, *Energy* 205 (2020) 118068.
- [23] J. Yang, Y. Zhang, Y. Li, Z. Wang, W. Wang, Q. An, W. Tong, Piezoelectric nanogenerators based on graphene oxide/PVDF electrospun nanofiber with enhanced performances by in-situ reduction, *Materials Today Communications*, 26 (2021) 101629.
- [24] N. Scriven, Retraction: Electrospun hybrid nanofibers of poly (vinylidene fluoride) and functionalized graphene oxide as a piezoelectric energy harvester, *Sustainable Energy Fuels*, 5 (2021) 590-590.
- [25] S.K. Karan, D. Mandal, B.B. Khatua, Self-powered flexible Fe-doped RGO/PVDF nanocomposite: an excellent material for a piezoelectric energy harvester, *Nanoscale*, 7 (2015) 10655-10666.
- [26] M. Il'ina, O. Il'in, O. Osotova, S. Khubezhov, N. Rudyk, I. Pankov, A. Fedotov, O. Ageev, Pyrrole-like defects as origin of piezoelectric effect in nitrogen-doped carbon nanotubes, *Carbon*, 190 (2022) 348-358.
- [27] J.-H. Ji, B.S. Kim, J. Kang, J.-H. Koh, Improved output performance of hybrid composite films with nitrogen-doped reduced graphene oxide, *Ceramics International*, (2021).
- [28] R. Kumar, S. Sahoo, E. Joanni, R.K. Singh, K. Maegawa, W.K. Tan, G. Kawamura, K.K. Kar, A. Matsuda, Heteroatom doped graphene engineering for energy storage and conversion, *Materials Today Communications*, 39 (2020) 47-65.
- [29] S.J. Lee, J. Theerthagiri, P. Nithyadharseni, P. Arunachalam, D. Balaji, A.M. Kumar, J. Madhavan, V. Mittal, M.Y. Choi, Heteroatom-doped graphene-based materials for sustainable energy applications: A review, *Renewable and Sustainable Energy Reviews* 143 (2021) 110849.
- [30] T. Zhu, S. Li, B. Ren, L. Zhang, L. Dong, L. Tan, Plasma-induced synthesis of boron and nitrogen co-doped reduced graphene oxide for super-capacitors, *Journal of Materials Science* 54 (2019) 9632-9642.
- [31] I.T. Kim, M.J. Song, Y.B. Kim, M.W. Shin, Microwave-hydrothermal synthesis of boron/nitrogen co-doped graphene as an efficient metal-free electrocatalyst for

oxygen reduction reaction, *International Journal of Hydrogen Energy* 41 (2016) 22026-22033.

[32] D.C. Marcano, D.V. Kosynkin, J.M. Berlin, A. Sinitskii, Z. Sun, A. Slesarev, L.B. Alemany, W. Lu, J.M. Tour, Improved synthesis of graphene oxide, *ACS Nano*, 4 (2010) 4806-4814.

[33] Z. Sun, Z. Yan, K. Yue, A. Li, L. Qian, Novel high-performance electromagnetic absorber based on Nitrogen/Boron co-doped reduced graphene oxide, *Composites Part B: Engineering*, 196 (2020) 108132.

[34] C. Yu, H. Fang, Z. Liu, H. Hu, X. Meng, J. Qiu, Chemically grafting graphene oxide to B, N co-doped graphene via ionic liquid and their superior performance for triiodide reduction, *Nano Energy*, 25 (2016) 184-192.

[35] W. Cheng, X. Liu, N. Li, J. Han, S. Li, S. Yu, Boron-doped graphene as a metal-free catalyst for gas-phase oxidation of benzyl alcohol to benzaldehyde, *RSC advances*, 8 (2018) 11222-11229.

[36] H. Fang, C. Yu, T. Ma, J. Qiu, Boron-doped graphene as a high-efficiency counter electrode for dye-sensitized solar cells, *Chemical Communications*, 50 (2014) 3328-3330.

[37] Y. Wang, C. Wang, Y. Wang, H. Liu, Z. Huang, Boric acid assisted reduction of graphene oxide: a promising material for sodium-ion batteries, *ACS Applied Materials & Interfaces*, 8 (2016) 18860-18866.

[38] W. Cheng, X. Liu, N. Li, J. Han, S. Li, S. Yu, Boron-doped graphene as a metal-free catalyst for gas-phase oxidation of benzyl alcohol to benzaldehyde, *RSC Adv.*, 8 (2018) 11222-11229.

[39] H. Fang, C. Yu, T. Ma, J. Qiu, Boron-doped graphene as a high-efficiency counter electrode for dye-sensitized solar cells, *Chem. Commun.*, 50 (2014) 3328-3330.

[40] Z.S. Wu, A. Winter, L. Chen, Y. Sun, A. Turchanin, X. Feng, K. Müllen, Three-dimensional nitrogen and boron co-doped graphene for high-performance all-solid-state supercapacitors, *Advanced Materials*, 24 (2012) 5130-5135.

[41] Z. Ling, Z. Wang, M. Zhang, C. Yu, G. Wang, Y. Dong, S. Liu, Y. Wang, J. Qiu, Sustainable synthesis and assembly of biomass-derived B/N co-doped carbon

nanosheets with ultrahigh aspect ratio for high-performance supercapacitors, *Advanced Functional Materials*, 26 (2016) 111-119.

[42] B. Jaleh, A. Jabbari, Evaluation of reduced graphene oxide/ZnO effect on properties of PVDF nanocomposite films, *Applied Surface Science*, 320 (2014) 339-347.

[43] N. Soin, D. Boyer, K. Prashanthi, S. Sharma, A.A. Narasimulu, J. Luo, T.H. Shah, E. Siores, T. Thundat, Exclusive self-aligned β -phase PVDF films with abnormal piezoelectric coefficient prepared via phase inversion, *Chem. Commun.*, 51 (2015) 8257-8260.

[44] X. Cai, T. Lei, D. Sun, L. Lin, A critical analysis of the α , β and γ phases in poly (vinylidene fluoride) using FTIR, *RSC Advances*, 7 (2017) 15382-15389.

[45] P. Martins, A. Lopes, S. Lanceros-Mendez, Electroactive phases of poly (vinylidene fluoride): Determination, processing and applications, *Progress in Polymer Science*, 39 (2014) 683-706.

[46] K. Shi, B. Sun, X. Huang, P. Jiang, Synergistic effect of graphene nanosheet and BaTiO₃ nanoparticles on performance enhancement of electrospun PVDF nanofiber mat for flexible piezoelectric nanogenerators, *Nano Energy*, 52 (2018) 153-162.

[47] M.T. Ong, E.J. Reed, Engineered piezoelectricity in graphene, *ACS Nano*, 6 (2012) 1387-1394.

[48] X. Yang, W.A. Daoud, Synergetic effects in composite-based flexible hybrid mechanical energy harvesting generator, *J. Mater. Chem. A*, 5 (2017) 9113-9121.

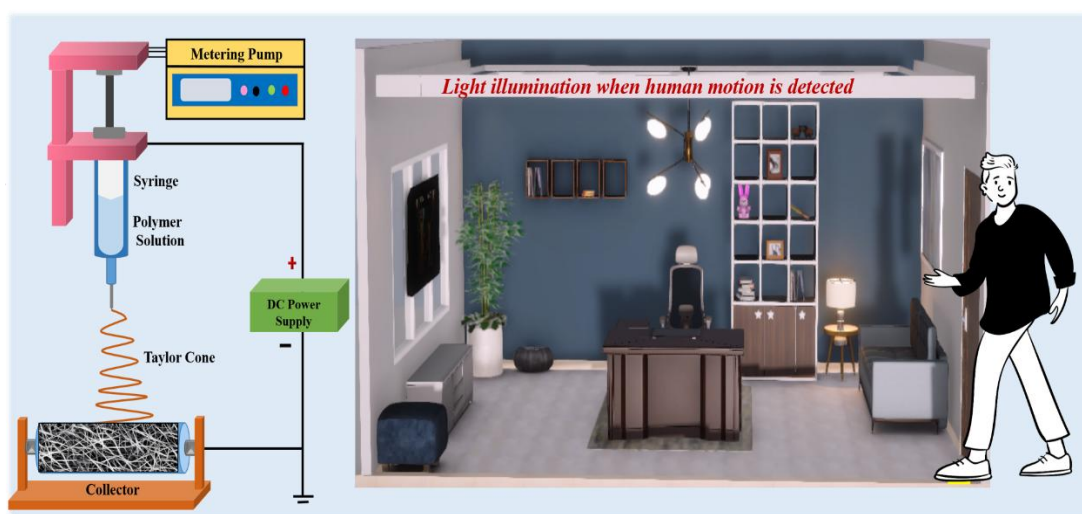
[49] X. Li, Z.-H. Lin, G. Cheng, X. Wen, Y. Liu, S. Niu, Z.L. Wang, 3D fiber-based hybrid nanogenerator for energy harvesting and as a self-powered pressure sensor, *ACS Nano*, 8 (2014) 10674-10681.

[50] H. Kuang, Y. Li, S. Huang, L. Shi, Z. Zhou, C. Gao, X. Zeng, R. Pandey, X. Wang, S. Dong, Piezoelectric boron nitride nanosheets for high performance energy harvesting devices, *Nano Energy*, 80 (2021) 105561.

[51] S. Sriphan, T. Charoonsuk, T. Maluangnont, N. Vittayakorn, High-performance hybridized composited-based piezoelectric and triboelectric nanogenerators based on BaTiO₃/PDMS composite film modified with TiO₂ nanosheets and silver nanopowders cofillers, *ACS Appl. Energy Mater.*, 2 (2019) 3840-3850.

CHAPTER 4

Synergistic effect of N-doped rGO nanofillers concentration and electrospinning technique on the output performance of PVDF nanocomposite based triboelectric nanogenerator for self-powered electronics and wireless sensor applications



As the power generated by piezoelectric nanogenerators (PENG) is insufficient to drive electronic devices, the present chapter will focus on the fabrication of highly efficient triboelectric nanogenerators (TENG) to harvest ambient mechanical. Specifically, two distinct strategies have been employed to enhance the performance of TENG. The first method involves incorporation of conductive nanofillers, such as reduced graphene oxide (rGO) and nitrogen-doped rGO (N-rGO), while the second approach focuses on modifying the morphology of the triboelectric layer using electrospinning techniques. By combining the electrical conductivity of rGO/N-rGO and the tailored nanostructured morphology of electrospun PVDF fibers, the chapter investigates how these strategies can improve energy harvesting efficiency. This study systematically examines the influence of nanofiller concentration and fiber morphology on the triboelectric properties of the TENG, aiming to optimize performance parameters. Additionally, the chapter highlights the potential of these TENGs in powering portable electronics and smart systems, such as motion sensors for IoT applications. This work provides valuable insights into the development of efficient, flexible, and sustainable power sources for the next generation of wearable and wireless technologies.

4.1 rGO Embedded Polymer Nanocomposite Layer for Improved Performance of Triboelectric Nanogenerator

4.1.1 Introduction

The global energy crisis with the technological advancement and increase in human population has become one of the major problem that motivated the researchers all around the world to actively seek for innovative solutions to generate electricity from unconventional renewable energy sources. In light of this, various technologies have been developed and studies are still ongoing to harvest energy from sustainable energy sources, such as, solar, thermal, vibration, wind etc.[1-4] Among these technologies, TENG operating on principle of triboelectrification and electrostatic induction have garnered considerable attention as an innovative technology which converts mechanical energy from diverse sources into electrical energy. Because of its working principle, TENGs possess several advantages over other energy harvesting device due to their outstanding performance in energy harvester with strong output signal, cost-effectiveness, robustness, simple design, and abundant choice of materials[5-7]. Also, it is well known that the surface charge density of triboelectric materials has a significant impact on TENG output performance. Therefore, various methods have been adopted by the researchers to improve TENG performance. Among, the various approaches, two major approaches are: first one is to select a suitable friction material with markedly different polarities and structural optimization as the performance of the device highly depends on structure and material selection. The other method includes the surface modification with micro/nanostructures formation, doping composition, and charge injection to improve and regulate the friction ignition effect[8-10]. A lot of materials organic, inorganic, polymer etc. have been explored since the invention of TENG in 2012 and their triboelectric series have been made, in which polymers currently dominates the triboelectric series due to their high charge transfer capacity[11, 12]. PVDF is one of the most versatile polymer which serve as negative triboelectric layer in TENG due to its high electronegativity, and flexibility, which keeps PVDF in the frontline of polymer to integrate with TENG[13-15]. Till now, several methods have been used to boost the performance of PVDF based TENG by electrospinning, microstructure formation, porous structure formation which increases the effective

contact surface area of PVDF[16]. Another, possible way to enhance the output performance of the PVDF based TENG is the addition of optimized concentration of nanofillers in polymer matrix [17-19]. For this it has been observed that reduced graphene oxide is preferred over the other materials because of its electron trapping capabilities, good conductivity, and higher electronegativity which helps in efficiently capturing external electrons.

Hence, in this study, we propose a polymer composite film based TENG by coupling of PVDF nanocomposite film with the nylon film. The rGO nanosheets with different weight percentage (0.5, 1.0, 1.5, 2.0 wt%) are incorporated into the PVDF polymer matrix and subjected to structural and morphological characterization to confirm successful doping of nanofiller into polymer matrix. The TENG's electrical output performance is optimized by subjecting it to tapping via a dynamic shaker at different force and frequency parameters. A maximum voltage, and current of 95.9 V, and 16.8 μ A is produced by device with 1.5 wt% of rGO. Furthermore, the device's ability to harvest energy is showcased through capacitor charging and powering of LEDs. Thus, the present studies demonstrate an easy and efficient approach for boosting TENG's performance by addition of the nanofillers and extend its potential application in self-powered and wearable devices.

4.1.2 Experimental Details

In the present study rGO is synthesized using hydrothermal method as reported in our previous study[21].

4.1.2.1 Synthesis of PVDF and PVDF/rGO Nanocomposite Films

For the synthesis of PVDF polymer nanocomposites films firstly, various weight percentages of synthesized rGO (0.5, 1.0, 1.5 and 2.0 wt%) are mixed in 10 ml of N, N-dimethylformamide and stirred vigorously until rGO completely disperse in the solvent. Then, 1gm of the PVDF powder is slowly added to the prepared solution of rGO dispersed DMF and stir for 30 minutes to form a homogenous composite solution. Using a micropipette, the prepared solutions is drop casted onto the glass substrate and dried in oven at 90° C. After natural cooling down, the films were immersed in distilled

water to obtain the free standing composite films. The same procedure is used for synthesis of the PVDF film without addition of the rGO.

The nylon films are synthesized by the phase-inversion processes reported by Soin et al.[22]

4.1.2.2 Fabrication of TENG

Furthermore, TENG device is fabricated by assembling the PVDF and PVDF/rGO nanocomposite with the nylon film in vertical contact-separation mode. For this, as prepared PVDF/rGO nanocomposite and nylon films are cut into 2x2 cm² and used as the two active triboelectric layers. Aluminum tape is applied to the back side of each film to act as electrodes, while copper wire is utilized to establish electrical connections.

4.1.3 Results and Discussion

4.1.3.1 Material Characterization

Several characterizations techniques are used to confirm successful synthesis of reduced graphene oxide (rGO).

Initially, different concentration of rGO (0.0, 0.5, 1.0, 1.5, and 2.0 wt%) are mixed with PVDF to form the polymer nanocomposite films and are labelled as P, PR1, PR2, PR3, and PR4 respectively. The crystallinity of PVDF and its composite films with varied concentration of rGO (0, 0.5, 1.0, 1.5, and 2.0 wt%) are analyzed by the X-ray diffraction measurements (Figure 4.1.1 (a)). All the films exhibit two characteristic peak at diffraction angle of $2\theta = 18.3^\circ$ and 20.4° respectively. The peak at 18.3° corresponds to (020) reflection plane and is associated with α phase, whereas peak at 20.4° is attributed to β phase of (110/200) reflection plane [23, 24]. As we increase the concentration of rGO, the peak intensity associated with the β phase rises, but it falls after 1.5 wt %. Furthermore, the peak conforming to rGO is not observed in XRD spectra, which may be due to relatively lower diffraction intensity and lower concentration of rGO in PVDF nanocomposite film. For, further better understanding of crystallographic phase in polymer nanocomposite films, FTIR spectroscopy is further used to quantify rise in the content of β phase of PVDF after doping it with

rGO. Figure 4.1.1 (b) shows that several vibrational groups are present in FTIR spectra of films and absorbance peaks corresponding to different phases (α , β , and γ phase) are indicated in the spectra[25]. Moreover, when we dope rGO in the polymer matrix, the intensity of peak corresponding to non-polar α phase got diminished and relative fraction of electroactive polar β phase is determined using the following equation (4.1.1)

$$F(\beta) = \frac{A_{\beta}}{1.26A_{\alpha} + A_{\beta}} \times 100\% \quad (4.1.1)$$

Where, A_{α} and A_{β} are the absorption intensities at 762 and 840 cm^{-1} respectively. The calculated value of relative fraction of electroactive polar phase $F(\beta)$ of prepared samples P, PR1, PR2, PR3, and PR4 are 58%, 64.4%, 71.1%, 77.1%, and 75.3% respectively and corresponding results are illustrated in Figure 4.1.1 (c).

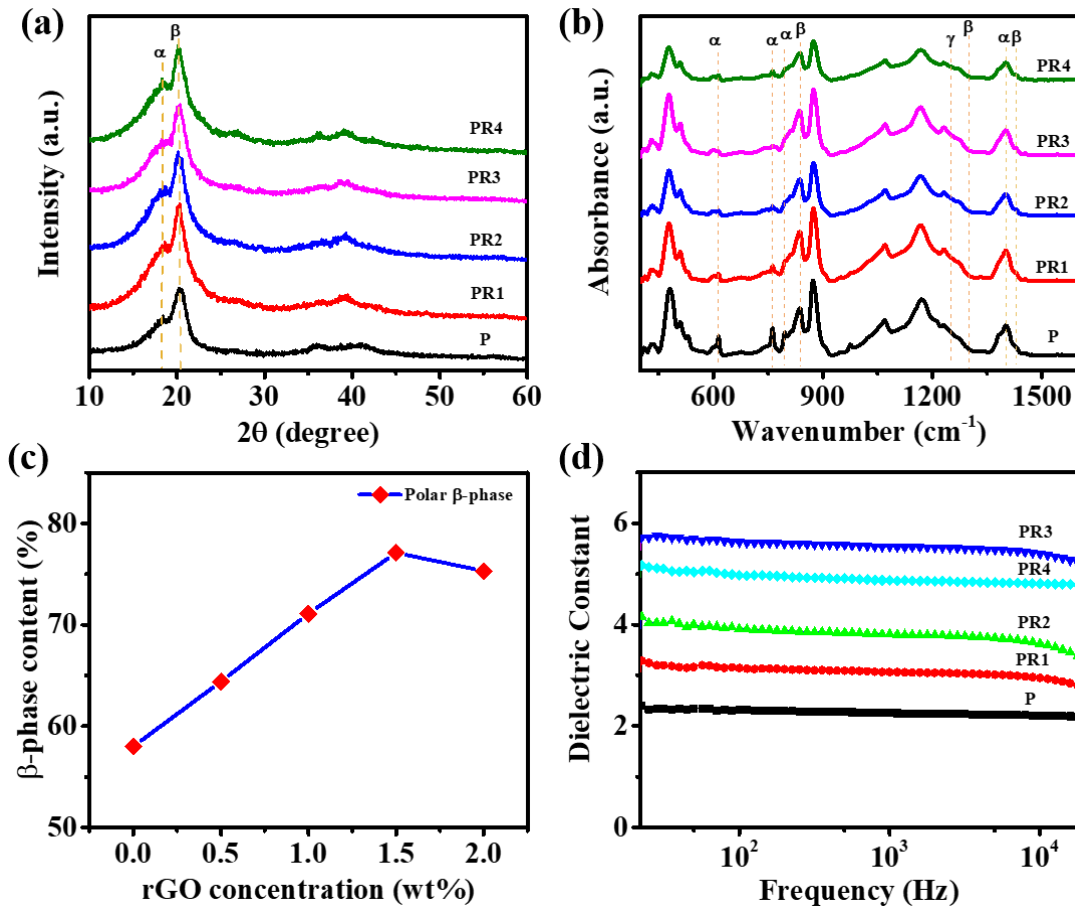


Figure 4.1.1 (a) XRD pattern, (b) FTIR spectra, (c) content of electroactive polar β phase and (d) dielectric constant of PVDF nanocomposite films with different weight percentage of rGO.

The percentage of β phase content in PVDF nanocomposite films is enhanced significantly with increase in rGO concentration upto 1.5 wt%, and further addition of the nanofillers reduces its value. The possible reason behind initial increase in the value of $F(\beta)$ upto certain concentration and thereafter decreases can be understood by the fact that when we add rGO in PVDF matrix, the crystallinity of nanocomposites first increases due to the interaction between surface charges (i.e. oxygen containing functional group and delocalized π electron) of rGO with the CH_2 and CF_2 dipoles of PVDF which helps in gradual enhancement in the nucleation of polar β phase by maximizing all trans (TTTT) molecular conformation[21, 26]. But, after certain concentration of rGO nanosheets (i.e. 1.5 wt% in our case), the alignment of the polymer chain got disturbed resulting in suppressing tendency of β phase formation, which arise because of poor dipole arrangement in PVDF chain[24, 27]. Also, it has been reported in the literature that, dielectric constant of the triboelectric material is an important property which helps in improving TENGs device performance. Therefore, the dielectric constant of PVDF and its composite films are measured as a function of frequency with the help of LCR meter (Figure 4.1.1 (d)). With increases in the rGO concentration the dielectric constant of the PVDF film increases from 2.4 to 3.3, 4.1, 5.7 and 5.2 corresponding to the 0.5, 1.0, 1.5, and 2.0 wt% of rGO nanofillers. As expected 1.5 wt% (i.e. PR3) have maximum dielectric constant which is consistent with the XRD and FTIR studies. This increase in dielectric constant value after addition of nanofillers is due to formation of microscopic dipole and a network of microcapacitors which increases capacitance of nanocomposite film. However, the subsequent decrease in value from 1.5 to 2.0 wt% occurs due to the establishment of a conductive pathway, leading to a reduction in the films capacitance. Hence, 1.5 wt% of the nanofillers is the optimum amount for generation and retention of significant quantity of triboelectric charges on dielectric layer. The surface morphology of PVDF and its composite films with varied concentration of rGO is illustrated in Figure 4.1.2 (a-e). It can be clearly seen from the figures that rGO nanosheets are uniformly dispersed within the PVDF matrix without any agglomeration of rGO nanosheets.

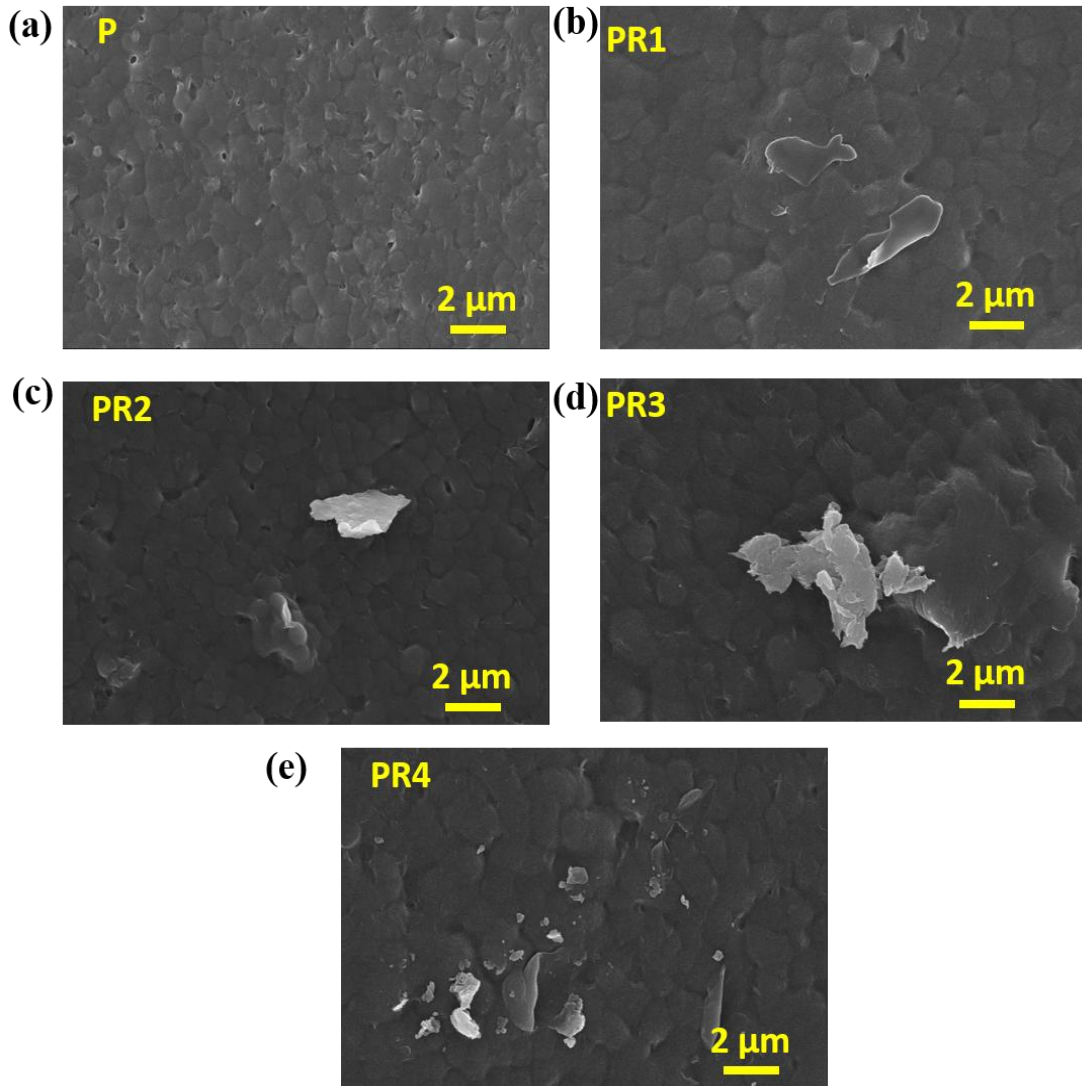


Figure 4.1.2 FESEM micrographs of (a-e) PVDF and PVDF nanocomposite films with varied concentration of rGO.

4.1.3.2 Electrical Characterization of TENG

TENG is fabricated by coupling of PVDF and PVDF-rGO nanocomposite films with nylon as two highly negative and positive triboelectric layers operating in a simple vertical contact separation mode. In order to assess TENG's performance, a series of tests are carried out systematically by tapping nanogenerator with the help of electrodynamic shaker. Initially, electrical outputs including, open-circuit voltage (V_{OC}), and short-circuit current (I_{sc}) are measured with different concentration of rGO as depicted in Figure 4.1.3 (a-b). TENG with 1.5 wt% loading amount of rGO (i.e. PR3

based TENG) generates the highest V_{OC} , and I_{SC} of 95.9 V, and 16.8 μA in contrast to pristine PVDF based TENG which can generate V_{OC} , and I_{SC} of 35.4 V, and 2.3 μA . While, PR1, PR2, and PR4 film based nanogenerator can produce V_{OC} , I_{SC} of 48.1 V, 74.9 V, 81.9 V, 5.4 μA , 8.9 μA , and 12.7 μA respectively.

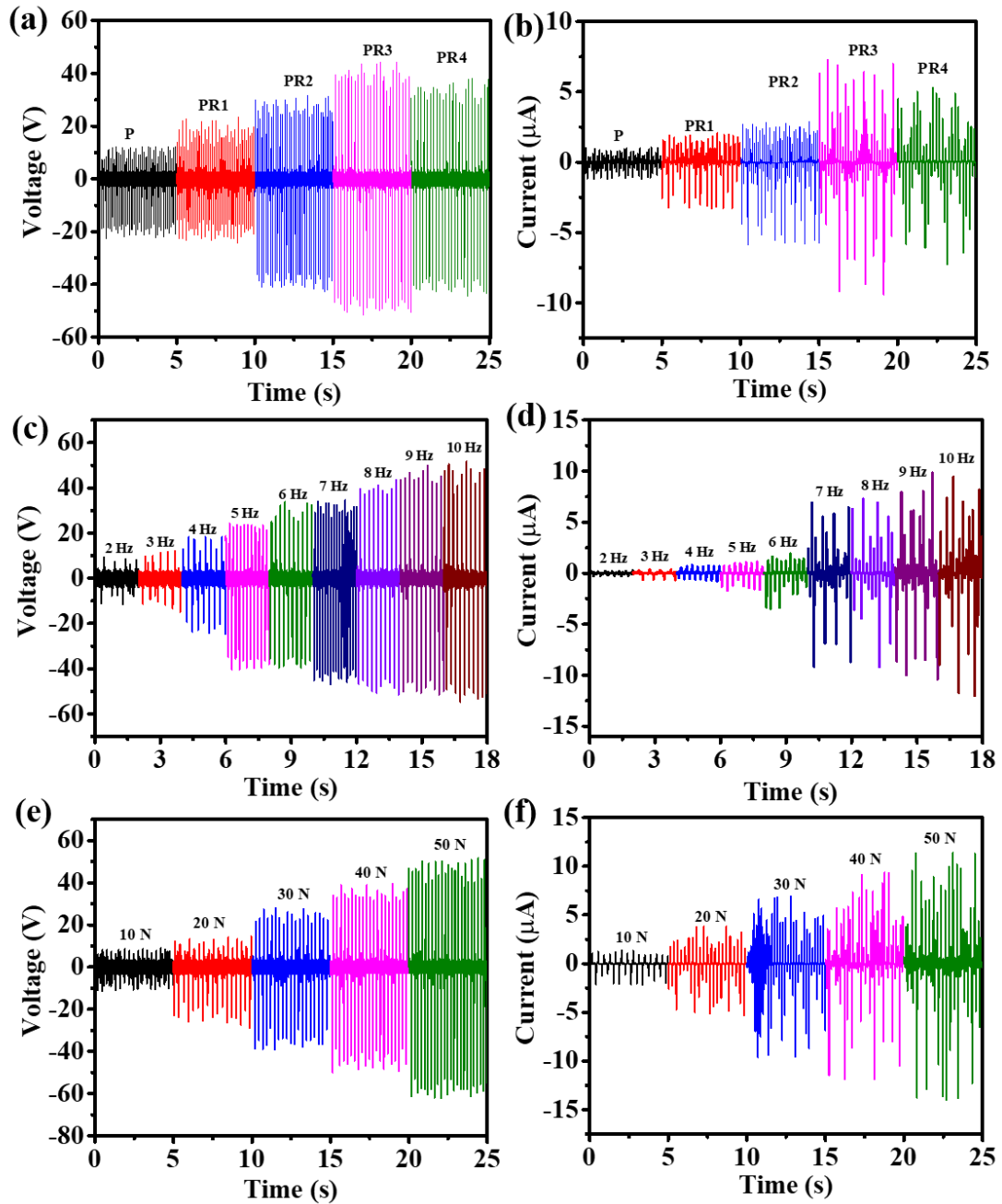


Figure 4.1.3 Measured open-circuit voltage, and short-circuit current waveforms of the TENG obtained by (a-b) varying the concentration of rGO in PVDF, (c-d) by varying input frequency, and (e-f) impact force on the TENG with 1.5 wt% of rGO.

The maximum output performance of 1.5 wt% of rGO is also supported by the FTIR and dielectric studies which shows maximum content of β phase and dielectric constant corresponding to 1.5 wt% of rGO doping in PVDF matrix. Moreover, the impact of input excitation force and frequency on TENG output performance with 1.5 wt % of rGO (PR3) is also investigated and the corresponding V_{OC} , and I_{SC} waveforms are shown in Figure 4.1.3 (c-d). The frequency of tapping is also varied from 2 Hz to 10 Hz, with a highest value of voltage and current of ~ 107 V and $22 \mu\text{A}$ is attained at 10 Hz frequency. In the same way, the impact of applied force on the output capabilities of the TENG with 1.5 wt% rGO is explored through force variations ranging from 10 N to 50 N (Figure 4.1.3 (e-f)). At a forceful impact of 50 N, the TENG yields a maximum voltage and current of around 113 V and $20 \mu\text{A}$, respectively. It is clearly illustrated from the Figure 4.1.3 (c-f) that both the frequency and force follows similar rising pattern for voltage, and current. The enhanced open-circuit voltage and short-circuit current in relation to operating frequency and force may be attributed to the following reasons. First, is the faster charge transfer at higher tapping frequency, secondly, when we increase the impact force, there is increase in the elastic deformation and effective contact area in the polymer nanocomposite film causing a rise in TENG capacitance which may be helpful in storing the more triboelectric charges, as a result improved the TENG performance[28, 29].

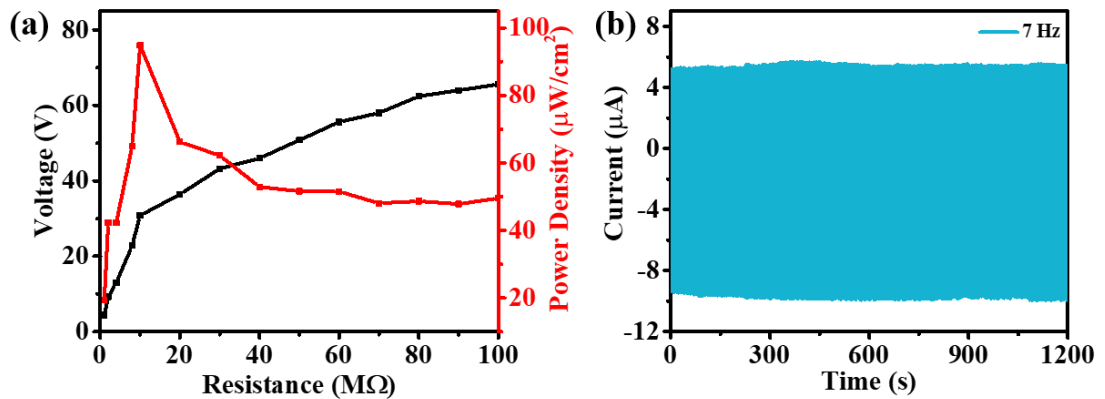


Figure 4.1.4 (a) Output voltage and power density measurements as a function of varied resistance, and (b) Durability of PVDF/rGO based TENG with 1.5 wt% of rGO.

To investigate the ideal output condition of the as-fabricated TENG, the generated voltage is also measured as a function of load resistance ranging from 1 $\text{M}\Omega$ to 100 $\text{M}\Omega$

as shown in Figure 4.1.4 (a). The optimal TENG can deliver a maximum power density of $\sim 95 \mu\text{W}/\text{cm}^2$ across a matching load resistance of $10 \text{ M}\Omega$. The durability of the as-fabricated TENG is illustrated in Figure 4.1.4 (b), which shows excellent stable cyclic operation of TENG over 1200 cycles with negligible change in the value of current. These results demonstrate that good durability of TENG for long-term applications.

4.1.4 Summary

In summary, we have successfully fabricated PVDF/rGO nanocomposite film based TENG and thoroughly examined the impact of rGO doping on TENG performance by coupling of PVDF nanocomposite films with the nylon film. The results showed that addition of rGO in PVDF matrix greatly improves nucleation of crystalline β -phase, dielectric and charge transfer property of PVDF film, resulting in the improved performance of the TENG device. A maximum voltage and current of 95.9 V, and 16.8 μA is obtained by PR3 film based TENG (i.e. 1.5 wt% of rGO), whereas pristine PVDF film based TENG can only generate 35.4 V voltage and 2.4 μA current. Also, this device produces a highest power density of $\sim 95 \mu\text{W}/\text{cm}^2$ when connected to matching load resistance.

4.2 PVDF/N-rGO Nanofibers based Sustainable Triboelectric Nanogenerator for Self-Powered Wireless Motion Sensor

4.2.1 Introduction

Triboelectric nanogenerator based on the conjunction of tribology and interfacial charge transfer is considered as a potential candidate for designing self-sufficient power system which can also operate as self-powered sensor by harvesting energy from various mechanical motions in our day to day life including human motion, vibration, water waves, friction, rotation etc.[13, 30] Beside this, TENG also bestow superior advantages over the other energy harvesting technologies such as high efficiency, diverse material choice, ease of fabrication, cost-effectiveness paving the way for developing self-powered system. Nevertheless, whether TENG is used as an energy harvesting module or self-powered sensors, the performance of TENG still requires further optimization to boost the energy conversion efficiency of device for practical applications.

In previous section, we have demonstrated that adding an optimal concentration of conducting nanofillers (i.e. rGO) can improve the output performance of PVDF based TENG due to its excellent electron trapping ability, higher electronegativity, optimal conductivity, and presence of different functional groups which helps in improving the charge trapping capabilities, dielectric properties and surface potential of the polymer materials[18, 26, 30, 41]. Moreover, nitrogen doping in graphene is also reported to increase the charge density, and induces interfacial capacitance, which can further boost the performance of the nanogenerator[42, 43]. In addition to incorporation of nanofillers, synthesizing polymer nanofibers are also reported to enhance the TENG performance by creating nanoscale roughness in the frictional layers which imparts unique characteristics, such as, enhanced effective surface area, hierarchically porous structure, and mechanical flexibility. Thus, by keeping in mind all aspects mentioned above, this study aims to design an efficient triboelectric nanogenerator. To achieve this, we employed two key strategies: the incorporation of nanofillers and the use of electrospinning techniques to enhance the nanogenerator's output performance. To achieve this, firstly PVDF and its nanocomposite films are synthesized via drop casting method with varied content of nitrogen doped rGO(N-rGO) to determine optimum concentration of N-rGO i.e. 1.5 wt% obtained from our measurements. After that nanofibers mat of PVDF and PVDF with 1.5 wt% of N-rGO are synthesized with

electrospun technique and coupled with nylon nanofiber mat to fabricate TENG with superior triboelectric performance. The results demonstrate that PVDF/N-rGO-Nylon nanofibers (NFs) delivers remarkable enhanced performance with an open-circuit voltage of 368 V, and short-circuit current of $\sim 35\mu\text{A}$ in comparison to PVDF-Nylon drop casted films based TENG which can only deliver output voltage and current of 92 V and $10\mu\text{A}$ respectively. Furthermore, energy harvesting capabilities of the fabricated TENG is evaluated and demonstrated by harnessing biomechanical energy from various human motions and powering various electronic devices, such as, LEDs, thermometer, watch, alarm clock and calculator through bridge rectifier. Besides energy harvester, TENG is also showcased as an active self-powered motion sensor, capable of automatically activating lights during night time. The results demonstrate the sustainable and efficient solution for energy harvesting and smart sensing applications.

4.2.2 Experimental Details

4.2.2.1 Synthesis of PVDF and PVDF/N-rGO Nanocomposite Films and Nanofibers

N-rGO is synthesized via hydrothermal method as reported in our previous paper[21]. Firstly, pristine PVDF and its nanocomposite films with varied content of N-rGO (0.25, 0.1, 0.5, 1, 1.5, and 2 wt%) are synthesized via the drop casting method. For this, different content of N-rGO is ultrasonically dispersed in 10 ml of DMF for 1 hour. Then, 1 gm PVDF is mixed thoroughly in the above-prepared solutions via magnetic stirring with PTFE bar for two hours to obtain a homogenous solution. The solutions are then drop-casted onto glass substrate and kept in oven at 90°C for two hours. Following natural cooling, coated glass substrates are immersed in the distilled water to obtain the freestanding films. For comparison, we have also prepared PVDF and PVDF nanocomposite films via electrospinning technique. To synthesize nanofibers, PVDF and PVDF/N-rGO (1.5 wt%) solution is filled in the 10 ml plastic syringe, and electrospinning is performed by VPD40CH electrospinning equipment, applying high voltage of 12 kV while maintaining a distance of 12 cm between syringe needle and aluminum collector, where the drum speed is set at 250 rpm. Moreover, the nanocomposite fiber mat is fabricated by electrospinning at a constant flow rate of 1 ml/h and under a relative humidity of approximately 35%. Finally, the nanofibers collected on the aluminum foil are oven-dried at 60°C overnight.

4.2.2.2 Synthesis of Nylon Film and Nanofibers

Nylon films are prepared by the phase-inversion process[22]. Furthermore, nanofibers of nylon are synthesized by dissolving nylon 6 pellets in the formic acid in 1:10 weight ratio by constantly stirring at 70°C for 3 hours. Subsequently, solution is filled in the 10 ml syringe and electrospinning is carried out at 25 KV supply voltage with flow rate of 0.5 ml/h maintaining a distance of 10 cm between needle and collector. Finally, the obtained nanofibers are dried in an oven to remove the remaining moisture content therein.

4.2.2.3 Fabrication of TENG

The electrospun PVDF/N-rGO nanofibers and Nylon nanofibers are employed as two opposite triboelectric materials for fabricating TENG to work in simple contact separation mode. Then both the PVDF/N-rGO and nylon nanofibers are cut in the requisite size i.e. 3x2 cm² and an aluminum tape is adhered on the back side of both materials to serve as an electrode followed by the external wiring connection with the copper wire for electrical measurements.

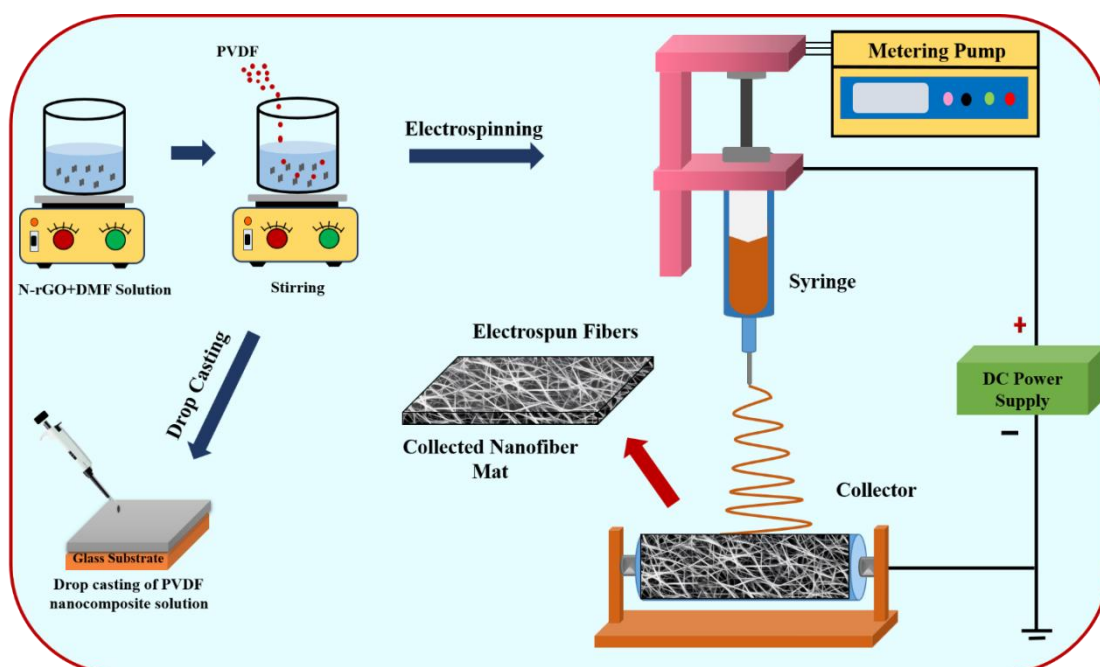


Figure 4.2.1 A schematic representation of step by step synthesis of PVDF and PVDF nanocomposite films prepared via drop casting and electrospinning method.

4.2.3 Results and Discussion

4.2.3.1 Materials Characterization

Figure 4.2.1 depicts the detailed synthesis procedure for fabrication of PVDF/N-rGO nanocomposite films via drop casting and electrospinning technique. The PVDF nanocomposite films are used as a negative triboelectric material owing to its strong ability to gain electrons because of presence of highly electronegative fluorine group, high mechanical stability, and biocompatibility, while nylon film is chosen for their high positive charge affinity and mechanical stability, and serve as a positive triboelectric layer. Thus, both PVDF nanocomposite films and nylon are utilized as active triboelectric materials in TENG fabrication. Furthermore, electrospinning of these polymeric solutions leads to formation of nanofibrous films with increased surface roughness and higher effective contact area, which increases accumulation of triboelectric surface charges, resulting into improved performance of TENG. The surface morphology of synthesized films and nanofibers are characterized via the field-emission scanning electron microscopy (FESEM). Figure 4.2.3 (a-f) depicts FESEM micrographs of drop-casted PVDF and PVDF nanocomposites films with different weight percentage of N-rGO (0.25, 0.5, 1, 1.5, 2 wt%) and their photographic image are shown in Figure 4.2.2.

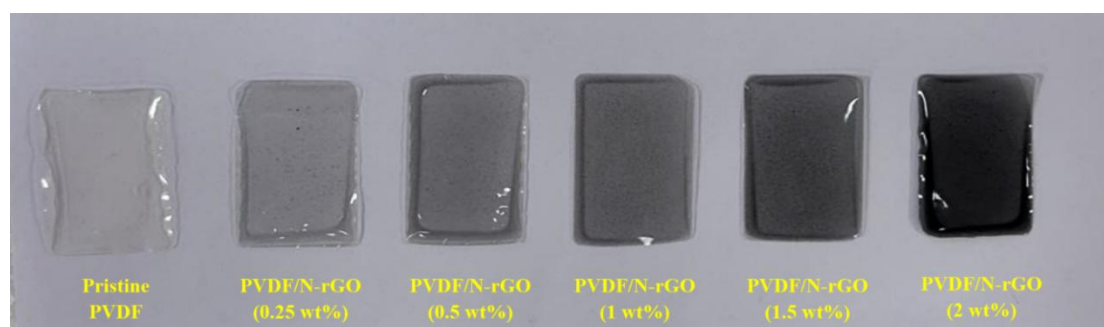


Figure 4.2.2 Photographic image of PVDF and PVDF nanocomposite films with different weight percentage of N-rGO prepared by drop-casting method.

The pure PVDF film exhibits smooth surface with few nanopores formed as a result of solvent evaporation during the phase inversion process. Furthermore, a uniform dispersion of N-rGO nanosheets in PVDF matrix is observed with doping of N-rGO in different concentration. Also, at higher concentration (2 wt%) of N-rGO, aggregation of N-rGO nanosheets have been observed, indicating 1.5 wt% is the ideal doping level.

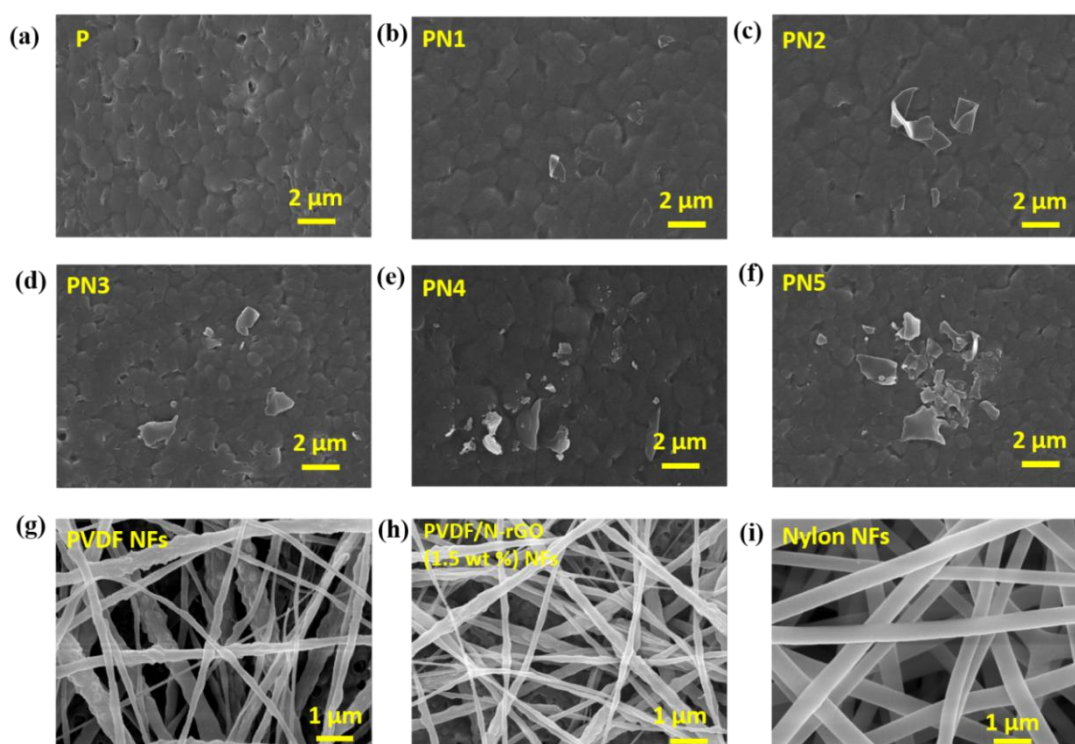


Figure 4.2.3 FESEM images of (a-f) drop casted PVDF and PVDF nanocomposite films with different weight percentage of N-rGO (0, 0.25, 0.5, 1, 1.5, and 2 wt%), and (g-i) electrospun PVDF, PVDF/N-rGO(1.5 wt%), and nylon nanofibers mat.

Moreover, to further verify the presence of N-rGO in the PVDF/N-rGO films, EDAX analysis was performed, and the corresponding spectra are shown in Figure 4.2.4- Figure 4.2.8. The results reveal that the pure PVDF film contains only carbon and fluorine, while the PVDF/N-rGO nanocomposite films also exhibit additional elements, namely oxygen and nitrogen. Furthermore, as the N-rGO content increases, the nitrogen content in the nanocomposite films rises accordingly. The increasing nitrogen concentration confirms the successful incorporation of N-rGO in films with varying blend ratios.

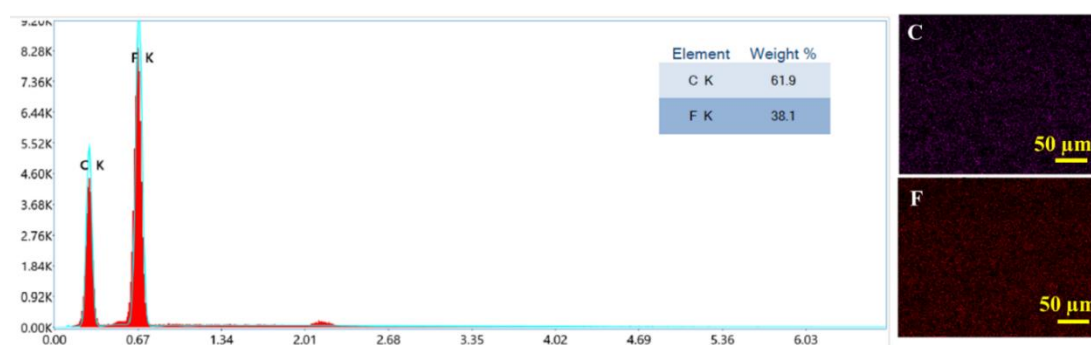


Figure 4.2.4 EDAX spectrum with the elemental mapping image of all elements present in PVDF film.

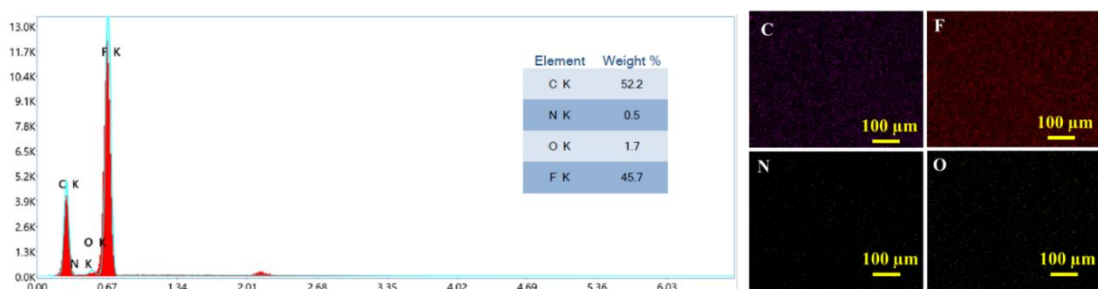


Figure 4.2.5 EDAX spectrum with the elemental mapping image of all elements present in PVDF/N-rGO film with 0.5 wt % of N-rGO.

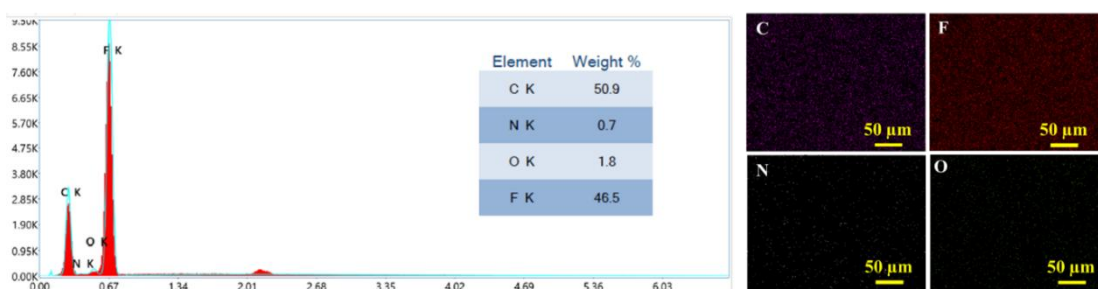


Figure 4.2.6 EDX spectrum with the elemental mapping image of all elements present in PVDF/N-rGO film with 1 wt % of N-rGO.

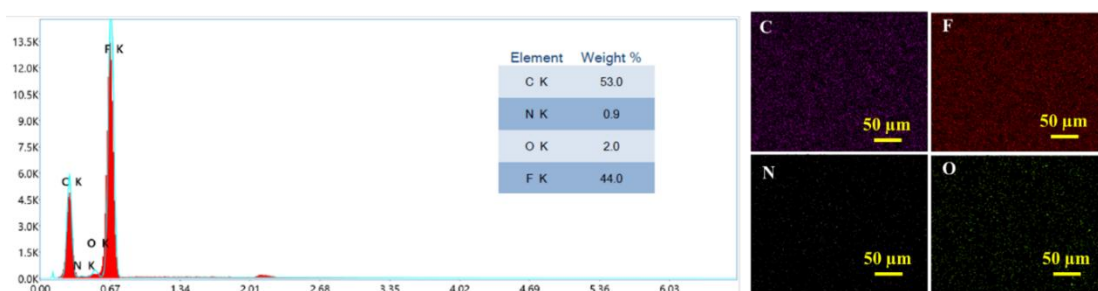


Figure 4.2.7 EDX spectrum with the elemental mapping image of all elements present in PVDF/N-rGO film with 1.5 wt % of N-rGO.

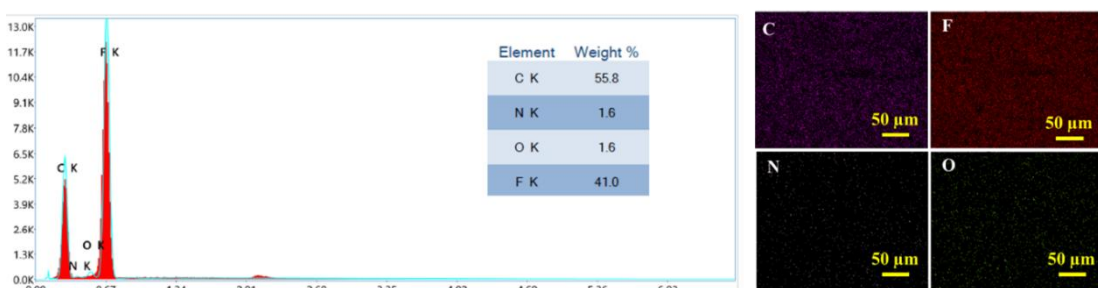


Figure 4.2.8 EDX spectrum with the elemental mapping image of all elements present in PVDF/N-rGO film with 2 wt % of N-rGO.

The FESEM images of PVDF, PVDF/N-rGO (1.5 wt%), and nylon nanofibers shown above in Figure 4.2.3 (g-i) exhibit the formation of bead free fibrous network without aggregation of nanosheets in the PVDF nanocomposite films, suggesting that the electrospinning parameters selected in this study are optimum. Moreover, a small decrease in the diameter of nanofibers is also observed after introduction of the N-rGO in the polymer solution, which may be attributed to enhanced charge density of polymeric solution, resulting in fiber stretching during electrospinning process[31]. Moreover, to examine the influence of doping and electrospinning on crystalline structure and properties of polymer film, XRD, FTIR and dielectric measurements are also carried out.

The XRD pattern of pristine PVDF and PVDF composite films and nanofibers mat is displayed in Figure 4.2.9 (a). As illustrated in the figure, all the samples exhibit two diffraction peaks corresponding to α and β -phase. The main diffraction peak observed at $2\theta=20.2^\circ$, corresponds to (200)/(110) plane of crystalline β -phase and a less intense peak at $2\theta= 18.4^\circ$ belongs to (111) plane is ascribed to the non-polar α phase of PVDF. Moreover, observations from the XRD plot indicate a slight increase in the intensity of the peak associated with the polar electroactive phase in nanocomposite films in comparison to pristine PVDF film. This suggests that the incorporation of N-rGO into PVDF matrix, stimulates nucleation of polar β phase. Also, no peaks corresponding to N-rGO is seen in XRD pattern, this could be due to presence of very low content of N-rGO in nanocomposite films[32]. In addition to this, the intensity of the peak corresponding to polar β -phase is further increased for both electrospun PVDF and PVDF/N-rGO nanofiber mat. This may be attributed to uniaxial stretching of PVDF solution during the course of electrospinning because of electrostatic repulsion between the surface charges across jet in applied electric field which leads to transition from non-polar α - phase to electroactive polar β -phase.

To further verify these results, FTIR analysis is carried out to quantify the increase in crystalline β -phase. Figure 4.2.9 (b) depicts, FTIR spectra of PVDF, PVDF nanocomposite films and fibers mat. The vibrational bands at 613, 762, 796, 974, 1382 cm^{-1} are designated to nonpolar α -phase of PVDF, while characteristic vibrational bands around 840, 1279, and 1400 cm^{-1} are attributed to electroactive polar β -phase [25, 33].

The characteristic vibrational band around 840 cm^{-1} is attributed to mixed mode of CF_2 asymmetric stretching and CH_2 rocking vibrations.

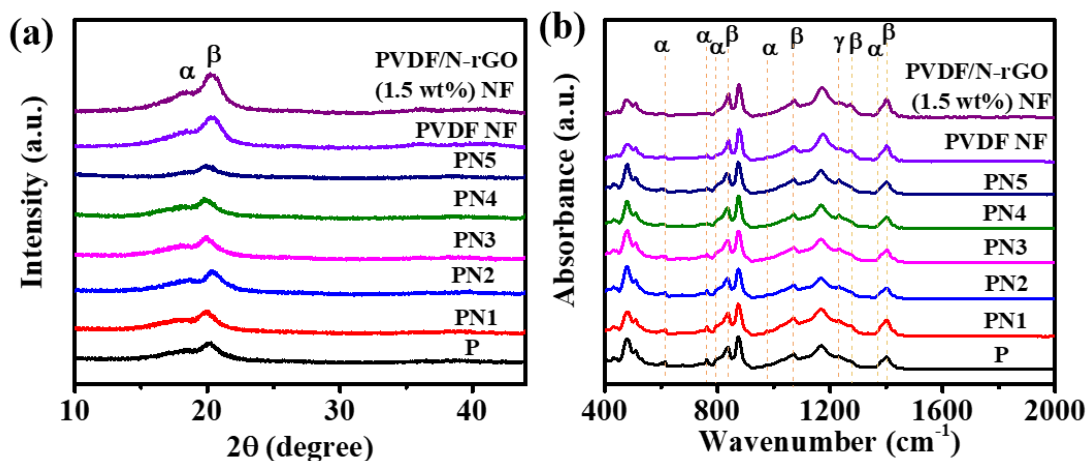


Figure 4.2.9 (a) XRD, and (b) FTIR, analysis of drop casted PVDF, and PVDF nanocomposite films with different weight percentage of N-rGO (0, 0.25, 0.5, 1, 1.5, and 2 wt%) and electrospun PVDF and PVDF/N-rGO (1.5 wt%) nanofibers prepared by electrospinning technique

It should be noted that compared to pristine PVDF film, the intensity of characteristic peak of α phase at 762 cm^{-1} assigned to $\text{C(F)}\text{-C(H)}\text{-C(F)}$ skeletal bending and CH_2 rocking sharply decreases after addition of N-rGO in PVDF matrix demonstrating significant role of N-rGO doping in the development of crystalline β -phase. Furthermore, Lambert-Beer law is utilized to determine the relative fraction of β -phase ($F(\beta)$) in polymer nanocomposite films. The value of relative fraction of β -phase in polymer composite films experience a rise in the value from 59.8 % to 74.6 % as the content of N-rGO varies from 0 to 1.5 wt%, thereafter its value decreases. The initial increase in the value of $F(\beta)$ up to a certain concentration, followed by a decrease can be attributed to the interaction dynamics within the PVDF/N-rGO matrix[34]. The initial increase in the crystallinity after introduction of N-rGO stems from the interaction between CH_2 and CF_2 dipoles of PVDF with the local electric field around the filler, which helps in nucleation of polar β phase by promoting the maximization of the all-trans (TTTT) molecular conformation. However, beyond a specific concentration of N-rGO (i.e. 1.5 wt%), the alignment of the polymer chains becomes disrupted which hinders the propensity for β -phase formation by diminishing dipole arrangement within the PVDF chain. Furthermore, similar results are obtained for the electrospun nanofiber,

where the value of $F(\beta)$ can reach upto 79.6 % in PVDF/N-rGO nanofiber. These results illustrate that both the inclusion of nanofillers and the utilization of electrospinning techniques are effective strategies for stimulating the formation of electroactive β -phase of PVDF.

As we know that the TENG performance is highly influenced by the transferred charge density, which is dependent on dielectric property, and surface potential and surface roughness of the material used in TENG fabrication[29]. Therefore, dielectric constant of PVDF and its composite films with different concentration of N-rGO is measured. Figure 4.2.10 illustrate dielectric constant of PVDF film as a function of frequency where increase in the content of N-rGO (0 to 1.5 wt%), results in rise of dielectric constant from 2.7 to 4.5, 5.6, 7.05, and 10.8 respectively.

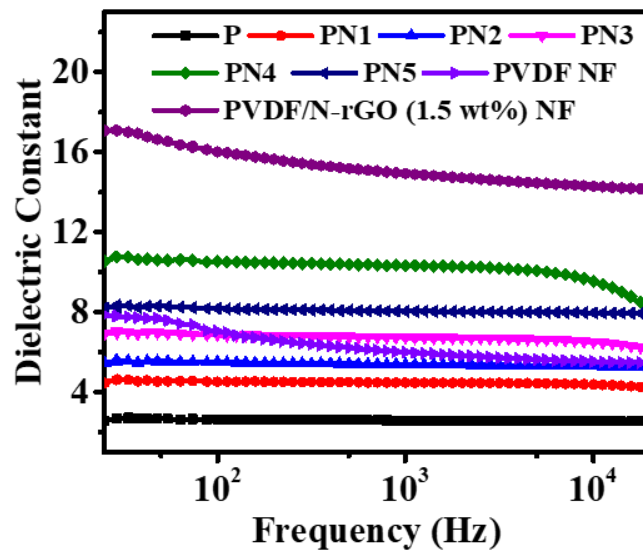


Figure 4.2.10 Dielectric constant measurements of drop casted and electrospun PVDF, and PVDF nanocomposite films/nanofibers.

Moreover, the value of dielectric constant further increases from 7.9 to 17.2 in PVDF composite nanofiber mat. The rise in dielectric constant may be attributed to following fact: firstly, incorporation of conducting nanofillers in the polymer matrix results into formation of micro capacitor network in PVDF film which enhanced the capacitance of nanocomposite films. Another possible reason is the polarizability of the PVDF upon application of the electric field, which results in the formation of dipoles between N-rGO surface atoms in PVDF chain[29]. Furthermore, a slight decrement in the dielectric

constant to 8.3 is observed for 2 wt% N-rGO sample and is attributed to the percolation limit of PVDF/N-rGO nanocomposite[29, 35, 36]. Hence, 1.5 wt% N-rGO is considered as optimal concentration for efficient charge transportation due to increase in conductivity of nanocomposite films which improve charge density of nanogenerator.

Furthermore, to better understand the influence of doping and electrospinning on surface potential and charge transfer mechanism between two triboactive polymer films, Kelvin Probe Force Microscopy (KPFM) measurements are performed. Figure 4.2.11 (a-f) display the surface potential maps of drop casted films and electrospun nanofibers made of polymer and polymer N-rGO nanocomposite materials, across a $2\ \mu\text{m} \times 2\ \mu\text{m}$ surface. The relative value of surface potential (V_{CPD}) of PVDF film is 1.33V, whereas addition of N-rGO (1.5 wt%) in PVDF induce a shift in surface potential of PVDF towards negative value. The value of V_{CPD} measured for PVDF/N-rGO film is 0.96 V. Besides this, the value of V_{CPD} obtained for nylon film is 2.76 V.

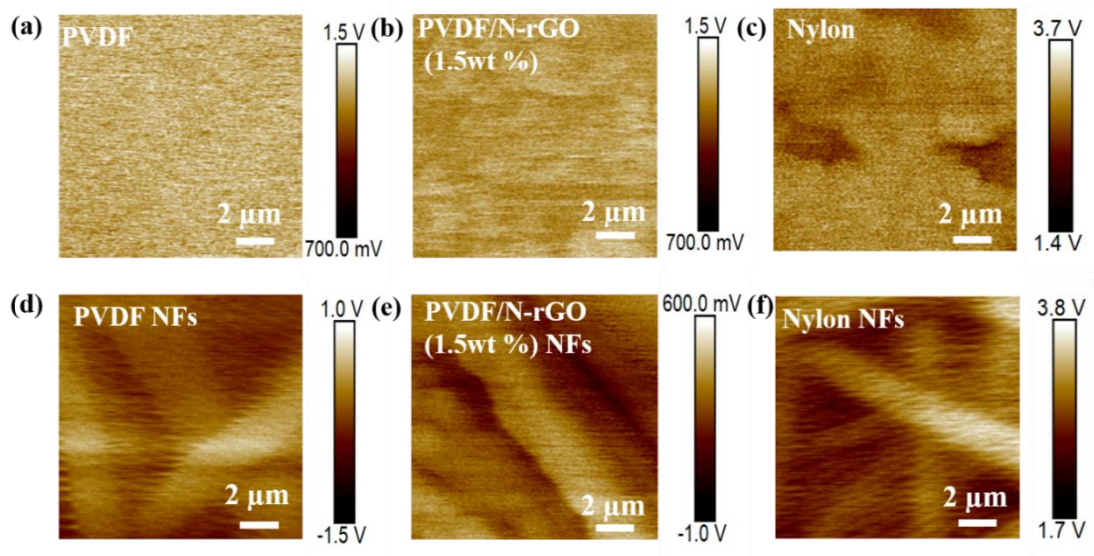


Figure 4.2.11 (a-f) KPFM surface potential mapping of pristine PVDF, PVDF/N-rGO (1.5 wt%) and nylon films and electrospun nanofibers mat scanned over a surface of $2 \times 2\ \mu\text{m}^2$.

Consequently, the potential difference (ΔV_{CPD}) between two triboelectric layers, increases from 1.43 V for nylon /PVDF to 1.8 V for nylon/PVDF/N-rGO films. The increase in the ΔV_{CPD} in case of PVDF nanocomposite film is due to increase in surface roughness, polarization after addition of nanofillers which increases charge trapping

capabilities of the nanocomposite film[28, 37]. Similar results have been obtained for the PVDF and PVDF/N-rGO nanofibers, where the value of V_{CPD} obtained for PVDF, and PVDF/N-rGO (1.5 wt%) nanofibers mat are 1.27 V, and 0.62 V, while for nylon fiber the value of V_{CPD} obtained 2.91V. In case of nanofibers, ΔV_{CPD} further enhanced from 1.64 V for pure PVDF to 2.28 V after addition of N-rGO.

In TENG, more is the potential difference between two materials, higher charge transfer will occur to attain an equilibrium state thereby, enhancing the output performance of nanogenerator. Therefore, charge transfer behavior is an important parameter to determine the voltage generated and to know about the triboelectric polarities of the materials. The charge transfer process strongly relies on work function and potential difference between two materials, therefore the work function of all the materials is also calculated to confirm the direction of charge flow. The work function difference between sample and tip is given by following equation

$$\phi(sample) = \phi(tip) - eV_{CPD} \quad (4.2.1)$$

where, $\phi(sample)$ is work function of the triboelectric material, $\phi(tip)$ is work function of tip, e is electronic charge. The calculated value of work function of drop casted PVDF, PVDF/N-rGO and nylon films are 4.26, 4.64 and 2.69 respectively, whereas the value of work function obtained for electrospun nanofibers of PVDF, PVDF/N-rGO and nylon are 4.33, 4.9 and 2.89 respectively. In both the cases, nylon have smallest work function potential in comparison to PVDF and PVDF nanocomposite films/nanofibers. Therefore, flow of electrons from nylon to PVDF and PVDF/N-rGO will take place when they come in contact with each other to equalize the fermi level difference as shown in energy band diagram (Figure 4.2.12 (a))[38]. As a result, PVDF and PVDF/N-rGO experiences negative charge electrification while nylon surface experiences positive charge electrification. Additionally, higher work function of PVDF/N-rGO in comparison to PVDF will shift the fermi level to more negative value, enlarging the difference between nylon and PVDF/N-rGO(Figure 4.2.6 (b))[31, 39]. Thus, more electrons will flow from nylon to PVDF/N-rGO thereby boosting the device performance.

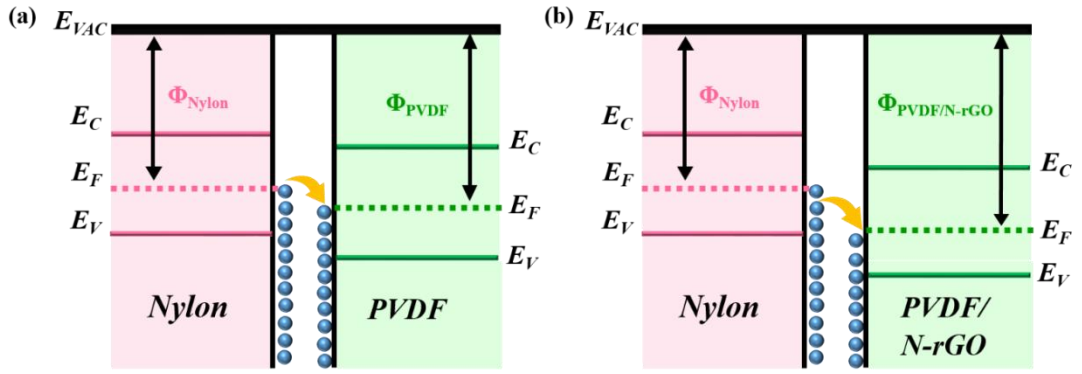


Figure 4.2.12 (a-b) A schematic band diagram illustrating the characteristic electronic energy level to describe TENG mechanism.

Moreover, the output enhancement mechanism and contact electrification between surfaces in presence of mechanical stimuli can be further understood by the overlapped electron cloud model (OEC). Figure 4.2.13 (a-b) shows the electron transfer process of tribo-negative pristine PVDF and PVDF/N-rGO nanocomposite when they are pressed into contact with tribo-positive nylon where $E_{F(Nylon)}$, $E_{F(PVDF)}$, and $E_{F(PVDF/N-rGO)}$, represents the fermi level of nylon, pristine PVDF and PVDF/N-rGO, and ΔE , and ΔE_N represent the greatest energy difference between nylon and pristine PVDF and PVDF/N-rGO. Initially, when nylon film does not come in contact with PVDF film, the electron cloud of these materials do not overlap with each other and no transfer of charges takes place between them. But when these two materials are pressed together to come in contact with each other, the potential barrier (ΔE) between them starts decreasing and transfer of electrons take place between the atoms until there fermi levels reaches equilibrium state (i.e. $E_{F(Nylon)} = E_{F(PVDF)}$) and their electron cloud overlap with each other. Moreover, when we add N-rGO nanosheets in PVDF matrix, the fermi level of PVDF/N-rGO shifts downwards due to enhanced surface polarization, as confirmed by the KPFM measurements where PVDF/N-rGO films exhibits higher work function in comparison to PVDF film.

As the fermi level of nylon is constant, therefore the potential barrier ΔE_N between PVDF/N-rGO and nylon increases in comparison to ΔE (i.e. energy difference between PVDF and nylon films). Hence, more charges will transfer from nylon to PVDF/N-rGO in comparison with pristine PVDF thereby increasing the output performance of PVDF/N-rGO based nanogenerator. These results are in accordance

with FTIR, and dielectric measurements where addition of nanofillers together with the electrospinning technique leads to an increase in β phase as well dielectric constant of PVDF film.

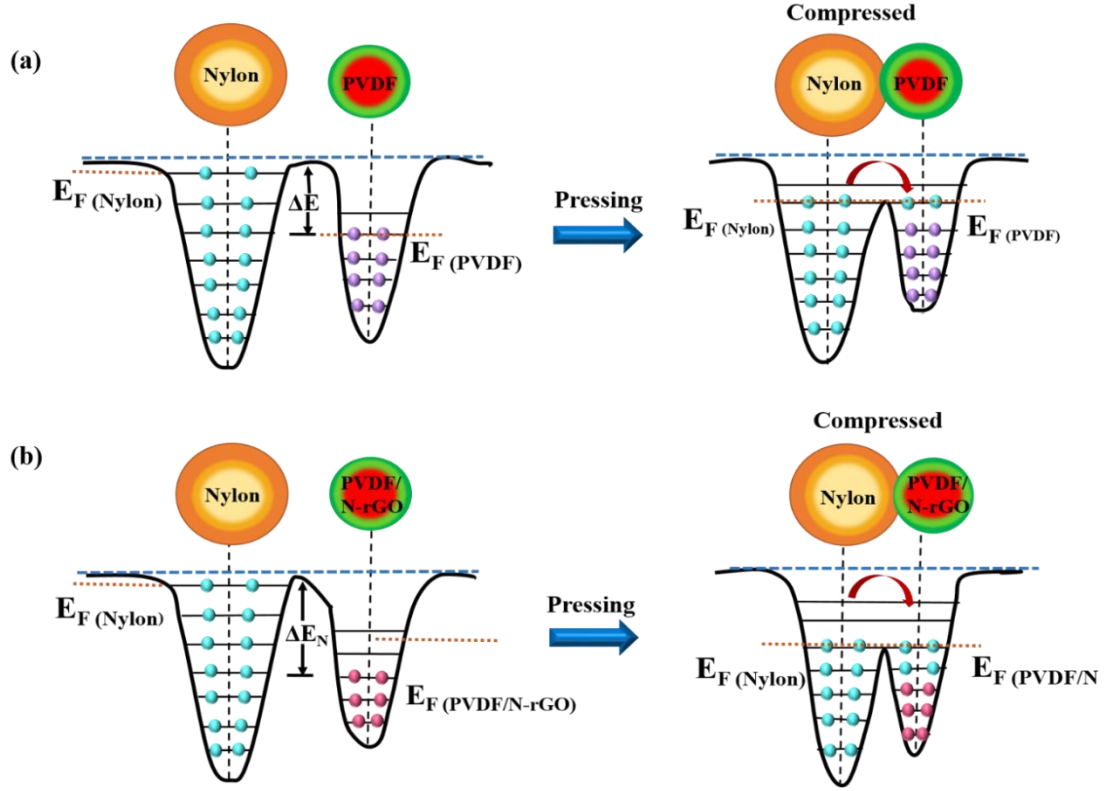


Figure 4.2.13 Electron cloud potential well model of (a) PVDF and (b) PVDF/N-rGO composite films.

4.2.3.2 Theroretical Investigations and COMSOL Simulation

As we know, that in vertical contact-separation mode the output voltage is given by the following V-Q-x relation[40, 41]

$$V(t) = -\frac{Q}{A\epsilon_0} (d_0 + x(t)) + \frac{\sigma x(t)}{\epsilon_0} \quad (4.2.2)$$

where, σ is the surface charge density, $x(t)$ is the time dependent distance between two triboelectric materials, ϵ_0 is permittivity of the free space, and d_0 is thickness of the dielectric film.

The open circuit voltage (V_{OC}), and transferred charges in short-circuit condition (Q_{SC}) is given by equations:

$$V_{oc} = \frac{\sigma x(t)}{\varepsilon_0} \quad (4.2.3)$$

$$Q_{sc} = \frac{A\sigma x(t)}{d_0 + x(t)} \quad (4.2.4)$$

and the corresponding short-circuit current (I_{sc}) is given as

$$I_{sc} = \frac{dQ_{sc}}{dt} = \frac{A\sigma d_0}{(d_0 + x(t))^2} \frac{dx}{dt} = \frac{A\sigma d_0 v(t)}{(d_0 + x(t))^2} \quad (4.2.5)$$

Moreover, the surface charge density is defined as

$$\sigma = \frac{C\Delta V}{S} = \frac{\varepsilon_0 \varepsilon_r \Delta V}{d} \quad (4.2.6)$$

$$C = \frac{\varepsilon_0 \varepsilon_r S}{d} \quad (4.2.7)$$

Here, ε_r is the relative dielectric constant, and C is capacitance

It can be deduced from the above equations that TENG's output performance depends on triboelectric charge density, separation between two layers, and speed of relative movement between two layers. Moreover, the output voltage of the nanogenerator depends on charge density which in turn depends on the capacitance of the TENG working in contact separation mode [42]. Therefore, to fabricate high performance TENG, we have to maximize value of capacitance which depends mainly on the dielectric constant, and frictional contact area. Consequently, it can be inferred from above equations that the output voltage of TENG will rise with increase in materials dielectric property and effective surface area. These observations align with prior findings, where the triboelectric charge density of the TENG is significantly influenced by the materials dielectric property, thickness, and distance between two layers[43]

Furthermore, COMSOL simulations via finite element method (FEM) is carried out for quantitative understanding of the surface potential distribution between two triboelectric layers of the TENG. Figure 4.2.14 (a-b) illustrates the stimulated potential distribution plot for the PVDF nanofibers and PVDF/N-rGO(1.5 wt%) nanofibers with nylon nanofibers. It can be clearly observed from the plots that the value of potential difference is enhanced after doping of N-rGO in the PVDF matrix which results in more charge transfer between PVDF/N-rGO nanofiber and nylon nanofibers in comparison of

pristine PVDF and nylon nanofibers, thereby improving the output performance of TENG[28, 44]. These results are in correlation with the experimental results where doping of the conducting nanofillers i.e. N-rGO improves the electroactive polar β phase, dielectric properties and surface potential difference between two layers, resulting in improved device performance.

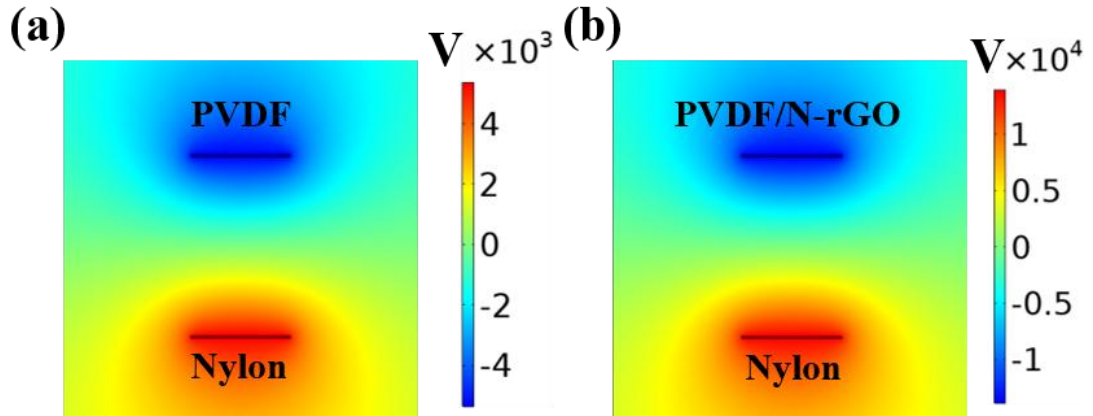


Figure 4.2.14 COMSOL simulation of (a) PVDF and (b) PVDF/N-rGO nanocomposite films.

4.2.3.3 Electrical Characterization of TENG

To investigate the influence of nanofillers and electrospinning technique on the output performance of the TENG device, detailed electrical characterization is systematically conducted by tapping the as fabricated TENGs with the help of dynamic shaker. Initially, PVDF composites films synthesized using drop casting method with varied loading content of N-rGO (0, 0.25, 0.5, 1, 1.5, 2 wt% named as P, PN1, PN2, PN3, PN4, PN5) is coupled with nylon film to design TENG devices. The electrical performance of these devices are then evaluated in terms of open-circuit voltage (V_{OC}) and short-circuit current (I_{SC}) measurements to optimize the concentration of N-rGO.

Figure 4.2.15 (a-c) illustrates the V_{OC} , I_{SC} , and charge waveforms of the drop-casted PVDF nanocomposite films based TENG device with varied concentration of N-rGO at 8 Hz frequency. The recorded waveforms clearly depicts that the output voltage, and current of the polymer nanocomposites film, first increases gradually with increase in content of N-rGO from 0 to 1.5 wt%, thereafter on further increasing the content of N-

rGO to 2 wt% a reversible trend, leading to decrease in output voltage and current value to 144 V, and 16 μ A.

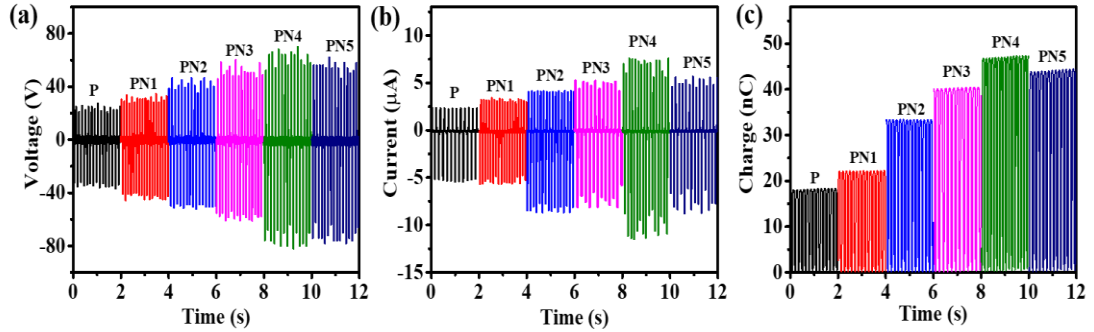


Figure 4.2.15 (a) The open-circuit voltage, (b) short-circuit current, and (c) charge measurements of drop casted PVDF and PVDF nanocomposite films with different weight percentage of N-rGO (0, 0.25, 0.5, 1, 1.5, and 2 wt%).

Meanwhile, similar trends are observed in the charge measurements, where the charges values first increases from 18 nC (PVDF film) to 46 nC (PVDF/ N-rGO (1.5 wt%) nanocomposite film), and then subsequently its value decreases to 43 nC for polymer nanocomposite film with 2 wt% N-rGO. The maximum V_{OC} , I_{SC} , and charge of 156 V, 20 μ A, and 40 nC is produced by the PN4 film based nanogenerator with 1.5 wt% loading content of N-rGO, whereas pristine PVDF (P) film based nanogenerator can only generate V_{OC} , I_{SC} , and charge of 67.2 V, 7 μ A, and 18 nC respectively. This enhancement in the output performance is ascribed to ample charge transfer paths produced by honeycomb structure and charge trapping abilities of the N-rGO which results in enhanced β -phase and dielectric constant of polymer nanocomposite films[45]. Further decrease in performance of TENG with 2 wt% N-rGO might be attributed to formation of conducting network of N-rGO in PVDF film. Moreover, to check the impact of tapping frequency on device performance, all the fabricated TENG with varied concentration of N-rGO are tapped with the help electrodynamic shaker in 2Hz to 10 Hz frequency range and corresponding results are shown in Figure 4.2.16 (a-b). The results reveals that both output voltage and current follows the similar trends of increasing gradually with tapping frequency which could be attributed to the faster charge transfer at higher frequency. Thus, from all the measurements we can conclude

that best performance corresponds to N-rGO with 1.5 wt% content. Hence, 1.5 wt% content of N-rGO is the optimum concentration for fabricating TENG.

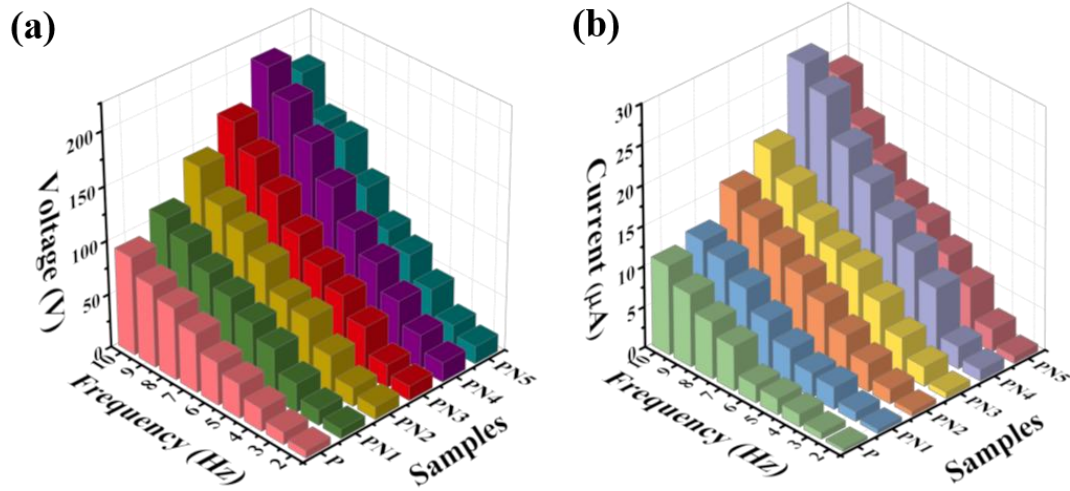


Figure 4.2.16 The output (a) voltage, and (b) current measurements of PVDF and PVDF nanocomposite films based TENG as a function of varied frequency.

To further enhance TENG's output performance, we have prepared nanofiber (NF) mats of PVDF, PVDF nanocomposite films with 1.5 wt% of N-rGO, and nylon using the electrospinning technique and their electrical performance are assessed by adjusting the tapping frequency from 2 Hz to 10 Hz. Figure 4.2.17 (a-c) illustrates the dependence of the V_{OC} , I_{SC} , and charges on the operating frequency for PVDF and PVDF/N-rGO nanofibers mat. As it can be seen from Figure 4.2.17 (d-e), the PVDF NFs mat based device shows the enhancement in the output voltage from 8.6 V to 156 V, while corresponding current values increases from 0.7 μ A to 16 μ A respectively as we vary the tapping frequency. Meanwhile, the PVDF/N-rGO NF mat based device can generate more output voltage and current under the same operating frequency. Specifically, the output voltage of the PVDF/N-rGO NF mat gradually increases from 19.4 V to 368 V, while the current rises from 1.8 μ A to 35 μ A. Moreover, the charges produced by the both PVDF and PVDF nanocomposite follows the similar trend as an impact of excitation frequency, where maximum charge of 80 nC is produced by nanocomposite fiber mat, whereas PVDF fiber based TENG can produce 56 nC charge (Figure 4.2.17 (f)). These results demonstrate that the V_{OC} , I_{SC} , and charges increased linearly as the

input frequency vary from 2 Hz to 10 Hz. Additionally, influence of impact force on device performance of PVDF/N-rGO NF based nanogenerator is also investigated by varying the force upto 50 N and respective waveforms are presented in Figure 4.2.17 (g-i). The maximum V_{OC} , and I_{SC} , of, 376 V, and 40 μA , is recorded at 50 N force.

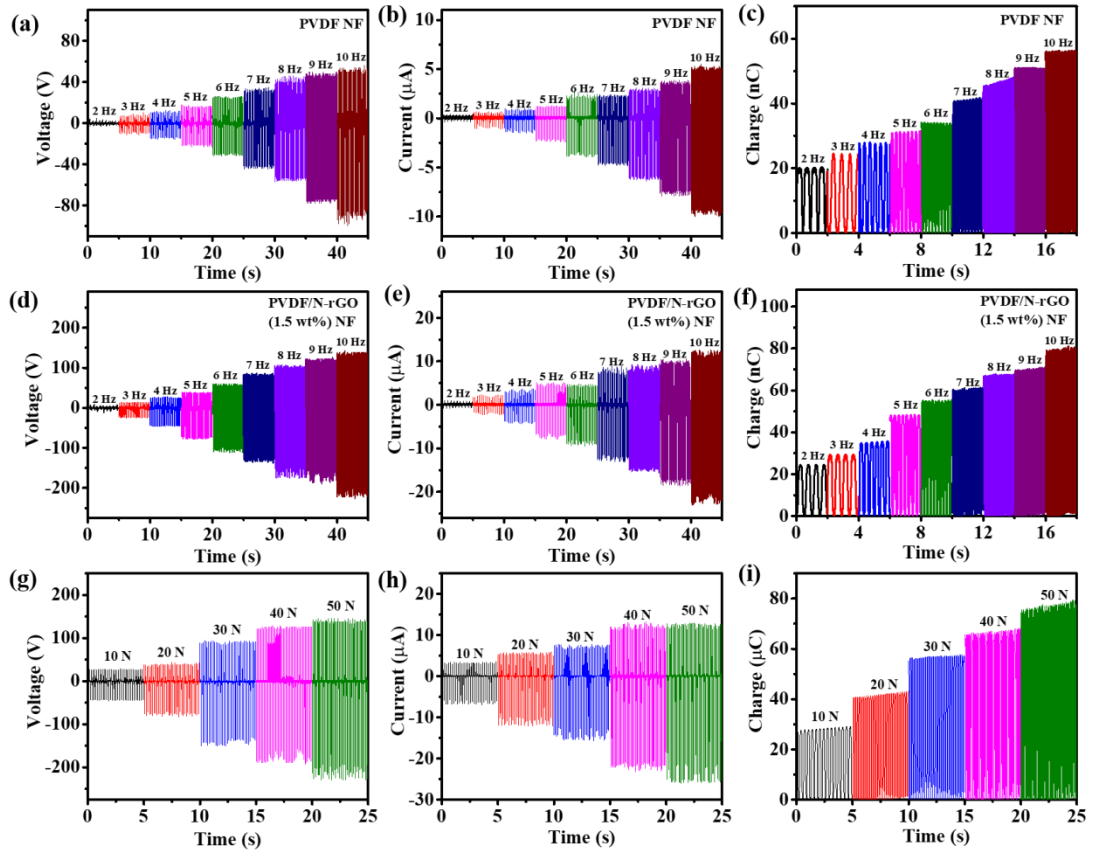


Figure 4.2.17 The open-circuit voltage, short-circuit current and charge measurements of (a-c) pristine PVDF nanofibers mat, and (d-f) PVDF/N-rGO (1.5 wt%) nanofibers mat based TENG at variable frequency, (g-i) output performance of the PVDF/N-rGO (1.5 wt%) based TENG under different impact force.

As we know maximum power can be delivered at the matching load resistance of nanogenerator. Therefore, to examine optimal output condition of TENG, the output voltage of PVDF film, PVDF/N-rGO (1.5 wt%) film, and PVDF nanofibers and PVDF/N-rGO (1.5 wt%) nanofibers are measured across varying load resistance and corresponding power density is measured (Figure 4.2.18 (a-b)). The output voltage peaks of all the samples first increase with increase in the load resistance and then gets saturated.

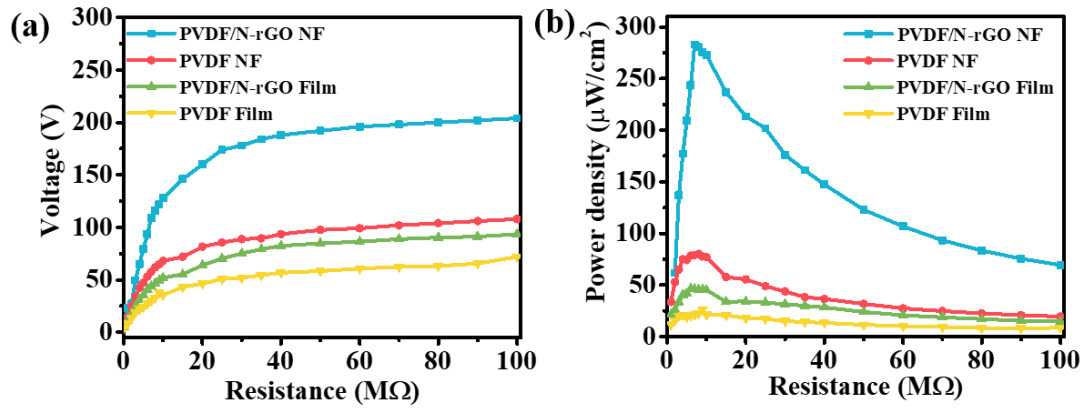


Figure 4.2.18 The variation of (a) output voltage and (b) power density of TENGs as a function of load resistance.

Figure 4.2.18 (b) shows the comparison of output power density of all the four fabricated TENGs where maximum power density of $\sim 282.8 \mu W/cm^2$ is achieved by the PVDF/N-rGO nanofibers based TENG at matching load resistance of 8 $M\Omega$, which is three times higher than the power density of PVDF nanofibers based TENG and six times higher than that of PVDF/N-rGO drop casted film. Thus, it can be concluded from the above results that addition of conducting nanofillers (N-rGO), boost the output performance of both the drop casted film and electrospun PVDF nanofibers. Moreover, in comparison to drop casted films, electrospun nanofibers of PVDF nanocomposite generates more power which is in accordance with the dielectric studies and surface potential measurements, where nanofibers have large dielectric constant and potential difference (ΔV_{CPD}) than the drop casted films. Hence, PVDF/N-rGO (1.5 wt%) nanofibers is used for further characterization. The comparison in electrical performance of PVDF/N-rGO nanofiber based TENG with other TENG reported in the literature is illustrated in Table 4.1.

Table 4.1 Comparison of the output performance of fabricated TENG with other reported TENG

Triboelectric materials		Electrode	Device size (cm ²)	V _{OC} (V)	I _{SC} (μA)	Power density (μW/cm ²)	Ref.
Material 1	Material 2						
rGO-ZnSnO ₃ /PDMS	Paper	Aluminum	2×2	410	13	200	[46]
PVDF/polystyr ene	Copper	Copper	3×3	165	11.1	66.3	[47]
PVDF-MoS ₂	PDMS	Aluminum	-	189	1.6	104	[48]
PVDF- MoS ₂ /CNT	Nylon	Copper	6×6	300	11.5	-	[49]
PVDF/titania monolayer	Copper	Copper	2×2	52	22.7	92	[50]
PVDF/Mustard seeds	ITO coated PET	Aluminum	3×3	126	-	33	[51]
PVA/MXene	Silk fibroin	Metal	-	118	-	108	[52]
MoS ₂ /PAN	Nylon	Aluminum	2×2	245	5.1	175	[53]
PTFE	Silk fibroin	Aluminum	3×3	238	12.6	26.3	[54]
PDMS	Nylon	Graphene	-	397	6.8	33	[55]
FEP	Copper	Copper	2×2	400	5	-	[56]
PTFE	Cellulose	Aluminum	-	460	23	180	[57]
ZiF-67	FEP	Aluminum	4.5×4.5	280	70	235	[58]
PVDF/N-rGO	Nylon 6	Aluminum	3×2	368	35	282	This Work

In addition to high performance of TENG, reliability and mechanical stability of obtained output signal is also an important parameter for longer operation of device. Therefore, to check mechanical stability of nanogenerator, we have measured open-circuit voltage of the PVDF/N-rGO NFs TENG for consecutive five months, which shows negligible deterioration in the output performance of TENG (Figure 4.2.19 (a)). Besides, stability in voltage signals, the stability of current is also evaluated by pressing and releasing triboelectric layers for over 5000 s under the constant frequency (Figure 4.2.19 (b)) with inset showing the current waveforms. These results demonstrate the excellent long term durability and stability of nanogenerator, thus making them suitable for flexible electronics applications.

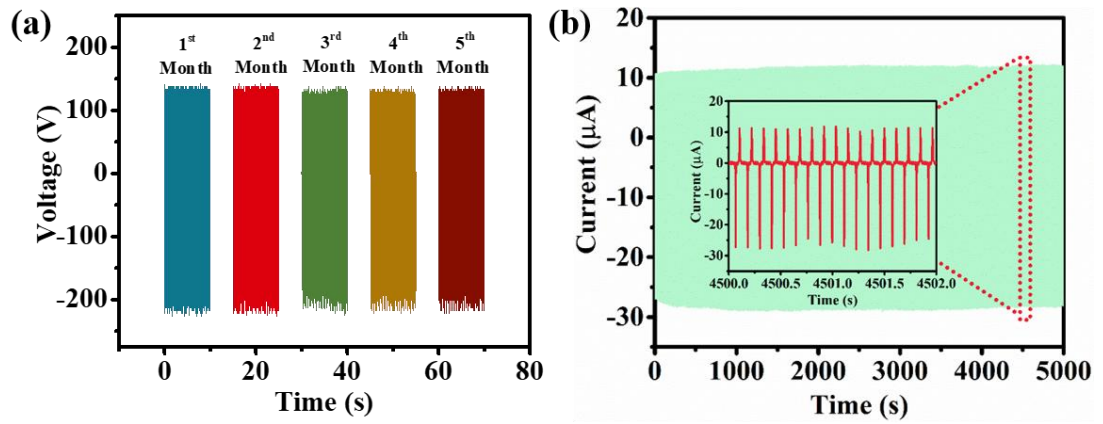


Figure 4.2.19 (a) Durability of PVDF/N-rGO nanofiber based TENG with stable output voltage over 5 months, and its (b) Mechanical stability with consistent current output over 5000 seconds.

4.2.4 Applications of TENG

4.2.4.1 Capacitor Charging and Deriving Electronic Devices

To validate TENG's energy harvesting capabilities for practical applications, it is required to convert AC signal generated by TENG into desired form to operate the commercial devices and sensors. Thus, a full wave bridge rectifier IC (DB107) is used to convert AC signals generated by TENG to DC signals. The rectified output generated by TENG under periodic press-release cycle is then used to investigate the charging capabilities of various capacitors (1, 2.2, 10, 33 μF) and the corresponding charging curves are depicted in Figure 4.2.20 .

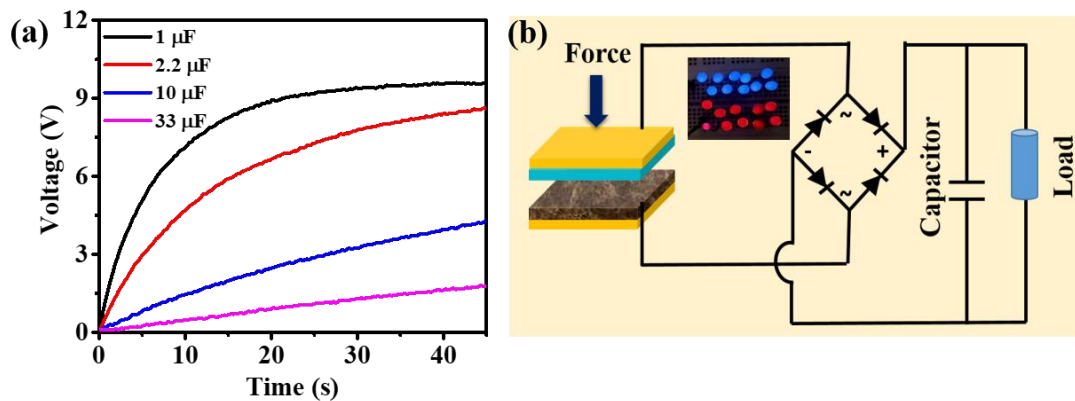


Figure 4.2.20 (a) Capacitor charging curves of various capacitors (1, 2.2, 10, 33 μF) charged through TENG, (b) A schematic circuit diagram for powering LEDs with inset showing the photographic images of LEDs powered by TENG.

As evident from these curves, a small capacitor ($1\mu\text{F}$), need less time to charge and reach a maximum voltage of $\sim 9.5\text{ V}$ within 45 s. In contrast, a larger capacitor ($33\mu\text{F}$) only reaches around 1.6 V within the same time frame, given a tapping frequency of 6 Hz . The energy stored in the capacitors are utilized to power commercial LEDs connected in series with cooresponding circuit diagram is illustrated in Figure 4.2.20 (b),. In addition to this, output generated by TENG is also used for driving electronic device, such as, thermometer, digital watch, and hygrometer and their charging-discharging curves are depicted in Figure 4.2.21 (a-c) with inset showing the turn on conditions of these devices.

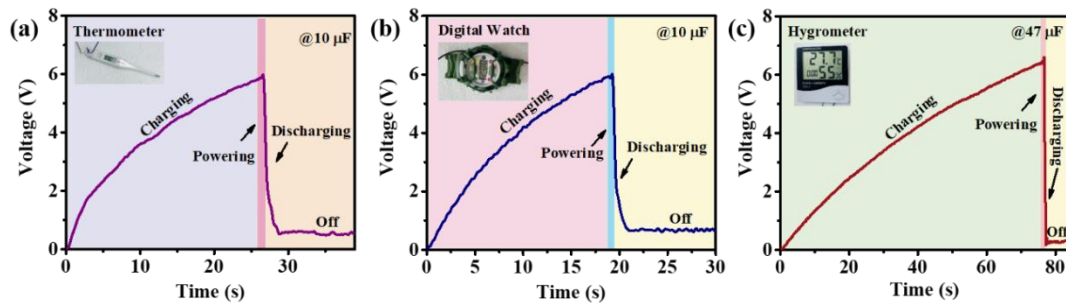


Figure 4.2.21 The charging/discharging curve of capacitor to power (a) thermometer, (b) digital watch, and (c) hygrometer from the energy harvested by TENG after storing it to capacitor.

4.2.4.2 Biomechanical Energy Harvesting

The human body is considered as a vast energy source, where different biomechanical movements of various parts of body possess their own characteristics and contains accessible energy which goes wasted. Hence, it is important to harvest the energy from human motions. Thus, besides the charging of capacitors and driving electronic devices, the fabricated TENG can also be employed as a biomechanical energy harvester which can produce electricity from various biomechanical movements of body parts. Figure 4.2.22 (a-d) shows the utilization of TENG in scavenging the energy from human motions, such as, gentle pressing with different fingers and thumb tapping with the inset showing the respective photographic image. The TENG is also pinched with the fingers at different pace slow, medium and fast and the respective waveforms generated are shown in Figure 4.2.22 (e). The sensitivity of the TENG is analyzed by blowing with mouth which can generate a maximum voltage of $\sim 22\text{ V}$, indicating excellent sensitivity of TENG (Figure 4.2.22 (f)). In addition to this, the TENG is subjected to knocking,

elbow tapping and foot tapping and corresponding wave forms are illustrated in Figure 4.2.22 (g-i).

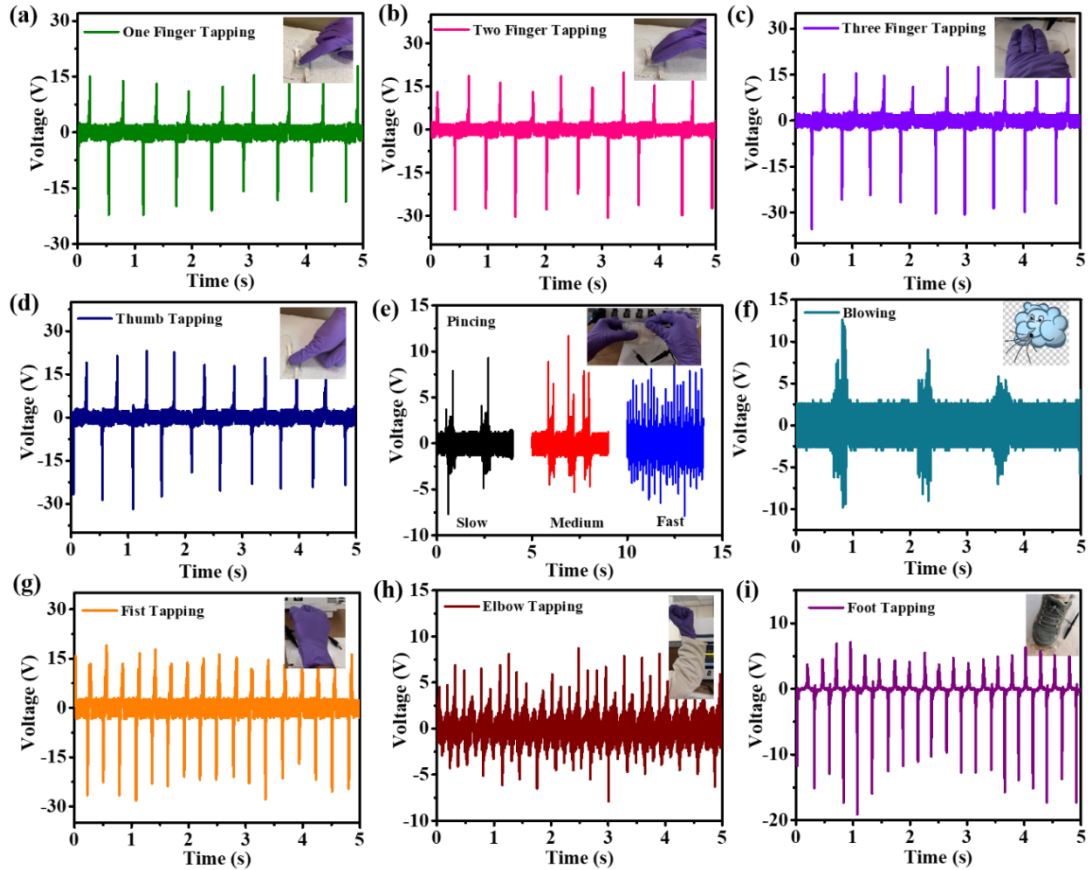


Figure 4.2.22 The output voltage waveforms produced by PVDF/N-rGO(1.5 wt%) nanofibers based TENG from various human motions (a-c) Tapping with one, two and three fingers, (d) thumb tapping, (e) pinching of TENG with different pace, (f) blowing, (g-i) fist, elbow and foot tapping.

4.2.4.3 TENG as Self-powered Motion Sensor

As, the PVDF/N-rGO nanofibers based TENG can sense even smaller contact separation very quickly, so its most promising application is in self-powered sensing platform. In the smart era, we all are surrounded by the different types of sensors among which motion sensors are most common ones that are implemented from residential homes to commercial buildings. These sensors can detect human motion/presence and can facilitate the automatic control of light, thereby optimizing energy consumption. However, these motion requires external power source for their continuous operation, leading to the significant consumption of energy. The real time application of TENG is

showcased through development of a self-powered motion sensor capable of illuminating lights automatically in response to human movements. Figure 4.2.23 (a-c) shows the detailed electronic circuit design for the light control system which consist of mainly two components: electrical signal acquisition module and signal processing module which interact with each other via wireless communication unit.

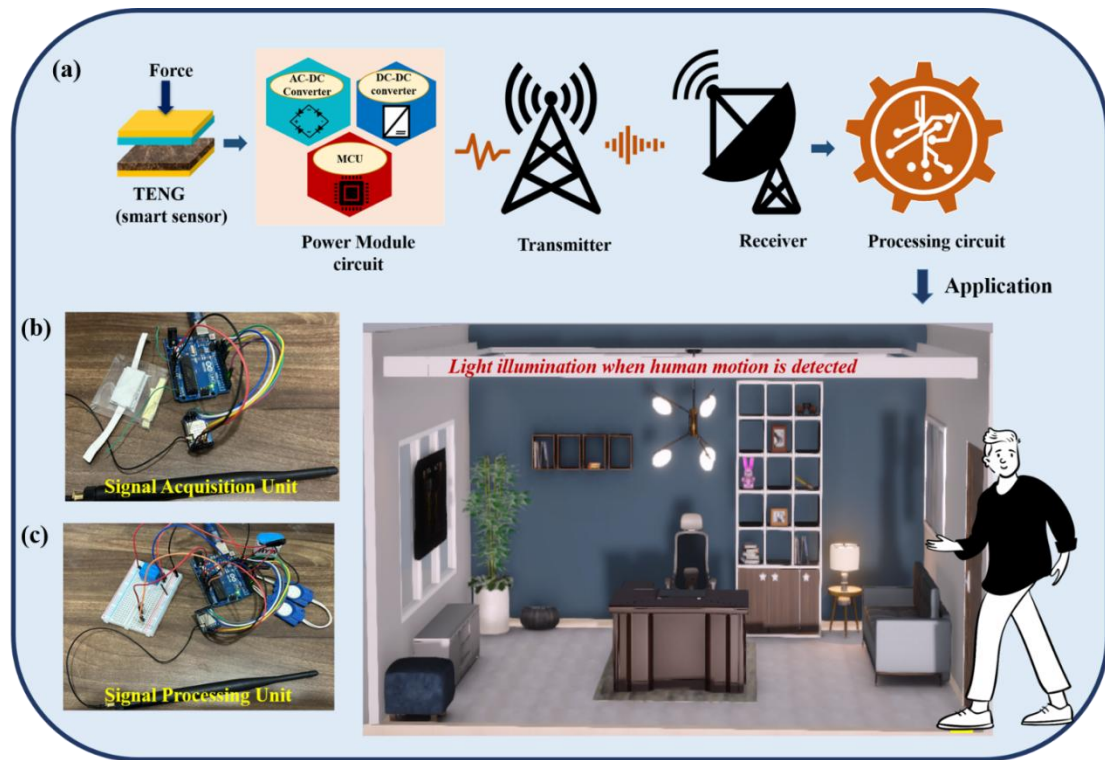


Figure 4.2.23 (a) A schematic showing the block diagram of a self-powered smart lighting system for automatically ON the lights in night time, with (b-c) photographic image of signal acquisition unit and signal processing unit.

During the operation of light control system, whenever any mechanical motion from finger or by foot is experienced by the TENG, a voltage signal is generated by the TENG. The microcontroller unit (MCU) modulates these signals into binary instructions (1 or 0) and transmits them to the signal processing unit via the wireless communication unit. After receiving the signals, MCU compares the signal and based on the control information provided by sensors (TENG and light sensor) about darkness and human presence, will set the relay to “ON” or “OFF” condition. Thus, making a smart decision to operate the light. Thus, when these motion sensors are placed in corridors, streets, homes etc. and peoples walk over them, the light will turn “ON”

automatically in night time or when intensity of light is less than certain limit by retrieving the information from light sensor. Meanwhile, during day time the lights remain inactive (OFF) regardless of people walking over them. Hence, the present study illustrates the potential application of TENG as a self-powered motion sensor.

4.2.5 Summary

In summary, we have investigated the synergistic effect of N-rGO blending and electrospinning technique on the dielectric, charge transfer and triboelectric property of PVDF polymer material for energy harvesting application. The TENG comprises of PVDF/N-rGO nanofibers as one of the triboelectric layer, showed significant enhancement in the electrical performance in comparison to pristine PVDF film prepared via drop casting method. A maximum output voltage of 368 V and current of 35 μ A is generated by the PVDF/N-rGO nanofiber based TENG device with a power density of $\sim 282.8 \mu\text{W}/\text{cm}^2$, which is six times higher than the power density of the drop casted PVDF/N-rGO film under impedance matching condition. This improved performance of the TENG is credited to both additions of N-rGO and electrospinning which increases the crystalline β phase, dielectric constant, surface roughness and charge trapping capabilities of PVDF film. The energy scavenged by TENG is used to drive electronic devices and charging of capacitors. The fabricated TENG can effectively harness energy from human motions and exhibits excellent durability and stability under several contact separation cycles. In addition, the as fabricated TENG is used to develop a self-powered human-machine interface for smart lighting system which can automatically turn on the lights upon human motion detection. This study not only provides insights into the mechanisms underlying the enhanced performance of nanogenerators but also presents a practical application for self-powered motion sensors, contributing to the advancement of sustainable energy harvesting technologies and smart sensor systems.

References

- [1] Z. Kinas *et al.*, "High-performance triboelectric nanogenerator based on carbon nanomaterials functionalized polyacrylonitrile nanofibers," *Energy*, vol. 239, p. 122369, 2022.
- [2] S. Sripadmanabhan Indira, C. Aravind Vaithilingam, K. S. P. Oruganti, F. Mohd, and S. J. N. Rahman, "Nanogenerators as a sustainable power source: State of art, applications, and challenges," vol. 9, no. 5, p. 773, 2019.
- [3] C. Wu, A. C. Wang, W. Ding, H. Guo, and Z. L. Wang, "Triboelectric nanogenerator: a foundation of the energy for the new era," *Advanced Energy Materials*, vol. 9, no. 1, p. 1802906, 2019.
- [4] H. Li *et al.*, "A wearable solar-thermal-pyroelectric harvester: Achieving high power output using modified rGO-PEI and polarized PVDF," vol. 73, p. 104723, 2020.
- [5] C. Wu, T. W. Kim, and H. Y. Choi, "Reduced graphene-oxide acting as electron-trapping sites in the friction layer for giant triboelectric enhancement," *Nano Energy*, vol. 32, pp. 542-550, 2017.
- [6] D. Zhang, Z. Xu, Z. Yang, and X. Song, "High-performance flexible self-powered tin disulfide nanoflowers/reduced graphene oxide nanohybrid-based humidity sensor driven by triboelectric nanogenerator," *Nano Energy*, vol. 67, p. 104251, 2020.
- [7] K. Cheng, S. Wallaert, H. Ardebili, and A. Karim, "Advanced triboelectric nanogenerators based on low-dimension carbon materials: A review," *Carbon*, vol. 194, pp. 81-103, 2022.
- [8] R. Mao *et al.*, "Deep-learning-assisted low-cost flexible cotton yarn-based triboelectric nanogenerator for ultra-sensitive human-computer merging interfaces," *Nano Energy*, vol. 111, p. 108418, 2023.
- [9] S. A. Lone *et al.*, "Recent advancements for improving the performance of triboelectric nanogenerator devices," *Nano Energy*, vol. 99, p. 107318, 2022.
- [10] Y. Zou, J. Xu, K. Chen, and J. Chen, "Advances in nanostructures for high-performance triboelectric nanogenerators," *Advanced Materials Technologies*, vol. 6, no. 3, p. 2000916, 2021.
- [11] H. Zou *et al.*, "Quantifying the triboelectric series," *Nature communications*, vol. 10, no. 1, p. 1427, 2019.

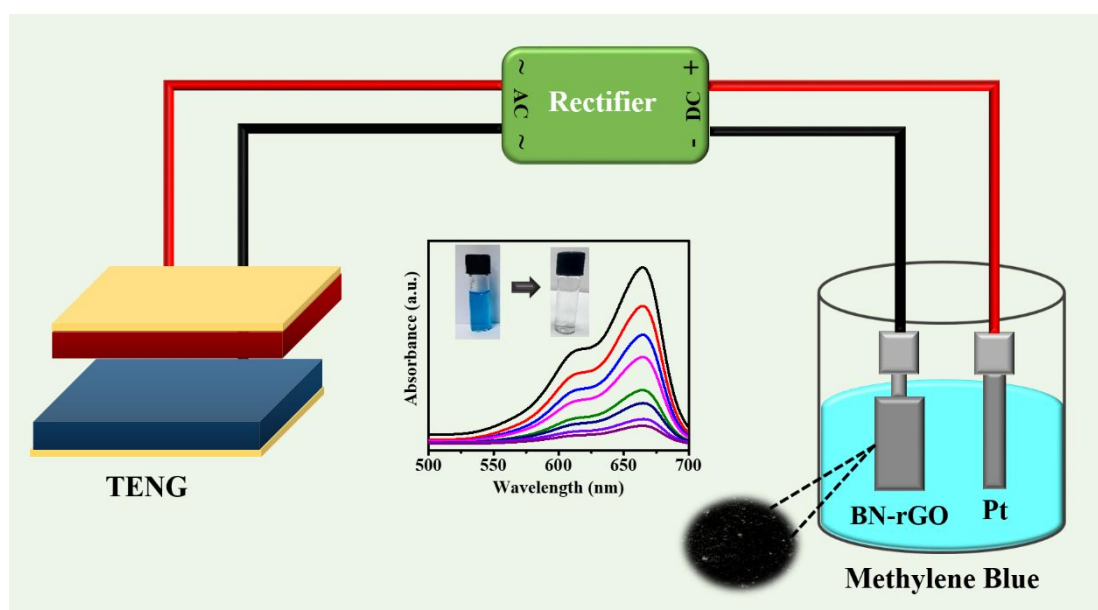
- [12] G. Khandelwal, N. P. Maria Joseph Raj, and S. J. Kim, "Materials beyond conventional triboelectric series for fabrication and applications of triboelectric nanogenerators," *Advanced Energy Materials*, vol. 11, no. 33, p. 2101170, 2021.
- [13] P. Pandey *et al.*, "Nafion-mediated barium titanate-polymer composite nanofibers-based triboelectric nanogenerator for self-powered smart street and home control system," *Nano Energy*, vol. 107, p. 108134, 2023.
- [14] M. Tayyab *et al.*, "Enhanced output in polyvinylidene fluoride nanofibers based triboelectric nanogenerator by using printer ink as nano-fillers," *Nano Energy*, vol. 77, p. 105178, 2020.
- [15] H. H. Singh and N. Khare, "Flexible ZnO-PVDF/PTFE based piezo-tribo hybrid nanogenerator," *Nano Energy*, vol. 51, pp. 216-222, 2018.
- [16] Y. Wang, Y. Yang, and Z. L. Wang, "Triboelectric nanogenerators as flexible power sources," *npj Flexible Electronics*, vol. 1, no. 1, p. 10, 2017.
- [17] S. Rana, V. Singh, and B. Singh, "Recent trends in 2D materials and their polymer composites for effectively harnessing mechanical energy," *iScience*, p. 103748, 2022.
- [18] R. F. S. Muktar Ahmed *et al.*, "Sucrose assisted chemical-free synthesis of rGO for triboelectric nanogenerator: Green energy source for smart-water dispenser," *Nano Energy*, vol. 106, p. 108085, 2023.
- [19] G.-Z. Li *et al.*, "A high-performance transparent and flexible triboelectric nanogenerator based on hydrophobic composite films," *Nano Energy*, vol. 75, p. 104918, 2020.
- [20] D. C. Marcano *et al.*, "Improved synthesis of graphene oxide," *ACS Nano*, vol. 4, no. 8, pp. 4806-4814, 2010.
- [21] S. Rana, V. Singh, and B. Singh, "Tailoring the Output Performance of PVDF-Based Piezo-Tribo Hybridized Nanogenerators via B, N-Codoped Reduced Graphene Oxide," *ACS Applied Electronic Materials*, vol. 4, no. 12, pp. 5893-5904, 2022.
- [22] N. Soin *et al.*, "High performance triboelectric nanogenerators based on phase-inversion piezoelectric membranes of poly(vinylidene fluoride)-zinc stannate (PVDF-ZnSnO₃) and polyamide-6 (PA6)," *Nano Energy*, vol. 30, pp. 470-480, 2016.

- [23] A. Anand, D. Meena, K. K. Dey, and M. C. Bhatnagar, "Enhanced piezoelectricity properties of reduced graphene oxide (RGO) loaded polyvinylidene fluoride (PVDF) nanocomposite films for nanogenerator application," *Journal of Polymer Research*, vol. 27, no. 12, pp. 1-11, 2020.
- [24] S. K. Karan, D. Mandal, and B. B. Khatua, "Self-powered flexible Fe-doped RGO/PVDF nanocomposite: an excellent material for a piezoelectric energy harvester," *Nanoscale*, vol. 7, no. 24, pp. 10655-10666, 2015.
- [25] X. Cai, T. Lei, D. Sun, and L. Lin, "A critical analysis of the α , β and γ phases in poly (vinylidene fluoride) using FTIR," *RSC Advances*, vol. 7, no. 25, pp. 15382-15389, 2017.
- [26] S. Rana and B. Singh, "Polymer nanocomposite film based piezoelectric nanogenerator for biomechanical energy harvesting and motion monitoring," *Journal of Materials Science: Materials in Electronics*, vol. 34, no. 25, p. 1764, 2023.
- [27] R. Bhunia, S. Gupta, B. Fatma, Prateek, R. K. Gupta, and A. Garg, "Milli-Watt Power Harvesting from Dual Triboelectric and Piezoelectric Effects of Multifunctional Green and Robust Reduced Graphene Oxide/P(VDF-TrFE) Composite Flexible Films," *ACS Applied Materials & Interfaces*, vol. 11, no. 41, pp. 38177-38189, 2019.
- [28] L. Shi *et al.*, "High-performance triboelectric nanogenerator based on electrospun PVDF-graphene nanosheet composite nanofibers for energy harvesting," *Nano Energy*, vol. 80, p. 105599, 2021.
- [29] T. Bhatta *et al.*, "High-performance triboelectric nanogenerator based on MXene functionalized polyvinylidene fluoride composite nanofibers," *Nano Energy*, vol. 81, p. 105670, 2021.
- [30] P. Gajula, J. U. Yoon, I. Woo, S.-J. Oh, and J. W. Bae, "Triboelectric touch sensor array system for energy generation and self-powered human-machine interfaces based on chemically functionalized, electrospun rGO/Nylon-12 and micro-patterned Ecoflex/MoS₂ films," *Nano Energy*, vol. 121, p. 109278, 2024.
- [31] Y. He, H. Wang, Z. Sha, C. Boyer, C.-H. Wang, and J. Zhang, "Enhancing output performance of PVDF-HFP fiber-based nanogenerator by hybridizing silver nanowires and perovskite oxide nanocrystals," *Nano Energy*, vol. 98, p. 107343, 2022.

- [32] M. M. Abolhasani, K. Shirvanimoghaddam, and M. Naebe, "PVDF/graphene composite nanofibers with enhanced piezoelectric performance for development of robust nanogenerators," *Composites Science and Technology*, vol. 138, pp. 49-56, 2017.
- [33] K. Tashiro, Y. Itoh, M. Kobayashi, and H. Tadokoro, "Polarized Raman spectra and LO-TO splitting of poly (vinylidene fluoride) crystal form I," *Macromolecules*, vol. 18, no. 12, pp. 2600-2606, 1985.
- [34] Y. Zhang *et al.*, "Crystallization behavior and phase-transformation mechanism with the use of graphite nanosheets in poly (vinylidene fluoride) nanocomposites," *Journal of Applied Polymer Science*, vol. 125, no. S1, pp. E314-E319, 2012.
- [35] S. Tu, Q. Jiang, X. Zhang, and H. N. Alshareef, "Large dielectric constant enhancement in MXene percolative polymer composites," *ACS nano*, vol. 12, no. 4, pp. 3369-3377, 2018.
- [36] S. Jang, H. Kim, Y. Kim, B. J. Kang, and J. H. Oh, "Honeycomb-like nanofiber based triboelectric nanogenerator using self-assembled electrospun poly (vinylidene fluoride-co-trifluoroethylene) nanofibers," *Applied Physics Letters*, vol. 108, no. 14, 2016.
- [37] S. Cheon *et al.*, "High-Performance Triboelectric Nanogenerators Based on Electrospun Polyvinylidene Fluoride–Silver Nanowire Composite Nanofibers," *Advanced Functional Materials*, vol. 28, no. 2, p. 1703778, 2018.
- [38] M. Li *et al.*, "Filling the gap between topological insulator nanomaterials and triboelectric nanogenerators," *Nature communications*, vol. 13, no. 1, p. 938, 2022.
- [39] P. Bai *et al.*, "Dipole-moment-induced effect on contact electrification for triboelectric nanogenerators," *Nano Research*, vol. 7, no. 7, pp. 990-997, 2014.
- [40] S. Niu *et al.*, "Theoretical study of contact-mode triboelectric nanogenerators as an effective power source," *Energy & Environmental Science*, 10.1039/C3EE42571A vol. 6, no. 12, pp. 3576-3583, 2013, doi: 10.1039/C3EE42571A.
- [41] B. Yang, W. Zeng, Z.-H. Peng, S.-R. Liu, K. Chen, and X.-M. Tao, "A Fully Verified Theoretical Analysis of Contact-Mode Triboelectric Nanogenerators as a Wearable Power Source," *Advanced Energy Materials*, vol. 6, no. 16, p. 1600505, 2016.

CHAPTER 5

Optimizing B, N Co-doped rGO concentration in electrospun PVDF nanofibers for triboelectric nanogenerator-driven water remediation



In this chapter, we have presented a self-powered dye degradation system for removing the organic pollutants from the wastewater by coupling of triboelectric nanogenerator (TENG) with BN-rGO as an one of the electrode used in dye degradation system. A high-performance TENG was initially developed by optimising the BN-rGO concentration within the PVDF matrix, achieving a maximum power density of $336 \mu\text{W}/\text{cm}^2$ at an optimal BN-rGO content of 1.5 wt%. The electrical power generated by the TENG is used to degrade the toxic and carcinogenic methylene blue dye through an oxidation process facilitated by OH radicals at the electrode interface, achieving complete degradation within 100 minutes. The present works shed light on integration of TENG with carbon based materials as an electrode for designing an efficient and sustainable, self-powered electrochemical degradation system for wastewater remediation applications.

5.1 Introduction

With the rapid acceleration in urbanization and industrialization, the environmental pollution and energy scarcity has become one of the pressing issue that possess significant threat to the human society and ecosystem[1-3]. Large amount of organic pollutants in air and water, especially organic dyes generated from industries, such as, textiles, printing, dyeing, cosmetics and electroplating contains harmful and carcinogenic compounds, which seriously endangers/significantly affects the human health and cause great damage to aquatic life and ecological system[4, 5]. Therefore, it is necessary and imperative to develop efficient, sustainable and eco-friendly methods to remove organic dyes from wastewater. Nowadays, numerous strategies are developed for removing the pollutants from the wastewater[6]. These strategies are mainly divided into two categories, first is the separation of organic pollutants through adsorption which is not effective as it simply transfers contaminants from one place to another and thereafter organic pollutants require further treatment. Another approach is advanced oxidation processes which degrade the organic pollutants through photocatalysis, piezocatalysis, electrocatalysis, electron-fenton catalysis etc. Among these techniques, electrocatalytic degradation have gained significant interest for its clean, versatility, higher effectiveness and environmental compatible approach[7]. However, its practical application to large scale is still restricted due to high consumption of the electrical energy. To solve these problems, one of the possible ways is to design a self-powered degradation system for wastewater treatment by using renewable energy which is a key solution for energy sustainability and environmental issue. In view of this, several types of energy harvesting technologies are employed to drive the electrochemical systems. Among the various emerging harvesting technologies, triboelectric nanogenerator stands out to be a promising technology which can convert randomly distributed, irregular and waste mechanical energy into electrical energy based on the coupling effect of contact electrification and electrostatic induction. TENG offers several advantages, such as wide range of material choice, flexible structural design, ability to operate at low frequency domain, cost-effectiveness making its prospects in multitudinous applications including self-powered devices[8], smart agriculture[9], Internet of things[10], implantable device[11], and blue energy[12]. However, to foster the usage of TENG in efficient self-powered degradation system,

certain issues need to be address for successful integration of TENG with dye degradation system[13]. Firstly, the output performance of TENG plays a crucial role in determining their degradation efficiency, which strongly depends on material choice and their structure. Therefore, suitable material selection and simple device structure should be utilized to design a self-powered system for unnecessary energy loss during large scale grid integration. Second, is the selection of cathode which decides the degradation efficiency of organic pollutants and can make the reaction faster[14, 15]. These issues can be overcome by integration of high performance TENG with a catalysis with good performance and selectivity to be used as an active cathode material for developing a self-powered degradation system for wastewater treatment.

Herein, we have designed a polymer nanofiber based TENG by coupling of PVDF and PVDF nanocomposite films with nylon film as two triboelectric layers as a power supply and then apply it to electrochemical degradation system to degrade the methylene blue dye. Initially, we optimized the concentration of nanofillers by investigating the effect of boron-nitrogen co-doped reduced graphene oxide (BN-rGO) weight percentage on the TENG's output performance. The results showed that the PVDF/BN-rGO nanofiber-based TENG, with 1.5 wt% BN-rGO, produced a maximum output voltage of 380 V, current of 36 μ A, and power density of 336 μ W/cm². Finally, the power generated by the TENG is utilized to degrade methylene blue dye, which take 14 hours to degrade completely. Additionally, the potential application of BN-rGO nanofillers is also demonstrated to be an effective cathode catalysis that can significantly reduce the degradation time of methylene blue dye. When the catalytic activity of BN-rGO is combined with the power generated by the TENG for dye degradation, the process was notably accelerated, and methylene blue dye can completely degrade within 105 minutes. The present work offers an efficient pathway for designing an efficient and sustainable self-powered dye degradation system for wastewater treatment applications.

5.2 Experimental Section

5.2.1 Synthesis of PVDF/BN-rGO and Nylon Nanofibers

The hydrothermal route is opted for synthesis of BN-rGO nanosheets as described in our previous work[16] electrospinning method is employed for fabrication of

nanofibers of PVDF, PVDF/BN-rGO and nylon. To prepare the electrospinning solution, different amounts of BN-rGO (0.25, 0.5, 1, 1.5, 2 wt%) are dissolved in DMF separately and stirred continuously to obtain homogeneous solution. Thereafter, 1g PVDF is added to above solution and mixed thoroughly at 60° C to obtain an ideal viscosity required for electrospinning process. Afterwards, the resulting mixture is loaded in 10 ml syringe and electrospinning is carried out by maintain the flow rate of 1 ml/h at 12 kV voltage and the distance between collector and needle is 10 cm. The obtain nanofibers are dried in oven overnight at 60° C before further use. The PVDF nanofibers are prepared via similar route without addition of BN-rGO powder sample. The PVDF/ BN-rGO nanocomposites with varied concentration of BN-rGO (0, 0.25, 0.5, 1, 1.5, 2 wt%) are labelled as P, PBN1, PBN2, PBN3, PBN4, and PBN5.

Nylon nanofibers are prepared by dissolving nylon 6 pellets in formic acid at a weight ratio of 1:10, with continuous stirring at 70°C for 3 hours. The resultant mixture is then loaded into a 10 mL syringe, and electrospinning is carried out at 25 kV supply voltage, with 0.5 mL/h flow rate. The distance between needle and the collector was set at 10 cm. After electrospinning, the resulting nanofibers were dried in an oven to eliminate any residual moisture.

5.2.2 Fabrication of TENG

To fabricate the TENG in vertical contact-separation mode, PVDF and PVDF composite nanofibers were used as the negative triboelectric layer, while nylon nanofibers served as the positive triboelectric layer. Conductive aluminium adhesive tape is attached on the back of both the positive and negative triboelectric layers, functioning as electrodes. Copper wires were then connected to the system for external wiring and electrical measurements. To assemble the TENG, both films, measuring 3 cm x 2 cm, were securely affixed to acrylic sheets using double-sided tape.

5.3 Results and Discussion

5.3.1 Material Characterization

To analyse the synergetic effect of addition of nanofillers (i.e. BN-rGO) in PVDF matrix, along with the electrospinning, a set of comprehensive characterizations are carried out. In the electrospinning method, the electrostatic repulsion between surface charge along

the jet cause the uniaxial stretching of PVDF solution in presence of electric field, leading to the crystallization transition from the non-polar α -phase to polar β -phase[17, 18]. The higher content of the β -phase and enhanced degree of crystallinity generally encourage a stronger dipolar orientation within the molecular structure of the material. This improved dipolar alignment, in turn, improves the triboelectric properties. Additionally, when BN-rGO nanosheets are added to PVDF solution and subjected to electrospinning, electrostatic interactions arise between hydrogen or fluorine atoms in PVDF and the functional groups on BN-rGO. These two effects simultaneously improve the mechanical and dielectric properties of nanofibers, which is supported by XRD, FTIR, and FESEM studies. Figure 5.1 (a) shows the XRD spectra of PVDF nanocomposites fibres with varied content of BN-rGO. All the samples exhibit two characteristic peaks, one at 20.2° correspond to (200)/(110) reflection plane of polar β phase, which is associated with all trans conformation. Whereas, another peak at 18.4° correspond to non-polar α phase with trans-gauche-trans-gauche (TGTG) linkage[19, 20]. The intensity of diffraction peak corresponding to β phase increases significantly after addition of BN-rGO, which might be due to enhanced electrostatic interaction of $-\text{CH}_2$ and $-\text{CF}_2$ dipoles of PVDF with functional groups present in BN-rGO.

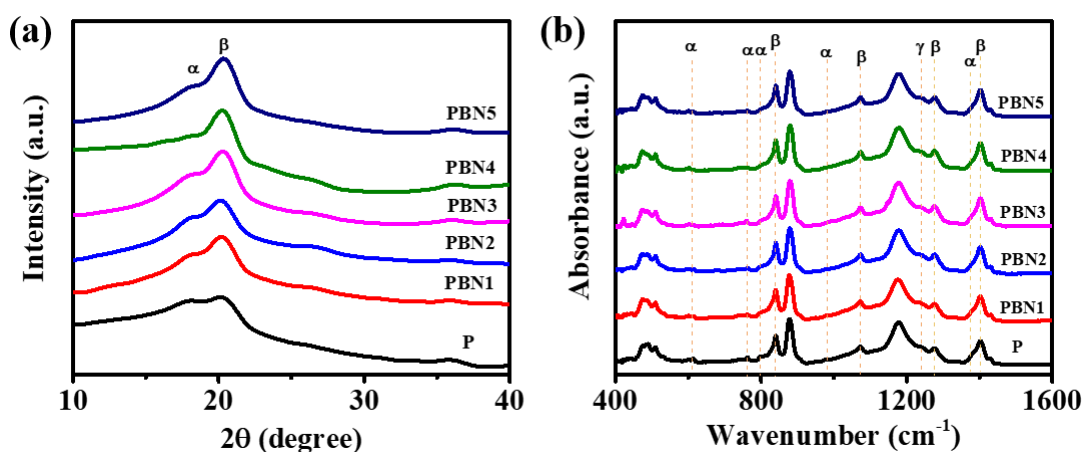


Figure 5.1 (a) XRD, and (b) FTIR spectra of electrospun PVDF nanofibers with different weight percentage of BN-rGO.

To further confirm the increment in electroactive polar β phase in PVDF nanofiber after addition of BN-rGO, FTIR analysis is carried out. Figure 5.1 (b) presents the FTIR spectra of PVDF and PVDF nanocomposite fibres, showing vibrational bands at 840,

1276, and 1402 cm^{-1} , which are associated with the crystalline polar β -phase[21, 22]. Meanwhile, the characteristic vibrational bands located at 612, 762, 795, 974 and 1382 cm^{-1} correspond to nonpolar α phase of PVDF. The FTIR spectra indicate that adding BN-rGO to the PVDF matrix enhances the β -phase peak at 840 cm^{-1} , while the α -phase peak at 762 cm^{-1} gradually diminishes. This suggests a consistent transformation from the nonpolar α -phase to the polar β -phase in PVDF due to the addition of nanofillers, as well as the poling and stretching effects during electrospinning. The relative content of the β -phase in nanofibers was determined using Lambert-Beer law. The calculated β -phase content for pristine PVDF nanofibers is 74.1%, whereas for PVDF/BN-rGO films, it reaches 77.5%, 78.4%, 80.9%, 85.9%, and 77.8% for 0.025, 0.5, 1, 1.5, and 2 wt% of BN-rGO, respectively, suggesting that 1.5 wt% is the optimal nanofillers concentration. The decrease in β -phase content at 2 wt% may be due to the interaction dynamics of BN-rGO within the PVDF matrix, which disrupts polymer chain alignment and hinders β -phase formation[23-25].

Figure 5.2 shows the FESEM micrographs of PVDF and PVDF/BN-rGO nanofibers prepared via electrospinning technique. FESEM images shows that electrospun nanofibers with uniform thickness and smooth surface, having diameter $\sim 200 \pm 140$ nm are prepared without any bead formation. Furthermore, the addition of BN-rGO has minimal effect on the microstructure and morphology of the PVDF nanofibers, indicating successful intercalation of BN-rGO nanosheets within the PVDF matrix.

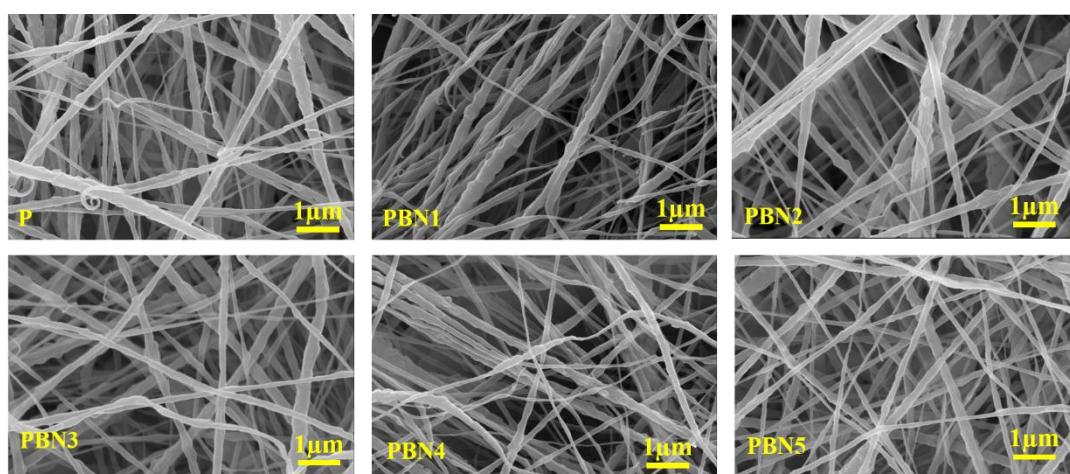


Figure 5.2 FESEM micrographs of electrospun PVDF and PVDF composite nanofibers with different weight percentage of BN-rGO.

As TENG is a capacitive energy device, and its capacitance can significantly affect its output performance[26, 27]. Typically, a higher dielectric constant results in greater capacitance and increased charge transfer density. Consequently, enhancing the dielectric constant of the materials can substantially improve the output performance of the TENG. Therefore, to evaluate the dielectric characteristics of PVDF nanofibers with varying BN-rGO loading, an LCR meter is used to measure capacitance of nanofibers by sandwiching the nanofiber mat between two copper plates, thereby forming a parallel plate capacitor. The dielectric constant (k) can be calculated using the capacitance (C) measured with LCR meter, according to the following equation

$$k = \frac{Cd}{A\epsilon_0} \quad (5.1)$$

Where d is thickness of nanofiber film, A is electrode area, and ϵ_0 is permittivity of free space. The Figure 5.3 illustrates the dielectric constant values of PVDF nanofibers with varying concentrations of BN-rGO. As the nanofillers content increases from 0 to 1.5 wt%, the dielectric constant rises progressively from 5.4 to 7.1, 9.2, 12.1, and 16.7, respectively. However, at 2 wt% BN-rGO, the dielectric constant decreases to 14.1.

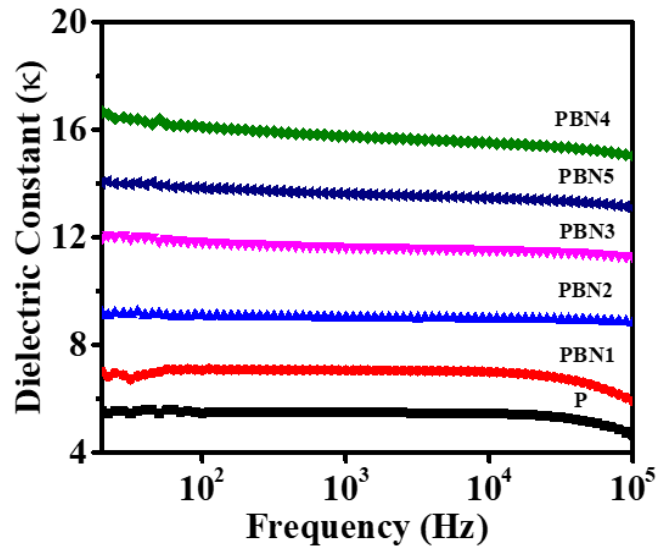


Figure 5.3 Dielectric constant measurements of electrospun PVDF and PVDF composite nanofibers with different weight percentage of BN-rGO.

These findings align with the FTIR studies. The initial increase in the dielectric constant of the PVDF nanofibers upon the addition of BN-rGO is attributed to the formation of a

micro-capacitor network and the emergence of microscopic dipoles within the PVDF matrix, which enhance the film's dielectric properties. The slight decrement observed at 2 wt% is likely due to reaching the percolation limit[18, 28, 29].

5.3.2 Electrical Characterization of TENG

The electrical performance of the PVDF nanofibers based TENG with varied concentration of BN-rGO, is optimized by conducting a series of test with the help of electrodynamic shaker and function generator, which allows meticulous control over both frequency and amplitude, facilitating a thorough investigation of how different vibration parameters (frequency, force and acceleration) influence the energy harvesting efficiency of the device. By adjusting these parameters, the device performance in terms of open-circuit voltage, short-circuit current and transferred charges are analyzed. The open circuit voltage (V_{OC}) and short-circuit current (I_{SC}) of PVDF nanofibers mat with varried concentration of BN-rGO at 8 Hz frequency is illustrated in Figure 5.4.

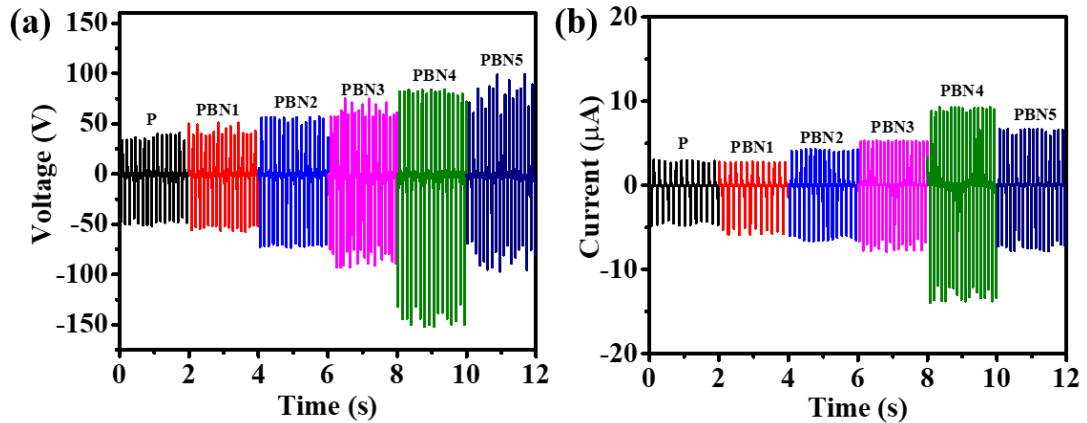


Figure 5.4 (a) The open-circuit voltage, and (b) short-circuit current measurements of electrospun PVDF and PVDF composite nanofibers with different weight percentage of BN-rGO.

The result indicate that PVDF/BN-rGO fim based TENG with 1.5 wt% of BN-rGO obtained the highest output performance, generating a voltage and current of 242 V and 24 μ A which is ~ 2.6 times the voltage, and ~ 3 times the current generated by PVDF nanofiber based TENG. As we know that output voltage of a TENG depends on triboelectric charge density which is in turns depends on the dielectric property of the material, and interlayer distance between them. Therefore, we can conclude that output

voltage of TENG tends to increase with increase in the dielectric property of the material. Considering these factors, the observed trend of rising TENG output voltage and current with increasing BN-rGO concentration up to 1.5 wt%, followed by a subsequent decrease, could likely be attributed to the following reasons: Initial increase in the output performance of PVDF nanocomposite nanofibers based TENG upto 1.5 wt% of BN-rGO is due to increase in dielectric constant of PVDF nanofiber, after addition of conducting nanofillers (i.e. BN-rGO) which creates the charge trapping sites within the PVDF matrix thus boosting the device performance. Thereafter, on further addition of conductive nanofillers i.e 2 wt% of BN-rGO in PVDF matrix led to formation of conductive network within PVDF matrix, causing the leakage effects and dielectric loss, as a result output performance of TENG decreases. Moreover, the impact of input excitation frequency on the output performance of the PVDF and PVDF nanocomposite nanofibers based TENG is analyzed by tapping the nanogenerator in frequency range 2 Hz to 10 Hz, and cooresponding output voltage and current generated is shown in Figure 5.5 (a-b).

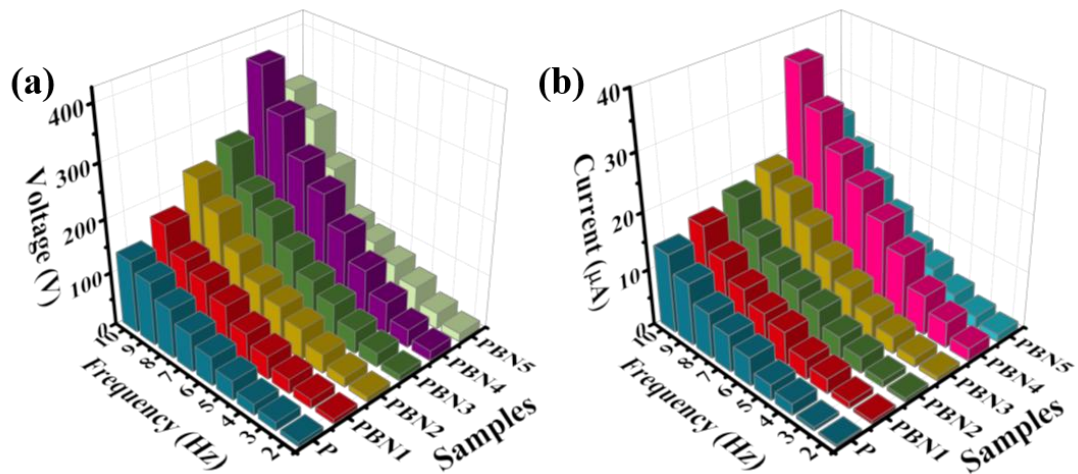


Figure 5.5 (a) The open-circuit voltage, and (b) short-circuit current measurements of electrospun PVDF and PVDF composite nanofibers as a function of varied frequency.

Hence, it can be obtained from the results that 1.5 wt% of BN-rGO is optimum concentration of doping and subsequent analysis of TENG is performed by using PVDF/BN-rGO nanofibers mat with 1.5 wt% of BN-rGO, considering its high performance. Firstly, effect of impact frequency on TENG performance in terms of Voc, Isc, and charge generated is analyzed and their waveforms produced at different

frequencies are illustrated in Figures 5.6 (a-c). A maximum voltage, current and charge of 380 V, 36 μ A and 80 nC is generated by the PVDF/BN-rGO (1.5 wt%) nanofibers mat TENG. The increase in output performance of TENG with rise in the impact frequency is due to the higher charge transfer rate and improved energy transfer efficiency, resulting in higher output performance of TENG [30].

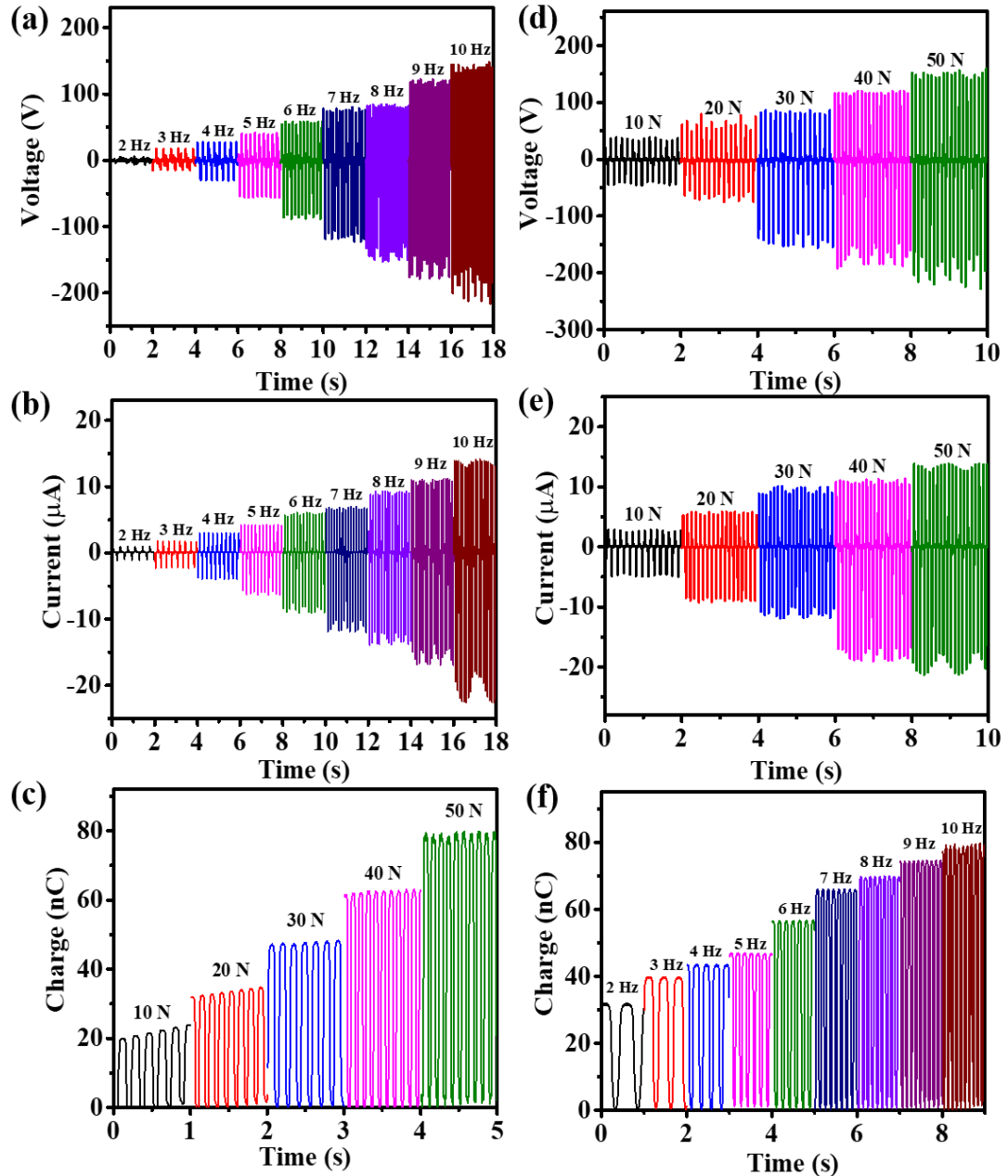


Figure 5.6 The open-circuit voltage, short-circuit current, and charge measurements of electrospun PVDF/BN-rGO (1.5 wt%) composite nanofibers based TENG (a-c) as a function of varied frequency, and (d-f) under different impact force.

Additionally, we have also evaluated the output performance of TENG under different tapping force. Figure 5.6 (d-f) illustrates the V_{oc} , I_{sc} , and charge waveforms of TENG as a function of varied force, ranging from 10 N to 50 N. The improved triboelectric output observed with higher contact force can be attributed to an increase in effective contact area, which facilitates greater triboelectric charge generation.

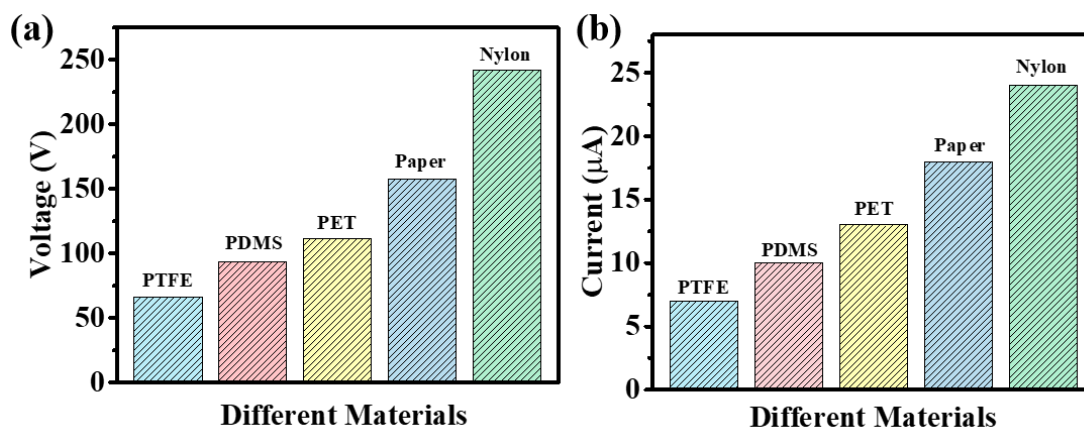


Figure 5.7 (a) The open-circuit voltage, and (b) short-circuit current measurements of electrospun PVDF/BN-rGO (1.5 wt%) composite nanofibers based TENG by varying the second triboelectric layer.

In regard to the analysis of effect of different triboelectric layer on output performance of TENG, we have fixed PVDF/BN-rGO nanofiber mat as first triboelectric layer, while the second layer was systematically varied among different materials: PTFE, PDMS, PET, paper, and nylon. Figure 5.7 depicts the V_{oc} , and I_{sc} generated by TENG by using different triboelectric layer. This approach allowed for a comparative assessment of how each material influences TENG performance. The Figure 5.7 (a-b) illustrates the open-circuit voltage (V_{oc}) and short-circuit current (I_{sc}) generated by the TENG with each of these triboelectric layers, providing insights into the optimal material choice for enhanced energy output. These results demonstrates that the TENG with nylon and PVDF/BN-rGO produces maximum output performance among various materials.

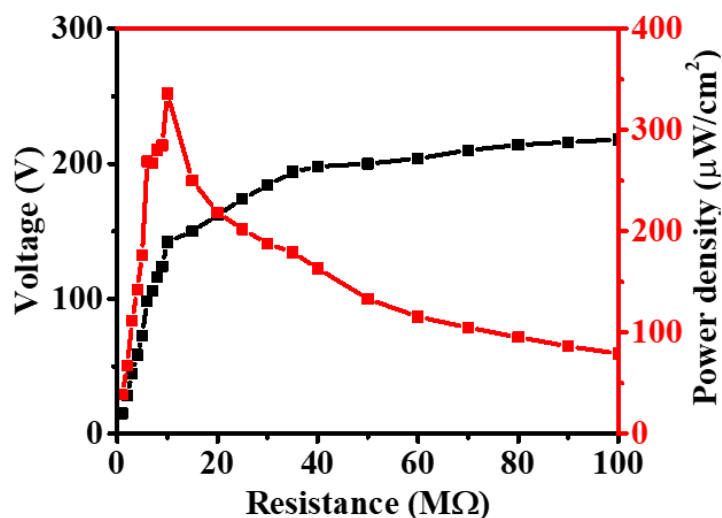


Figure 5.8 The variation of output voltage and power density of PVDF/BN-rGO (1.5 wt %) based TENG as a function of load resistance.

The nanogenerator delivers maximum output power, when the load impedance is optimally matched. Therefore, power density measurements are carried out as a function of varied resistance, which reveals that a maximum power density of $336 \mu\text{W}/\text{cm}^2$ is obtained for TENG at $10 \text{ M}\Omega$ resistance and is illustrated in Figure 5.8. Furthermore, the stability and durability of TENG is assessed by measuring the output current over 1500 s at 8Hz frequency, showing the stable operation of TENG without any degradation in current values (Figure 5.9).

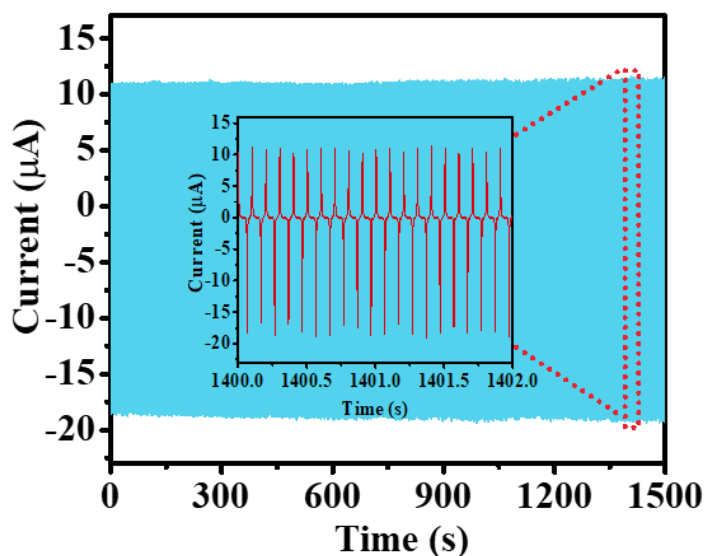


Figure 5.9 Durability of PVDF/BN-rGO (1.5 wt %) nanofiber based TENG with consistent current output over 1500 seconds.

5.4 Application of TENG

5.4.1 TENG as a Power Source for Electrochemical Reduction of Methylene Blue Dye

In order to evaluate the potential application of TENG in wastewater treatment application, a self-powered dye degradation system is constructed by employing TENG as a power source to degrade methylene blue dye from the wastewater, which provides bias potential and current to generate electric field. This electric field accelerates the separation and movement of charge carriers, which in turn enhances the efficiency of degradation processes. By boosting the energy available for carrier transfer, TENGs effectively support faster and more efficient breakdown or degradation of targeted substances. A schematic diagram showing the setup for the self-powered dye degradation system is illustrated in Figure 5.10.

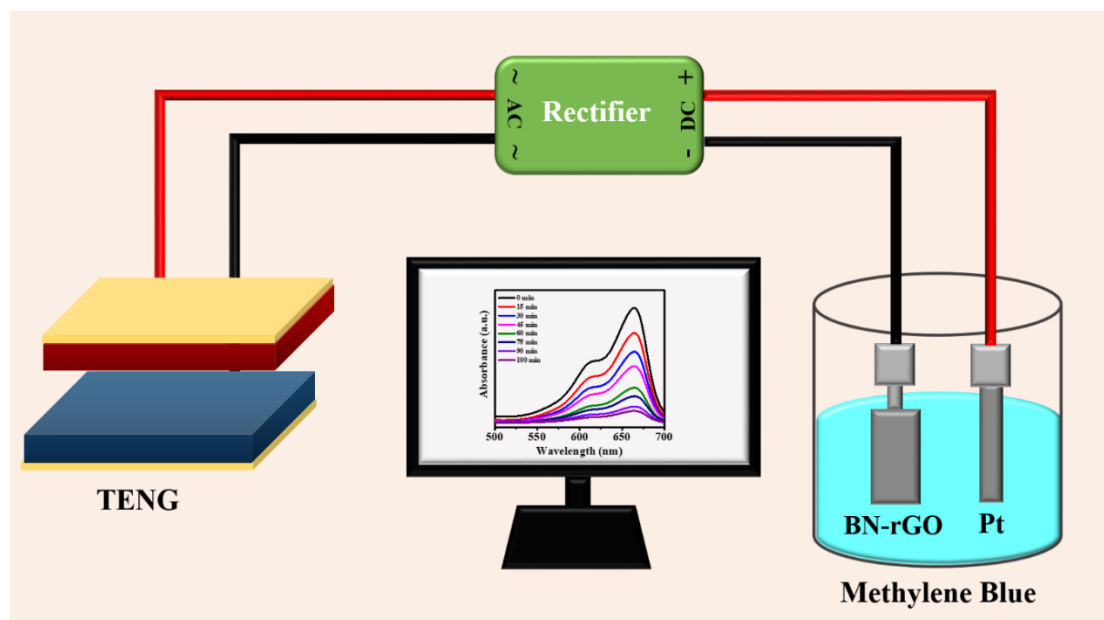


Figure 5.10 A schematic of self-powered dye degradation system for methylene blue dye.

In the typical process, aqueous solution of methylene blue (0.01g/L) is placed in the beaker and platinum wires are used as two working and counter electrodes used in the system. In this work, we have utilized two approaches to assess the decomposition of methylene blue. First is the degradation of dye, where TENG is employed as power source and another is the usage of BN-rGO as a working electrode instead of platinum electrode together with the TENG to degrade the methylene blue dye. Here, prepared solution is stirred at constant speed to maintain uniform concentration and after regular interval of

time, some amount of solution is taken out and its absorbance spectra is recorded. The UV spectra of methylene blue solution and its discoloration process is shown in Figure 5.11(a-b), which shows that characteristic absorption peak of Methylene blue i.e. at 664 nm decrease gradually with increase in degradation time, indicating methylene blue is removed successfully.

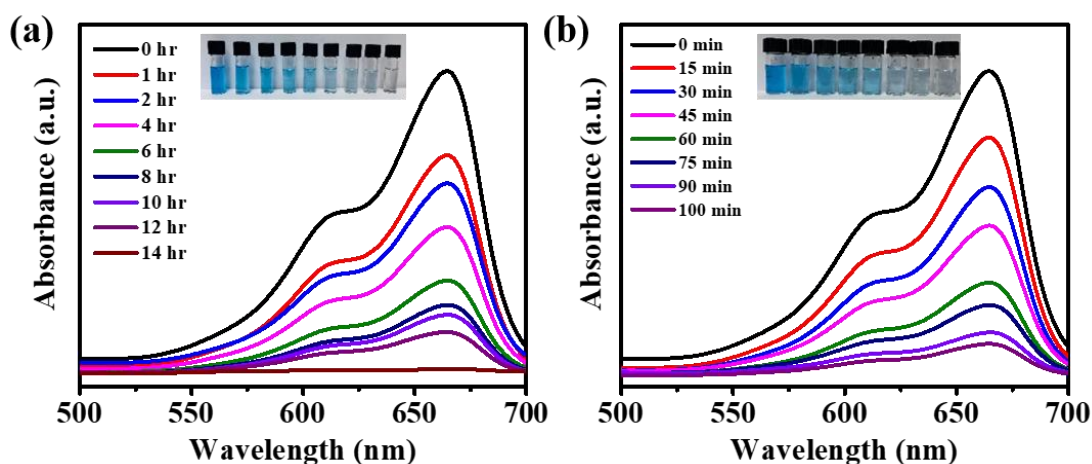
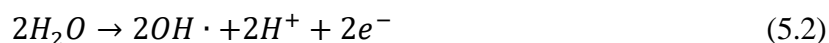
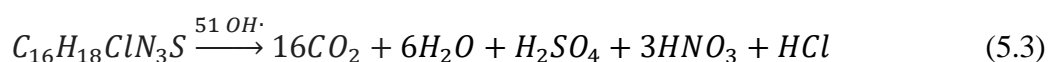


Figure 5.11 UV-vis spectra of dye degradation of methylene blue driven by TENG (a) when platinum is used as active electrodes and, (b) when BN-rGO is used as an active electrode.

When only TENG is employed as power source to degrade the methylene blue dye it takes 14 h to completely degrade the dye, whereas when BN-rGO is used as working electrode instead of platinum, the colour of methylene blue solution decays from blue to colorless within 100 minutes. The faster degradation mechanism in presence of BN-rGO is due to its high surface area and enhanced conductivity and advantage of electron collection and transportation, which makes the degradation process faster [31]. Here, the degradation of organic pollutants follows the direct electron transfer mechanism, where organic pollutants are oxidized on the anode surface by hydroxyl radicals (OH \cdot), which are electrogenerated through the water discharge process and then adsorbed onto the anode and occurs in accordance to following equations[32-34]



These OH radicals then react with methylene blue and result in its breakdown into CO $_2$ and H $_2$ O as given in following reactions



Moreover, pseudo first order kinematics is used to explore the kinematics of degradation of methylene blue dye which can be expressed as

$$kt = -\ln\left(\frac{C}{C_0}\right) \quad (5.4)$$

where C_0 is concentration of methylene blue dye at $t = 0$, C is the concentration at any time t . while k and t are the rate constant and the time in minutes, respectively. The kinetics of electrochemical degradation of methylene is illustrated in Figure 5.12 (a-b). Additionally, after approximately 2 hours, the electrochemical degradation efficiency of the dye reaches 35.55% when powered solely by the TENG. However, when the TENG is paired with a BN-rGO electrode, the dye removal efficiency significantly increases to 86.41%. These results demonstrates the potential application of TENG in wastewater remediation application by using the ambient mechanical energy.

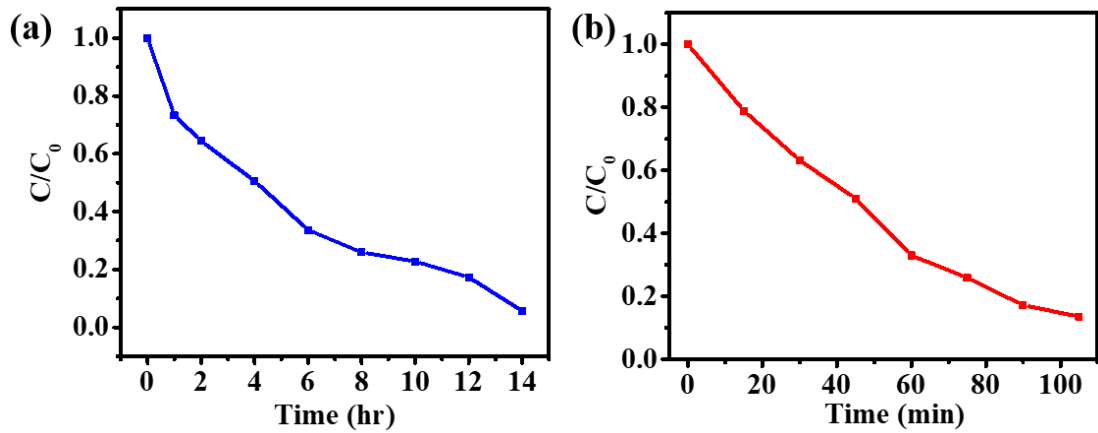


Figure 5.12 The degree of degradation of methylene blue dye driven by TENG (a) when platinum is used as active electrodes and, (b) when BN-rGO is used as an active electrode.

5.5 Summary

In summary, we have successfully optimized the concentration of BN-rGO as nanofillers to design an efficient triboelectric nanogenerator (TENG) and presented a self-powered dye degradation system aimed at removing organic pollutants from wastewater. By adjusting the BN-rGO content within a PVDF matrix, we developed a high-performance TENG that achieves a maximum power density of $336 \mu\text{W}/\text{cm}^2$ at an optimal BN-rGO concentration of 1.5 wt%. The electrical power generated by the TENG is harnessed to degrade the toxic and carcinogenic methylene blue dye through

an oxidation process facilitated by OH radicals at the electrode interface. Furthermore, the study demonstrates that when TENG is used only as a power source, the degradation of methylene blue dye takes 14 hours. However, with BN-rGO as an active electrode and power source, the degradation time is significantly reduced to just 100 minutes. Thus, by leveraging the advantage of TENG and electrode materials, this work introduces an effective approach for converting ambient mechanical energy into stable electrical output, paving the way for advancement in self-powered electrochemical systems for the degradation of organic pollutants in wastewater.

References

- [1] J. Che, Y. Gao, Z. Wu, J. Ma, Z. Wang, C. Liu, Y. Jia, X. Wang, Review on tribocatalysis through harvesting friction energy for mechanically-driven dye decomposition, *Journal of Alloys and Compounds*, 1002 (2024) 175413.
- [2] D. Chen, Y. Cheng, N. Zhou, P. Chen, Y. Wang, K. Li, S. Huo, P. Cheng, P. Peng, R. Zhang, Photocatalytic degradation of organic pollutants using TiO₂-based photocatalysts: A review, *Journal of Cleaner Production*, 268 (2020) 121725.
- [3] B. Zhao, N. Chen, Y. Xue, H. Shi, H. Xu, M. Li, C. Sun, Y. Xing, B. Gao, B. Ma, Challenges and perspectives of tribocatalysis in the treatment for dye wastewater, *Journal of Water Process Engineering*, 63 (2024) 105455.
- [4] S. Ho, Low-cost adsorbents for the removal of phenol/phenolics, pesticides, and dyes from wastewater systems: A review, *Water*, 14 (2022) 3203.
- [5] L. Qi, J. Wang, X. Dai, F. Ning, P. Yang, J. Chen, Y. Li, J. Chen, Y. Zhao, X. Zhang, Interspersed Reticulate Cu₂WS₄ Nanocrystal–PVDF/Ni Triboelectric Nanogenerators for Rhodamine B Degradation, *ACS Applied Nano Materials*, 6 (2023) 22015-22024.
- [6] M. Zhang, W.-Z. Song, T. Chen, D.-J. Sun, D.-S. Zhang, C.-L. Li, R. Li, J. Zhang, S. Ramakrishna, Y.-Z. Long, Rotation-mode liquid-solid triboelectric nanogenerator for efficient contact-electro-catalysis and adsorption, *Nano Energy*, 110 (2023) 108329.
- [7] N. Xuan, C. Song, G. Cheng, Z. Du, Advanced triboelectric nanogenerator based self-powered electrochemical system, *Chemical Engineering Journal*, 481 (2024) 148640.
- [8] Y. Zhou, M. Shen, X. Cui, Y. Shao, L. Li, Y. Zhang, Triboelectric nanogenerator based self-powered sensor for artificial intelligence, *Nano Energy*, 84 (2021) 105887.
- [9] S. Dai, X. Li, C. Jiang, J. Ping, Y. Ying, Triboelectric nanogenerators for smart agriculture, *InfoMat*, 5 (2023) e12391.
- [10] X. Cao, Y. Xiong, J. Sun, X. Xie, Q. Sun, Z.L. Wang, Multidiscipline applications of triboelectric nanogenerators for the intelligent era of internet of things, *Nano-Micro Letters*, 15 (2023) 14.

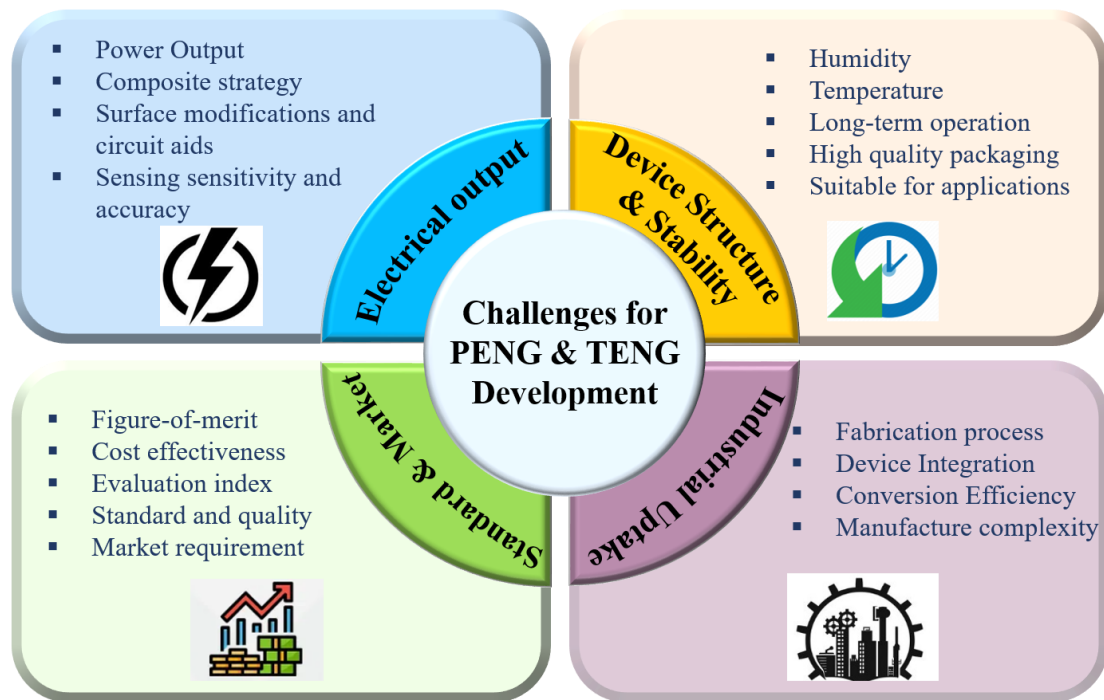
- [11] Z. Liu, H. Li, B. Shi, Y. Fan, Z.L. Wang, Z. Li, Wearable and implantable triboelectric nanogenerators, *Advanced Functional Materials*, 29 (2019) 1808820.
- [12] Z.L. Wang, T. Jiang, L. Xu, Toward the blue energy dream by triboelectric nanogenerator networks, *Nano Energy*, 39 (2017) 9-23.
- [13] X. Cao, Y. Jie, N. Wang, Z.L. Wang, Triboelectric nanogenerators driven self-powered electrochemical processes for energy and environmental science, *Advanced Energy Materials*, 6 (2016) 1600665.
- [14] D. San Roman, D. Krishnamurthy, R. Garg, H. Hafiz, M. Lamparski, N.T. Nuhfer, V. Meunier, V. Viswanathan, T. Cohen-Karni, Engineering three-dimensional (3D) out-of-plane graphene edge sites for highly selective two-electron oxygen reduction electrocatalysis, *ACS catalysis*, 10 (2020) 1993-2008.
- [15] Y. Zhu, M. Tian, Y. Chen, Y. Yang, X. Liu, S. Gao, 3D printed triboelectric nanogenerator self-powered electro-Fenton degradation of orange IV and crystal violet system using N-doped biomass carbon catalyst with tunable catalytic activity, *Nano Energy*, 83 (2021) 105824.
- [16] S. Rana, V. Singh, B. Singh, Tailoring the Output Performance of PVDF-Based Piezo-Tribo Hybridized Nanogenerators via B, N-Codoped Reduced Graphene Oxide, *ACS Applied Electronic Materials*, 4 (2022) 5893-5904.
- [17] J. Zheng, A. He, J. Li, C.C. Han, Polymorphism control of poly (vinylidene fluoride) through electrospinning, *Macromolecular rapid communications*, 28 (2007) 2159-2162.
- [18] T. Bhatta, P. Maharjan, H. Cho, C. Park, S.H. Yoon, S. Sharma, M. Salauddin, M.T. Rahman, S.M.S. Rana, J.Y. Park, High-performance triboelectric nanogenerator based on MXene functionalized polyvinylidene fluoride composite nanofibers, *Nano Energy*, 81 (2021) 105670.
- [19] S. Rana, B. Singh, rGO-Embedded Polymer Nanocomposite Layer for Improved Performance of Triboelectric Nanogenerator, *Journal of Electronic Materials*, 53 (2024) 6640-6649.
- [20] H.H. Singh, S. Singh, N.J.C.S. Khare, Technology, Design of flexible PVDF/NaNbO₃/RGO nanogenerator and understanding the role of nanofillers in the output voltage signal, 149 (2017) 127-133.

- [21] X. Cai, T. Lei, D. Sun, L. Lin, A critical analysis of the α , β and γ phases in poly (vinylidene fluoride) using FTIR, RSC Advances, 7 (2017) 15382-15389.
- [22] B. Jaleh, A. Jabbari, Evaluation of reduced graphene oxide/ZnO effect on properties of PVDF nanocomposite films, Applied Surface Science, 320 (2014) 339-347.
- [23] S.S. Nardekar, K. Krishnamoorthy, P. Pazhamalai, S. Sahoo, S.J. Kim, MoS₂ quantum sheets-PVDF nanocomposite film based self-poled piezoelectric nanogenerators and photovoltaically self-charging power cell, Nano Energy, 93 (2022) 106869.
- [24] R. Bhunia, S. Gupta, B. Fatma, Prateek, R.K. Gupta, A. Garg, Milli-Watt Power Harvesting from Dual Triboelectric and Piezoelectric Effects of Multifunctional Green and Robust Reduced Graphene Oxide/P(VDF-TrFE) Composite Flexible Films, ACS Applied Materials & Interfaces, 11 (2019) 38177-38189.
- [25] S.K. Karan, D. Mandal, B.B. Khatua, Self-powered flexible Fe-doped RGO/PVDF nanocomposite: an excellent material for a piezoelectric energy harvester, Nanoscale, 7 (2015) 10655-10666.
- [26] Z.L. Wang, On Maxwell's displacement current for energy and sensors: the origin of nanogenerators, Materials today, 20 (2017) 74-82.
- [27] G. Li, J. Zhang, F. Huang, S. Wu, C.-H. Wang, S. Peng, Transparent, stretchable and high-performance triboelectric nanogenerator based on dehydration-free ionically conductive solid polymer electrode, Nano Energy, 88 (2021) 106289.
- [28] S. Tu, Q. Jiang, X. Zhang, H.N. Alshareef, Large dielectric constant enhancement in MXene percolative polymer composites, ACS nano, 12 (2018) 3369-3377.
- [29] S. Jang, H. Kim, Y. Kim, B.J. Kang, J.H. Oh, Honeycomb-like nanofiber based triboelectric nanogenerator using self-assembled electrospun poly (vinylidene fluoride-co-trifluoroethylene) nanofibers, Applied Physics Letters, 108 (2016).
- [30] J. Chun, B.U. Ye, J.W. Lee, D. Choi, C.-Y. Kang, S.-W. Kim, Z.L. Wang, J.M. Baik, Boosted output performance of triboelectric nanogenerator via electric double layer effect, Nature communications, 7 (2016) 12985.

- [31] J. Singh, A.S. Dhaliwal, Electrochemical and photocatalytic degradation of methylene blue by using rGO/AgNWs nanocomposite synthesized by electroplating on stainless steel, *Journal of Physics and Chemistry of Solids*, 160 (2022) 110358.
- [32] A.Y. Goren, Y.K. Receptoğlu, Ö. Edebali, C. Sahin, M. Genisoglu, H.E. Okten, Electrochemical Degradation of Methylene Blue by a Flexible Graphite Electrode: Techno-Economic Evaluation, *ACS Omega*, 7 (2022) 32640-32652.
- [33] A. Baddouh, M.M. Rguiti, B. El Ibrahimi, S. Hussain, M. Errami, V. Tkach, L. Bazzi, M. Hilali, Anodic oxidation of methylene blue dye from aqueous solution using SnO₂ electrode, *Iranian journal of chemistry and chemical engineering*, 38 (2019) 175-184.
- [34] M. Panizza, A. Barbucci, R. Ricotti, G. Cerisola, Electrochemical degradation of methylene blue, *Separation and Purification Technology*, 54 (2007) 382-387.

CHAPTER 6

Conclusions and Future Scope of Work



This chapter provides a comprehensive summary of the primary conclusions derived from the research presented in this thesis. It also outlines potential future directions that could extend and deepen the scope of the current research, identifying areas for continued exploration and potential innovation. These prospective pathways are intended to guide future studies, building on the foundation established in this thesis to further advance knowledge and applications in energy harvesting technology.

6.1 Summary of Research Work

This thesis addresses the development and enhancement of energy-harvesting technologies, specifically focusing on piezoelectric and triboelectric nanogenerators for applications in wearable electronics, wireless sensing, and environmental remediation. In light of increasing global energy demands, the need for sustainable solutions is paramount, especially in the realm of low-power, autonomous devices like those used in healthcare, AI, and IoT. This work delves into the fabrication, optimization, and application of PVDF-based piezoelectric and triboelectric nanogenerators, analyzing how nanofillers enhance the output performance of these devices. Key challenges in capturing ambient mechanical energy have been identified and effectively addressed through the following approaches. Firstly, reduced graphene oxide and its heteroatom dopant variants i.e. boron, nitrogen and boron nitrogen co-doped rGO were successfully synthesized via hydrothermal method and employed as effective nanofillers to improve the output performance of piezoelectric nanogenerators. The results demonstrate that these nanofillers significantly improve the output performance, with the PVDF/BN-rGO-based PENG generating a maximum voltage of 20.4 V and current of 15.9 μ A. This enhanced performance is attributed to the nucleation of electroactive polar β -phase content in the PVDF nanocomposite films, along with the formation of a conductive network within the polymer matrix that facilitates better charge transfer, thereby increasing the overall output. The study also explored the effect of varying input frequencies on the performance of all piezoelectric nanogenerators (PENGs), finding that each device achieved peak performance at a frequency of 6 Hz. The potential application of PENG was demonstrated by effectively harnessing biomechanical energy from human motions. Thereafter, to further boost performance, a hybrid nanogenerator (HNG) combining piezoelectric and triboelectric effects was developed by layering the PVDF/BN-rGO film with PDMS. This HNG achieved a maximum output voltage of 57.6 V and was able to charge capacitors and power devices like LEDs and calculators. Overall, this study demonstrates that incorporating graphene derivatives into PVDF matrices significantly enhances energy harvesting efficiency, providing a promising solution for self-powered wearables and portable electronics. Secondly, this thesis explores the effects of rGO and nitrogen-doped rGO (N-rGO) concentrations in PVDF

films to optimize TENG performance. The research involved optimizing the nanofillers concentration and employing electrospinning technique, which improves surface-to-volume ratio, thereby increasing effective contact area and charge density of triboelectric layers. For this purpose, we fabricated various triboelectric energy harvesters using PVDF nanocomposite films and nylon film, adjusting the weight percentage of rGO and N-rGO in the PVDF matrix by drop-casting method. Compared to the bare PVDF film, the TENG with 1.5 wt% rGO and N-rGO achieved maximum output voltages of 98.4 V and 156 V at 8 Hz, respectively, while the undoped PVDF film-based TENG produced only 67.2 V. These results indicate that 1.5 wt% is the optimal concentration for rGO and N-rGO, as higher concentrations result in performance decline due to the formation of a conductive network within the PVDF matrix. Additionally, N-rGO-based TENGs produced higher output than those with pure rGO, likely due to the higher capacitance of N-rGO. Further, we fabricated nanofiber mats of PVDF and PVDF/N-rGO with 1.5 wt% N-rGO and nylon using electrospinning. This approach yielded a maximum voltage, current, and power density of 368 V, 35 μA , and $\sim 282.8 \mu\text{W}/\text{cm}^2$ respectively under impedance-matching conditions. In addition, effects of tapping frequency and impact force on TENG performance was also analyzed showing that increased frequency and force improve output performance of TENG by enhancing charge transfer and effective contact area. COMSOL software were used to simulate the surface potential relationship between the two TENG layers. The TENG was successfully used to power small electronics and functioned as a self-powered motion sensor, showcasing its potential for cost-effective, high-performance energy harvesting in human-machine interfaces and wireless sensing systems.

Finally, to expand the TENG applications, PVDF nanofibers doped with boron-nitrogen co-doped rGO (BN-rGO) were tested for efficient energy harvesting and environmental remediation. Optimal energy output was achieved with a BN-rGO concentration of 1.5 wt%, yielding peak values of 380 V, 36 μA , and $336 \mu\text{W}/\text{cm}^2$ respectively. We have also explored the influence of different counter triboelectric layers by replacing nylon with PTFE, PDMS, PET, paper, and nitrile gloves. Among these, the PVDF/BN-rGO paired with nylon exhibited the best output, potentially due to the higher electronegativity

difference between PVDF/BN-rGO and nylon. Finally, we developed a self-powered dye degradation system using the TENG as an energy source to degrade methylene blue dye in wastewater. Without a catalyst, the TENG-enabled system required 12 hours for complete degradation. However, when combined with a catalyst, the degradation time was significantly reduced to just 100 minutes. This study highlights the potential of an efficient, sustainable TENG-catalyst system for wastewater remediation using mechanical energy. Together, these studies highlight the promise of doped rGO nanofillers in improving the performance of flexible nanogenerators, showcasing applications from self-powered devices to environmental remediation systems. This work contributes valuable insights toward the development of cost-effective, high-performance energy harvesters for the next generation of sustainable technologies.

6.2 Future Prospective

The ultimate objective of energy harvesting technology is to design self-sufficient and fully operational systems that do not rely on external power sources for their operation. By addressing the current challenges and limitations, the present thesis highlights several promising directions for developing efficient piezoelectric and triboelectric nanogenerators to power modern portable and wearable devices, as well as wireless self-powered sensors. The following areas present opportunities for further investigation:

1. **Material Innovation and Optimization:** Developing new materials with enhanced mechanical and electrical properties can dramatically improve energy conversion efficiency. Future research could focus on discovering or synthesizing materials that offer higher durability, flexibility, and compatibility under various environmental conditions, enabling broader applications of nanogenerators.
2. **Advanced Structural Design:** Optimizing the architecture of nanogenerators, such as incorporating micro- or nanoscale features, could enhance energy harvesting performance. Research on structural modifications, like layered or porous designs, can increase the effective surface area and improve interaction with mechanical stimuli, thereby boosting energy output.
3. **Surface Modification Techniques:** Techniques like nanopatterning, ion irradiation, and lithography can enhance surface characteristics, making nanogenerators more

efficient. Further studies on these techniques could improve the charge transfer processes and make the devices more responsive to mechanical forces.

4. **Hybrid Energy Harvesting Systems:** As the current generated by the PENG and TENG are still low to expand its horizon of applications. Therefore, by integrating mechanical energy harvesters with other energy harvesting systems, such as electromagnetic or pyroelectric devices, holds potential for multi-source energy collection and improves the power density of device. This hybrid approach could lead to devices capable of simultaneously harvesting energy from various ambient sources, creating more reliable and consistent power outputs.
5. **Integration with Energy Storage Systems:** Pairing energy harvesters with efficient storage systems, like supercapacitors or batteries, is crucial for practical applications. Future research could focus on seamless integration of nanogenerators with storage systems, allowing for stable energy supply in off-grid or portable electronics and wearable devices.
6. **Advanced Power Management Circuits:** Efficient power management circuits are crucial for optimizing the output of nanogenerators. These circuits regulate and store the harvested energy, matching the circuit impedance to the nanogenerators output to reduce conversion losses. Future studies could focus on designing circuits with high power conversion efficiency, adaptable power conditioning, and reliable energy storage, ensuring consistent operation across diverse energy inputs.
7. **Exploring Environmental and Biocompatible Applications:** Developing nanogenerators for applications in biocompatible and eco-friendly devices will require materials that are safe and sustainable. Research into biodegradable materials for short-term applications or non-toxic, stable alternatives for long-term use can extend the applicability of nanogenerators to fields like biomedical devices and environmental sensing. In the healthcare sector, self-powered devices for monitoring or therapeutic applications are highly desirable. Future work could involve developing nanogenerators that harness biomechanical energy, such as body movements, to power sensors, pacemakers, or drug delivery systems, reducing reliance on conventional batteries.

8. **Application-Specific Customization and Optimization:** Future work should focus on tailoring nanogenerator designs to meet specific application requirements. For example, wearable electronics may need lightweight, flexible nanogenerators with high power density and low mechanical stiffness, while industrial sensors might prioritize durability and higher energy outputs. Further exploration into specialized designs and application-driven optimizations can improve the practical viability of these devices.

By exploring these areas, future research can build on the insights from this thesis to expand the capabilities and applications of mechanical energy harvesting technologies, making them viable for a wide range of practical and sustainable uses.

Review

Recent trends in 2D materials and their polymer composites for effectively harnessing mechanical energy

Shilpa Rana,¹ Vishal Singh,¹ and Bharti Singh^{1,*}

SUMMARY

Self-powered wearable devices, with the energy harvester as a source of energy that can scavenge the energy from ambient sources present in our surroundings to cater to the energy needs of portable wearable electronics, are becoming more widespread because of their miniaturization and multifunctional characteristics. Triboelectric and piezoelectric nanogenerators are being explored to harvest electrical energy from the mechanical vibrations. Integration of these two effects to fabricate a hybrid nanogenerator can further enhance the output efficiency of the nanogenerator. Here, we have discussed the importance of 2D materials which plays an important role in the fabrication of nanogenerators because of their distinct characteristics, such as, flexibility, mechanical stability, nontoxicity, and biodegradability. This review mainly emphasizes the piezoelectric, triboelectric, and hybrid nanogenerator based on the 2D materials and their van der Waals heterostructure, as well as the effect of polymer-2D composite on the output performance of the nanogenerator.

INTRODUCTION

The rapid growth in population and industrialization has aggravated the significant ecological deterioration and energy crisis worldwide due to the consumption and depletion of fossil fuels. Fossil fuels provide the most significant contribution as a common energy source, but their limited reserve in nature makes it difficult to provide it for the future generation. Therefore, several efforts have been made by the scientific community over the past decades by exploring sustainable, renewable, and green energy sources to fulfill the future demand of energy in an effective and environment-friendly way. Besides this, with the forthcoming Internet of things (IoT) and artificial intelligence era, the need for smart electronics with multiple functionalities, portable, flexible, and miniaturization concepts are highly desirable (Liu et al., 2019, 2021a, 2021b). Till now, most of the energy requirements in the electronic devices are fulfilled by the batteries even though it endows several drawbacks due to their short life span, durability, short charging/discharging, heavyweight, rigid, bulky, and overheating nature (Armand and Tarascon, 2008; Van Noorden, 2014). This results in an exacerbated overall performance in the context of portability and wearability of such devices. Because some of these electronic devices work only a few hours, energy harvesting/storage devices with high energy density and capacities are required to meet the growing demand for energy to address the emerging energy needs. Therefore, a self-powered electronic device, with the energy harvester as the source of energy that can scavenge the energy from ambient sources present in our surrounding to power up its electronic components and sensors, as well as storing the excess energy for later use for continuous and stable operation, has become a viable alternative for the cumbersome batteries that require frequent recharge/replacement. Such technologies are especially vital for medical applications. So far, various energy harvesting technologies have been developed as a means to supply power to these electronic devices to form a self-powered system, such as, photovoltaic cells for harnessing solar energy (Behura et al., 2019); piezoelectric (Jung et al., 2011) and triboelectric nanogenerator (TENG) (Niu and Wang, 2015) for harnessing mechanical energy; thermoelectric (Xie et al., 2017) and pyroelectric generator (Yang et al., 2012) for harnessing thermal energy. Among these energy harvesting technologies, mechanical energy harvesting is of the utmost importance because of its omnipresence which is not restricted by weather, space, and time, unlike solar energy harvesters where the performance of solar cells is strongly dependent on the light illumination and weather conditions; and thermal energy harvesters, which has a disadvantage due to small thermal gradients and low efficiency.

¹Department of Applied Physics, Delhi Technological University, Main Bawana Road, Delhi 110042, India

*Correspondence: bhartisingh@dtu.ac.in
<https://doi.org/10.1016/j.isci.2022.103748>



Tailoring the Output Performance of PVDF-Based Piezo–Tribo Hybridized Nanogenerators via B, N-Codoped Reduced Graphene Oxide

Shilpa Rana, Vishal Singh, and Bharti Singh*

Cite This: *ACS Appl. Electron. Mater.* 2022, 4, 5893–5904

Read Online

ACCESS |



Metrics & More



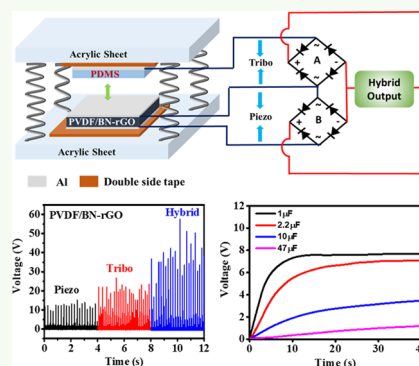
Article Recommendations



Supporting Information

ABSTRACT: Recently, piezoelectric and triboelectric nanogenerators are explored extensively for harvesting energy from mechanical vibrations via piezoelectric and triboelectric effects. The output efficiency of these nanogenerators can be improved further by combining their piezoelectric and triboelectric effects to fabricate a hybrid nanogenerator. In the present work, first, piezoelectric energy harvesters are fabricated to investigate the effects of the introduction of reduced graphene oxide (rGO), single-heteroatom (N)-doped rGO, and boron/nitrogen-codoped rGO in enhancing the piezoelectric performance of a poly(vinylidene fluoride) (PVDF)-based nanogenerator. Then, the film showing the highest piezoelectric performance (i.e., PVDF/BN-rGO) is coupled with a PDMS film to fabricate a hybrid nanogenerator. In comparison to a pristine PVDF-based nanogenerator, the PVDF/BN-rGO-based piezoelectric nanogenerator device exhibits ~ 2 times enhancement in output voltage and ~ 6 times enhancement in piezoelectric current, whereas the hybrid nanogenerator with the corresponding composite film shows better electrical performance, producing an output voltage and current of 57.6 V and 28.8 μ A, respectively. The improved performance of the nanogenerator is ascribed to the synergistic effect of piezoelectric and triboelectric effects together with the addition of codoped rGO in the PVDF matrix, which increases the remnant polarization and dielectric property of the PVDF nanocomposite film. Finally, the output generated by the hybrid nanogenerator is used to power 15 light-emitting diodes (LEDs) and a calculator. The present work has shown the importance of rGO and its derivatives for energy harvesting applications.

KEYWORDS: piezoelectricity, triboelectricity, hybrid nanogenerator, reduced graphene oxide, energy harvesting



1. INTRODUCTION

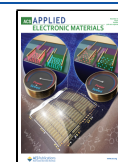
An upsurge in the growing energy demands, with the development of the internet of things (IoT), portable electronics, and wearable/wireless technologies, has sparked great interest in the field of energy-harvesting technologies. Among the various energy-harvesting technologies, scavenging of electrical energy from wasted mechanical energy via piezoelectric and triboelectric effects has stirred up a huge interest not only in overcoming energy crisis issues to power microelectronic systems but also in realizing their application in designing a flexible, wearable, self-powered system.^{1–4} On the one hand, piezoelectric nanogenerator (PENG) devices have profound great importance in energy harvesting due to their thin, highly flexible, and mechanical stretchable nature (in some cases), which allows them to be mounted on any type of surface. However, there has been only a minor improvement in the output performance of nanogenerators from a few nW to a few μ W since the invention of the first PENG, which hinders their application in high-powered devices,^{5,6} whereas on the other hand, a triboelectric nanogenerator (TENG) based on triboelectrification and electrostatic induction has been demonstrated to generate more output power with a high

energy conversion efficiency (85%), and its diverse material choice, simple structure, cost effectiveness, and ease of fabrication make it more promising to scavenge energy under different small mechanical and biomechanical actions with variable amplitude and frequency.^{7–9} However, standard practices used for enhancing the performance of TENGs, such as physical and chemical surface modification,¹⁰ charge injection,¹¹ printing of a specific structure,⁴ and electric polarization,¹² are complex and difficult to implement on a large scale. Therefore, coupling/integration of both piezoelectric and triboelectric effects to collect more energy from a single source (mechanical energy) is a promising approach for developing a self-powered sustainable power source with enhanced energy conversion efficiency.¹³ This is because the

Received: August 17, 2022


Accepted: November 1, 2022

Published: November 17, 2022





Polymer nanocomposite film based piezoelectric nanogenerator for biomechanical energy harvesting and motion monitoring

Shilpa Rana¹, and Bharti Singh^{1,*} 

¹ Department of Applied Physics, Delhi Technological University, Main Bawana Road, Delhi 110042, India

Received: 3 April 2023

Accepted: 24 August 2023

Published online:
4 September 2023

© The Author(s), under
exclusive licence to Springer
Science+Business Media, LLC,
part of Springer Nature, 2023

ABSTRACT

With the advancement in the wearable technologies such as, smart watches, electronic skin, and wearable portable device, scavenging the biomechanical energy from human movements have gained considerable attention for designing self-sustainable power system. Here, we have reported a flexible piezoelectric device that can be conformably adhered to the human body in order to harness the energy from diversification of touch and motion. For this, we have fabricated a polyvinyl difluoride (PVDF) polymer based flexible piezoelectric nanogenerator (PNG) device that can harness energy from various human motions and convert it to useful electrical energy. To further improve the performance of PVDF based nanogenerator, hydrothermally synthesized nanosheets of reduce graphene oxide (rGO) and boron doped rGO are embedded in PVDF matrix as a conductive nanofiller materials to enhance the device output performance. Among all fabricated devices based on pristine PVDF (P), rGO doped PVDF (PR) and, boron doped rGO (PBR), the latter generates a maximum voltage and power density of 13.8 V and $\sim 42.3 \mu\text{W}/\text{cm}^2$ respectively, which is then used to light up series of commercially available LEDs. Finally, PBR film based PNG is demonstrated to harvest energy from different types of human motion which includes finger tapping, elbow bending, foot tapping, leg folding, and wrist movements. This device demonstrates the potential use of polymer nanocomposite films in self-powered wearable devices.

1 Introduction

With the technological advancement, flexible, wearable and, miniaturized microelectronic devices with diverse functionality are rapidly becoming the part of our mundane life by affecting various aspects of human life from health monitoring, and entertainment to information and communication technology [1, 2]. One of the

important factors for continuous and stable operation of these flexible and wearable electronic devices is the sustainable power supply. Till now, batteries have been used as one of the most reliable and economical sources to supply power to these electronic devices but their frequent recharging and replacement process, bulky nature and disposal difficulty are becoming challenge for their long term application and environmental safety [3, 4].

Address correspondence to E-mail: bhartisingh@dtu.ac.in



rGO-Embedded Polymer Nanocomposite Layer for Improved Performance of Triboelectric Nanogenerator

Shilpa Rana¹ · Bharti Singh¹

Received: 7 January 2024 / Accepted: 29 August 2024 / Published online: 12 September 2024
© The Minerals, Metals & Materials Society 2024

Abstract

A triboelectric nanogenerator (TENG) working on a contact electrification and electrostatic induction principle is a promising energy source for fulfilling the energy demand of low power electronic devices by converting the ambient mechanical energy to useful electrical energy. Here, a polymer nanocomposite film-based triboelectric nanogenerator has been designed by embedding reduced graphene oxide (rGO) nanosheets in a polyvinylidene fluoride (PVDF) matrix as one of the friction layers. The PVDF nanocomposite film-based TENG was constructed and examined for structural, electrical, and surface properties with varied weight percentages of rGO nanofillers (0.0 wt%, 0.5 wt%, 1.0 wt%, 1.5 wt%, and 2.0 wt%). The experimental results demonstrate that the addition of rGO in a PVDF matrix considerably increased the output performance of the TENG device. The TENG device with 1.5 wt% of rGO can deliver the maximum output voltage and current of 95.9 V, and 16.8 μ A, respectively, which are ~ 3 and ~ 7 times the voltage and current produced by pristine PVDF film-based TENG. The enhanced performance of the nanogenerator is attributed to the addition of conductive nanofillers in the polymer matrix which improves the surface charge density of polymer nanocomposite films by forming a conduction network, resulting in more effective charge transfer. Moreover, the output of the nanogenerator is stored in the capacitor and used to drive commercial LEDs, revealing the TENGs' potential applications for designing self-powered electronic devices.

Keywords Triboelectrification · Nanogenerator · Energy harvesting · rGO

Introduction

The global energy crisis with the technological advancement and increase in the human population has become one of the major problems that has motivated researchers all over the world to actively seek for innovative solutions to generate electricity from unconventional renewable energy sources. In light of this, various technologies have been developed and studies are still ongoing to harvest energy from sustainable energy sources, such as solar, thermal, vibration, wind, etc.^{1–4} Among these technologies, triboelectric nanogenerators (TENGs) operating on the principle of triboelectrification and electrostatic induction have garnered considerable attention as an innovative technology which converts

mechanical energy from diverse sources into electrical energy. Because of their working principle, TENGs possess several advantages over other energy-harvesting devices due to their outstanding performance in energy harvesting with strong output signals, cost-effectiveness, robustness, simple design, and abundant choice of materials.^{5–7} Also, it is well known that the surface charge density of triboelectric materials has a significant impact on TENGs' output performance. Therefore, various methods have been adopted by researchers to improve the TENG performance, among which two major approaches are (1) to select a suitable friction material with markedly different polarities and structural optimization, as the performance of the device greatly depends on the structure and material selection, and (2) surface modification with micro-/nanostructure formation, doping composition, and charge injection to improve and regulate the friction ignition effect.^{8–10} Many materials, organic, inorganic, polymer, etc., have been explored since the invention of the TENG in 2012, and their triboelectric series have been made in which polymers currently dominate the triboelectric series

✉ Bharti Singh
bhartisingh@dtu.ac.in

¹ Department of Applied Physics, Delhi Technological University, Main Bawana Road, Delhi 110042, India



PVDF/N-rGO nanofibers based sustainable triboelectric nanogenerator for self-powered wireless motion sensor

Shilpa Rana^a, Himani Sharma^b, Renuka Bokolia^a, Kamlesh Bhatt^c, Rajendra Singh^c,
Ramcharan Meena^d, Bharti Singh^{a,*}

^a Department of Applied Physics, Delhi Technological University, Main Bawana Road, Delhi, 110042, India

^b Department of Physics, Doon University, Dehradun, 248001, India

^c Department of Physics, Indian Institute of Technology Delhi, Hauz Khas, New Delhi, 110016, India

^d Materials Science Division, Inter-University Accelerator Centre, New Delhi, 110067, India

ARTICLE INFO

Keywords:

Self-powered sensor
Mechanical energy harvesting
Sustainable power source
PVDF/N-rGO nanofibers mat

ABSTRACT

The wireless sensor networks, a critical component of Internet of Things (IoT) play a pivotal role in smart era where numerous microelectronic devices, sensors are connected wirelessly to one another. However, the need for massive distributed energy for perpetual operation of sensors and wireless transmission modules has become a major issue. Therefore, to address these issues, we have designed a self-powered motion sensor using PVDF and nitrogen doped rGO (N-rGO) nanocomposite film. The fabricated triboelectric nanogenerator (TENG) enables real-time control in human machine interface by wirelessly transmitting sensing data obtained from real time human motion detection for smart home. By employing nanofillers and electrospinning techniques, a significant enhancement in electrical performance of PVDF based TENG is achieved. PVDF/N-rGO(1.5 wt%) nanofiber-based TENG exhibits superior performance compared to conventional PVDF film based TENGs prepared using drop casting techniques, delivering maximum output voltage, current, and power density of 368 V, 35 μ A and 282.8 μ W/cm² respectively. Furthermore, real-time application of TENG is illustrated by powering electronic devices and harnessing mechanical energy from human movements. These findings provide valuable insights into the development of self-powered human-machine interface for managing wireless sensing system.

1. Introduction

The advent of 5G technologies and the internet of things (IoT) era where numerous electronic devices and sensors are interconnected and constantly communicating with each other have significantly impacted human lives [1–3]. On the one hand, these technologies require a widely distributed smart sensors and wireless transmission modules to ensure the successful interaction between humans and electronic devices. Whereas, on the other side power consumption of these electronics have become the major issue because of their multifunctional nature and miniaturization. Till now, batteries and electrical cable power supply have served the purpose of powering these device but they are inefficient and ineffective because of their short lifespan, which necessitate frequent recharging and replacement; environmental hazardous; and distribution of these device and sensors in remote and harsh environment where it become difficult to provide wired supply to devices all the time [4,5]. In this regard, self-powered devices and sensors that can

work efficiently and sustainably without any external power source are highly desirable [6,7]. Many promising clean alternatives for energy harvesting technologies have come fore in this regard which can not only offset the shortcomings of limited lifespan of batteries but also helps in designing self-sustained power system by harnessing the ambient energy present in our surrounding which includes solar energy, biochemical energy, thermal energy, mechanical energy. Among, various form of energy, mechanical energy is extensively prevalent and is largely unaffected by weather, time and working environment constraints. Specifically, triboelectric nanogenerator based on the conjunction of tribology and interfacial charge transfer is considered as a potential candidate for designing self-sufficient power system which can also operate as self-powered sensor by harvesting energy from various mechanical motions in our day to day life including human motion, vibration, water waves, friction, rotation etc. [8,9] Beside this, TENG also bestow superior advantages over the other energy harvesting technologies such as high efficiency, diverse material choice, ease of

* Corresponding author.

E-mail address: bhartisingh@dtu.ac.in (B. Singh).

<https://doi.org/10.1016/j.carbon.2024.119926>

Received 7 September 2024; Received in revised form 9 December 2024; Accepted 15 December 2024

Available online 17 December 2024

0008-6223/© 2024 Elsevier Ltd. All rights are reserved, including those for text and data mining, AI training, and similar technologies.

Bio-data

Shilpa Rana is a research scholar at Delhi Technological University (DTU), Delhi, where she has been conducting research in the Department of Applied Physics since July 2019. She holds a Master's degree in Condensed Matter Physics from the Department of Physics, Deenbandhu Chhotu Ram University of Science and Technology, Murthal Sonapat (Haryana), in year 2017. She also earned a Bachelor of Science (Physics Hons) from the University of Delhi in 2014. She has been recognized for her academic excellence, receiving the Commendable Research Award from DTU in both 2023 and 2024. Her current research focuses on the fabrication of efficient piezoelectric and triboelectric nanogenerators for various applications.